UTS UNIVERSITY
OF TECHNOLOGY
SYDNEY

Assessment of Seismic Behaviour of Large LNG Tanks Considering Soil- Foundation- Structure Interaction

by Noor Sharari

Thesis submitted in fulfilment of the requirements for
the degree of

Doctor of Philosophy

under the supervision of: A/Prof. Behzad Fatahi
Prof. Hadi Khabbaz
Dr. Aslan Hokmabadi

University of Technology Sydney
Faculty of Engineering and Information Technology (FEIT)

July 2022

CERTIFICATE OF ORIGINAL AUTHORSHIP

I, **Noor Sharari,** declare that this thesis, is submitted in fulfilment of the requirements for the award of Doctor of Philosophy, in the School of Civil and Environmental Engineering at the University of Technology Sydney.

This thesis is wholly my own work unless otherwise reference or acknowledged. In addition, I certify that all information sources and literature used are indicated in the thesis.

This document has not been submitted for qualifications at any other academic institution. This research is supported by the Australian Government Research Training Program.

Signature of Candidate

Production Note:
Signature removed prior to publication.

Noor Sharari
Sydney, November 2021

Sincerely Dedicated to

My Father and Mother

Ibrahim & Mountaha

I owe you two my life and all the success

My husband Hussam, thank you for being with me during this journey

Saad and Hamad my sweethearts

ACKNOWLEDGEMENT

LIST OF PUBLICATIONS

1. Sharari, N., Fatahi, B., Hokmabadi, A., & Xu, R. (2022). Seismic resilience of extra-large LNG tank built on liquefiable soil deposit capturing soil-pile-structure interaction. *Bulletin of Earthquake Engineering*. 23,1-57.

2. Sharari, N., Fatahi, B., Hokmabadi, A. S., & Xu, R. (2022). Impacts of Pile Foundation Arrangement on Seismic Response of LNG Tanks Considering Soil–Foundation–Structure Interaction. *Journal of Performance of Constructed Facilities*, *36*(1), 04021110.

3. Sharari, N., Fatahi, B., Hokmabadi, A., & Xu, R. (2022). Impacts of Steel LNG Tank Aspect Ratio on Seismic Vulnerability Subjected to Near-Field Earthquakes. In *Proceedings of the 5th International Conference on Sustainable Civil Engineering Structures and Construction Materials* (pp. 941-956). Springer, Singapore.

4. Sharari, N., Fatahi, B., & Hokmabadi, A. S. (2020). Impact of Wall Support Conditions on Seismic Response of Ground-Supported Reinforced Concrete Containment Tanks. *WIT Transactions on The Built Environment*, *198*, 139-151

TABLE OF CONTENTS

LIST OF FIGURES

LIST OF TABLES

LIST OF NOTATIONS

$A_g(t)$	Horizontal ground acceleration
A_{loop}	Area of one hysteresis loop
A^{ff}	Area of influence of free-field elements
C_b	Outward wave speed at the lateral boundaries of a numerical model
C_{con}	Sloshing period coefficient
$C_h(T)$	Spectral shape factor
C_{imp}	Acceleration coefficient
Ck	Initial kinematic hardening modulus
C_l	Coefficient of impulsive period
cp	Dilatational (pressure) speed
Cs	Kinematic hardening modulus for steel
c_{sv}	Shear wave speeds
Cu	Undrained shear strength of soil
D	Tank diameter
D_K	Building damping ratio
dt	Tensile damage parameter
dc	Compressive damage parameter
d_s	damping of the infinite boundary in the normal directions
d_p	damping of the infinite boundary in the shear directions
E_0	Intial elastic stiffness of concrete
E_c	Elastic modulus of the concreter
E_s	Elastic modulus of the 9% Ni steel
E_{soil}	Modulus of elasticity of soil
E_r	Elastic modulus of the rebar
F	Yield surface function
$F_{boundary}$	Resultant normal force acting on an interface element
$f(\sigma - \alpha)$	Equivelant Mises stress
f_{bo}	Biaxial compressive yield strengths
f_{co}	Uniaxial compressive yield strengths

F^{ff}	Force generated in the free-field element
f'_c	Concrete compressive strength
f_y	Tensile yield stress
f_{ult}	Ultimate tensile strength
G_{inf}	Infinite element shear modulus of soil
G_{max}	Maximum shear modulus of soil
G_{sec}	Secant shear modulus of soil
G_{tan}	Tangent shear modulus of soil
h	Overclosure or gap level
H	Height of tank
H_{con}	Convective mass height
H_{imp}	Implusive mass height
H_L	Fluid design level
$I_1`, I_1$	Modified Bessel functions of order 1 and its derivative
I_g	Reduction factor modulus
K_c	Tensile to the compressive meridian ratio
K_{con}	Convective mode spring stifness
K_h	Horizontal stiffness for SFSI system
K_r	Rotational stiffness for SFSI system
M_{con}	Covective mass
M_{imp}	Implusive mass
M_{fod}	Foundation mass
M_{total}	Liquid mass
$(N_1)_{60cs-Sr}$	Equivalent SPT value
N_{max}	Coffiecient for fualt distance
P	Contact pressure
PGA	Peak ground acceleration
p_{con}	Convective pressure
$p_i \text{ and } p_{imp}$	Impulsive pressure
$\bar{p}$	Hydrostatic stress
$\bar{q}$	Von Mises effective stress
R	Return period factor

R^2	Coefficient of determination
R_{tank}	Tank radiuos
r	Cylindrical coordinates of tank
S	Deviatoric stress tensor
S_r	Residual shear strength
t	Time
T	Structure period
T_{imp}	Impulsive natural period
T_{imp}^*	Impulsive natural period with SFSI effect
T_{con}	Convective natural period
t_u	Equivalent uniform thickness of the tank wall
v	Poisson's Ratio
V_s	Shear wave velocity
Z	Hazard factor
z	Cylindrical coordinates of tank
$\langle \cdot \rangle$	Macaulay bracket
α	Back stress
α^{dev}	Devatoric part of back stress tensor
α^s	Back stress at large plastic strains
$\alpha_{damping}$	Rayleigh coefficients viscous damping
$\beta_{damping}$	Rayleigh coefficients viscous damping
$\dot{\bar{\varepsilon}}^{pl}$	Equivalent plastic strain rate
$\bar{\varepsilon}_c^{in}$	Inelastic crushing strain
$\bar{\varepsilon}_c^{pl}$	Compressive plastic strain
$\bar{\varepsilon}_t^{cr}$	Cracking strain
$\bar{\varepsilon}_t^{pl}$	Tensile plastic strain
$\dot{\varepsilon}^{pl}$	Plastic flow rate
ε_t^{pl}	Tensile plastic strain
ε_c	Compressive strain
ε_{eng}	Nominal strain values
ε_t	Tensile strain

ε_{true}	True (logarithmic) strain
ϵ	Eccentricity of plastic potential surface
γ_k	Hardening modulus decreasing rate
γ_{ref}	Refernce shear strain
γ	Cyclic shear strain
γ_l	Non-diamntional factor
ρ	Fluid density
ρ_{soil}	Soil density
ρ_c	Concrete density
ρ_r	Steel rebar density
ρ_{steel}	Ni steel desity
γ_k	Hardening modulus decreasing rate
δ	Elongation
ξ	Non-dimensional coordinates
$\xi_{damping}$	Soil damping
ξ_{max}	Maximum damping ratio
ς	Non-dimensional coordinates
$\bar{\sigma}_{max}$	Maximum principal effective stress
$\bar{\sigma}_c$	Effective compressive stress
$\bar{\sigma}_t$	Effective tension stress
σ_c	Compression stress
σ_{eng}	Nominal stress- strain values
σ_t	Tensile stress
σ_{t0}	Tensile stress at failure
σ_{true}	Cauchy stress
σ_{ult}	Ultimate stress
$\acute{\sigma}_{vc}$	Effective vertical stress
σ_y	Yield stress
$\sigma|_0$	Initial yield stress
θ	Cylindrical coordinates of tank
τ	The shear stress
$\tau_{critical}$	Critical contact shear stress

τ_{rev}	Shear stress at the reversal point
ψ	The dilation angle
μ	Friction coefficient

ABSTRACT

During the past decades, demand for Liquefied Natural Gas (LNG) tanks has increased. Indeed, the LNG is cleaner and cheaper fuel for power generation compared to oil and coal. The LNG industry is growing rapidly, and many LNG tanks are constructed in seismically active coastal regions; hence, potential damage or leakage due to cracking triggered by an earthquake can result in destructive environmental and safety issues. These LNG tanks are usually built near the seashore to reduce the cost and increase the flexibility of LNG transportation and storage. Often the foundation soil in coastal regions is not capable of bearing the load of such heavy structures. Thus usually, deep foundations are used to support these tanks. Indeed, pile foundations are commonly used for these large tanks to transfer the load to competent ground layers and control the settlement. Generally, assessing the seismic resilience of these critical infrastructures is essential to ensure the availability and security of services during and after large earthquakes. Considering the complexity of the seismic analysis and design of such structures due to the Fluid-Structure Interaction (FSI) and Soil–Foundation-Structure Interaction (SFSI) effects, advanced modelling and analysis are required.

This thesis conducts the three-dimensional fully nonlinear coupled SFSI and FSI numerical simulations for LNG tanks using the direct method. The nonlinear time history analysis and free vibration analysis are conducted to assess the seismic safety and dynamic characteristics of LNG tanks under different pile foundation types and liquefiable soil deposits. The fluid-structure interaction effects are captured using a mechanical model, which captures both convective and impulsive hydrodynamic components. Nonlinear kinematic hardening soil model adopted in this study is also

verified and implemented to capture the hysteretic damping of the soil and the variation of the shear modulus with the cyclic shear strain developed in the soil. Infinite boundary elements are assigned to the numerical model, and proper interface elements, capable of modelling sliding and separation between the foundation and soil elements, are considered. This thesis conducts the numerical analyses with the help of the High-Performance Computer (HPC) at the University of Technology Sydney (UTS), taking a few weeks to a month for a single analysis to run due to the complexity of the system.

To assess the effect of different pile foundation options on the seismic response of LNG tanks, different pile foundation types, including an end-bearing pile foundation and a pile-raft foundation with two different frictional pile lengths, are investigated. The results show the importance of the SFSI effect in evaluating the seismic response of LNG tanks built on pile foundations. Furthermore, the significant effect of the deep foundation system choice on the dynamic response of the LNG tanks is highlighted. Indeed, the seismic analysis and the design of LNG tanks in practice need to carefully consider the SFSI effects implementing direct method of analysis to ensure both kinematic and inertial interactions are captured accurately when analysis LNG tanks on pile foundations. Moreover, the numerical results show that presence of liquified soil layer alter the dynamic properties of LNG tank by lengthen the natural period and increase the damping of the LNG tank, soil, and foundation system. In addition, the presence of liquified soil layer significantly reduces the impulsive forces applied on LNG tank wall, while no significant change is observed for the convective forces. Hence, presence of the liquefied soil layer can absorb the seismic energy and reduce the seismic forces transferred to the superstructure. The predictions show that with increasing the thickness of the liquefied soil layer, the kinematic interaction increases, directing more seismic forces to the piles supporting the LNG tank, which can potentially result in yielding and failure of the piles.

CHAPTER 1   INTRODUCTION

1.1 General

Liquified natural gas (LNG) storage tanks are an essential part of every LNG terminal, as the worldwide demand for this energy source has grown considerably over the past few years. The size of these reservoirs has increased accordingly to improve the efficiency of global trade (e.g. import and export processes). In contrast to coal and oil, the production and use of this clean energy source has increased as a source of energy for domestic usages like electricity, heating, and cooling. Similarly, in the industrial sector, this energy source is used as a fuel for factories and vehicles, with trade-offs considered in terms of costs and sustainability.

The LNG terminals are often located in coastal areas, where the large and extra-large LNG tanks are positioned on unfavourable soil conditions. Hence, a rigorous foundation system is required for these heavy structures due to the low bearing capacity of the supporting soil. Deep foundations (i.e. pile foundations) and ground improvement are the most popular options to support these tanks. Moreover, the risk of natural hazards like earthquakes, flooding, and tsunamis leading to lateral loads necessitates special design considerations to address the lateral loading requirements for these structures. It is also essential to consider the low bearing capacity of the soil that is responsible for reducing the lateral capacity of the piles. Consequently, these factors should be considered in the lateral loading requirements that govern LNG tank design (Kausel et al. 1978; Sakr and Vinson 1979; Willford et al. 2010; Chang et al. 2012). Massive LNG tanks are commonly supported by large pile groups ranging in the hundreds to thousands

to fulfil the bearing capacity requirements and to control displacement and settlement (Jones 2021). In typical/traditional practice, the LNG tank and the supported foundation design and analysis are done independently in two phases: the basic design phase, in which the tank size, mass and foundation capability (to meet seismic load requirements) are evaluated, and the detailed design phase, in which the design of structural parts is performed in detail (Sato et al. 2020). For the basic design phase, the superstructure and the foundation are usually designed based on traditional structural engineering assumptions for rigid foundations, and geotechnical engineers use a superstructure load to design the foundation system. The use of this approach for the seismic analysis and design of LNG tanks is inefficient since it ignores the effect of Soil–Foundation–Structure Interaction (SFSI). This effect is related to a procedure in which the soil response is impacted by the effect of the structure's motion and vice versa (Rodriguez and Montes 2000; Wolf and Song 2002; Dutta and Talukdar 2004; Wang et al. 2013). For LNG tank design, often free-field site response analysis is used to find the response spectrum at the ground surface for the seismic analysis results while disregarding SFSI effects (McCullough et al. 2009). This approach can be considered in areas with low seismicity and stiff ground conditions (e.g. LNG tanks founded on rock). However, the most common locations for LNG tanks are soft soils in coastal regions, and SFSI therefore significantly affects the seismic response of LNG tanks significantly, particularly in areas with moderate to high seismicity (Veletsos and Tang 1990; Kim et al. 2002; Hokmabadi et al. 2019).

The analysis and design of LNG tanks under seismic loading using an approach that considers the foundation, superstructure and simplified soil dynamic response on the pile foundation separately and independently often results in structural and geotechnical engineers commonly making crude assumptions (Lin et al. 2010; Lin et al. 2012). Indeed,

the current common design practices consider the seismic response of LNG tanks inefficiently, particularly in terms of its overall design and the support foundation system.

In addition, the LNG tank is considered a complex structure. Each tank seismic response can vary based on various factors such as the tank material, the foundation system (i.e. pile group geometry, number, and length), and soil conditions. Many previous studies have investigated the seismic response of structures such as buildings, bridges, and tunnels, by including SFSI effects. These studies have proved that SFSI has a significant impact on the design and analysis of these structures influencing their safety and reliability. At the same time, previous research outcomes have verified that SFSI can significantly alter the seismic response for different structures (Mizuno et al. 1996; Chen et al. 2010; Zhang et al. 2011). For instance, SFSI effects contribute to an increase in foundation rocking, which increases the lateral deflection of the building, mainly in mid-to high-rise buildings, compared with the assumption of a rigid foundation and ignoring SFSI (Mendoza and Auvinet 1988; Tokimatsu et al. 1996; Gazetas and Apostolou 2004). The dynamic properties of the structure alter when SFSI effects are included, as this can elongate the fundamental period of vibration and the energy damping rate (Esteva 1987; Anastasopoulos et al. 2007; Chen et al. 2010). Meanwhile, the research on the seismic behaviour of LNG tanks, including SFSI, is limited, due to the complexity of LNG tanks and the nature of seismic loading in such structures, as the liquid inside the tank generates hydrodynamic forces, which impact the tank wall and its base. These loads transfer to the foundation and the supporting soil, and considering these effects is more significant for LNG tanks than for other structures, such as typical buildings. Therefore, the nonlinearity of the material and the structure play a significant role in the overall response of the LNG tank. Including the potential yielding of the soil or the structural materials can also threaten the LNG tank's functionality and safety. Indeed, the failure of these tanks during

seismic events would lead to severe safety concerns and significant environmental and economic consequences. Thus, including the SFSI effects on these structures is essential in order to assess the ground response, design the superstructure and foundation systems accurately and safely and optimise the design (Zhang et al. 2011; Yan et al. 2019).

1.2   Objectives and scope of this study

The key aim of this study is to assess the SFSI effects on the LNG tank superstructure, foundation, and soil seismic response, incorporating appropriate material models for the superstructure foundation and soil, to capture the nonlinear response and the potential yielding under seismic loads, using integral approach modelling. The specific objectives of this research are:

1. To identify the research gap in the seismic analysis of LNG tanks, including SFSI effects, based on a review of previous research, and to propose an appropriate methodology to investigate the identified research gap.

2. To develop an appropriate three-dimensional numerical model capable of capturing the material and geometric nonlinearities using integral approach modelling and the direct method of analysis.

3. To evaluate and assess the capability of the kinematic hardening model to capture the seismic wave propagation in the soil medium and incorporate it into the seismic analysis of the LNG tank.

4. To study the impacts of pile foundation arrangement on the seismic response of LNG tanks considering SFSI effects.

5. To assess the seismic resilience of extra-large LNG tanks built on a liquefiable soil deposit, capturing soil–foundation–structure interaction.

6. To understand and investigate the influence of contemporary problems such as the tank aspect ratio and the tank wall connection condition on the seismic response of LNG tanks.

1.3   Thesis organisation

This thesis has been organised into seven chapters. The introduction, objectives and scope of the study are presented in the current chapter. The overview of the other six chapters is as follows:

Chapter 2 provides an overview of the LNG tank types and the current practice for seismic design and performance assessment of these tanks. Furthermore, the factors that affect the seismic performance of liquid storage tanks (including LNG tanks), like soil–foundation–structure interaction (SFSI) and fluid–structure interaction (FSI), are explained. Finally, the existing research studies related to seismic performance of LNG storage tanks and the need for further research are highlighted.

Chapter 3 presents a numerical investigation assessing the impacts of foundation type on the seismic behaviour of large LNG tanks, considering SFSI effects. This chapter assesses LNG tank seismic responses for different foundation types, namely an end-bearing pile foundation and a pile–raft foundation with two different frictional pile lengths. This chapter highlights the significance of SFSI effects on LNG tank seismic response using the direct method of analysis simulating the entire system in one step.

Chapter 4 presents an assessment and implementation of the advanced nonlinear kinematic hardening model to denote soil dynamic/seismic behaviour, utilising stiffness degradation and hysteresis damping with cyclic shear strain. In this chapter, the capability of the nonlinear kinematic hardening model programmed in ABAQUS to capture the seismic wave propagation through the soil medium is assessed for different soil site

classes. The results are verified with the well-known stiffness degradation and hysteresis damping soil model in FLAC 3D.

Chapter 5 presents an assessment of the seismic resilience of extra-large LNG tanks built on liquefied soil deposits in which the analysis includes SFSI effects. This chapter highlights the vulnerability of LNG tanks to intense earthquake loads in areas with weak, loose sandy soil found in coastal areas. Indeed, LNG tanks are commonly located in coastal regions with sand deposits and liquefaction is a real concern under earthquakes.

Chapter 6 highlights the effects of several contemporary structural issues impacting the overall LNG tank seismic response. This chapter presents the effects of the aspect ratio (*H/D*) of inner steel LNG tanks on the seismic safety of these tanks under strong earthquake shaking, while mechanical model to represent the fluid–structure interaction effects is implemented. In addition, the results of numerical investigations on the impacts of wall support conditions for the outer concrete containment namely hinge and fixed on the seismic response of LNG tanks are presented.

Chapter 7 presents the conclusions of the current research and recommendations for future research.

CHAPTER 2   LITERATURE REVIEW

2.1   General

Liquid storage tanks are vital structures for supplying water and storing chemical products like refined petroleum and liquified natural gas (LNG). Water storage tanks are considered an essential link for domestic daily use. These tanks are usually located near the usage area to ensure a continuous supply. In comparison, chemical and refined petroleum storage tanks are used in industrial applications and energy power supply sector. Thus, for ease of transference in terms of the import and export of these products, the best location for these tanks is near coastal areas (i.e. at the seaside). The seismic vulnerability of these structures is a special matter beyond the economic cost of their damage or failure. Indeed, they need to remain completely functional and secure during and after severe earthquake events (Nagashima et al. 2011; Calderón et al. 2016). The water stream from water storage tanks is critical immediately following destructive earthquake shaking to prevent disease outbreaks and to control potential consequent fires. For petroleum and chemical storage tanks, there is a high risk of potential leakage or damage, which can result in uncontrolled fires due to the highly flammable material inside these tanks. This can cause death and injuries to both humanity and the environment, as happened in the 1964 Niigata and 1964 Alaska earthquakes (Satake and Abe 1983; Pegler and Das 1996).

Looking at liquified natural gas storage tanks, the LNG is mainly from methane, and it is liquified and stored at atmospheric pressures with operating temperatures around - 166 Cº. LNG is liquified to reduce the storage volume 600 times, by converting it from

a gas to a liquid state to increase LNG storage capacity and transference efficiency (Christovasilis and Whittaker 2008). LNG tanks should be designed wisely for a safe and secure performance and meet the requirements of low temperature and vapor tightness. Accordingly, the LNG is usually contained within a vertical circular steel container made from a material with high ductility (i.e. low-temperature conditions). In addition, a second container is needed for external protection and vapor tightness or confinement. The second container or barrier can be made from RC or steel. Researchers have found that using a 9% nickel steel for the inner tank leads to improved ductility performance, and that surrounding it with insulation materials helps prevent heat exchange and temperature leakage (Chen et al. 2004; Lisowski and Czyżycki 2011).

Due to the high demand for LNG, the capacity of LNG tanks has increased dramatically. Thus, they can have a diameter ranging from 65 to 85 meters and a total height between 35 m and 50 m, which can offer efficient, extra-large LNG containment. Large LNG containment systems have a fundamental vibration frequency in the range of 2 Hz to 10 Hz, where the fundamental frequency for most earthquake vibrations is observed (Tajirian 1998). Because of the LNG tank multi-layer design and the necessity of including the effects of soil–foundation–structure and fluid–structure interactions, the seismic analysis of these structures is complex. In addition, these tanks may present a significant danger in strong earthquakes, during which many liquid storage tanks are readily destroyed, as observed in several real-world cases. Therefore, understanding the seismic performance of these tanks is critical, especially when the supporting soils have a low seismic bearing capacity (Son and Kim 2019).

This chapter provides an overview of the LNG tank types and their seismic design and performance. Furthermore, the factors that affect the seismic performance of liquid storage tanks (including LNG tanks), like soil–foundation–structure interaction (SFSI)

and fluid–structure interaction (FSI), are defined. Finally, the current research studies related to seismic performance of on LNG storage tanks are explained.

2.2   Overview of LNG tanks
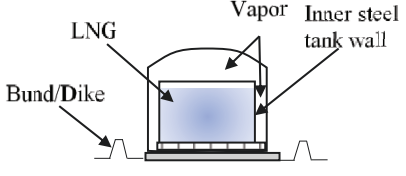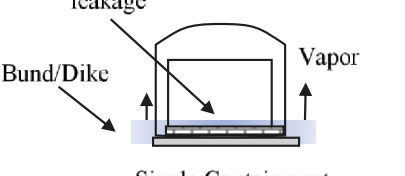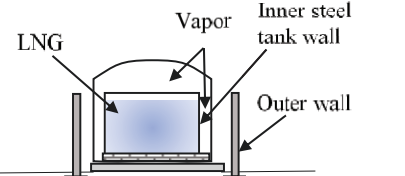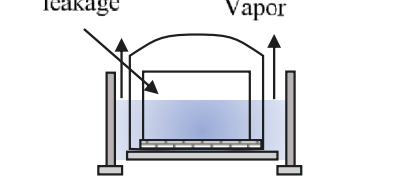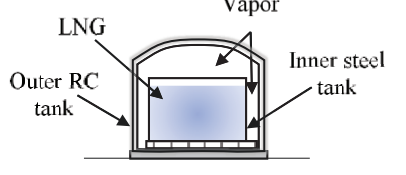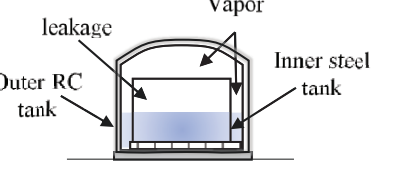
Ground-supported LNG tanks have various integrated systems, namely single, double, and full containment LNG tank systems. These integrated systems are defined by the American National Fire Protection Association NFPA-59A (2019) and the European–British standard EN BS 14620-2 (2006). In general, all these integrated systems contain two tank walls, and the differences between them are in the functionality of each tank wall. For example, when the inner steel cylinder tank holds LNG liquid and vapours alone, this system is defined as single containment. At the same time, the second wall serves as an exterior barrier and as insulation if the inner tank fails under emergency conditions and the LNG leaks. This second wall, called a dike or bund wall, around the inner steel tank, limits the spread of LNG into the surrounding environment. Meanwhile, for double containment, the internal/primary steel and the outer/secondary containment walls are designed to hold the LNG during normal operations and in the case of leakage, respectively.

The outer walls offer external protection, and the inner walls are located within 6 m of the outer walls to reduce the spill of LNG in the case of leakage. The difference between single and double LNG tanks is related to the dike/bund border. For a single LNG tank, significant ground restraint (via the dike or bund wall) is required to contain the LNG in the case of leakage. However, for double LNG tanks, the outer wall is designed as secondary containment for the entire amount of the LNG in case it is drained out of the primary container. For a full containment LNG tank, the inner steel tank is a primary container for the LNG, while the outer RC tank is for external protection, vapor

containment, and secondary containment of LNG in case of leakage. This outer LNG tank has a fixed roof to control the LNG vapor in both normal and emergency cases. If the LNG spills from the inner steel tank, the outer tank is designed to hold the LNG and maintain the vapor tightness for the whole system. This LNG tank type is the most integral system and is preferred in current practice, and it has been improved to increase the tank capacity significantly.

Table 2.1 presents the different LNG tank types and the functionality for each part under normal operating conditions and in the case of emergency or leakage. The seismic design and performance of the LNG tanks at different seismic hazard levels are discussed in the next section.

Table 2.1 Comparison between the LNG tanks' different integration systems (after Lee et al. 2017).

Parameter	Normal/operational condition	Containment in leakage/emergency condition	Cryogenic requirement (contain LNG)	Vapor tightness
Single containment LNG tank type			Inner/primary container	Only inner/primary container
Double containment LNG tank type			Inner/primary and outer/secondary containment	Only inner/primary container
Full containment LNG tank type			Inner/primary and outer/secondary containment	Inner/primary and outer/secondary containment

2.3   Seismic design and analysis of LNG tanks

In general, the seismic design and analysis of liquid storage tanks are different from those of traditional buildings and bridges. More specifically, bridges and buildings are subjected to inertial earthquake loading, acting as a base shear force. In comparison, liquid storage tanks are subjected to inertial earthquake loads like base shear force as well as further hydrodynamic forces, resulting in additional pressure along the tank wall and base (Jaiswal et al. 2007). Usually, liquid storage tanks can be classified based on their support type, such as ground support tanks at ground level, elevated tanks above ground level, and in-ground tanks (i.e. buried tanks). They can also be classified based on tank configuration, that is, circular or rectangular, or based on the tank wall material, namely steel or RC (Hafez 2012; Malhorta et al. 2000). However, the seismic design methodologies are similar for all tanks containing liquid. At the same time, a few seismic performance criteria can vary due to the different purposes and liquid storage requirements. Thus, each tank category presents a set of unique challenges and is designed according to specified codes and standards (Bandyopadhyay et al. 1995; Malhotra et al. 2000).

Figure 2.1 shows the LNG full containment tank in more detail. This tank typically consists of an inner steel tank, outer RC walls, a fixed RC roof, and a base slab (see Figure 2.1a). These tanks usually are supported by a pile foundation system (see Figure 2.1b). The design of these tanks is based on American codes NFPA 59A, API 620, and ACI 376, European codes BS EN 1473 and Eurocode-8, and the Australian/New Zealand code AS/NZS1170.4. The common practice design procedure consists of a preliminary stage and a detailed or refined stage. In the preliminary stage, the initial calculations are based on either simplifying assumptions or rules of thumb to find the inner tank capacity and

the initial dimensions, in addition to the foundation capability for seismic load requirements. Hence, in the detailed design stage, the initial size and loads are integrated into the more rigorous and refined model. In the detailed design stage, accurate representations of each component of the LNG tank and the interactive behaviour between these components are considered (Sato et al. 2020).

(a)
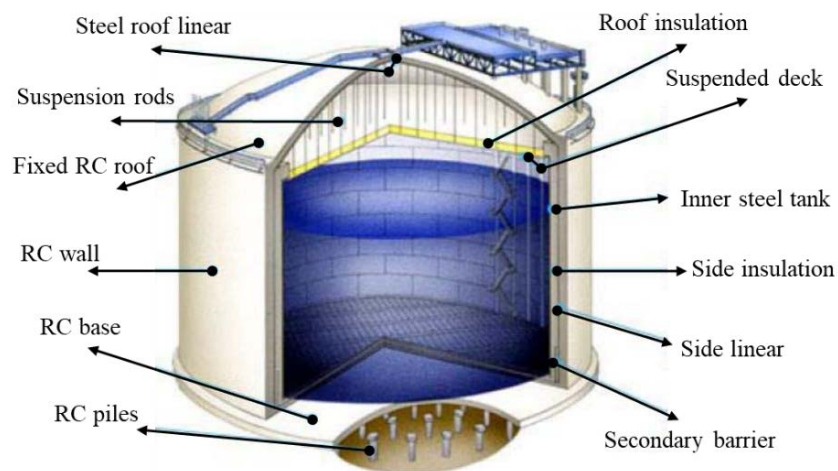
(b)

Figure 2.1 Full containment LNG tank components (a) Example for full containment LNG tank (Lun et al. 2006), and (b) Details of the full containment LNG tank components (after Jo et al. 2018).

In the detailed design stage, the initially proposed design is usually evaluated considering earthquake loads. The seismic performance of the LNG tank is assessed for operating basis earthquake (OBE) and safe shutdown earthquake (SSE) seismic hazard levels; these two seismic hazard levels correspond to 475-year and 10,000-year return periods, respectively (Zhang et al. 2011). The OBE and SSE ground motions are determined by site-specific analysis and defined using 5% damped response spectra following regulatory requirements. For each seismic hazard level, the LNG tank is required to comply with the performance objectives. For example, it should remain operable during and after an earthquake at the OBE seismic level (NFPA 59A 2019; Sato et al. 2020).

In comparison, no loss of the overall structural integrity of the LNG tank when it is subjected to the SSE seismic level is acceptable. Thus, an inelastic response is not permitted at the OBE load level. However, a limited inelastic response is permitted with SSE motions to prevent failure/collapse entirely (NFPA 59A 2019; BS EN 1473 2016). After the preliminary design of an LNG tank is proposed, a few adjustments are usually made to the foundation system, particularly the pile foundation system (i.e. pile numbers, lengths, and layout). Once the foundation system is proposed, a seismic analysis is performed for the LNG tank, including fluid and soil-structure interaction effects. The foundation loads for OBE and SSE seismic hazard levels are then evaluated and checked. The foundation system must be checked in terms of bearing capacity and monitoring settlements. Thus, the differential settlement and soil liquefaction potential need to be considered. This process is repeated until the foundation loads and superstructure design are compatible. Figure 2.2 shows the flowchart of the seismic design process for an LNG tank supported by a pile foundation.
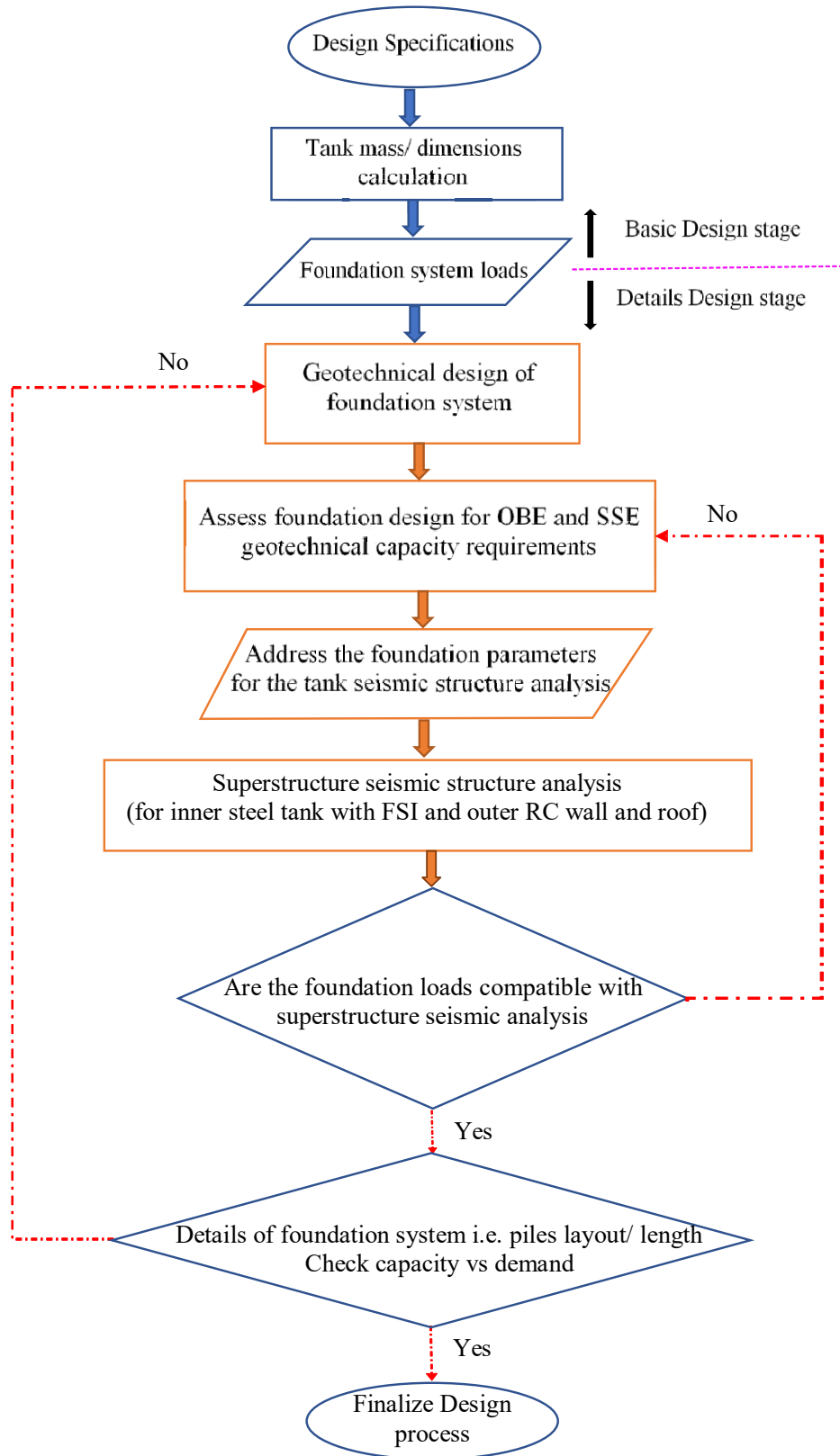
Figure 2.2 Design flowchart for LNG tank and foundation system (after Peiris et al. 2006).

Referring to Figure 2.2, which shows the seismic design flowchart for the LNG tank supported by pile foundation, it is evident that the LNG tank and the supporting foundation design and analysis are completed independently in the basic design and detailed design stages. In this method, free-field site response analysis is used to define the response spectra for the OBE and SSE hazard levels at the ground surface, ignoring the SFSI effects (McCullough et al. 2009). This approach results in crude assumptions for the overall design of the LNG tank, particularly the seismic response of the support foundation system (Lin et al. 2012).

2.4   Factors affecting the seismic performance of LNG tanks

Several factors affect the seismic response of liquid storage tanks, including the effects of fluid–structure interaction, soil–foundation–structure interaction, and dynamic soil behaviour, which need to be considered in the seismic design and analysis of liquid storage tanks. These factors are discussed in the following sections.

2.4.1   Fluid-Structure Interaction (FSI) effect

The seismic behaviour of liquid storage tanks has been studied extensively (Jacobsen 1949; Jacobsen and Ayre 1951; Haroun 1983; Veletsos 1974; Liu 1981; Housner 1957). Hydrodynamic forces form along the tank wall, where seismic forces move from the tank base to the liquid inside the tank. Usually, liquid hydrodynamic forces are separated into two components. The first component is accelerated with tank walls acting as additional masses, and the second component generates multiple sloshing waves on the liquid surface. Housner (1957) was the first to create an analytical model for these hydrodynamic forces. In this model, the two hydrodynamic pressures were divided into impulsive and convective components, and the tank was considered with the rigid base

condition. Figure 2.3 explains Housner (1957) mechanical model. Here it is evident that the fluid–structure interaction is divided into two independent/uncoupled pressure components, with each component simplified into single equivalent mass. Due to the considerable diversity in both natural periods, these two masses have an uncoupled effect on the tank system. When the spring–mass approach is used, these two concentrated masses are connected to the tank wall to present the impulsive and convective hydrodynamic forces. The M_{imp} joined to the tank wall by a rigid link at a specific height (i.e. H_{imp}) which represents the height of the impulsive pressure effect. M_{con} is created by the liquid sloshing in various waves; this mass connected with the tank wall through springs indicates the long period sloshing motion of the liquid at a certain height (i.e. H_{con}). It should be noted that the impulsive mass is the primary source of base shear and overturning moments for the global tank seismic response (Kalantari et al. 2019). At the same time, the convective mass adjusts the liquid height in the tank and the free-broad surface. Both hydrodynamic components contribute considerably to the axial and hoop forces on the tank wall (Malhotra 1997).

The single degree of freedom oscillators used in Housner (1957) model depend on the total tank height (H) and tank diameter (D). Indeed, it can also be affected by liquid height (H_L), total liquid mass (M), and gravity acceleration (in g unit) according to the following relationships:

$$M_{imp} = M \ \frac{\tanh(\sqrt{3}R/H_L)}{\sqrt{3}R/H_L} \tag{2.1}$$

$$M_{con} = M \ \frac{1}{4} \sqrt{\frac{27}{8} \frac{R}{H_L}} \ \tanh(\sqrt{\frac{27}{8} \frac{R}{H_L}}) \tag{2.2}$$

$$H_{imp} = \frac{3}{8} H_L \tag{2.3}$$

$$H_{con} = H \left(1 - \cfrac{1}{\sqrt{\cfrac{27}{8}}\cfrac{R}{H_L} \tanh\left(\sqrt{\cfrac{27}{8}}\cfrac{H_L}{R}\right)} + \cfrac{1}{\sqrt{\cfrac{27}{8}}\cfrac{H_L}{R} \sinh\left(\sqrt{\cfrac{27}{8}}\cfrac{H_L}{R}\right)}\right) \qquad (2.4)$$

$$K_{con} = M_{con} \left(\cfrac{g}{R} \sqrt{\cfrac{27}{8}} \tanh\sqrt{\cfrac{27}{8}}\cfrac{H_L}{R} \right) \qquad (2.5)$$

where, R is tank radius, and K_{con} is the effective stiffness for the convective mode.

Various studies have revised Housner (1957) basic model for a better assessment of FSI effects. For example, the Housner (1957) model includes the rigid effect of the impulsive component only. Therefore, to consider the tank wall flexibility effect on the impulsive pressure component, Haroun and Housner (1981) revised the mechanical model and divided the impulsive mass (M_{imp}) into flexible and rigid components to consider the effect of tank wall deformation on the impulsive pressure. Furthermore, Veletsos and Yang (1990) modified the mechanical model for further valuation of the convective components by considering two convective modes in their mechanical model. The work of each of these studies was included in the *Guidelines for the Seismic Design of Oil and Gas Pipeline Systems"* (Veletsos 1984). Lastly, Malhotra et al. (2000) modified the mechanical model presented by Veletsos and Yang (1990) and proposed their own mechanical model (Figure 2.4), which has been adopted by API 650 (2007) and API 620 (2013) as the standard for steel and cryogenic steel ground supported tanks (i.e. LNG inner tanks), respectively. The analytical relationships for the first impulsive mode of vibration T_{imp} and the first convective mode T_{con} are explained by Equations 2.6 and 2.7, where E_{steel} is the elastic modulus of the steel tank material, t_s is the tank wall thickness, C_{imp} and C_{con} are coefficients, and ρ_{liquid} is the mass density of the liquid.

$$T_{imp} = C_{imp} \cfrac{H_L \sqrt{\rho_{liquid}}}{\sqrt{E * \left(\cfrac{t_s}{R}\right)}} \qquad (2.6)$$

$$T_{con} = C_{con}\sqrt{R} \tag{2.7}$$
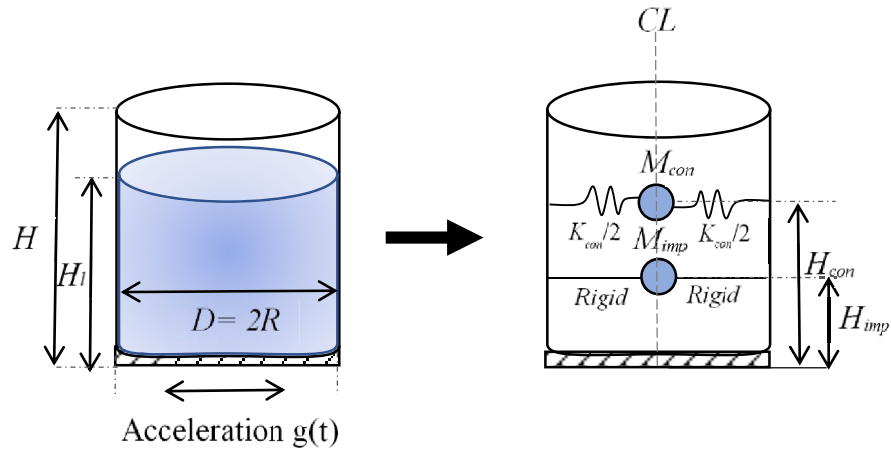
Figure 2.3 Analytical model for the dynamic behaviour of ground supported liquid storage tank (after Housner 1957).
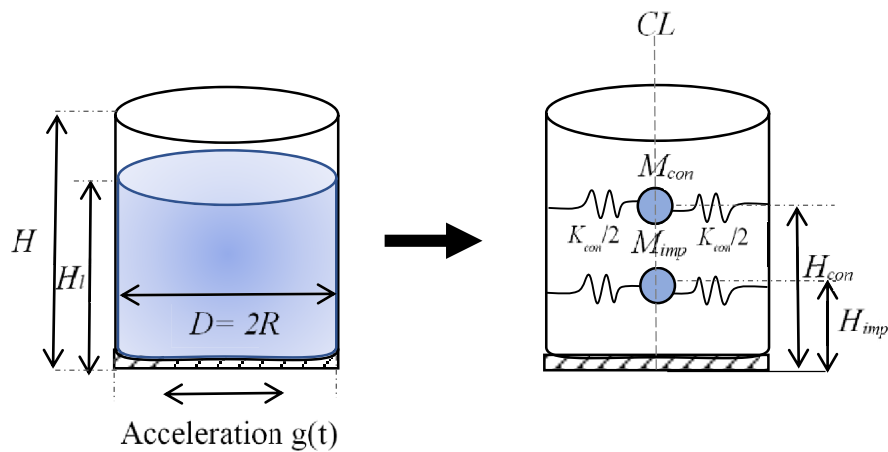
Figure 2.4 Mechanical models proposed by Malhotra et al. (2000)

It should be mentioned that the mechanical model proposed by Malhotra et al. (2000) is applicable to concrete, steel anchored tanks (i.e. rigid connection with the foundation), and unanchored tanks. Mainly, this model has correlated the hydrodynamic forces generated by accelerated liquid to the tank configuration system. Therefore, the aspect ratio of the tank in terms of the height of liquid to the tank radius (i.e. H_L/R) determines the percentage of the liquid mass that will rigidly accelerate with the tank wall in the impulsive mode of vibration (Veletsos 1984). Moreover, the mass will vibrate on

the surface in the form of convective waves. Most tanks with aspect ratios between 0.3 and 3 can be analysed with only these two vibration modes. The fundamental impulsive and convective modes together account for 85-98% of the total liquid mass in the tank. Thus, using only these modes is decided to be acceptable for tanks with these aspect ratios (Rammerstorfer 1990). Table 2.2 summarises the relationship between the tank aspect ratio and the impulsive and convective masses, coefficients, and heights of effect.

Table 2.2 Malhotra et al. (2000) mechanical model parameters for different tank aspect ratios

H_L/R	C_{imp}	C_{con} [s/$\sqrt{m}$]	M_{imp}/M	M_{con}/M	H_{imp}/H_L	H_{con}/H_L
0.3	9.28	2.09	0.176	0.824	0.40	0.521
0.5	7.74	1.74	0.3	0.7	0.40	0.543
0.7	6.97	1.60	0.414	0.586	0.401	0.571
1.0	6.36	1.52	0.548	0.452	0.419	0.616
1.5	6.06	1.48	0.686	0.314	0.439	0.690
2.0	6.21	1.48	0.763	0.237	0.448	0.751
2.5	6.56	1.48	0.810	0.19	0.452	0.794
3	7.03	1.48	0.842	0.158	0.453	0.825

Additional effort was made by Virella et al. (2006) to enhance the accuracy of the impulsive and convective pressure components on the liquid storage tank walls. This method is a rigorous and sound alternative model to Houser (1957) simplified mechanical model. In this model, instead of using one concentrated mass to represent the impulsive and convective forces, the masses are distributed along the tank wall in several segments using the added masses concept. This concept was initially presented by Westergaard (1933) to model the hydrodynamic pressure on water dams during earthquakes. In this technique, the impulsive and convective hydrodynamic forces along the tank wall are represented using a series of added masses m_{imp} and m_{con} instead of using single concentrated masses (Figure 2.4 and Figure 2.5). These masses are distributed on

segments of the tank walls divided by elevation (i.e. Δh). Hence, the effect of the hydrodynamic forces along the tank walls is well captured. This method is recognised by Eurocode-8 (2006) for the seismic design of liquid storage tanks. As explained in Eurocode-8 (2006), the distribution of the rigid impulsive and convective components of the hydrodynamic pressure (p_{imp} and p_{con}) can be given by the following expressions:

$$p_i(\xi,\varsigma,\theta,t) = C_{imp}(\xi,\varsigma)\,\rho_{liquid}\,R\,*A_g(t) \tag{2.8}$$

$$C_{imp}(\xi,\varsigma) = 2\gamma\sum_{n=0}^{\infty}\frac{(-1^n)}{\left(\grave{I}_1\left(\frac{v_n}{\gamma}\right)\right)v_n^2}\,cos(v_n\,\varsigma)I_1\left(\frac{v_n}{\gamma}\,\xi\right) \tag{2.9}$$

$$p_{con}(\xi,\varsigma,\theta,t) = C_{con}(\xi,\varsigma)\,\rho\,R\,*A_g(t)\,*\Gamma_{con} \tag{2.10}$$

$$C_{con}(\xi,\varsigma) = 2\sum_{n=1}^{\infty}\frac{cosh(\lambda_n\gamma\,\varsigma)\,J_1(\lambda_n\xi)}{(\lambda_n^2-1)\,J_1(\lambda_n)\,cosh(\lambda_n\gamma)} \tag{2.11}$$

$$\Gamma_{con} = \frac{2\,sinh(\lambda_n\gamma)[cosh(\lambda_n\gamma)-1]}{sinh(\lambda_n\gamma)\,cosh(\lambda_n\gamma)-\lambda_n\gamma} \tag{2.12}$$

where $\xi = r/R$ and $\varsigma = z/H_L$ are the coordinates parameters "non-dimensional"; R is the radius of the tank; r, θ, z are the components of cylindrical coordinates with their origin at the centre of the tank while the z axis is vertical; t is time; C_{imp} and C_{con} are impulsive and convective pressure distribution coefficients; $v_n = ((2n+1)/1)\,\pi$; $\gamma = H_L/R$; I_1 and $\grave{I}_1$ are mathematical functions "modified Bessel functions"; J_1, is the Bessel function of the first order for the convective mode; Γ_{con} is the participation factor for the convective pressure component for the nth Eigenmode; λ_n is the nth root of the first-order Bessel function (where the first three positive roots are $\lambda_1 = 1.841$, $\lambda_2 = 5.331$, $\lambda_3 = 8.536$), respectively; $Ag(t)$ is the ground acceleration time history in the free-field; ρ_{liquid} is the mass density of the contained liquid. Figure 2.5 represents the added mass concept for liquid storage tanks based on Eurocode-8 (2006).

Fluid–structure interaction in liquid storage tanks subjected to dynamic and seismic loads can be captured using mechanical models (analogues) such as those described above. These include, namely, the spring-mass and added mass concepts, which are considered an acceptable substitute for the tank–liquid system (i.e. FSI) in design codes such as API 650 and API 620 (2007 and 2013), ACI 350.2 (2009), Eurocode-8 (2006), and NZSEE (2009). Additionally, researchers have established different advanced general-purpose finite element (FE) models to study the FSI effect more precisely (Virella et al. 2006b; Bayraktar et al. 2010; Platek et al. 2010; Belostotskiy et al. 2015; Kolbadi et al. 2018; Zhang and Wan 2019; Rawat et al. 2020). The fluid finite elements method is considered a practical method to capture the FSI effects and the sloshing wave of liquid inside the tank. In this method, the problem of FSI is revised into a global finite element framework using a displacement-based approach, the Lagrangian approach, and acoustic finite elements techniques. However, Virella et al. (2006b) compared the added masses method with the advanced finite element method for capturing the FSI effects, and the added mass method proved its capability to capture the FSI effect reasonably well. Moreover, the added mass method can be used for complex tank geometries, particularly when soil–structure interaction needs to be considered (Spritzer and Guzey 2017).
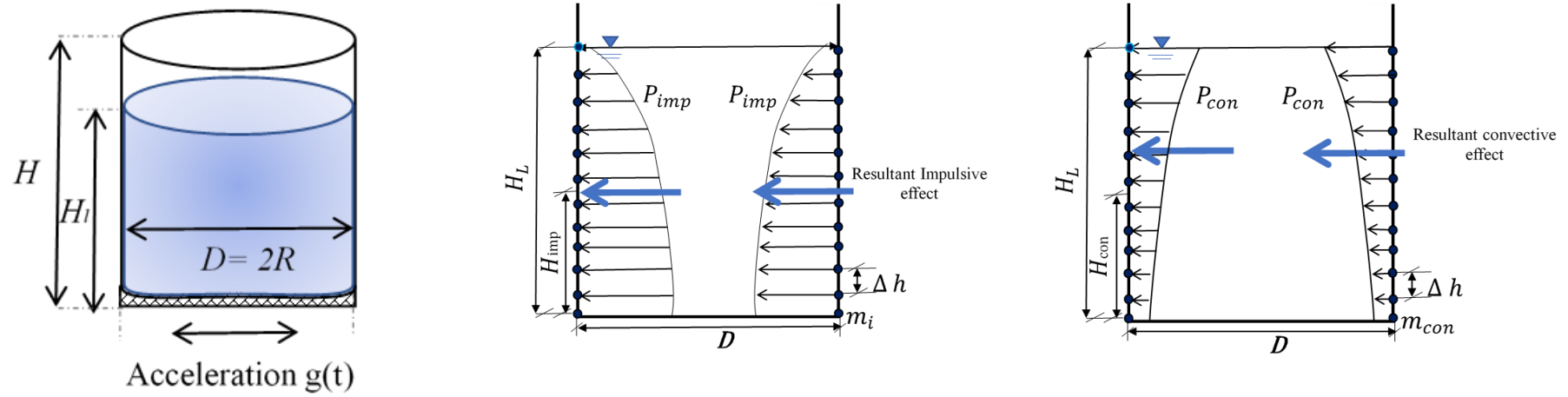
Figure 2.5 The mechanical model for impulsive and convective pressures using the added mass method according to Eurocode-8 (2006)

2.4.2 Soil-Foundation-Structure Interaction (SFSI) effects

The seismic response of the structure is significantly affected by two main factors: the effects of local site conditions on the wave striking the structure and the way the structure interacts with the foundation and the ground below, acknowledged as soil–foundation–structure interaction (SFSI). Past intense earthquake events, including the 1964 Alaska, 1985 Mexico City, and 1995 Kobe earthquakes, revealed that the consideration of seismic SFSI is crucial in the design of structures (Satake and Abe 1983; Mendoza and Auvinet 1988; Pegler and Das 1996; Chen et al. 2010). Earthquake features, travel path, local soil properties, and SFSI are the main aspects controlling the seismic excitement of the superstructure. Indeed, the first three of these aspects define the free-field ground motions, and the incapability of a foundation to follow the free-field motion refers to seismic soil–foundation–structure interaction SFSI (Kramer 1996).

2.4.2.1 *Free-field ground motion*

Seismic waves may travel through tens of thousands of kilometres of rock and less than 100 m of soil before they influence the ground surface. Seismic waves tend to change as they travel through different soil layers and mediums of different wave propagation velocities. As a result of several wave refractions, the seismic waves influence the ground surface in the near-vertical direction (Kramer 1996). The local site conditions can substantially affect the characteristics of these ground motions namely the frequency content of the signal, amplitude, and duration (Yoshida 2015). Figure 2.6 illustrates the ground response analysis and subsequent vertical spread of seismic waves in the vicinity of the soil surface.
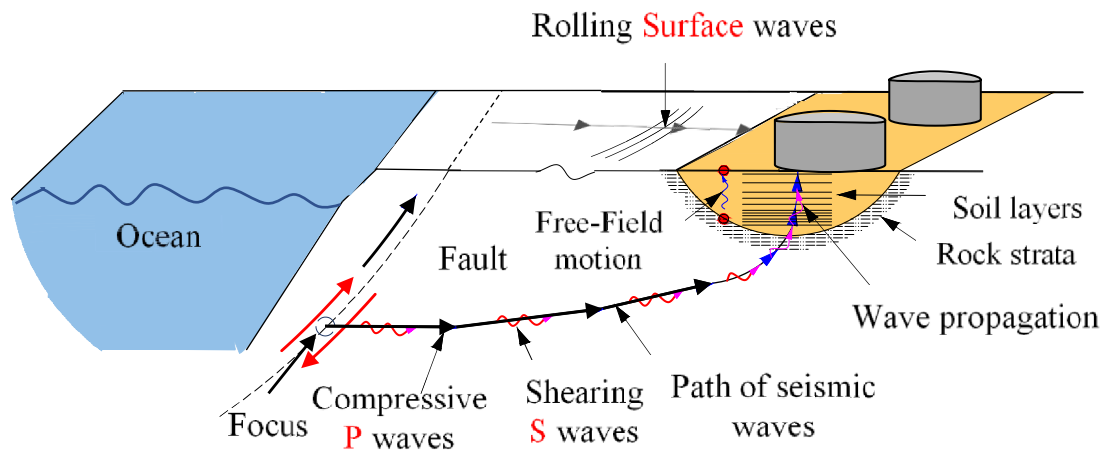
Figure 2.6 Analysis of the ground response and upward wave propagation near the shallow ground soil surface.

As the local site conditions can significantly affect the ground response motion, Idriss (1990) investigated the effect of soft soil deposits on the seismic site response using data collected from the San Francisco Bay and Mexico City areas (see Figure 2.7). He concluded that for low to moderate earthquake levels (PGA about 0.4 g or less), the peak ground acceleration (PGA) at soft soil sites would expected to be higher than that at rock sites. However, for more significant earthquakes with higher acceleration levels (PGA greater than 0.4 g), the small stiffness and nonlinearity of the soft soil prevented the growing of higher peak accelerations, compared with the high peak accelerations observed at rock sites. To illustrate the effect of local site conditions on the frequency content of the ground surface response, Figure 2.7 shows the average response spectrum of ground motion records from various soils, including rock, stiff soil, soft soil, and cohesionless soil (Seed et al. 1976; Kramer 1996). It is evident from Figure 2.7 that the deep, soft to medium soils create low frequency (long period) motion on the surface, whereas the rock and stiff soil sites create high frequency (short period) motion on the ground surface. In addition, as denoted in Figure 2.7, the rock site has a dominant period of 0.2 seconds, while the corresponding value for soft to medium soil sites is about 0.9 seconds. This effect is significant and needs to be considered for the seismic design of stiff structures with rather short periods of vibration, such as large

tanks on soft and cohesionless soils such as those in coastal, marine and unfavourable soil deposits. The seismic response of the structure can be affected by the properties of the ground motion. Therefore, consideration of the local site effects is essential for seismic analysis (Mylonakis et al. 2006; Li et al. 2014). The dynamic soil behaviours need to be captured using the equivalent linear method or fully nonlinear method for ground response analysis.
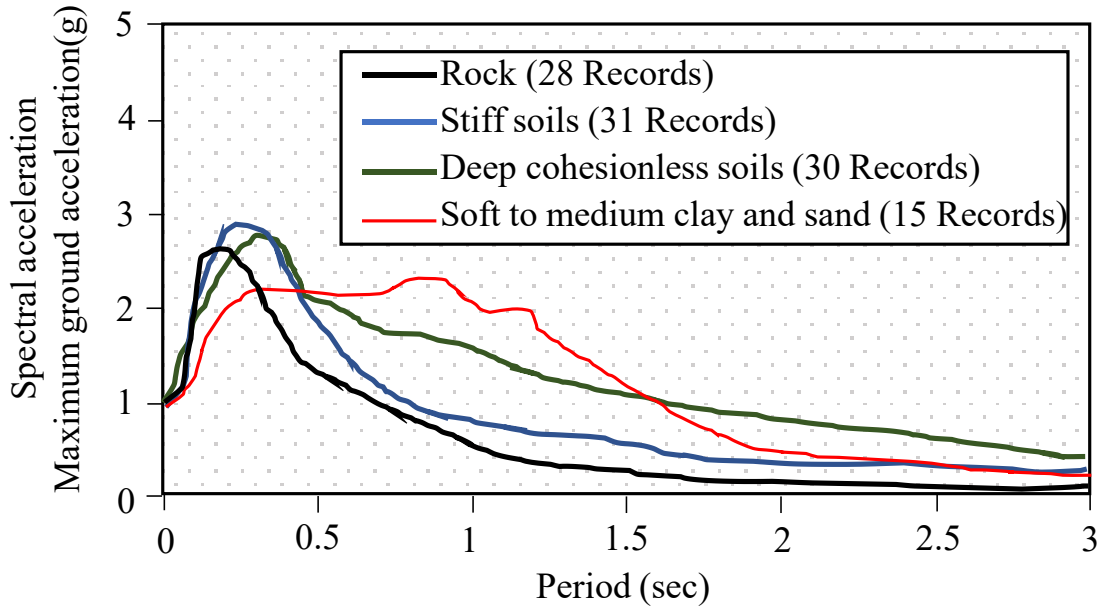
Figure 2.7 Typical normalized site response spectrum (5% damping ratio) for varied local site conditions (after Seed et al. 1976)

2.4.2.2 *Dynamic behaviour of soils*

Under earthquake shaking, soil shows nonlinear and hysteresis behaviour (Figure 2.8). Ambrosini (2006) highlighted the need for the appropriate representation of the dynamic soil response for seismic analysis. As shown in Figure 2.8, the soil response when subjected to cyclic loading can be described using the soil secant shear modulus (G_{sec}) and the corresponding damping ratio (ξ) of the hysteresis loop (Kramer 1996). According to Das (1983), G_{sec} and ξ can be determined via Equations (2.13) and (2.14), respectively.

$$G_{sec} = \frac{\tau_c}{\gamma_c} \tag{2.13}$$

$$\xi = \frac{W_D}{4\pi W_S} = \frac{1}{2\pi}\frac{A_{loop}}{G_{sec}\gamma_c^2} \tag{2.14}$$

where, τ_c and γ_c are the shear stress and cyclic shear strain values at the selected point. W_D is the energy dissipated through a loop, W_S is the determined strain energy, and A_{loop} is the area of the hysteresis loop (which is equal to W_D).
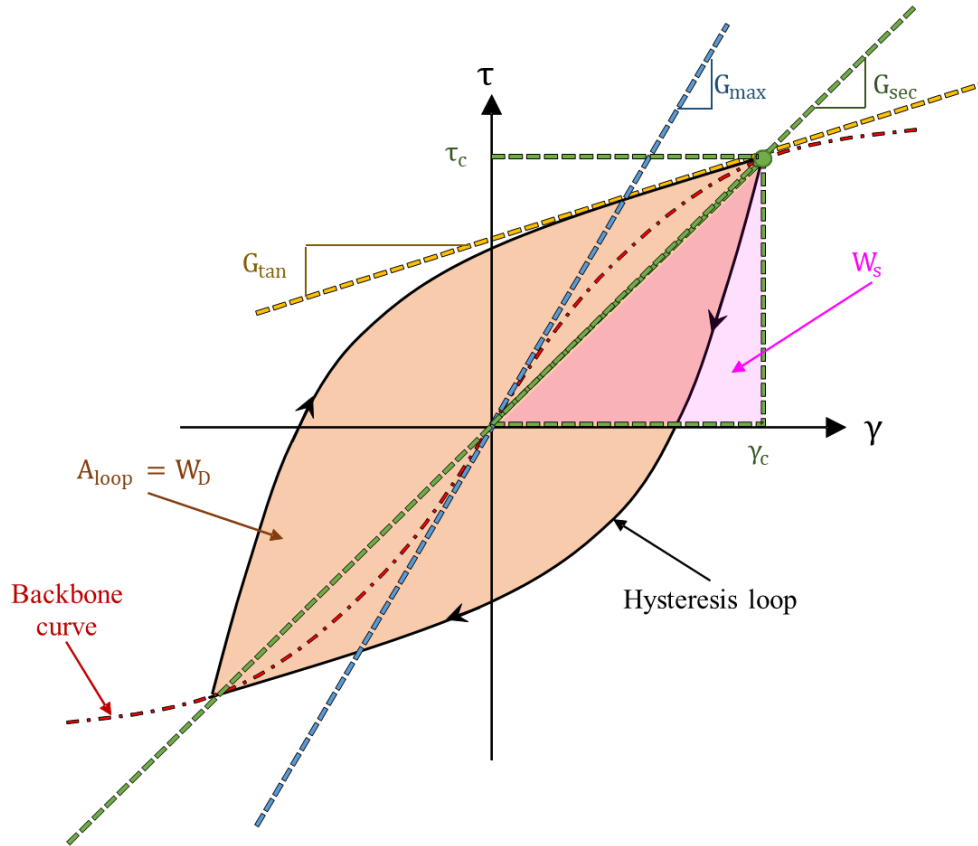
Figure 2.8 Cyclic behaviour of soil.

To capture dynamic characteristics of the soil required in a nonlinear analysis reasonably well, the backbone curve representing the change of G_{sec} with cyclic shear strain level should be considered, along with the corresponding damping due to the reduction of soil shear modulus, as shown in Figure 2.9. The secant shear modulus and damping ratio represent the nonlinear soil response in the equivalent linear analysis (El Naggar and Novak 1996). Figure 2.9 shows how the secant shear modulus of a soil (G_{sec}) and the corresponding damping ratio (ξ) change with the cyclic shear strain level (γ). As

a conclusion, the secant shear modulus is high for low shear strain amplitudes and reduces as the shear strain amplitude develops. In the equivalent linear method adopted by other researchers (Beresnev and Wen 1990; Zeghal and Elgamal 2000; Yunita and Apriadi 2015), one value of the secant shear modulus and the corresponding damping ratio are used which result in capturing the nonlinear soil response in an average sense.

However, to fully capture cyclic soil behaviour, the path of the hysteresis loop plus soil plastic deformation should be considered (Yeganeh and Fatahi 2019). In this way, the nonlinear response, stiffness degradation, and soil damping can be captured precisely. Implementing the nonlinear response of soil is necessary for seismic analysis, mainly when a risk of soil liquefaction may be present (Peiris et al. 2006). For example, during the rapid shaking of the ground under strong earthquakes, considerable pore water pressures can be developed in saturated loose granular soils under undrained conditions, resulting in reducing of the effective stresses and a considerable loss in the strength and stiffness of the soils. This phenomenon is called soil liquefaction, which is mainly influenced by the presence of groundwater, the soil particle size distribution, the soil in-situ relative density, the effective confining stress, and the ground motion features (Idriss and Boulanger 2008).
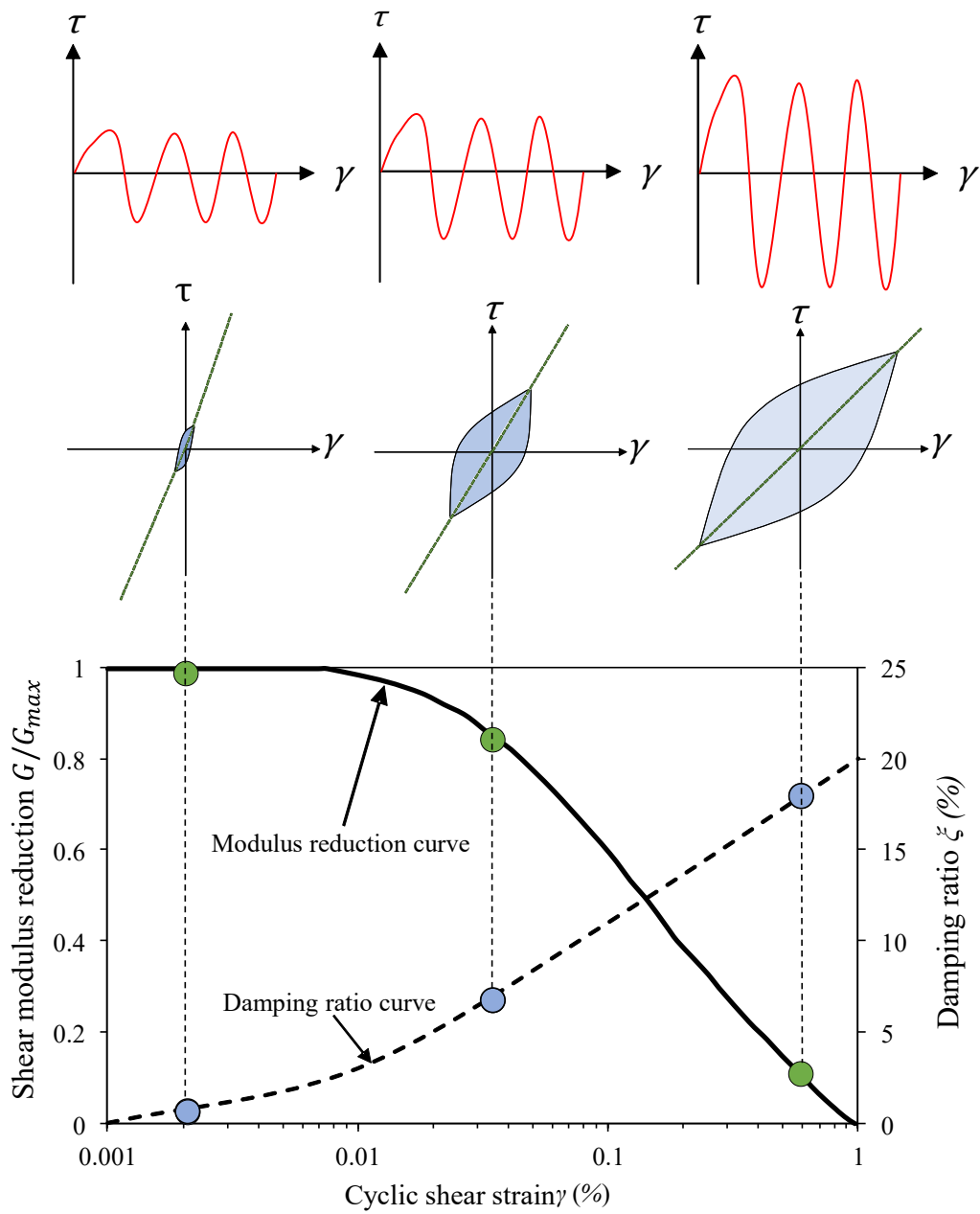
Figure 2.9 The decrease of shear modulus and the related damping ratio curves with cyclic shear strain.

2.4.2.3 Soil-foundation-structure interaction (SFSI) concept for liquid storage tanks

When a liquid storage tank is built on soft soil, this heavy and rather stiff structure would influence soil motion under seismic loading (Lou et al. 2011). This leads to the deviation of the foundation and structure from free-field motion due to SFSI. Free-field condition refers to ground motions that are not impacted by the vibrations or scattering

of seismic waves near or at the foundation level. Usually, practicing engineers assume a rigid soil base for the seismic analysis and design, as SFSI effects have been found to increase damping and the structure natural period (i.e. can be conservative). However, including SFSI leads to capturing the foundation translation and rotation, which can alter the seismic response of the structure. For liquid storage tanks, many researchers, such as Veletsos (1984), Haroun and Housner (1981), and Veletsos and Tang (1991), have investigated the dynamic behaviour of liquid storage tanks, including the effects of soil flexibility on the system response. Mainly, the SFSI effects can visibly affect the impulsive hydrodynamic component, but may not much affect the convective hydrodynamic component, which is associated with frequencies below than the tank–liquid system natural frequencies (Veletsos 1984). Therefore, the inclusion of the SFSI is mainly considered based on the model developed by Veletsos and Tang (1991) and is addressed by the well-established design codes such as NZSEE (2009) and Eurocode-8 (2006). In general, including the SFSI effect can modify the translational and rocking components of the mechanical model proposed by Malhotra (2000). According to Larkin (2008) these effects can be implemented by introducing translational and rotational stiffnesses (K_h and K_r). Moreover, Furthermore, Furthermore, when the soil's flexibility improves, the fundamental period of the tank-liquid system and total damping increase, minimizing the maximum force's response (see Figure 2.10).
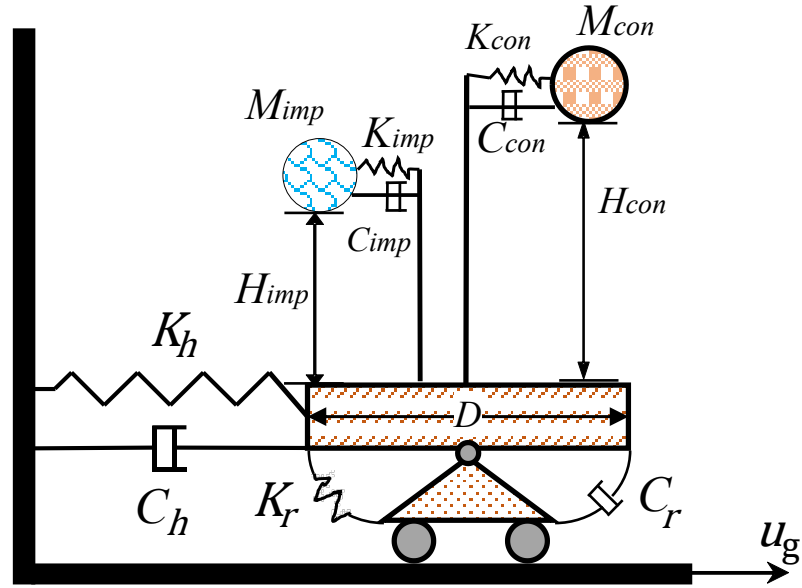
Figure 2.10 Mechanical models for the soil-tank-liquid coupled system (after Larkin 2008).

The translational and rotational stiffness (K_h and K_r) for circular rigid foundations supported at the surface of a homogeneous half-space is provided based on Lysmer (1978) theory, and explained on Equations 2.15 and 2.16 (refer to Givoli 1991):

$$K_r = \frac{8GR}{2 - \vartheta} \tag{2.15}$$

$$K_h = 8GR^3/3(1 - \vartheta) \tag{2.16}$$

where G and ϑ are the shear modulus and Poisson's ratio for soil, respectively.

In general, the natural period and damping of the tank liquid system, including the SFSI effect, can be considered using NSZEE (2009) guidelines as in the following relationships:

$$T_{imp}^* = 2\pi \sqrt{\frac{M_{imp} + M_{fod}}{K_h\, \alpha_h} + \frac{M_{imp}\, H_{imp}^2}{K_r \alpha_r}} \tag{2.17}$$

$$\xi = \xi_s + \frac{\xi_m}{(T^* + T)^3} \tag{2.18}$$

where, M_{fod} is the mass of the foundation, α_h and α_r are frequency-dependent factors converting static stiffnesses into dynamic ones based on Veletsos and Tang (1992), $and\ \xi_s$ is the radiation damping in the soil, and ξ_m is the material damping in the tank.

SFSI effects include two distinct effects, including *kinematic interaction* and *inertial interaction* effects, as illustrated in Figure 2.11 (Kausel 2010). Kinematic interaction refers to the process in which the structure foundation motions is impacted and thus differ from the free filed motions, as this stiff element (i.e. the foundation) scatters and reflects the seismic waves transferred through the soil layers. Inertial interaction denotes the displacement and rotation of the foundation which is due to the structural inertial forces, including base shear and moment (Wolf 1987; Stewart et al. 2012).

Many researchers have studied the seismic behaviour of various structures, including the effect of seismic SFSI. Existing methods for the simulation of SFSI systems comprise the Winkler methods, elastic continuum methods and numerical methods. Among these methods, the numerical method is the most advanced and rigorous one (Tian et al. 2018). Consequently, with access to powerful computers, researchers have been utilising advanced numerical techniques such as three-dimensional finite element or finite difference models quite regularly. The effects of material nonlinearity in terms of stress–strain response, diverse material properties, radiation damping, and the variations in the geometry of the supporting soil medium can be all captured in the dynamic soil–SFSI analysis using rigorous numerical methods (Meymand 1998; Dhatt et al. 2012).
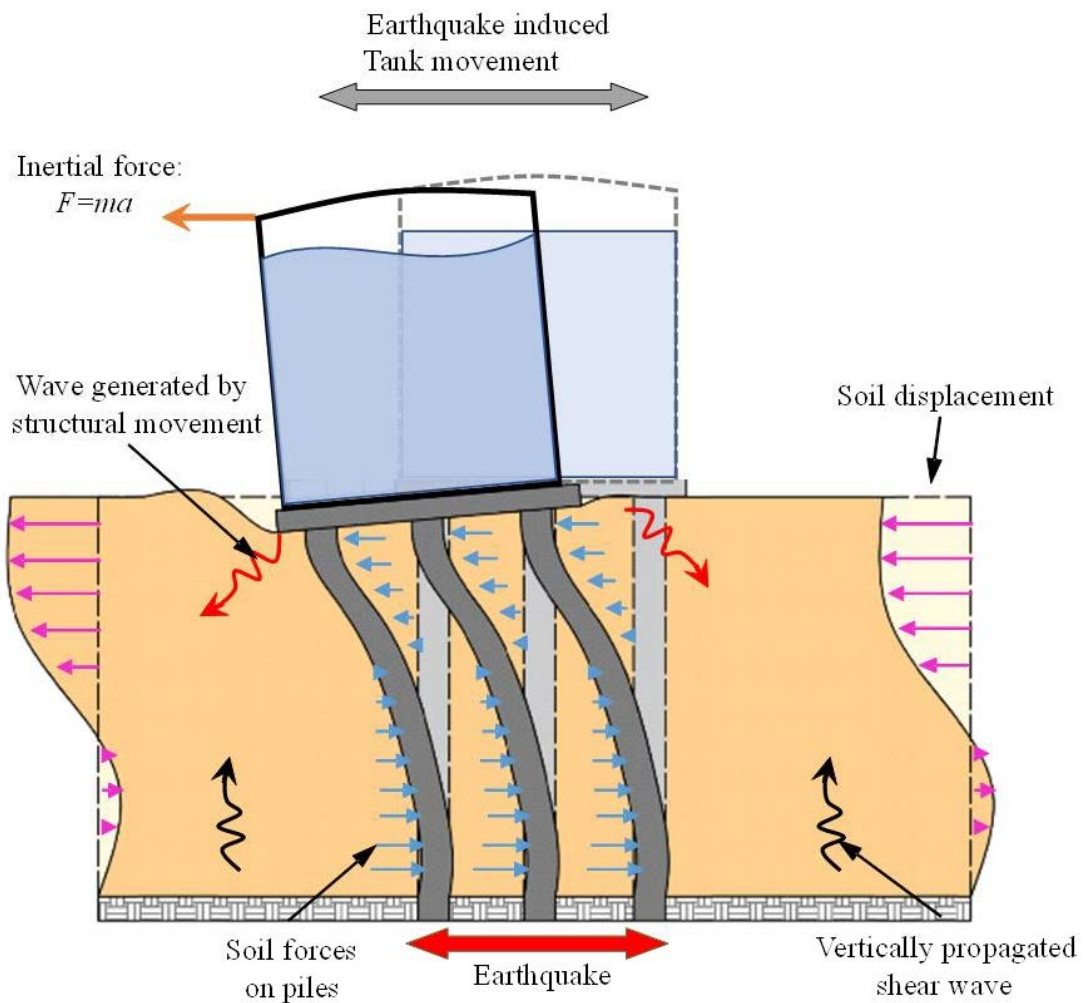
Figure 2.11 Illustration of kinematic and inertial interaction in a SFS system for liquid storage tank supported by pile foundation.

In general, SFSI can be used in dynamic analysis using numerical methods which follow one of two approaches: the substructure and direct methods. For the substructure method, as Gutierrez and Chopra (1978) explained, three main steps need to be implemented: firstly, the foundation input motion (FIM) of the foundation slab needs to be evaluated based on the assumption of a massless foundation system. Next, the impedance function, which describes the soil–foundation system stiffness and damping features, must be determined. Finally, the dynamic analysis of the structure supported on a compliant base, denoted by the impedance functions and exposed to a base excitation

of the FIM, would be conducted. This method has been implemented by many researchers for the seismic analysis of various structures (e.g. Kutanis and Elmas 2001; Allotey and El Naggar 2008; Carbonari et al. 2011). This method is based on the superposition principle, which limits it to linear soil and structure behaviours (Wolf 1989). Hence, the direct method can be used to fulfil the need for a technique capable of modelling the entire soil–foundation–structure system in one step and including both material and geometric nonlinearity (Carr 2008). Several researchers have implemented the direct method to conduct numerical studies for different foundations solutions considering soil–foundation–structure interaction and obtained reasonable results (e.g. Çelebi et al. 2012; Hokmabadi et al. 2014a; Nguyen et al. 2017; Sharma and Dey 2018; Xu and Fatahi 2019).

2.5 Observed damage to liquid storage tanks during previous earthquakes and previous research studies on seismic performance of LNG tanks

Over the past few decades, large earthquakes like 1964 Alaska, 1964 Niigata, 1966 Parkfield and 1994 Northridge have caused liquid storage tanks to experience failure or significant damage to the tank walls, roof, and foundation/supporting systems (Rinne 1967; Shibata 1974; Kono 1980; Rai 2002; Sezen and Whittaker 2006). Indeed, concrete tanks can be damaged as a result of cracks and leakage, while for steel tanks, the wall buckling is the main cause of failure.

The dynamic buckling phenomenon in steel tanks under seismic conditions is usually recognised as elastic or elastic-plastic buckling failure. Many studies have shown elastic-plastic buckling as an outward bulge close to the tank base (e.g. Djermane et al. 2014; Buratti and Tavano 2014; Shi et al. 2020). In these cases, the axial compression due to the overturning moment and the circumferential hoop stresses exceed the yield

limit for the tank wall. These forces can be generated by both the hydrostatic and hydrodynamic pressures at the bottom of the tank. Thus, this outward bulging occurs at the tank base known as the elephant's foot buckling mode of failure (Figure 2.12a). In addition, referring to Groh and Pirrera (2019), the diamond-shaped buckling, which is an elastic buckling, usually happens at small values of hoop stresses, as the inward hydrodynamic suction at the base level or the upper level of the tank wall (i.e. the secondary diamond shape buckling mode) goes beyond the outward hydrostatic pressure (see Figure 2.12b).

(a) elephant foot buckling around tank base
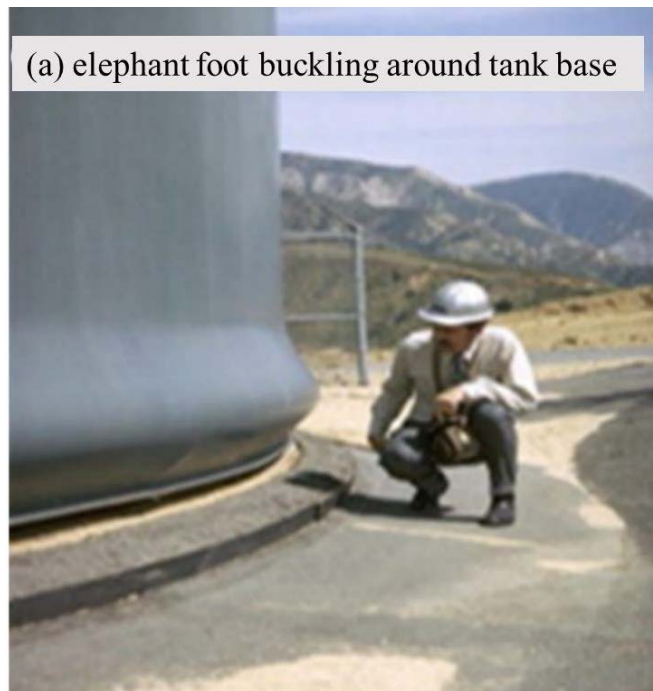
Figure 2.12 Observed damage for steel tanks under seismic load (a) elephant foot buckling example, and (b) diamond shape buckling (Malhotra et al. 2000)

LNG storage tanks are particularly susceptible to damage during strong earthquakes, where the failure of the inner steel of the LNG tanks may result in secondary tragedies such as fire and explosion. For example, in the 1964 Japan earthquake, the damage to the LNG tanks resulted in uncontrolled fires and explosions with severe pollution of the environment (Zhao ET AL 2020). The failure of LNG tanks during seismic events can impose severe safety concerns and have significant environmental and economic consequences and thus rigorous seismic analysis design of LNG tanks are crucial and essential (Zhang et al. 2011; Zhai et al. 2019).

Many researchers have investigated the seismic performance of LNG tanks using several approaches, including analytical, experimental, and numerical methods. Some of these studies were conducted assuming a rigid soil base (i.e. including only the superstructure part of the LNG tank), and few of them involved the SFSI effects. Most previous studies have investigated the seismic resilience of the inner steel tank, which has

direct contact with the LNG, and they have considered the fluid–structure interaction effects. Studies on the secondary concrete containment tanks, including SFSI effects for the entire system, have been less popular. For example, Graczyk and Moan (2008) considered the effect of the sloshing pressure on the resilience of LNG steel tank, including different liquid levels. In addition, they investigated the effects of base isolation on the seismic response of LNG tanks with different liquid levels using the finite element analysis (FEA) technique. Their numerical results revealed that the lead rubber bearings effectively avoided the transfer of significant seismic forces to the tanks and thus enhanced the LNG tanks seismic responses. Christovasilis and Whittaker (2008) calculated the effectiveness of seismic base isolation on the performance of the LNG tanks using numerical analysis and compared the seismic behaviour of the LNG tank with the simplified mechanical model, which is usually used for preliminary seismic analysis and the design of LNG tanks. They concluded that the mechanical models could be used confidently for the initial analysis and design of conventional and isolated LNG tanks. Recently, Dongyu Luo (2020) performed a shaking table test to assess the effect of the insulation layers on the seismic performance of the inner steel LNG tank under different ground motions. The results proved the beneficial effect of the insulation layer on the seismic response of the LNG tank.

In addition, the effect of the SFSI can significantly impact the seismic response of large capacity structures such as LNG tanks and several researchers investigated the SFSI effects on the seismic response of LNG tanks (Willford et al. 2010; Ruiz and Gutiérrez 2015; Tajirian et al. 2019). Sun and Cui (2015) highlighted the importance of including the SFSI effect on the seismic analysis of a base-isolated LNG tank by using a simplified mechanical model and elastic soil foundation. Their results illustrated the importance of SFSI in selecting the best isolation system.

Furthermore, Son and Kim (2019) highlighted the importance of SFSI effects on the seismic response of LNG tanks subjected to vertical earthquake components using numerical modelling and frequency domain analysis. Since many LNG tanks need to be constructed on unfavourable soil conditions, ground improvement techniques (e.g. deep cement mixing, jet grouting, stone columns) are usually needed to improve the supported soils. Hokmabadi et al. (2019) considered the impact of SFSI on the seismic response of a large LNG tank sitting on the improved ground, and they stressed the importance of conducting rigorous numerical modelling to optimise the seismic design of LNG tanks. The abovementioned studies underscore the need for advanced numerical methods for the seismic analysis of LNG, which can capture the SFSI using the direct method.

2.6 Summary

Considering the growing expansion of the LNG industry globally, the demand for LNG tanks has increased, leading to an increase in the capacity and size of these tanks. These heavy structures are often constructed near coastal areas with unfavourable soil conditions and in potential seismic regions, resulting in the essential examination of the seismic performance of these tanks and considering the different factors that affect their seismic responses.

Existing studies have explored the seismic safety of the inner steel LNG tanks and their seismic performance by capturing the FSI effect. However, only few studies have implemented the numerical analysis and adopted substructure technique and considered the SFSI effects for assessing the seismic performance of LNG tanks. Thus, this study investigates the SFSI and FSI effects on the seismic performance of LNG tanks using numerical analysis and the direct method of analysis.

In this thesis, investigations of the contemporary seismic SFSI problems for

LNG tanks, including the influence of different pile foundations and the effect of liquified soil deposits on the seismic performance of LNG tanks, are conducted using three-dimensional numerical modelling with advanced material models for soil, structure, and pile foundation system. Then, the seismic resilience of the inner steel and outer concrete tanks as well as the foundation system is evaluated by capturing both FSI and SFSI effects. In addition, the seismic performance of the inner steel tank with different aspect ratios (i.e. *H/D*) is evaluated. Moreover, the effect of wall base fixity on the outer LNG tank containment seismic performance is examined. Finally, the conclusions of the current study and recommendations for further research are presented.

CHAPTER 3   IMPACT OF PILE FOUNDATION ARRANGEMENT ON SEISMIC RESPONSE OF LNG TANKS CONSIDERING SOIL-FOUNDATION-STRUCTURE INTERACTION

3.1   General

The Liquefied Natural Gas (LNG) is cleaner and cheaper for power generation than traditional energy sources. Many tanks to store LNG are to be located at coastal areas with less favourable geotechnical conditions and often in the seismically active regions. The seismic loads acting on the LNG tanks are highly affected by the soil-foundation-structure interaction (SFSI) and evaluating this effect is quite challenging as a result of the nonlinear response of the structure and foundation interacting with the soil. This chapter presents the application of three-dimensional numerical simulation technique to study the impacts of foundation type on the seismic behaviour of a large LNG tank considering the SFSI effects. Fully nonlinear dynamic analysis under the influence of 1994 Northridge and 1995 Kobe earthquakes are performed using finite element analysis software ABAQUS to assess the LNG tank seismic response under different foundation types, namely, end-bearing pile foundation, pile-raft foundation with two different frictional pile lengths. The results show the importance of the SFSI effect in evaluation of the seismic response of LNG tanks built on pile foundations. Indeed, choice of the deep foundation system and composition of foundation in terms of raft effects and pile length can significantly change the dynamic response of LNG tank and thus seismic forces in the foundation and superstructure.

3.2 Introduction

Liquefied Natural Gas (LNG) is considered as an essential transition fuel from fossil fuels (coal and oil) to low-carbon future, while renewable energies mature technologically and economically (Gürsan and Gooyert 2021). LNG is a low-carbon fuel as compared to other fossil fuels and can synergize with renewable technologies to balance intermittent electricity outputs and provide uninterrupted energy even during peak hours with its flexible on-off cycles (Colombo et al. 2016). The LNG supply market has doubled in the last decade and it is anticipated that the next decade will see further growth, with energy growth predictions across Asia (countries like China, India, Indonesia, the Philippines, and others.) being much higher than the rest of the world. This is driven by expanding populations, rising standards of living, and the scale of urbanisation. Australian government has been discussing LNG as one of the reliable and affordable energy sources helping the energy transition market toward a new energy economy, particularly, in reginal Australia where energy intensive industries are located. Australian power grid has been moving away from coal, and LNG can play a significant role in the meantime when the economy is transitioning to greener energies and storage systems such as solar, wind, hydrogen, and batteries.

Australia has many LNG projects mainly in Queensland, Northern Territory and Western Australia, such as Queensland Curtis LNG, Gladstone LNG, Ichthys LNG, and Gorgon LNG to name few. The Newcastle gas storage facility in New South Wales is one of the major sites comprised of a 63,000 m³ non-pressurised LNG tank helping with domestic gas supply, in addition to providing energy security in the case of gas supply disruption events. Many people in need of energy are located far from gas fields. Liquefying natural gas is a way to move natural gas long distances when pipelines are too

impractical or costly to build. To achieve economies of scale throughout the LNG chain, the size of liquefaction plants and the cargo size of LNG vessels have steadily increased requiring an increase in the size of LNG storage tanks (Peiris et al. 2006). The large LNG tanks (Figure 3.1) are normally located in offloading terminals at coastal sites. The deep foundation (i.e. pile foundation) is considered as a robust solution to achieve the performance requirements of large LNG tanks at sites with poor ground conditions in several projects.

Figure 3.1 A large LNG tank at a coastal site in a region with high seismicity in east Asia.

The failure of LNG tanks during seismic events not only can impose severe safety concerns, but also can have significant environmental and economic consequences. As such, the seismic design of LNG tanks is crucially important (Zhang et al. 2011; Zhai et al. 2019). The conventional seismic design approach consists of undertaken free-field site response analysis to obtain the response spectrum at the ground surface for modal analysis ignoring SFSI effects (McCullough et al. 2009). While this approach can be considered

reasonable in areas with low seismicity and stiff ground conditions (e.g. LNG tank founded on rock), the SFSI significantly impacts the seismic response of the superstructure constructed on soft soils in areas with moderate to high seismicity (Veletsos and Tang 1990; Kim et al. 2002; Hokmabadi et al. 2019). The SFSI is a complex phenomenon and many experimental, numerical and analytical studies were conducted in the recent years to better understand the importance of SFSI and its implication in design (e.g. Nguyen et al. 2017; Xu and Fatahi 2019; Son and Kim 2019). Hokmabadi and Fatahi (2016) studied the choice of the foundation type on the seismic performance of structures considering SFSI effects and found that the choice of foundation type has a significant impact on the seismic response of buildings. Xu and Fatahi (2018) assessed the soil plasticity impact on the seismic response of buildings constructed on end-bearing pile foundations, and found that the shear forces and bending moments in the piles increased with increasing the soil Plasticity Index (PI), while the seismic response of building could move from life safe to near collapse level. Son and Kim (2019) assessed the SFSI effects on the seismic response of LNG tank subjected to vertical earthquake excitations using frequency domain analysis and highlighted the importance of soil-structure interaction.

This chapter aims to investigate the common design question on the impact of adopting different pile foundation types (e.g. end-bearing versus frictional piles) and different pile lengths on the seismic performance of an LNG tank under seismic loading. As the LNG is a green energy source the selection of LNG tank foundation type is important for both the LNG tank safety under extreme loadings like earthquake and the optimal solution for the cost and environmental impact (i.e. Life cycle solution). Therefore, implementing advanced nonlinear numerical analysis can prove the efficiency of using the end-bearing pile foundation option in term of the required design level and the safest option compared with frictional pile foundation, which can offer less material

for the more sustainable foundation option (i.e. less material) and satisfy the required level for both safety and performance. For this purpose, a three-dimensional numerical simulation in ABAQUS software is conducted. Numerical modelling details are explained, and results are presented and compared in terms of key design parameters.

3.3   Description of the adopted LNG tank and foundation

In this chapter, a 63,000 m^3 full containment LNG tank comprised of 9% Ni steel inner tank and Reinforced Concrete (RC) outer tank, which sits on the pile-raft foundation, is used to perform the nonlinear seismic analysis. The adopted LNG tank is an example of the modular LNG tank constructed in the high seismic region as reported by Son and Kim (2019). The overview of structural and geometrical characteristics of the adopted LNG tank in this study is illustrated in Figure 3.2**.** The total height of the outer RC tank is 29.27 m with a fixed reinforced concrete roof. The height of the outer tank wall is 21.9 m and the wall thickness is 700 mm. On the other hand, the height of the inner 9% Ni steel tank wall is 20 m, with a base radius of 32.5 m, and the average wall and base thicknesses are 20 mm and 40 mm respectively. Figure 3.2a represents the details for both inner and outer tanks sitting on a reinforced concrete foundation slab with a radius of 35.5 m and thickness of 1.0 m. In addition, Figure 3.2b shows the layout of the 229 reinforced concrete piles with a pile diameter of 1.0 m, which support the foundation slab. The adopted LNG tank is assumed to be sitting on a 30 m deep homogenous stiff clayey soil deposit, with an average shear wave velocity of 320 m/s, undrained shear strength 150 kPa, and Plasticity Index of 20% (i.e. low plasticity clay with USCS classification of CL). According to Australian standard AS1170.4 (2007) the site sub-soil is classified as Class *Ce* (i.e. shallow soil site). It is assumed that the bedrock is composed of strong rock allowing construction of end bearing piles on top (i.e. unit

weight of 2880 kg/m^3 and unconfined compressive strength of UCS =61.22 MPa). It should be mentioned that, based on AS3961 (2017) the atmospheric tanks shall be designed for seismic loading according to AS1170.4 if the tank is located in Zone A or Zone 2 locations specified in the code.
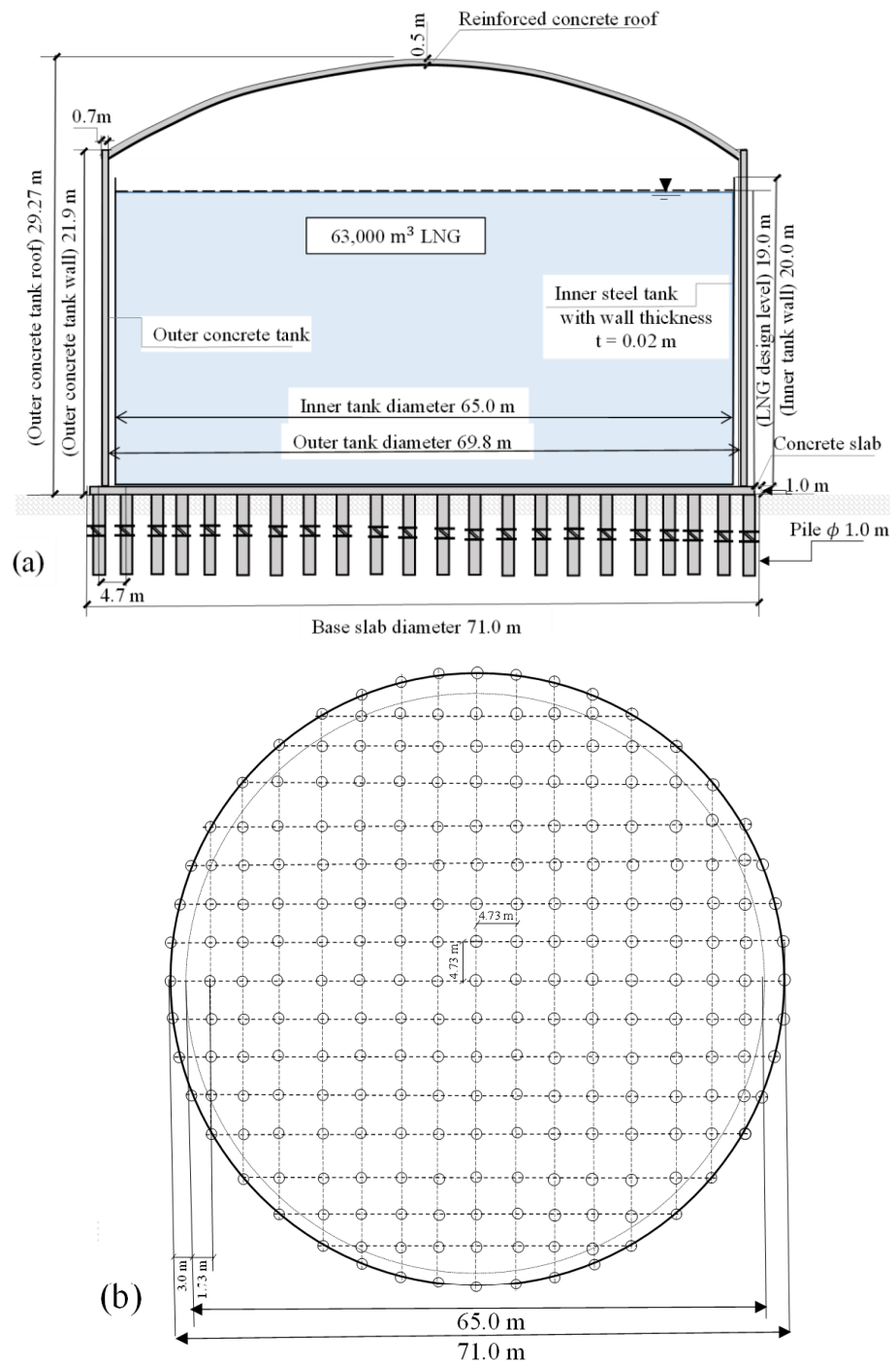
Figure 3.2 The LNG tank configuration adopted in this chapter: (a) section view of the superstructure and foundation, and (b) the plan view of 229 no. piles supporting the tank.

The three different choices of pile-raft foundation considered for supporting the adopted LNG tank and numerically simulated in this chapter are as follows (note that the foundation slab (i.e. raft) sits directly on the ground surface):

- Case 1: pile-raft foundation consists of end-bearing piles sitting on bedrock (Figure 3.3a).

- Case 2: pile-raft foundation consists of frictional piles with length of 25 m (Figure 3.3b)

- Case 3: pile-raft foundation consists of frictional piles with length of 20 m (Figure 3.3c).
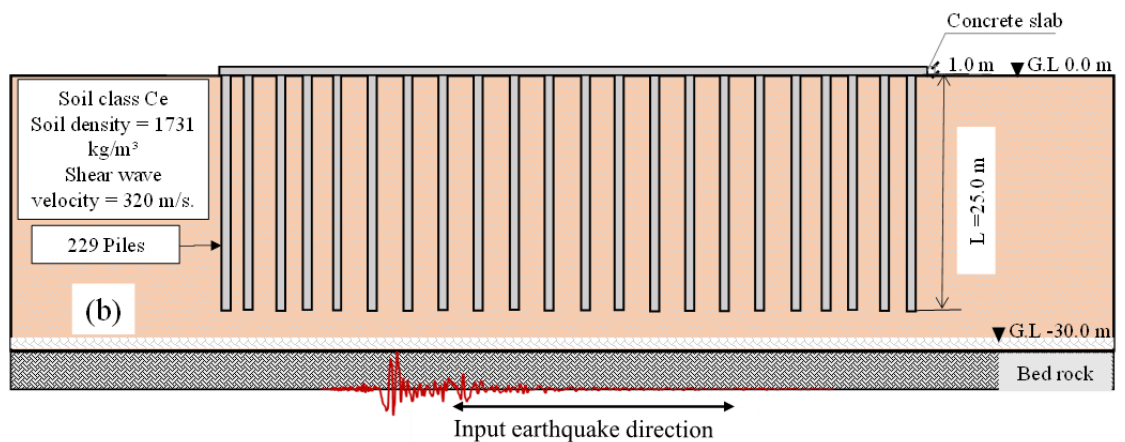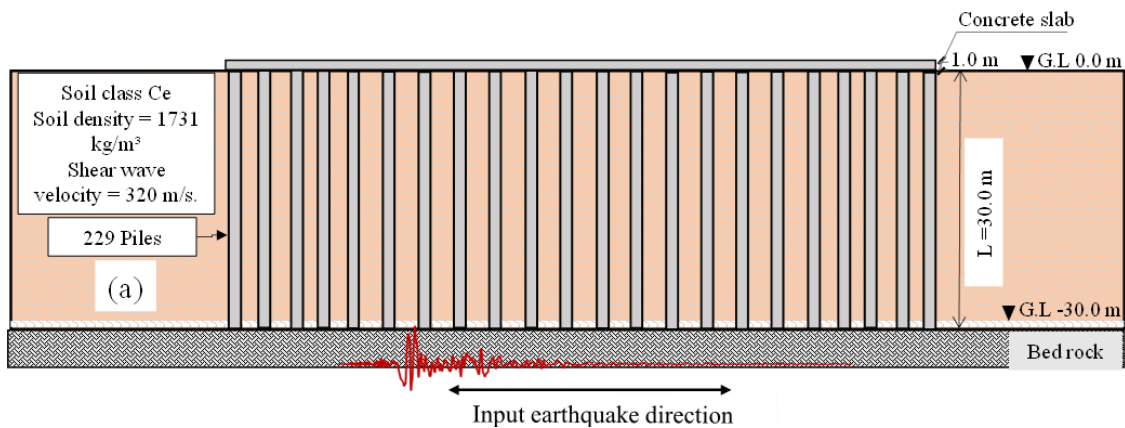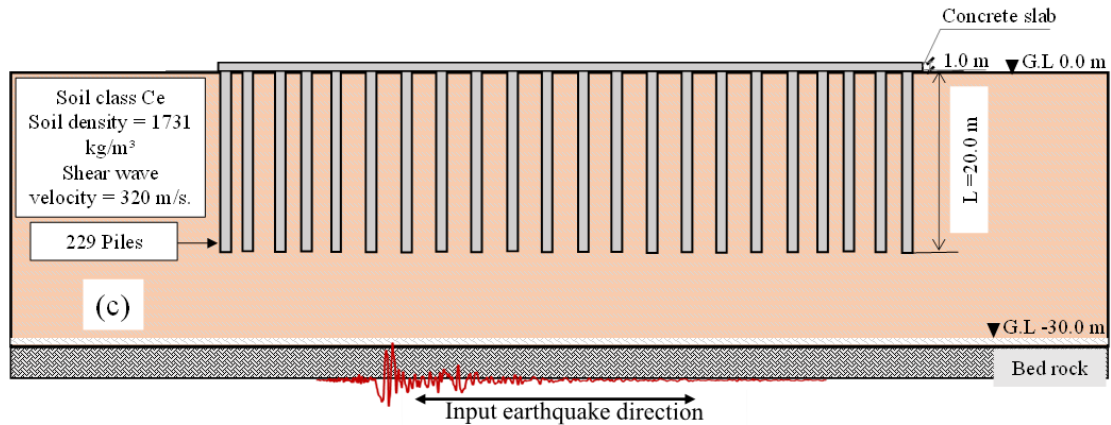
Figure 3.3 Three different choices of LNG tank foundation considered in this chapter, (a) end-bearing pile-raft foundation, (b) frictional pile-raft foundation with pile length of 25 m, and (c) frictional pile-raft foundation with pile length of 20 m.

3.4 Numerical modelling details

According to Kramer (1996), to study the SFSI effects, it is necessary to treat the structure, foundation and soil with the same rigour. Therefore, the finite element analysis is conducted, in this chapter, using ABAQUS (version 2018) for the numerical simulation of the LNG tank sitting on three different foundation types as in Figure 3.3 capturing the SFSI effects using direct method of analysis. ABAQUS is suitable for this kind of complex problems so it had been adopted by other researcher as Nguyen et al. (2016) for SFSI problems. Taking the advantage of the problem symmetry, only half of the model is simulated in this study, while appropriate boundary conditions are implemented as shown in Figure 3.4.
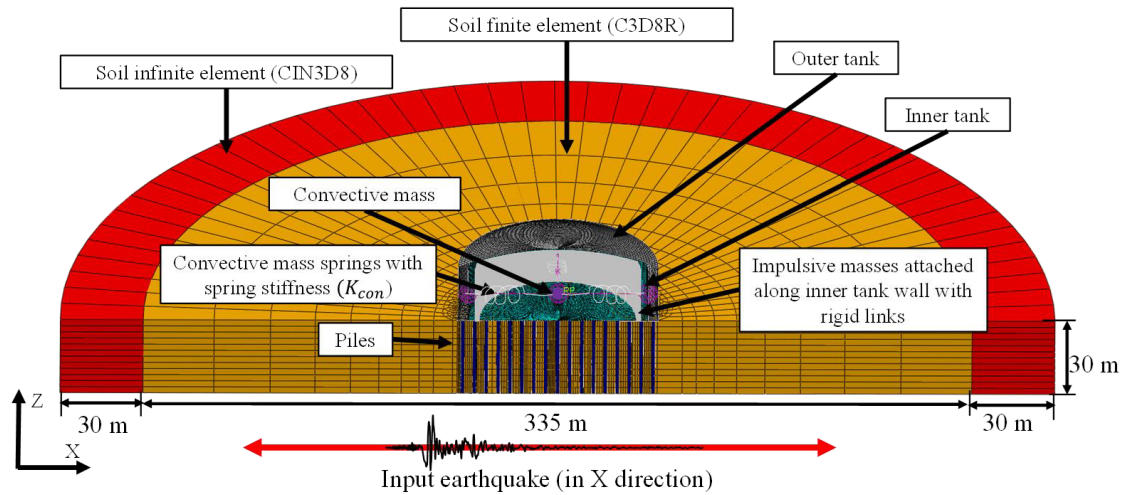
Figure 3.4 The adopted finite element model for the end-bearing pile foundation case and the modelling element details of the developed soil structure system.

3.4.1 Modelling of the superstructure

The overview of the developed finite element model is shown in Figure 3.4 for the case of the LNG tank sitting on end-bearing pile foundation as an example. For the outer RC and the inner 9% Ni steel tanks, the 4-nodes shell elements S4R were used, while the rebars in the RC were defined as layers of uniaxial reinforcement in the shell elements following the procedure recommended by Hafez (2012). To represent the elastic-plastic behaviour of the outer RC tank under the seismic loads, the concrete damage plasticity (CDP) model was used for concrete grade *C40*, where the adopted model parameters are summarized in Table 3.1. The vertical reinforcements were spaced around the RC tank wall every 3° along the circumference with a total of 120 vertical ordinary reinforcing steel bars, which had a yield strength of 400 MPa, the ultimate tensile strength of 600 MPa corresponding to the ultimate tensile strain of 0.14, the modulus of elasticity 205 GPa, and unit weight of 78 kN/m^3. These reinforcements extended from the bottom of the slab to the top of the roof. In addition, the horizontal layers of the prestressed tendons were used in the RC tank to ensure the stability and gas tightness of

the RC outer tank in normal conditions, and containment safety of the LNG in emergency conditions (i.e. to resistance hoop forces). These horizontal prestressed tendons were spaced every 0.6 m along the elevation of the RC tank with tendon yield strength of 1581 MPa, the ultimate tensile strength of 1860 MPa corresponding to the ultimate tensile strain of 0.0575, and unit weight of 78 kN/m^3.

Table 3.1 Adopted parameters for concrete grade *C40* for CDP model used in this chapter.

Parameter name	Symbol	Unit	Value	Reference
Compressive strength	f_c	MPa	40	Son and Kim
Mass density	ρ_c	kg/m^3	2640	(2019)
Dilation angle	ψ	Degree	36°	Lee and Fenves
Eccentricity	ϵ	-	0.1	(1998)
Compressive yield strength ratio	f_{b0}/f_{c0}	-	1.16	
Compressive stiffness recovery parameter	w_c	-	1	Hafez (2012)
The hydrostatic effective stress ratio	K	-	0.667	
Tensile stiffness recovery parameter	w_t	-	0	

The 9% Ni steel material which is recognized by the ASTM (2017) as A353-17 for cryogenic service temperatures, with the yield stress (f_y) and ultimate strength (f_{ult}) of 515 MPa and 690 MPa, respectively, was used in this study for the inner tank. Additionally, elastic modulus of the 9% Ni steel was considered to be 205 GPa. The 9% Ni steel material behaviour was modelled using the kinematic hardening rule with von Mises yield criteria, and the strain hardening modulus was equal to 3,888 MPa, so the metal inelastic behaviour under seismic loading can be captured similar to what was reported by other researchers (Bernier and Padgett 2020; Miladi and Razzaghi 2019; Razzaghi and Eshghi 2015).

3.4.2 Modelling of the fluid-tank interaction

To evaluate the hydrodynamic forces exerted on the LNG tank, the simplified mechanical models are generally used in practice. The FSI under seismic loads is due to two main vibration modes, namely the impulsive mode (rigid movement of the liquid) and the convective mode (the surface sloshing of the liquid) which can be captured via two different sets of spring-mass systems as recommended by Housner (1957). In this study, the LNG was modelled using a mechanical model based on the framework of Housner (1957) and Virella et al. (2006), as shown in Figure 3.5. The impulsive liquid response was modelled using the lumped added-mass method presented by Virella et al. (2006) which is also recognized by Eurocode-8 (2006), as a rigorous and well-established alternative to Houser (1957) mechanical impulsive mass method. In this method, the impulsive hydrodynamic pressure is modelled as series of added masses attached along tank wall via rigid springs. As the hydrodynamic pressure is distributed on the tank wall, the wall is divided to several segments and the pressure at each segment is calculated and modelled as an attached lumped mass m_{imp}, determined via Equation (3.3). These added masses are attached to the tank wall in both vertical and circumferential directions via a connecting element (i.e. Multi-points constraints *MPC* link in ABAQUS adopted in this chapter) which can capture the impulsive pressures. Indeed, by utilizing the distributed added-mass method, the response of the liquid storage tank under horizontal loading can be captured more precisely (Virella et al. 2006).

The convective mode is mostly uncoupled from and independent of the impulsive mode, and can have less impacts on the overall response of the liquid storage tank under horizontal loading, and thus many previous studies ignored the convective mode of liquid in the add-mass approach for the sake of simplicity (e.g. Virella et al. 2006; Buratti and Tavano 2014). However, in this study, the convective mass was included by using spring-

mass method recommended by API-650 (2007) for the sake of accuracy and reliability to capture extra forces and bending moments in the foundation-structure system. Thus, the impulsive and convective modes were both captured in the numerical modelling to assess the seismic behaviour of LNG tank and details are presented below.

Proposed mechanical model used for FSI modeling
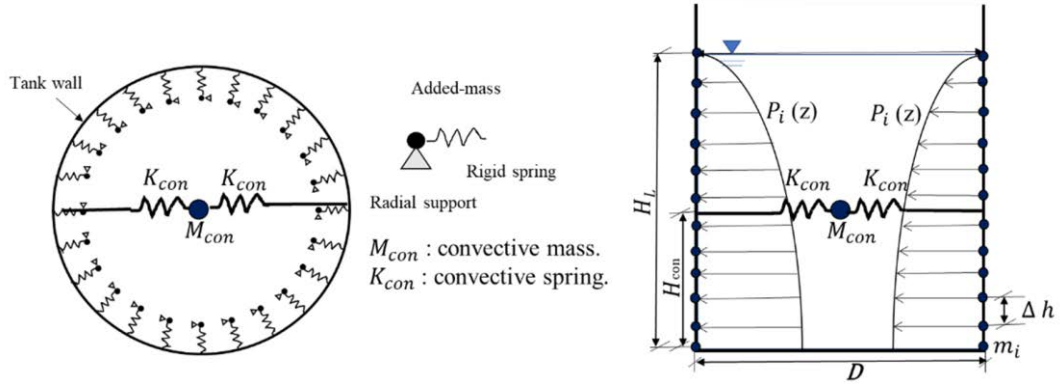
Figure 3.5 Proposed mechanical model used for FSI modelling in this chapter.

As explained in Eurocode-8 (2006), the impulsive component of the hydrodynamic pressure (p_{imp}) and can be given by the following expressions, to obtain the distributed impulsive masses m_{imp}:

$$p_{imp}(\xi, \varsigma, \theta, t) = C_{imp}(\xi, \varsigma) \rho R * A_g(t) \tag{3.1}$$

$$C_{imp}(\xi, \varsigma) = 2\gamma \sum_{n=0}^{\infty} \frac{(-1^n)}{\left(\grave{I}_1 \left(\frac{v_n}{\gamma} \right) \right) v_n^2} cos(v_n \varsigma) I_1 \left(\frac{v_n}{\gamma} \xi \right) \tag{3.2}$$

$$m_{imp} = \frac{p_{imp} \Delta h}{A_g(t)} \tag{3.3}$$

where $\xi = r/R$ and $\varsigma = z/H_L$ are the coordinates "non-dimensional", R is the radius of the tank, r, θ, z are components of cylindrical while the z axis is vertical, t is time, C_{imp} is impulsive pressure distribution coefficient, $v_n = ((2n+1)/1) \ \pi$, $\gamma = H_L/R$, I_1, $\grave{I}_1$ are mathematical functions "the modified Bessel functions" of order 1 and its derivative, respectively, $A_g(t)$ is the ground acceleration in the free-field condition, and ρ is the mass

51

density of the liquid. Indeed, Equation (3.3) was used to determine the lumped mass at each interior node of the inner tank, where Δh is the distance between the adjacent nodes along the tank wall elevation.

The convective hydrodynamic pressure was modelled using a spring-mass technique based on Houser (1957) framework, in line with the procedure adopted by several codes and regulation such as API-650 (2007). In this method the first convective mode of vibration is considered only in terms of a single convective mass (i.e. M_{con}) attached with the inner tank at a specific height equal to H_{con} (the centre of action or effective height of the convective mass) via springs with a stiffness equal to K_{con}, where in this study the springs connecting the mass to the tank wall in the horizontal direction, which is the direction of the applied earthquake load. The required parameters to capture the convective hydrodynamic effect can be determined using the following relations (API-650 2007):

$$M_{con} = 0.23 \frac{D}{H} \, tanh\left(3.67 * \frac{H}{D}\right) * M_{total} \tag{3.4}$$

$$C_{con} = \frac{0.578}{\sqrt{tanh\left(3.68 * \frac{H}{D}\right)}} \tag{3.5}$$

$$K_{con} = (2 * \pi * \frac{M_{con}}{T_{con}})\char`^2 \tag{3.6}$$

$$H_{con} = \frac{cosh\left(3.68 * \frac{H}{D}\right) - 1}{tanh\left(3.68 * \frac{H}{D}\right) \, sinh(3.68 * \frac{H}{D})} \tag{3.7}$$

where, M_{con} is convective mass, M_{total} is the total liquid mass , T_{con} is the convective period, C_{con} is sloshing period coefficient, K_{con} is the effective stiffness for the convective mode in N/m, H_{con} is the convective mass height, and H and D are the tank liquid height and radius, respectively.

3.4.3 Modelling of the soil deposit and the piles

The LNG tank sits on a 30 m deep class *Ce* clayey soil underlain by a strong class Bedrock, and the adopted soil mechanical properties are summarized in Table 3.2 These properties were obtained from actual in-situ and laboratory experiments and therefore they have merits over the assumed parameters. It is assumed that the water table is below the bedrock level. A simplified equivalent linear method based on Seed and Idriss (1969) was adopted in this chapter, which is a common simplified method adopted by practicing engineers to capture the shear strain compatible soil stiffness, capturing the soil nonlinearity in an average sense (Fatahi et al. 2018). In this method, a trial and error process utilising soil backbone curve were used to find the damping ratio and shear modulus of the soil corresponding to the maximum shear strain experienced by the soil. Thus, the adopted equivalent stiffness value for the soil is different for each earthquake record and foundation option, as the soil stiffness depends on the cyclic shear strain created in the soil deposit. In this chapter, after several trial and errors, the maximum shear strain in the soil deposit for LNG tank was obtained and is reported in Table 3.3 for both 1994 Northridge and 1995 Kobe earthquakes. The corresponding shear modulus reduction factors and damping ratios were obtained based on the backbone curves reported by Sun et al. (1988) (see Figure 3.6). It should be noted that Rayleigh damping model was used to consider variations of soil damping during the earthquake excitations with adopted mass damping factor (α) and stiffness damping factor (*ß)* reported in Table 3.3. The linear brick element, with reduced integration (C3D8R) solid elements were used to simulate the soil. Indeed, these linear elements are not stiff in bending, which is not critical for soil modelling, and the use of the reduce integration calculation scheme in these elements could facilitate the soil behaviour with acceptable computational cost (Dong et al. 2016), as these elements use less integration point in each direction than fully

integrated elements (i.e. These linear elements have only single integration point located in the element centroid). Moreover, the CIN3D8 (8-node linear one-way infinite brick) elements were used to represent the far-field soil, and these elements allowed the model to absorb the energy from the "unbounded" surrounding soil domain while the horizontal deformations were also simulated accurately.

Table 3.2 Soil properties adopted in this chapter.

Soil properties	Symbol	Unit	Value	Reference
Mass density	ρ_{soil}	kg/m^3	1731	Tabatabaiefar and Fatahi (2014); Rahvar (2006)
Shear Wave Velocity	V_s	m/s	320	
Poisson's ratio	v	-	0.39	
Maximum shear modulus	G_{max}	MPa	177.3	
Plasticity Index	PI	%	20	
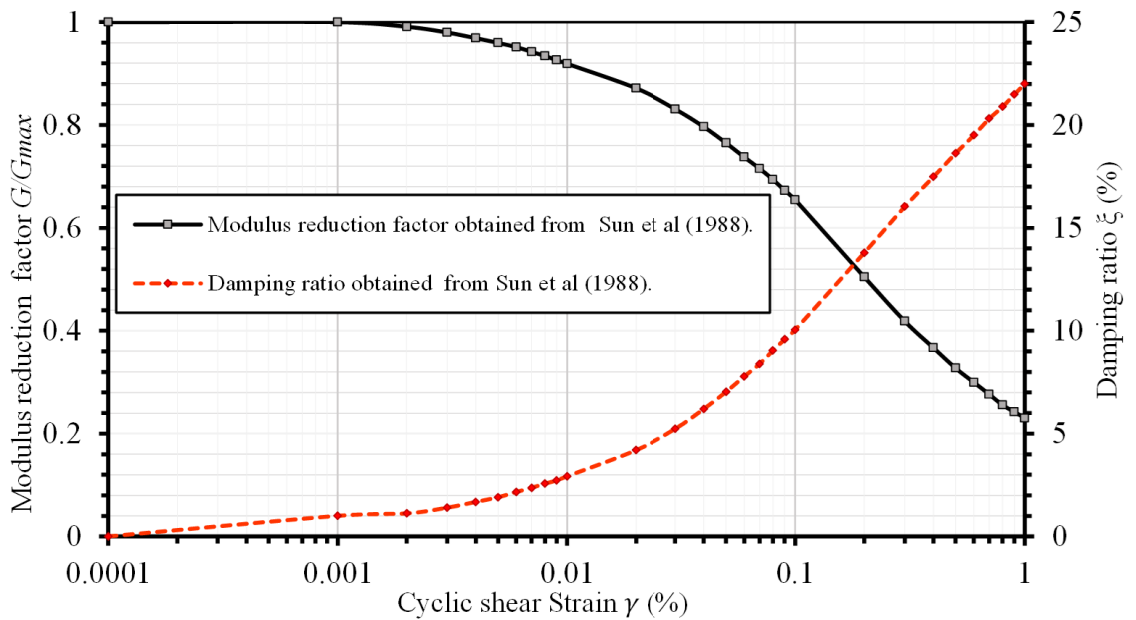
Figure 3.6 Backbone for cohesive soils (data from Sun et al. 1988).

Table 3.3 Adopted equivalent stiffness and damping values for the soil for different earthquakes and foundation options.

Earthquake	Foundation option	Maximum shear strain in the soil (γ_{max})	Adopted compatible shear modulus ratio of soil (G/G_{max})	damping ratio of soil (ξ)	Adopted Rayleigh damping parameters	Reference
1994 Northridge Earthquake	Frictional pile with L= 20 m	0.40%	0.39	16.0%	$\alpha = 3.39$ $\beta = 0.0057$	Sun et al. (1988)
	Frictional pile with L= 20 m	0.34%	0.42	17.3%	$\alpha = 3.67$ $\beta = 0.0061$	
	End-bearing pile with L= 30 m	0.29%	0.42	18.0 %	$\alpha = 3.81$ $\beta = 0.0063$	
1995 Kobe Earthquake	Frictional pile with L= 20 m	0.54%	0.32	17.0%	$\alpha = 3.61$ $\beta = 0.00608$	
	Frictional pile with L= 20 m	0.50%	0.33	17.5%	$\alpha = 3.71$ $\beta = 0.00618$	
	End-bearing pile with L= 30 m	0.45%	0.35	18.7%	$\alpha = 3.96$ $\beta = 0.0066$	

For simulating the piles, allowing convenient determination of bending moments and shear forces, hybrid method was used by embedding a flexible beam element into the centre of the solid pile element, as reported by other researchers (Rasouli and Fatahi 2019; Banerjee et al. 2014). Hence, each pile was modelled using C3D8R linear brick element with an embedded flexible linear beam element B31, where the flexural stiffness (*EI*) of the beam inside the pile was set as 1,000,000 times less than the pile flexural stiffness, so, it does not affect the pile structural response. Additionally, the elastic-perfectly plastic constitutive model was used to simulate the solid element of pile elements, thus the pile was modelled to behave elastically until the yielding stress in the concrete solid element would be reached, which is equals to the compressive strength of the *C40* concrete, as recommended by Shing and Tanabe (2001).

3.4.4 Modelling of interfaces, boundary conditions and adopted earthquakes

The contacts were defined between the raft, the piles and the soil deposit to consider any possible sliding or separation of these structural parts from the surrounding soil during the earthquake excitations. Since the contact pair approach was used, contacting surfaces needed to be defined as a "master surface" and a "slave surface". In this chapter, the soil surfaces around the piles, and at the frictional pile toes were considered as a master surface while the pile surfaces were considered as the slave surface. Additionally, the raft foundation (i.e. the outer tank slab foundation) was tied to the piles head via tie connection constraints, and was in a contact with the soil surface (the soil was defined as master surface while the bottom surface of the raft foundation was adopted as the slave surface). The hard contact algorithm was used to simulate the interaction of surfaces in the normal direction, which allowed separation of surfaces with zero tension capacity. The tangential behaviour of the interfaces followed the classical frictional model, utilising the coefficient of friction of $\mu= 0.3$, that corresponds to an interface friction angle of 19°. Regarding to the boundary conditions during the static analysis prior to the application of earthquake, the gravity load was applied, and the bottom of the soil deposit was fixed in all directions, and the vertical movements were allowed in the side boundaries, while the displacements normal to the side boundaries were prevented. However, during the dynamic analysis, when earthquake loads were applied, the one way 8 nodes infinite elements CIN3D8 were introduced on the side boundaries replacing the initial roller boundaries. These infinite elements represented the far-field soil; they are used to absorb the energy from the unbounded soil area (see Figure 3.4). These infinite elements were implemented to allow the vertical wave propagation through the soil medium, while preventing side waves from reflecting back into the

model. The dynamic response of these elements is governed by the following equation of motion:

$$\rho \, \ddot{u}_i = G \, \frac{\partial^2 u_i}{\partial x_i \partial x_j} + (\lambda + G) \frac{\partial^2 u_j}{\partial x_i \partial x_j} \tag{3.8}$$

The damping of the infinite boundary in the normal and shear directions is described by Equation (3.9):

$$d_p = G \frac{\lambda + 2G}{c_p}; \tag{3.9a}$$

$$d_s = \rho c_s \tag{3.9b}$$

where ρ is the soil density, G and λ are Lame's constants, cp and cs are the velocities of the compression wave and shear wave, respectively, dp and ds are the distributed damping of the boundary in the normal and shear directions, respectively, u_j is the particle displacement, x_i and x_j are the positions of noted i and j, respectively. It should be mentioned that the detailed inspection of the numerical results revealed that ground surface motions near the lateral boundaries closely matched the free-field ground motion, confirming the suitability of the adopted boundary conditions. The summary of the adopted elements used in this chapter are presented in Table 3.4. It should be note that the entire model was composed of 236848 elements and 263918 nodes and UTS Interactive High-Performance Computing facility (with 64 Cores and 515 GP Memory capacity) was used to run the simulations.

The settlements of the LNG tank under static gravity loading (prior to applying earthquake) from numerical model are 27.5 mm, 73.6 mm and 118.7 mm for 30 m long end-bearing, 25 m and 20 m long frictional pile-raft foundations, respectively. Two strong near field earthquakes adopted and applied in the horizontal direction, at the bedrock level below the soil deposit, were the 1994 Northridge and 1995 Kobe earthquakes with acceleration records shown in Figure 3.7.
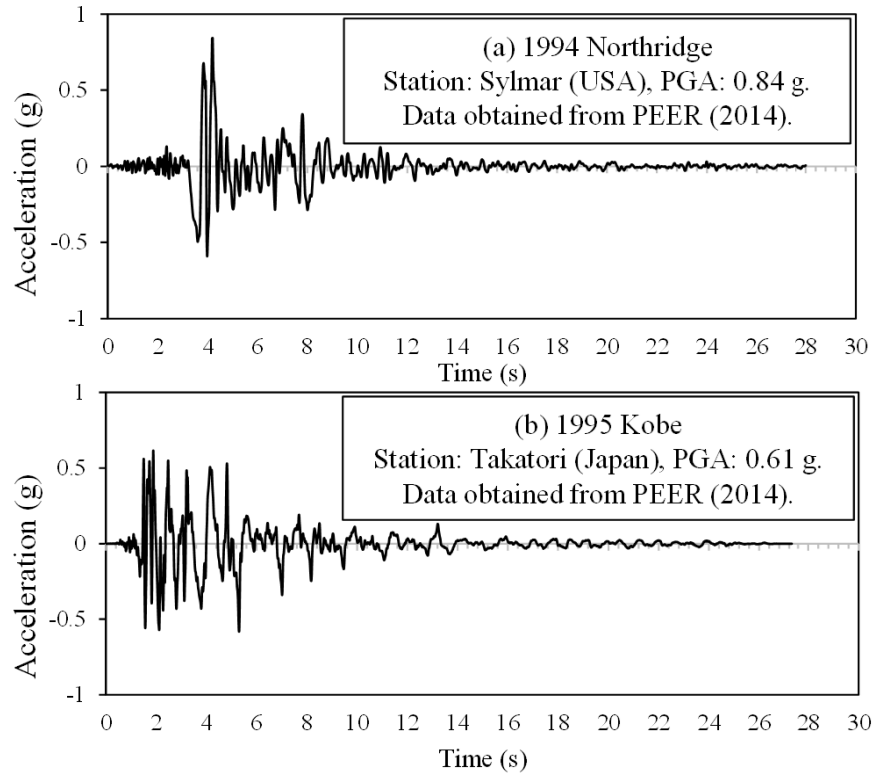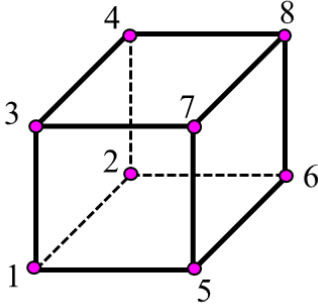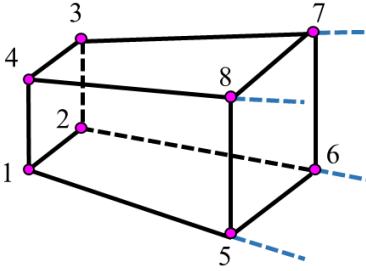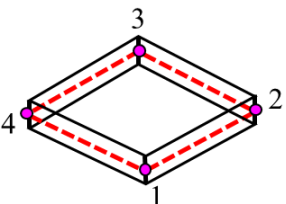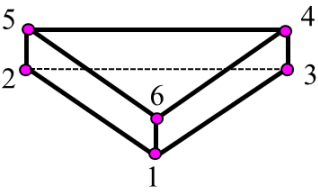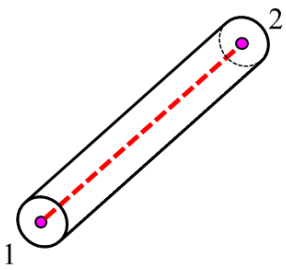
Figure 3.7 Adopted earthquake time histories in terms of the ground accelerations for (a) 1994 Northridge earthquake and (b) 1995 Kobe earthquake.

Table 3.4 details of the finite element types used in this chapter.

Part instance	Element name	Element type	Other features	Typical Illustration
Soil	Brick-8 (C3D8R)	8-node brick.	First order (Linear), reduced integration, and hourglass control.	Continuum solid element
Boundary Soil (free field boundary)	Brick-8 (CIN3D8)	8-node one-way infinite brick.	First order (Linear)3D infinite boundary element.	Infinite element
Inner tank, Outer tank, the raft, and the roof.	Thin shell-4 (S4R)	4-node doubly curved thin shell.	First order (Linear) Finite membrane strains element, reduced integration, hourglass control.	Membrane shell element
Pile	Triangular prism-6 (C3D6)	6-node triangular prism.	First order (Linear) element	Triangular prism (wedges)
Pile hybrid beam	Beam - 2 (B31)	2-node linear beam in space.	Shear flexible beam.	Beam element

3.5 Results and discussion

The free vibration analysis is conducted to verify the mechanical model implemented to model the liquid inside the tank. Besides, it is considered as an initial investigation for the foundation option effects on the dynamic properties of the LNG tank system.

3.5.1 Free vibration analysis

The modal analysis was performed on the fixed base LNG tank and the LNG tank on different foundation options using Block Lanczos algorithm, and thus the fundamental periods for the different foundation cases were determined. Indeed, the first impulsive and convective modes of the LNG liquid for fixed base condition (i.e. Excluding SFSI) were determined and corresponding periods were compared with the analytical solution presented in API-650 (2007) captured by Equation (3.10) and (3.11):

$$T_{con} = 1.8 * C_{con} * \sqrt{D} \tag{3.10}$$

$$T_{imp} = C_l \frac{H_L}{\sqrt{2000\frac{t_u}{D}}} \sqrt{\frac{\rho}{E}} \tag{3.11}$$

where, C_{con} is sloshing period coefficient [explained in Equation (3.5)], C_l is the coefficient for determining the impulsive period of tank system which depends on the *H/D* ratio, and could be obtained from API-650 (2007), t_u is the equivalent uniform thickness of the tank wall in mm, H_L is the fluid design level in meter, D is the diameter of the tank in meter, E is the modulus of elasticity of the inner tank in MPa, ρ is the fluid density in kg/m^3, which was assumed to be 470.9 kg/m^3 for LNG.

The natural periods of inner tank for the first convective and impulsive modes obtained and summarised in Figure 3.8 and Table 3.5. It can be noticed that the first

convective mode is related to the horizontal vibration of the convective mass attached with the horizontal springs, where the first impulsive mode is related to the liquid-shell vibration mode; usually, the impulsive mass vibrates in a beam type mode, while the tank shell vibrates in number of circumferential and axial waves, but here the tank shell vibrated as a beam type mode simultaneous with the impulsive vibration mode in the horizontal direction as impulsive masses were attached with rigid links to the inner tank wall.
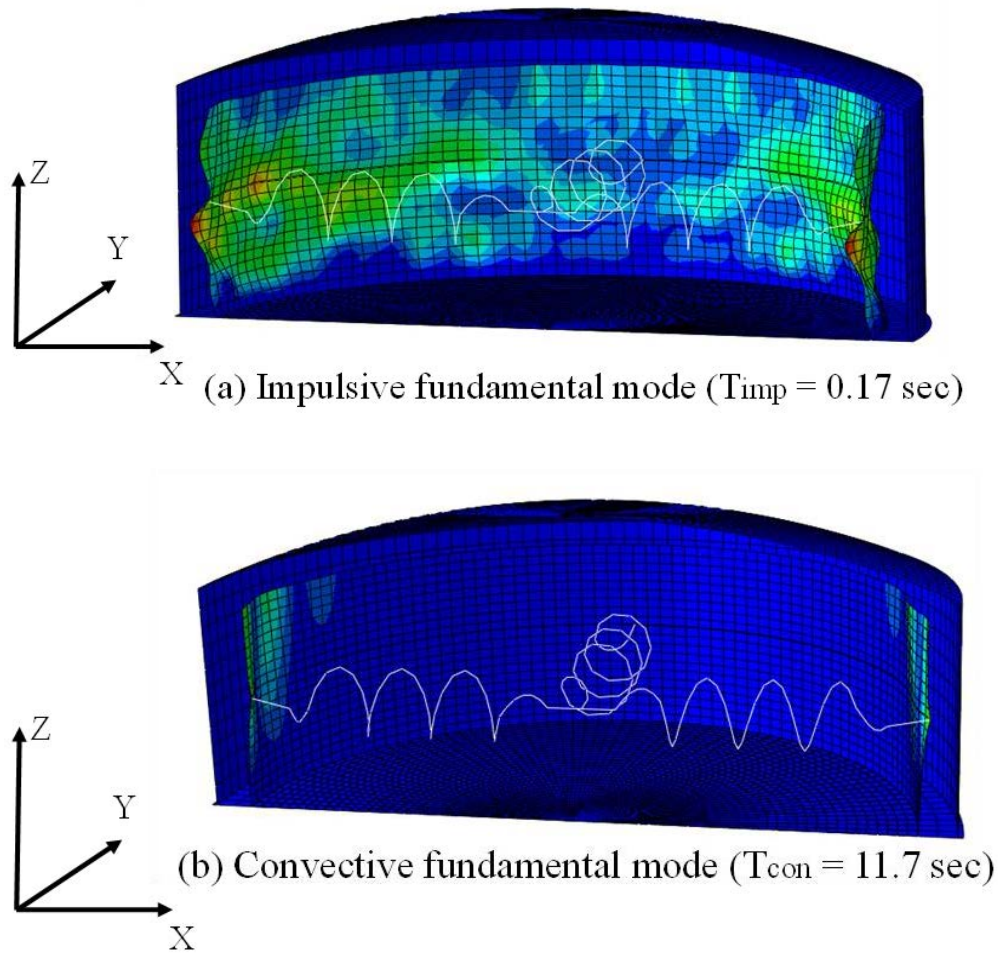
Figure 3.8 Impulsive and convective masses oscillations for the proposed mechanical model used in this study: (a) Impulsive mode, and (b) convective mode.

It can be noticed from Table 3.5 that the natural periods obtained from the numerical model for both the first impulsive and convective masses are in good agreement

with the analytical solutions presented in API-650 (2007). Therefore, the mechanical model proposed for the LNG tank to capture the FSI effects is suitable to investigate behaviour of the LNG tank with different foundation options. Consequently, the three piled raft foundation cases, i.e. end-bearing piles which are 30 m long, and the frictional piles with 25 m and 20 m length were used to conduct modal analysis and obtain the corresponding fundamental periods.

Table 3.5 Evaluation the fundamental periods of vibration obtained from numerical model and analytical solution.

Method of calculation	FEM prediction (this chapter)	API-650 (2007) Estimation
Impulsive fundamental period T_{imp} (sec)	0.17	0.18
Convective fundamental period T_{con} (sec)	11.77	10.37

Figure 3.9 represents the fundamental modes of vibration for each foundation case including SFSI. It is found that the first convective vibration mode was not affected by SFSI. While the fundamental impulsive vibration mode was impacted by SFSI. Figure 3.9 show that when the impulsive mode occurred, the whole LNG structure (i.e. the inner, outer and piles foundation) vibrated in the horizontal direction. Referring to Table 3.5, the first convective period of the tank is significantly higher than the corresponding first impulsive period. Indeed, Figure 3.10 show the response spectrum of the adopted earthquakes, where the fundamental mode of vibration for the coupling effect of the FSI and SFSI is more impacted by the first impulsive mode of LNG which located in the short period range while the first convective mode located in long period with very small spectral acceleration.
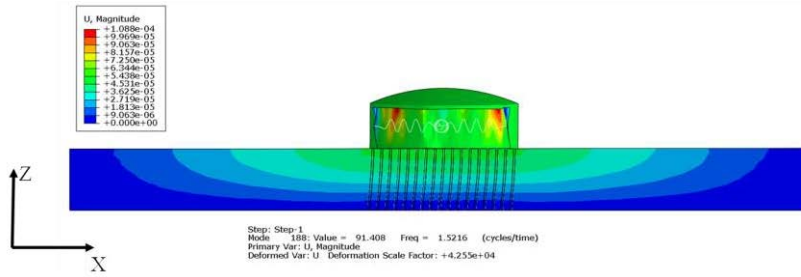
(a) Mode 1 for LNG tank on end-bearing pile foundation with pile length 30 m.
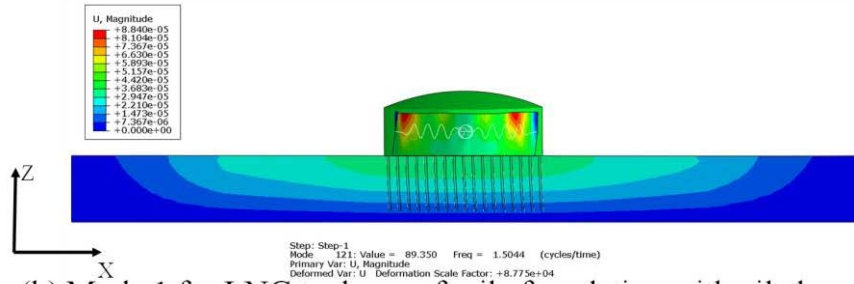
(b) Mode 1 for LNG tank on raft pile foundation with pile length 25 m.
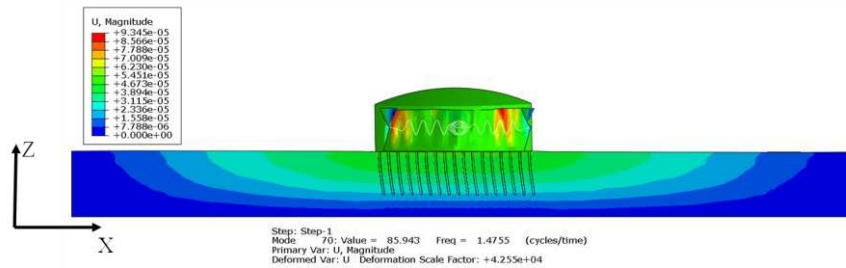
(c) Mode 1 for LNG tank on raft pile foundation with pile length 20 m.

Figure 3.9 The fundamental vibration mode shape for LNG tank with different foundation options: (a) End-bearing piled-raft foundation with pile length of 30 m, (b) Piled-raft foundation with pile length of 25 m, and (c) Piled-raft foundation with pile length of 20 m.
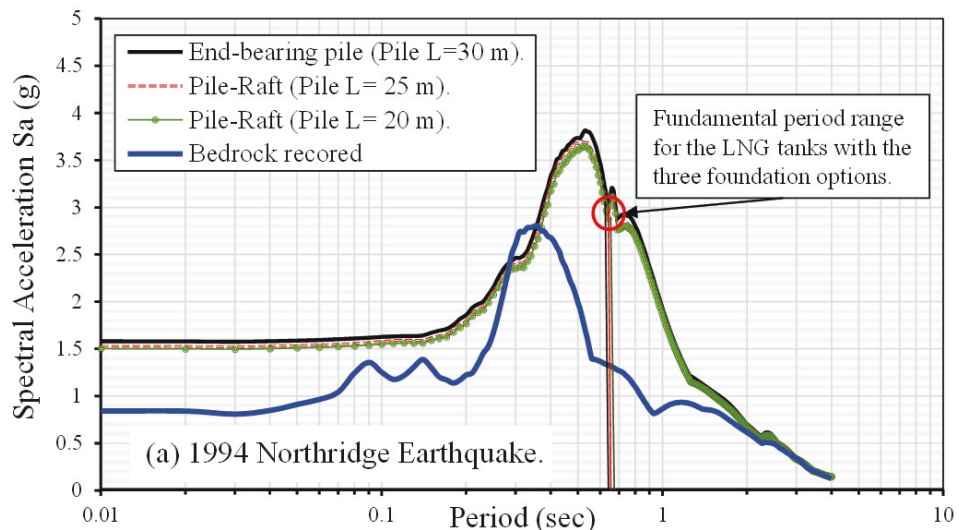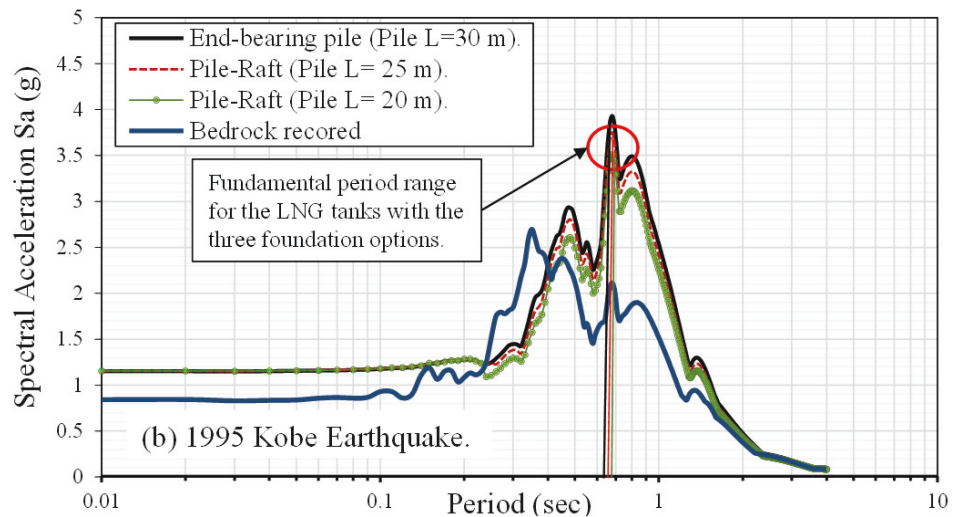
Figure 3.10 Response spectrum derived from the motion of foundation slab with 5% damping ratio under (a) 1994 Northridge Earthquake, and (b) 1995 Kobe earthquake.

Table 3.6 reports the natural periods of the LNG tank for three different foundation cases under both 1994 Northridge and 1995 Kobe earthquakes; as some of the soil properties were different for each earthquake the natural period for both earthquakes were reported. In general, the natural period of the LNG tank with the pile foundation increased significantly compared with fixed base case.

Table 3.6 Alterations of natural periods of LNG tank with different foundation types.

	1994 Northridge Earthquake		1995 Kobe Earthquake	
Foundation condition	Mode 1 (T_1)	Mode 2 (T_2)	Mode 1 (T_1)	Mode 2 (T_2)
Frictional pile with L= 20 m	0.678[*]	0.628	0.740[*]	0.688
Frictional pile with L= 25 m	0.667[*]	0.6267	0.731[*]	0.687
End-bearing Pile with L= 30 m	0.657[*]	0.625	0.728[*]	0.685
Fixed Base Tank	0.167[*]	0.158	0.167 [*]	0.158

[*] The fundamental natural period (sec)

Moreover, referring to Table 3.6, it can be seen that the dynamic response of the LNG tank was affected by the pile length and load bearing mechanism of the foundation.

For example, when the pile length increased, the system stiffness increased as more soil being replaced by concrete while the mass of the soil-structure system remained more or less similar, and consequently the natural period of the system decreased. Thus, it is essential to include the SFSI when conducting dynamic analysis of LNG tanks, as SFSI alerts the dynamic properties of the LNG tank system, directing different seismic forces to the structural elements.

3.5.2 Nonlinear time history results

The seismic analysis results were extracted and compared in terms of the response spectrum, tanks maximum acceleration profile, inner tank wall maximum structure response, and the pile seismic response (i.e. lateral displacements, shear forces and bending moments developed along the pile).

3.5.2.1 *Response spectrum*

Figure 3.10 illustrates the acceleration response spectrum of LNG tank based on the earthquake records arrived at the foundation slab level for the 1994 Northridge (Figure 3.10a), and the 1995 Kobe (Figure 3.10b) earthquakes. It is clear that by including the local site effect, the amplification in the spectral acceleration occurred, especially in period ranging from 0.5 to 2 seconds, where the LNG tank (soil-structure system) fundamental period is placed. Referring to Figure 3.10, the amplification in the spectral acceleration in some period ranges were slightly higher for the end-bearing pile foundation, in comparison to the other two foundation options. Moreover, the fundamental natural period for the end-bearing pile foundation is less than the frictional pile foundation; this means with stiffer foundation (e.g. end-bearing pile), more seismic energy can be transmitted to the superstructure compared with the more flexible foundation (e.g. frictional pile foundations). In addition, increasing the pile length in the

pile-raft foundation resulted in a minor increase in the spectral acceleration, and together with slight shortening of the structural period, resulted in the increased seismic energy transmitted to the superstructure.

3.5.2.2 *Maximum tank acceleration profile*

The maximum acceleration profiles for both the inner 9% Ni steel and outer RC tanks for the different foundation types were extracted and compared in Figure 3.11 and Figure 3.12. It should be noted that the acceleration profile was extracted along the tank wall when the maximum acceleration occurred at the top of the inner and outer tank walls in X direction at polar coordinate $\theta = 0°$ (parallel to the direction of applied earthquake).

Figure 3.11 shows the inner 9% Ni steel tank wall maximum acceleration under 1994 Northridge (Figure 3.11a) and 1995 Kobe (Figure 3.11b) earthquakes. As evident, the acceleration at the top of inner tank wall under 1994 Northridge earthquake increased by 25% and 13% when the foundation option changed from the frictional pile-raft with pile length 20 m to the 30 m long end-bearing pile and 25 m long frictional pile-raft, respectively. Similarly, for 1995 Kobe earthquake, the acceleration at the top of inner tank wall increased by 34% and 29% when the foundation option changed from the frictional pile-raft with pile length 20 m to the 30 m long end-bearing pile and 25 m long frictional pile-raft condition, respectively. In general, the acceleration profile for the inner tank varied along the tank height significantly. Similar observations were made for the outer RC tank as shown in Figure 3.12, where the maximum acceleration at the top of the outer RC tank wall was increased by about 16.5% and 23% when the foundation option changed from frictional pile-raft with pile length 20 m condition to the 30 m long end-bearing under the 1994 Northridge and the 1995 Kobe earthquakes, respectively.
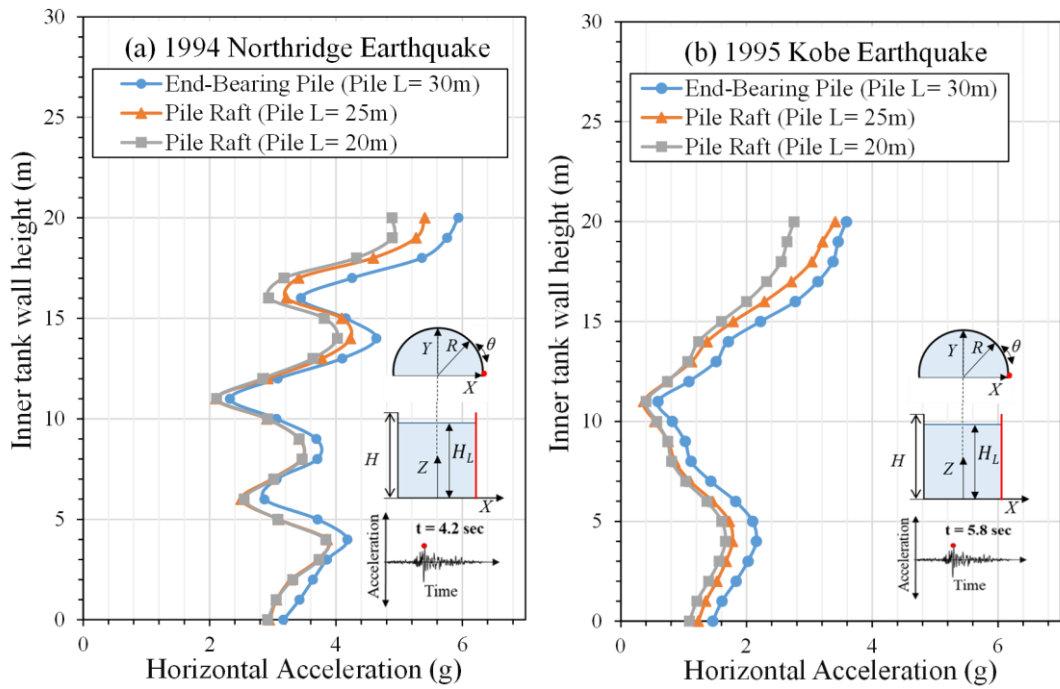
Figure 3.11 Maximum horizontal acceleration profile along inner 9% Ni steel tank wall for different foundation options subjected to (a) 1994 Northridge earthquake at t = 4.2 sec and (b) Kobe earthquake at t = 5.8 sec.
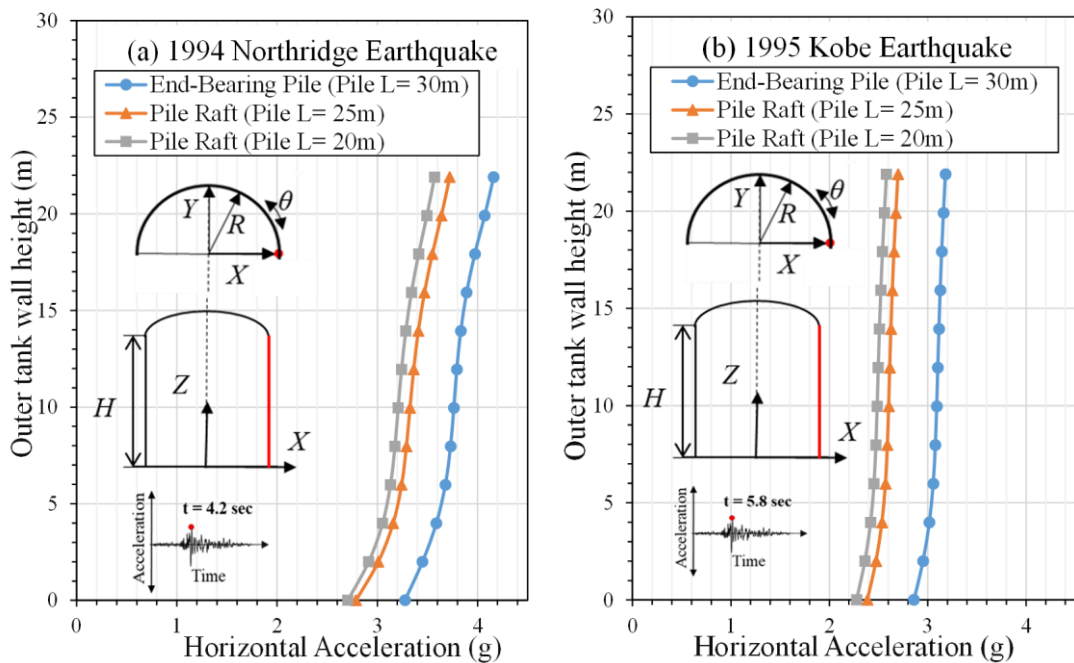
Figure 3.12 Maximum horizontal acceleration profile along outer tank wall for different foundation options subjected to (a) 1994 Northridge earthquake at t = 4.2 sec and (b) Kobe earthquake at t = 5.8 sec.

Figure 3.13 shows the horizontal acceleration distribution of the inner 9% Ni steel tank at 11 m elevation (at the convective mass level). In general, the acceleration distributes in the horizontal direction in maximum value at the horizontal line where $\theta = 0°$ and $180°$, while it decreases when it moves toward $\theta = 90°$. The maximum acceleration increased from the friction pile with 20 m length to end-bearing pile with pile length 30 m by 15 % and 65% for both 1994 Northridge and 1995 Kobe earthquakes, respectively.

(a) 1994 Northridge Earthquake

(b) 1995 Kobe Earthquake
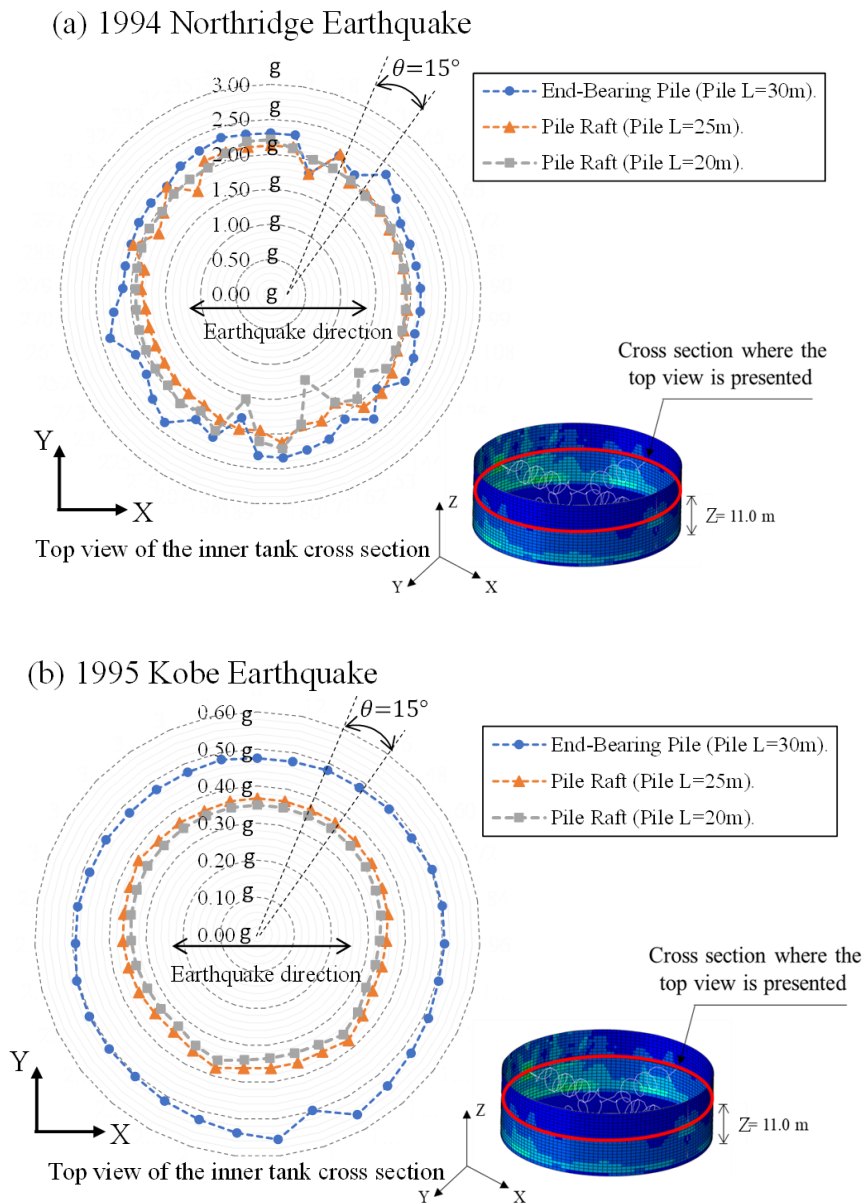
Figure 3.13 The horizontal acceleration of the at the cross section of the inner 9% Ni steel tank wall at 11 m elevation for different foundation options subjected to (a) 1994 Northridge earthquake at t = 4.2 sec and (b) Kobe earthquake at t = 5.8 sec.

68

Due to local site effect the acceleration of earthquake shear wave developed at the foundation slab has been amplified at the natural period of the soil-structure system resulting in the increase in Sa (i.e. approximately 3 times and 1.5 times under 1994 Northridge and 1995 Kobe earthquakes) as shown in Figure 3.10. Furthermore, the relatively high stiffness and self-weight (comparing to other normal structures such as residential buildings) leaded a higher acceleration, comparing to the input earthquake PGA, developed at the top of tank as Figure 3.11 presented (i.e. 5 – 6 g and 3 – 4 g for system excited by 1994 Northridge and 1995 Kobe earthquakes). According to Table 3.5 and Figure 3.10, Sa at fundamental period of soil-structure system under two different earthquakes are similar, which implies that the difference in maximum horizontal acceleration developed in the tank could be due to the effects of higher dynamic structural modes during earthquake. The increase trend of horizontal acceleration developed in tank due to change of foundation types (see Figure 3.11) follows the trend observed Figure 3.10, which is fundamentally due to the change in the natural period of the soil-structure system referring to Table 3.5.

As expected, the FSI (the presence of convective mass) has significant impact on the dynamic response of inner steel tank but less influence on the behaviour of outer RC tank, which highlights the importance of including the effects of FSI in large tank design. Comparisons show the difference in both inner steel and outer RC tanks accelerations between the foundation options, the end-bearing piles foundation option show the highest acceleration response comparing with frictional piles foundation, particularly for the outer tank; this indicates that with the more rigidity foundation option more seismic force transfer for LNG tank superstructure which need to be considered further in the LNG tank design.

3.5.2.3   The maximum structural response of the inner LNG tank walls

The safety of the steel shells of cylindrical liquid storage tanks, in general, related to their capacity against different failure modes. Where the shell buckling is the main failure mode for ground supported steel tanks (Brunesi et al. 2015; Dogangun et al. 2009). The demand requirements for the steel tanks related to the hydrodynamic forces which exert further hoop and axial forces in the steel tank wall and can cause the shell buckling. Thus, the axial force and the hoop force for circumferential unit width of the tank and radial displacements of the inner tank wall presented and discussed below for the different foundation options.

Dynamic hoop forces generated in the inner tank wall during earthquakes are induced by the liquid inertial forces applied to the tank, which are combination of impulsive and convective forces. These dynamic hoop forces are sensitive to geometry and thickness of tank wall shell, and if the exerted forces on the tank wall exceed the shell capacity, permanent deformation of the tank wall will be observed. Particularly, for the open top tank, the top of tank walls can potentially undergo sever damage (Spritzer and Guzey 2017). Shell buckling is the main failure mode for ground supported steel tanks. In particular, the elephant's foot buckling as a result of hydrodynamic or hydrostatic forces in the shell wall can occur when the tensile hoop forces and the axial compressive forces at the base of the tank (where these forces are the maximum) exceed the yield stress limit of the tank wall, resulting in elastic-plastic deformations. Moreover, when the thin shell wall buckles at the mid or the top section of the tank wall, a diamond shape buckling can occur. It should be noted that to meet the low temperature requirements for the LNG storage, special high strength steel material (i.e. 9% Ni steel) is used to meet the ductility requirements at low temperatures. The choice of the shell wall thickness is also governed by the welding issues to connect different sections of this cryogenic container to prevent

the possibility of brittle fracture in this sensitive tank (Kern et al. 2007). Figure 3.14 shows the distribution of the hoop forces for the inner LNG tank wall under 1994 Northridge and 1995 Kobe earthquakes, respectively. Where the maximum hoop forces observed around the mid height of the inner LNG tank wall (i.e. convective mass height) at polar coordinate $\theta = 0°$ on the X-axis of the tanks and occurred at t = 4.2 sec under 1994 Northridge and t = 5.8 sec under 1995 Kobe earthquake. In general, the maximum hoop forces found for the end-bearing pile foundation option while the minimum was for the friction pile with pile length equal to 20 m.
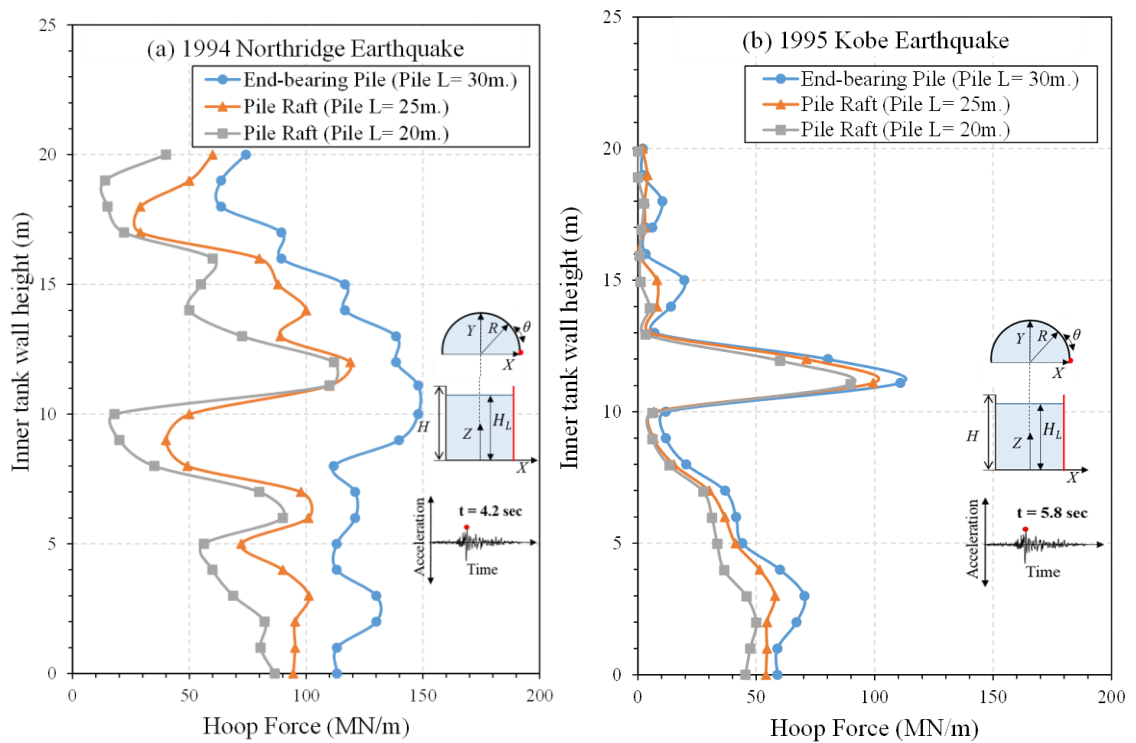
Figure 3.14 Distribution of the hoop forces in the tank wall at $\theta = 0°$: (a) 1994 Northridge earthquake at t = 4.2 sec and (b) Kobe earthquake at t = 5.8 sec.

For the axial forces (Figure 3.15) the maximum forces found at $\theta = 0°$ on the X-axis in the lower part of the LNG inner tank wall; as this vertical force along the tank wall it was increased from the top to the bottom along the inner LNG tank wall. In addition, the maximum axial forces increased with the increasing of the pile length. The effects of the axial and hoop forces on the inner tank wall response can be noticed in the radial

displacements predicted along the tanks wall. Figure 3.16 shows the radial displacement of the inner tank wall at t = 4.2 sec under 1994 Northridge and t = 5.8 sec under 1995 Kobe earthquake. The peak radial deformations were observed at the top of tank wall under 1994 Northridge earthquake **(Figure 3.16a)**, and at the mid height of the tank wall for the 1995 Kobe earthquake **(Figure 3.16b)**. The hoop and axial forces developed in the inner steel tank due to the excitation of 1994 Northridge earthquake is generally greater than those due to 1995 Kobe earthquake; a similar trend is also overserved in the distribution of acceleration (see Figure 3.13**)**. The un-uniform distribution of axial and hoop forces along inner steel tank is mainly due to the un-uniform distribution of horizontal acceleration caused by the effect of FSI, which then results in the pattern of radial displacement shown in Figure 3.16. The un-uniformity of displacement distribution along the height of tank confirms that buckling is the potential failure mode.
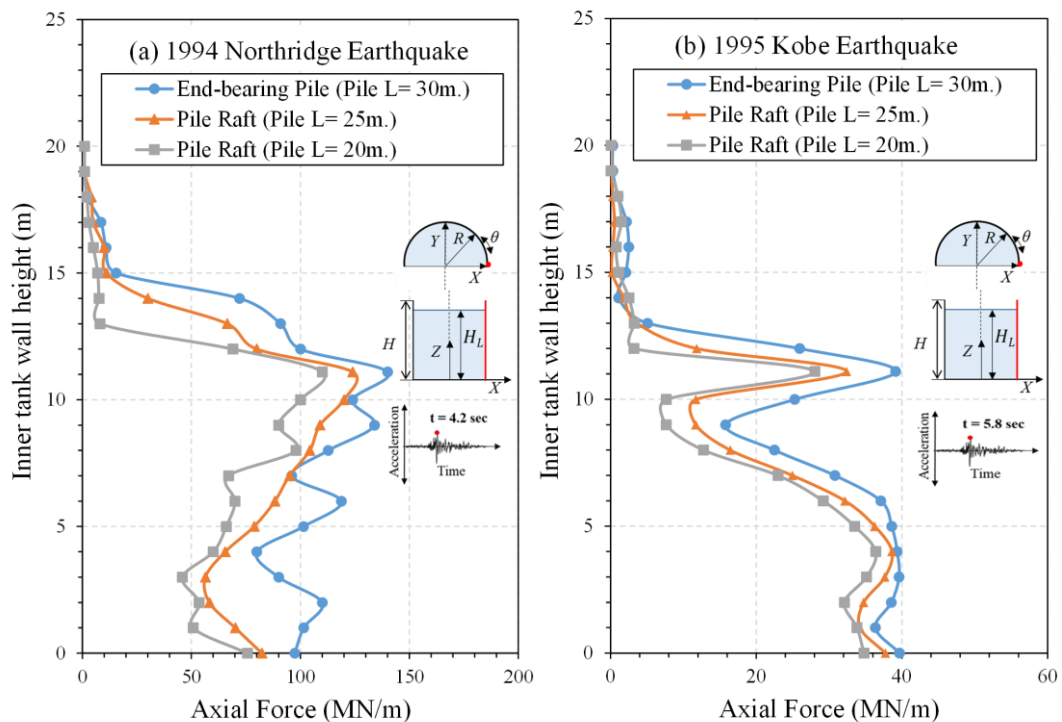
Figure 3.15 Distribution of the axial forces in the tank wall at θ = 0°: (a) 1994 Northridge earthquake at t = 4.2 sec and (b) Kobe earthquake at t = 5.8 sec.
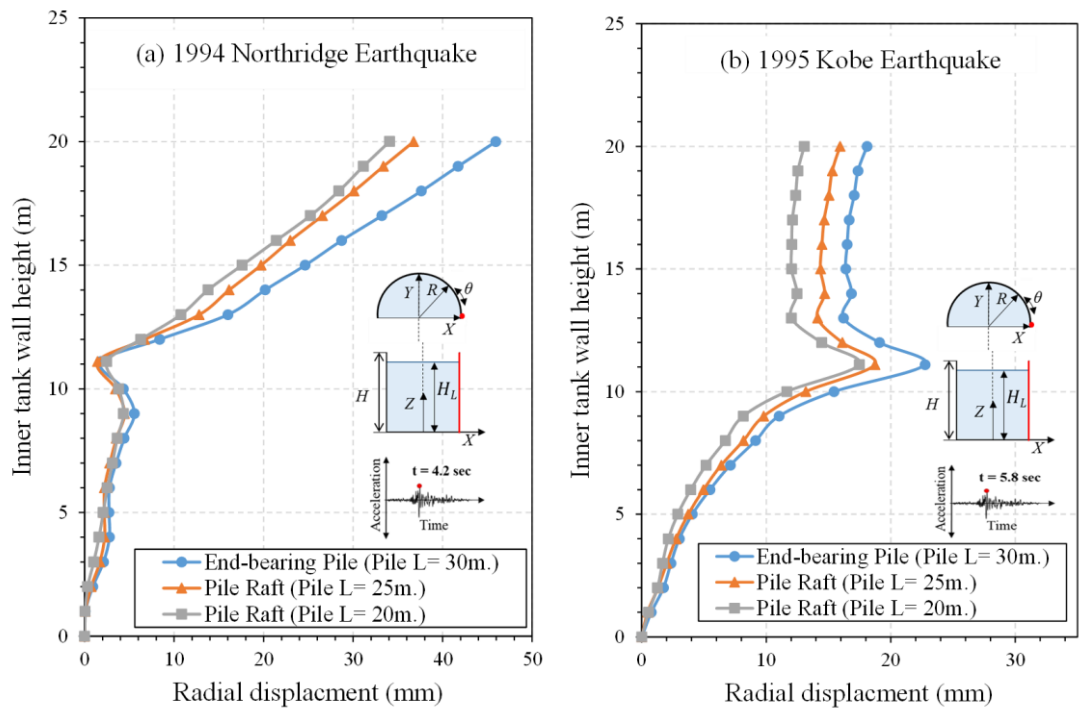
Figure 3.16 Distribution of the radial displacement along the inner tank wall height level of the three foundation options at θ = 0° for (a) 1994 Northridge earthquake at t = 4.2 sec and (b) Kobe earthquake at t = 5.8 sec.

The stress distribution of the 9% Ni steel inner tank wall is extracted and represented in Figure 3.17, for both 1994 Northridge (Figure 3.17a), and 1995 Kobe (Figure 3.17b) earthquakes when the maximum structural response was observed. The stress distribution is mainly affected by the hydrodynamic forces acting on the tank wall, while the maximum stress accoutred at the convective mass level. Figure 3.17a represents the maximum von Mises stress value for the 1994 Northridge earthquake which is exceeded the yield stress of the 9% Ni steel, as the stress-strain curve of the 9% Ni steel material represented in the Figure 3.17, for all foundation option, and it is significantly increased from frictional pile with pile length 20 m option (i.e. 516 MPa) to end-bearing pile with pile length 30 m (643 MPa) with 25 %; as the deformation on the inner tank wall is apparent in the end-bearing pile foundation option compared with the other two options. Figure 3.17b, represents the maximum von Mises stress value for the 1995 Kobe

earthquake which is exceeded the yield stress of the 9% Ni steel for all foundation option, it should mention that the difference in the von Mises stress was less significant among the foundation options under the 1995 Kobe earthquake, as the maximum von Mises stress increased from frictional pile with pile length 20 m option (i.e. 516 MPa) to end-bearing pile with pile length 30 m (538 MPa) with 6 %.
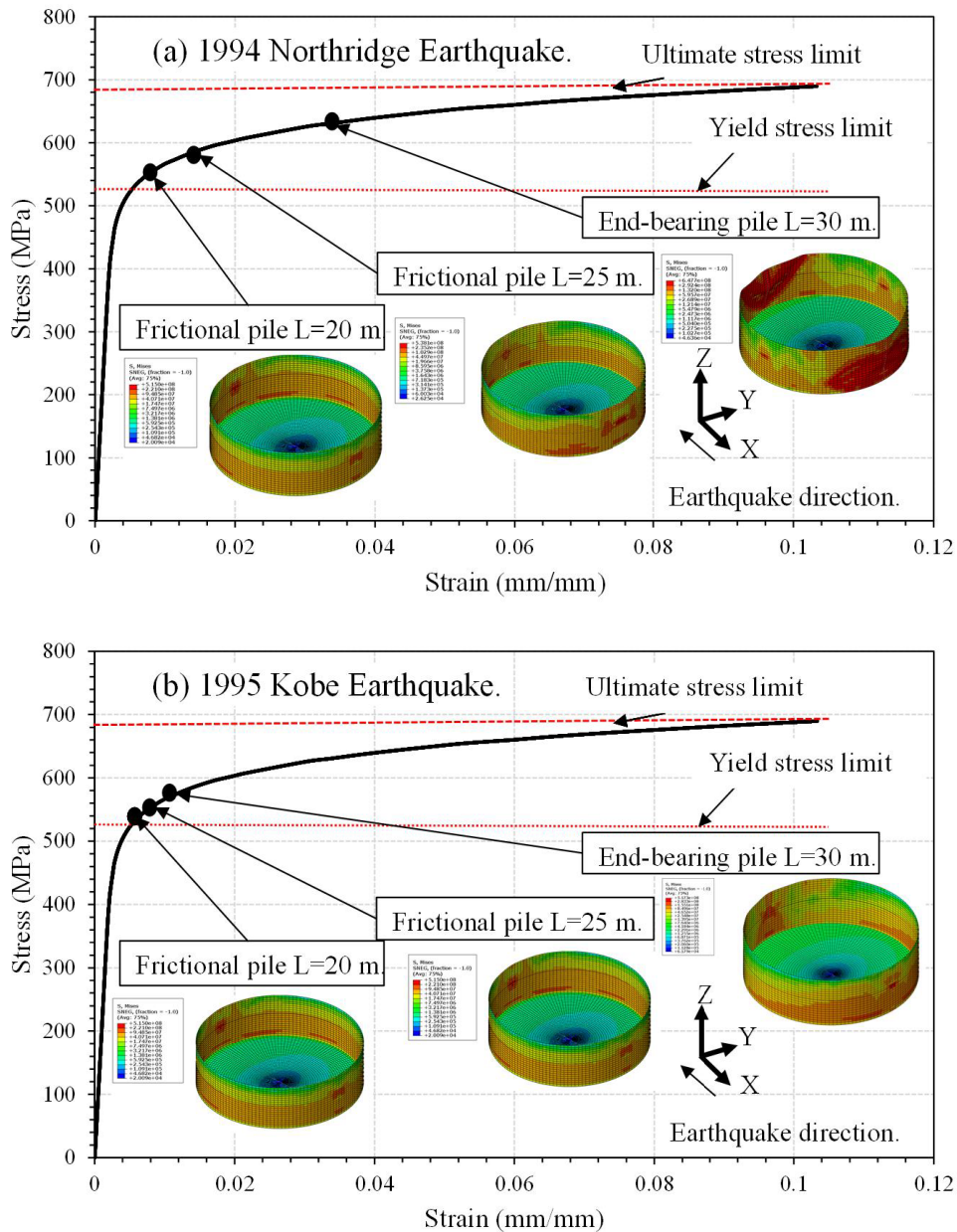
Figure 3.17 The maximum von Mises stress distribution on the inner 9% Ni steel tank wall and the location of the maximum stress on the stress- strain curve for 9% Ni steel under (a) 1994 Northridge earthquake at t = 4.2 sec and (b) Kobe earthquake at t = 5.8 sec.

3.5.2.4 Seismic response of pile foundation

To examine the impacts of foundation types on the response of piles in the group, the pile in the outermost ring of piles in *Y* direction as shown in Figure 3.18 is selected. When the maximum response (i.e. displacement) at the pile head occurred, the lateral displacement, shear force, and bending moment profiles along the pile length were recorded and reported as shown in Figure 3.18, Figure 3.19 and Figure 3.20. For the sake of convenient comparison, the normalized pile length (z/L, where z is the depth from the pile head and L is pile length) is reported.

Referring to Table 3.4 and Figure 3.9, as the pile length increased, the natural period of LNG tank decreased, and thus the end-bearing pile foundation directed the highest seismic energy to the system and thus resulted in maximum seismic response as observed in Figures 3.18-3.20. According to Figure 3.18, the maximum later deflection of the pile increased from 183 mm to 260.7 mm (i.e. 42% increase) and from 164 mm to 289 mm (i.e. 76% increase) when the pile length increased from 20 m in the frictional pile-raft to 30 m in the end bearing pile under the 1994 Northridge and the 1995 Kobe earthquakes, respectively. Figure 3.19 and Figure 3.20 show the shear force and bending moment envelopes along the pile length. It is clear that among all foundation options, the end-bearing pile foundation resulted in the maximum shear forces and bending moments in the piles. It should be noted that the seismic actions in the piles are due to kinematic and inertial interactions. According to Kramer (1996), kinematic interaction is induced by the inability of the foundation to match the deformation of the surrounding soil; and this type of interaction can alter the motion and vibration modes of the superstructure during earthquake. The inertial interaction however is due to the foundation movement introduced by the compliance of supporting soil, which is triggered by the mass of superstructure. Since the direct method of analysis was employed in this study, capturing

the kinematic and inertial interactions were inherent in the analysis and were considered in the fully coupled fashion.
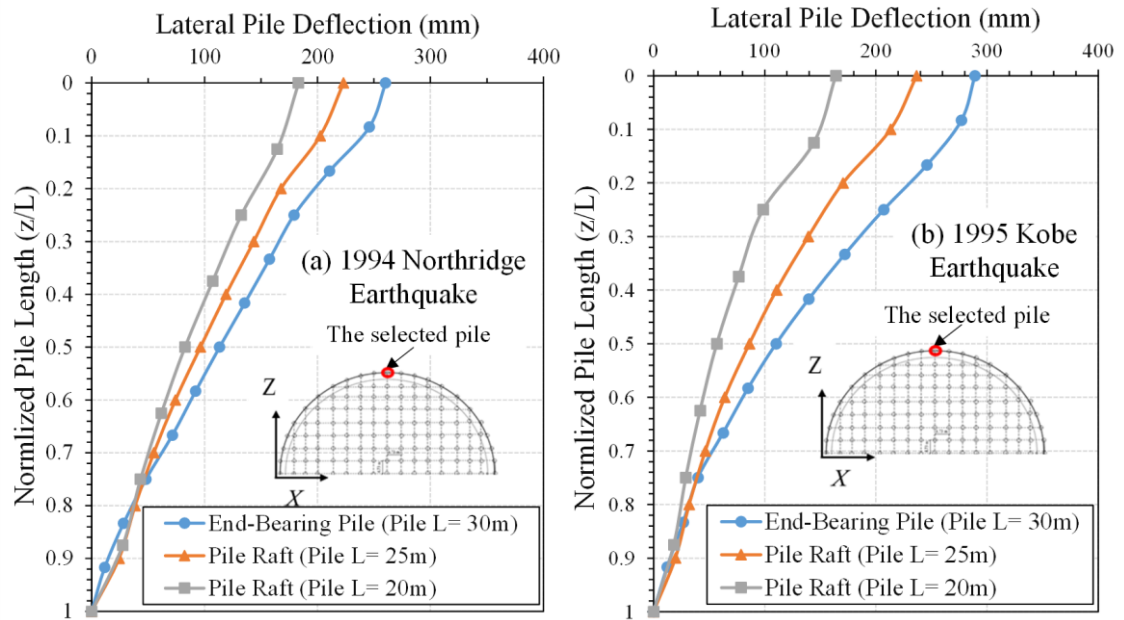
Figure 3.18 Maximum lateral pile displacement for different foundation types along the normalized pile length subjected to (a) 1994 Northridge earthquake at t = 4.2 sec and (b) Kobe earthquake at t = 5.8 sec.

The notable shear forces and bending moments in the top portion of the pile were generated mainly due to the inertial interaction stemmed from the motion of the LNG tank, and generally the impacts reduced with depth rapidly, whereas, the considerable bending moments and shear forces in the bottom portion of the piles were fully induced by the kinematic interaction due to the different movements between the piles and the soil during the seismic wave propagation as the inertial interaction could not reach there given the long length of the piles in this study (i.e. 20 m, 25 m and 30 m).
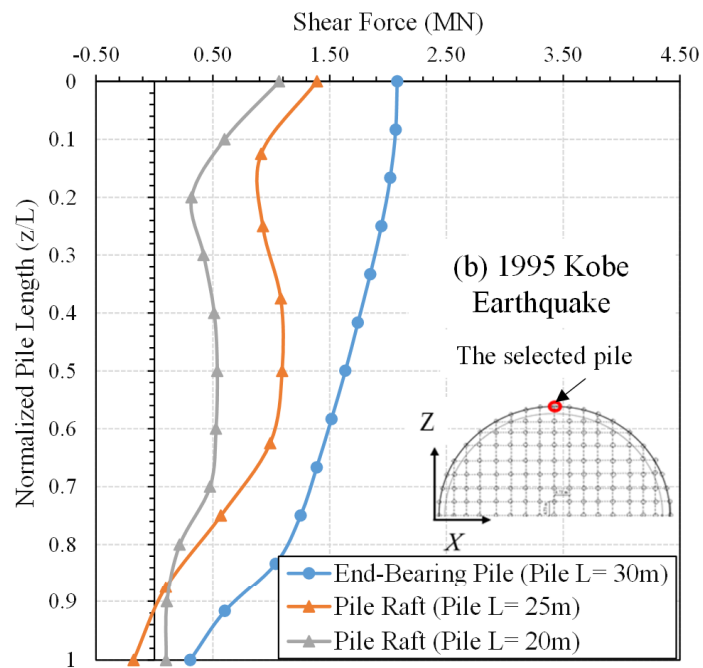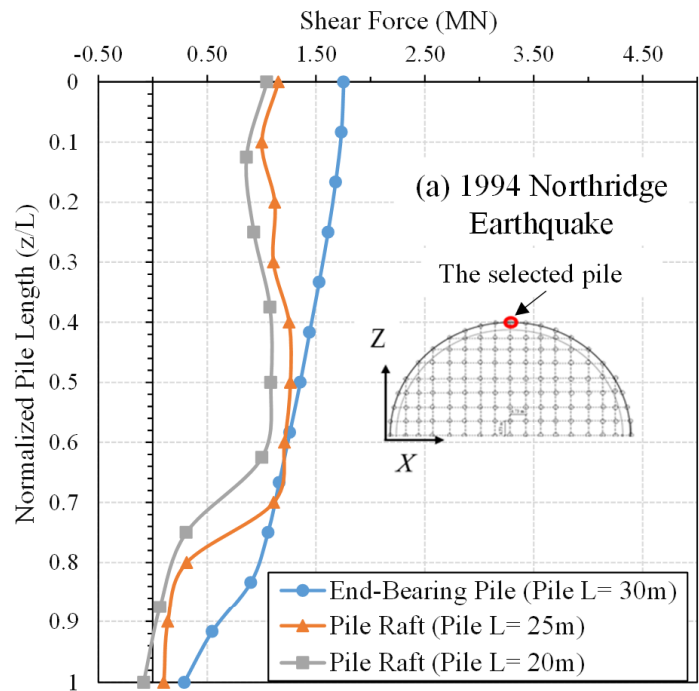
Figure 3.19 Maximum shear force profile imposed on the pile for different foundation types along the normalized pile length subjected to (a) 1994 1994 Northridge and (b) 1995 Kobe earthquakes.

By comparing the shear forces of the piles at ground surface level as reported in Figure 3.19, it can be noticed that the end-bearing pile foundation experienced 75% and

85% more shear forces than the 20 m long frictional pile-raft foundation, for the 1994 Northridge and the 1995 Kobe earthquakes, respectively. While increasing frictional pile length from 20 m to 25 m resulted in the amplification of the shear force on the pile head by 15% and 30% for 1994 Northridge and 1995 Kobe earthquakes, respectively. Indeed, the pile length and the "load-bearing mechanism" modifies the shear forces distributed along the pile; as collective kinematic and inertial interactions can impact the loads created along the pile elements. Similar observation can be made in Figure 3.20 for bending moments, where the bending moment of the pile at ground surface increased by 53% and 76% when the pile length enlarged from 20 m in frictional pile-raft to 30 m in end-bearing pile-raft under the applied earthquakes. The corresponding amplification in the bending moments were 31% and 35% when the pile length increased from 20 m to 25 m for the frictional pile-raft foundation under the applied earthquakes. Further, due to the change in load bearing mechanism (i.e. from frictional to end-bearing) the kinematic loads near pile toes increased, typically in terms of bending moment. This is due to the fact that the fixity at the toe of end-bearing pile inherently creates more stiffness/rigidity near pile toe resisting the movement of surrounding soil comparing to frictional piles whose toe should be flexible (i.e. easier to follow the movement of soil) during earthquake, which consequently cause more kinematic loads developed in end-bearing pile. The results also highlight the importance to adopt direct method in capturing appropriate inertia and kinematic effects on piles, as it is not readily for other methods such as sub-structural method to determine the effects.
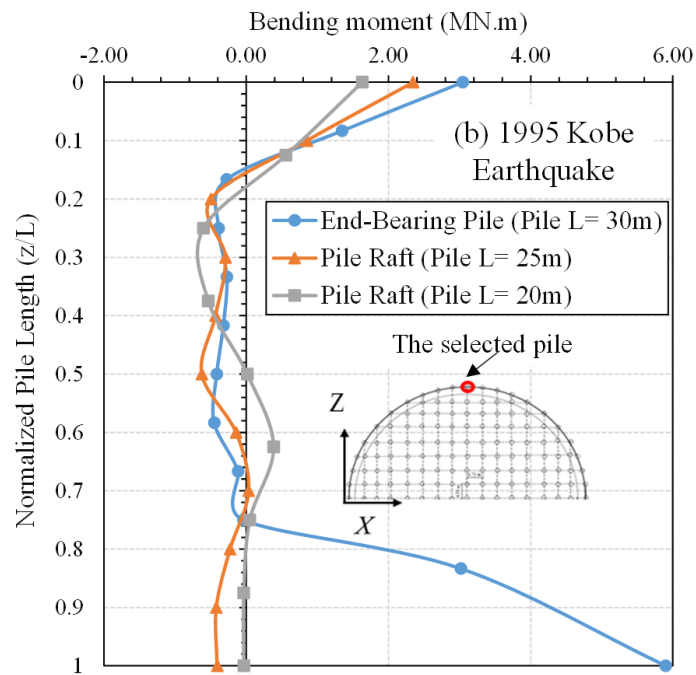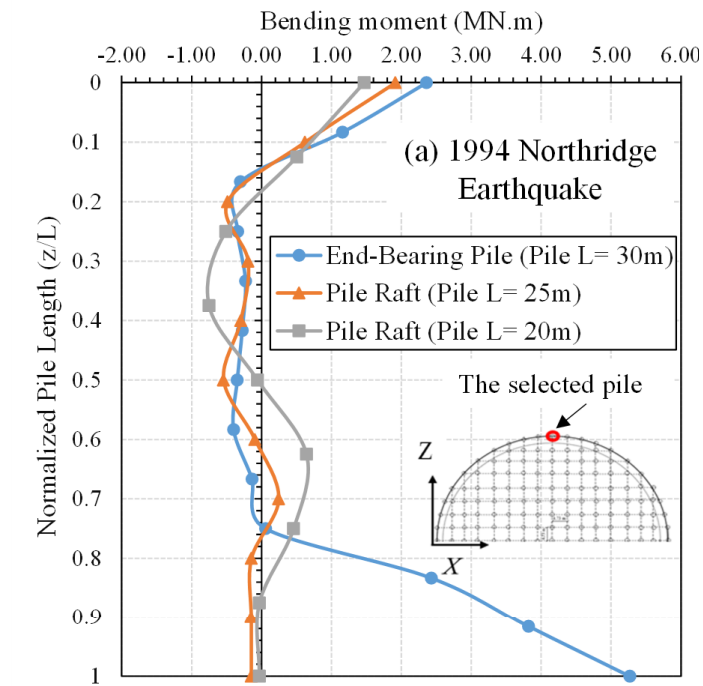
Figure 3.20 Maximum bending moment profile along the normalized pile length due for different foundation types subjected to (a) 1994 Northridge and (b) 1995 Kobe earthquakes.

3.6 Summary

A three-dimensional numerical model employing ABAQUS (2018) was created to conduct nonlinear time-history analyses for different pile foundation options supporting the LNG tank considering both the FSI and the SFSI effects. Finite element analyses were performed in terms of free vibration analysis using the Block Lanczos algorithm to obtain dynamic properties for each LNG tank foundation option and verify the FSI system. Moreover, the time history analysis was conducted using benchmark earthquake records considering both material and geometric nonlinearities in one analysis step (e.g. direct numerical technique). Spring-mass and added mass mechanical models were adopted to capture the FSI effects. The linear kinematic hardening rule was used to represent the inelastic behaviour of the steel inner tank, where the concrete damage plasticity model was used for simulation of the outer reinforced concrete containment. Interfaces were assigned to the boundaries of the soil and foundation to capture possible foundation sliding and gaping from the soil during the seismic loading. In this part of research, a simplified equivalent linear method was adopted to capture the soil nonlinearity in an average sense. At the same time, the Rayleigh damping model was also used to capture soil damping during the earthquake excitations. Appropriate infinite boundary elements were used at lateral boundaries to ensure the non-reflection of the seismic waves back to the model. at the bottom of the model, a rigid boundary condition was adopted to represent the firm bedrock. The earthquake input motions were applied at the bedrock horizontally and allowed to propagate upward through the entire model.

The effects of pile foundation type and load transmission mechanism (e.g., end-bearing versus frictional pile-raft foundation types) and frictional pile length were explicitly examined. The results demonstrated that consideration of SFSI was vital since it alerted the dynamic properties of LNG tanks built on all the adopted foundation types.

For example, the spectral acceleration and system natural period changed slightly for end-bearing pile foundation compared with assuming fixed base condition for LNG tank. In addition, with the LNG tanks on the end-bearing pile foundation, spectral accelerations were more considerable than the other two frictional pile foundation types.

It has been observed that the end-bearing pile foundation (e.g. the stiffer foundation system) transferred more seismic energy toward the LNG tank than the other two pile-raft foundation choices investigated in this study. Moreover, increasing frictional pile length for the pile-raft foundation option resulted in increasing SFSI effects, thus, transferring more seismic forces to the piles and superstructure. Moreover, increasing the kinematic and inertial interaction effects along the pile foundation with increasing the frictional pile length highlighted the importance of using the direct technique of analysis for the LNG tank and its foundation system under seismic load.

CHAPTER 4   ASSESSMENT OF THE KINEMATIC HARDENING MODEL CAPABILITY TO CAPTURE THE SEISMIC WAVE PROPAGATION IN SATURATED CLAY DEPOSIT

4.1   General

In this chapter, a simple nonlinear kinematic hardening (NKH) model, originally developed for cyclic behaviour of metals, commonly used by structural engineers and available in ABAQUS, is adopted to capture the soil stiffness degradation and damping variations with cyclic shear strain. Performance of this model is assessed by conducting a three-dimensional finite element analysis in the time domain for different site classes and earthquake records. Three soil deposits are adopted and classified based on the shear wave velocity as Site Classes C, D and E with corresponding shear wave velocities equal to 564 m/s, 270 m/s and 160 m/s, respectively. Moreover, 1994 Northridge, 1995 Kobe, 1940 El-Centro and 1979 Imperial Valley earthquakes are used in their original state as well as scaled to three different seismic demand levels and applied at the bedrock, while appropriate infinite boundaries are used to model the far-field soil and avoid reflection of the seismic waves back into the soil model. The seismic site response analysis is conducted and the performance of the nonlinear kinematic hardening (NKH) soil model for site response analysis is assessed through predicting shear stress – strain response, ground surface acceleration and acceleration response spectrum. Additionally, the predictions adopting NKH model programmed in ABAQUS is validated against well-known stiffness degradation and hysteresis damping (SDHD) soil model available in FLAC 3D. By comparing the nonlinear shear stress - strain response of the three soil deposits and different earthquakes, it can be observed that the nonlinear kinematic

hardening (NKH) model programmed in ABAQUS is capable of capturing the dynamic behaviour of the soil for the seismic wave propagation.

4.2 Introduction

Past earthquake events have highlighted importance of nonlinear stress- strain response of soil on variations of the seismic waves propagating within the soil medium particularly under strong ground motions (Trifunac and Todorovska 1996; Assimaki et al. 2005; Gičev and Trifunac 2019). Indeed, as the seismic waves propagate from the inception location as a result of fault rupture through the rocks layers, to local ground deposit and eventually to the foundation and the superstructure, the fundamental characteristics of the shaking may change significantly (Mylonakis et al. 1997; Gazetas and Ziotopoulou 2010; Assimaki and Shafieezadeh 2013). The response of the soil and variation of the seismic motion can impact performance of the superstructures particularly when site effects and soil-structure interaction aspects need to be captured. The process where the soil properties affect the seismic response of structure and vice-versa is referred to soil-structure interaction (Stewart et al. 1999). Many studies had highlighted the importance of soil characteristics on structural performance, where increasing the ground flexibility might introduce a translation and rotation of the foundation, which in turn amplify the displacement of the superstructure compared to the fixed-base condition (Kramer 1996; Mylonakis and Gazetas 2000; Gazetas and Apostolou 2004; Ma et al. 2009; Figini et al. 2012)

As explained by Wolf (1985), the free field motion which is the surface motion of the soil deposit is diverse from the bedrock as a result of site effect, vibrations of the structure or scattering of seismic waves near or at the foundation interface. Indeed, importance of site effect and variations of seismic wave characteristics while passing

through the soil deposit was observed in many past earthquakes such as the 1995 Kobe, the 1994 Northridge, and 1989 Loma Prieta earthquakes, to name few, and caused extensive damage (Aki 1993; Şafak 2001; Assimaki and Gazetas 2004; Navarro et al 2014; Anand and Kumar 2018).

Several researchers used experimental method to assess the site effect impacts on the seismic wave propagation through soil medium, where different techniques were implemented, such as microtremor measurements (Borcherdt 1970; Field and Jacob 1995; Lermo and Chávez-García 1993; Lermo and Chávez-García 1994). Generally, previous experiments for site response analysis assessed the soft soils response at the ground surface in terms of frequency of resonance and maximum amplification factor at that frequency. On the other hand, many researchers have been conducting rigorous numerical modelling to obtain further insight into the seismic site effects, and understand how the level of the building damage depend on the manner at which the seismic wave was changed after passing through the soil medium, and how the different soil deposits can alert the potential damage for major superstructures, such as bridges, underground structures and dams (Furumura and Kennett 1998; Hartzell et al. 2002; Montalva et al. 2016; Hattne et al. 2018).

It should be mentioned that the numerical analysis of seismic wave propagation and site response analysis can be conducted through several numerical methods, such as finite difference method (Bohlen and Saenger 2006; Frankel and Vidale 1992; Moczo et al. 2002), boundary element method (BEM) (Beskos 1997; Bonnet 1999; Dangla et al. 2005), the spectral element method, finite volume method, and finite element method (FEM) (Hughes et al. 2008; Ihlenburg and Babuška 1995; Semblat and Brioist 2009). The vital components impacting the reliability of any of the above mentioned numerical methods in the seismic site response or seismic soil structure interaction analysis, is

accurate representation of the soil dynamic behaviour via appropriate constitutive models, where the shear stiffness and the energy damping need to be captured accurately (Dobry and Gazetas 1988; Novak 1991; El Naggar and Novak 1996; Mylonakis 2001).

A key factor that any soil model needs to capture for accurate seismic wave propagation, is the shear stiffness degradation and the hysteresis damping amplification with the cyclic shear strain. Different researches have adopted different techniques to capture these nonlinearities and generally equivalent linear or fully nonlinear methods are adopted depending on the capabilities of the numerical code, computation time and available laboratory or field data to calculate the required parameters (Ghandil and Behnamfar 2015; Gičev et al. 2016) The equivalent linear method considers soil behaviour in an average sense; thus, it requires a trial and error procedure to find the compatible cyclic shear strain value for each earthquake record, and this method is sensitive to the applied seismic waves properties (Kontoe et al. 2014).

However, for the rigorous nonlinear approach, a suitable constitutive model available in commercial software packages to be used by practicing engineers is required.

This chapter aims to assess the suitability of the simple yet accurate nonlinear kinematic hardening (NKH) soil model to simulate the seismic wave propagation. This model which is developed to simulate nonlinear response of metals subjected to cyclic loading, is readily available in rigorous structural software packages and consequently, the structural engineers can implement this model in their seismic analysis for simulation of the soil, and easily simulate the entire soil-structure system in one step using direct method. In particular in this study, NKH soil model programmed in ABAQUS software is used for the seismic site response analysis in time domain for three different site classes (i.e. Site Classes C, D and E) according to IBC (2012) under the effect of four benchmark earthquakes, namely 1994 Northridge and 1995 Kobe earthquakes (near-field), and 1940

El Centro and 1979 Imperial Valley-06 earthquakes (far-field), which were used in their original state as well as scaled to three different hazard levels. The predictions in terms of shear stress – strain response, ground surface acceleration and acceleration response spectrum are verified against results from well established strain dependent hysteretic damping (SDHD) soil model available in FLAC3D software.

4.3 An overview of NKH soil model

The nonlinear kinematic hardening (NKH) model, available in ABAQUS, was adopted in this study to model the soil behaviour under cyclic loading. Originally, this model was developed for simulating behaviour of metals subjected to cyclic loading based on Armstrong and Frederick (1966) and Lemaitre and Chaboche (1994) work, while in this study it is evaluated and calibrated to be used for clay soils. This pressure-independent plasticity model based on von Mises yield criteria, and associated flow rule, can be considered as an appropriate model for nonlinear cyclic behaviour of pressure independent material, such as clays under undrained condition. The undrained conditions can be applied as a reasonable simplification to simulate the soil response of saturated fine-grained soils with low permeability subjected to rapid loading such as earthquake, in which the excess pore water pressure dissipation would be insignificant, and soil volume remains constant.

As explained by George et al. (2016) and Zhu (2019), the key parameters of this model are Young's modulus, Poisson's ratio, and stress - strain curve of stabilised loading cycle obtained from the triaxial shear test. The rate independent material behaviour is adopted in this model, which implements the additive rule for the total strain and written in terms of the elastic and plastic strain rates (i.e. $\dot{\varepsilon}_{ij}^{e}$ and $\dot{\varepsilon}_{ij}^{pl}$) as:

$$\dot{\varepsilon}_{ij} = \varepsilon^{\cdot e}_{ij} + \varepsilon^{\cdot pl}_{ij} \tag{4.1}$$

where the elastic part of the strain rate is described with the Hooke's law by means of isotropic linear elastic material, while the development of permanent deformation takes place when the stress overpasses the yield stress limit σ_y. Based on the modification suggested by Armstrong and Frederick (1966) on the original model, which was proposed by Chaboche and Lemaitre (1990), the yield surface of the adopted NKH constitutive model is defined as below:

$$F = f(\sigma_{ij} - \alpha_{ij}) - Y = 0 \tag{4.2}$$

$$Y = \sigma_{yi} + R \tag{4.3}$$

where, σ_{ij} is the stress tensor, Y is the yield surface size which is the combination of the initial yield stress σ_{yi} and the isotropic internal variable R. In addition, α_{ij} is the back-stress tensor, which determines the kinematic evolution of the yield surface in the stress space. $f(\sigma_{ij} - \alpha_{ij})$ denotes the equivalent Mises stress with respect to back stress α_{ij}, which is defined as below:

$$f(\sigma_{ij} - \alpha_{ij}) = \sqrt{\frac{3}{2}(S_{ij} - \alpha^{dev}_{ij}) : (S_{ij} - \alpha^{dev}_{ij})} \tag{4.4}$$

where, S_{ij} is the deviatoric stress tensor (defined as $S_{ij} = \sigma_{ij} + pI$, p is the equivalent pressure stress, and I is the identity tensor) and α^{dev}_{ij} is the deviatoric part of back stress tensor. Assuming the pressure independent material behaviour, the associated flow rule is adopted to obtain the required kinematic hardening flow rule as reported by Zhu (2019), and presented in Equation (4.5):

$$\varepsilon^{\dot{p}l} = \dot{\varepsilon}^{pl}_{eff} \frac{\partial f(\sigma - \alpha)}{\partial \sigma}) \tag{4.5}$$

where, $\dot{\varepsilon}^{pl}$ is the rate of plastic flow and $\dot{\varepsilon}^{pl}_{eff}$ is the equivalent plastic strain rate. The equivalent plastic strain considering isotropic Mises plasticity can be obtained from the equivalent plastic work as follows:

$$\dot{\varepsilon}_{eff}^{pl} = \sqrt{\frac{2}{3}\dot{\varepsilon}_{ij}^{pl}:\dot{\varepsilon}_{ij}^{pl}}$$

<div align="right">(4.6)</div>

The development of stresses in the material is captured via two parts, the isotropic hardening, which defines the change in the yield surface size as a function of equivalent plastic strain($\dot{\varepsilon}_{eff}^{pl}$), and the nonlinear kinematic hardening part, which describes the translation of the yield surface in the stress space through the back stress(α_{ij}). Therefore, the hardening rule of this model is a mixed nonlinear isotropic-kinematic hardening, making it suitable for simulating cyclic behaviour of soils as explained by Elia and Rouainia (2016) and Mucciacciaro and Sica (2018). Indeed, the nonlinear kinematic hardening component is denoted by the "superposition" of pure kinematic and relaxation (source of the nonlinear behaviour) terms, while the isotropic hardening component represents the strength reduction via shrinkage of the yield surface with the accumulative equivalent plastic strain induced by cyclic loading. It should be note that the size of yield surface (*Y*) follows a simple exponential law as reported by Zhu (2019) and defined below:

$$\sigma_y = \sigma_{yi} + Q(1 - e^{-b\,\dot{\varepsilon}_{eff}^{pl}})$$

<div align="right">(4.7)</div>

where, Q and b are the isotropic hardening parameters defining the change of the yield surface rate with equivalent plastic strain $\dot{\varepsilon}_{eff}^{pl}$. When Q equals zero then the yield surface *Y* remains unchanged (i.e. $\sigma_y = \sigma_{yi}$), and thus the general combined nonlinear isotropic-kinematic hardening model reduces to a nonlinear kinematic hardening model, which is adopted in this chapter.

The evolution of the nonlinear kinematic hardening components in the stress space is defined based on Ziegler (1959) kinematic hardening law as follows:

$$\dot{\alpha}_{ij} = (\frac{C_k}{\sigma_y}\left(\sigma_{ij} - \alpha_{ij}\right) - \gamma_k\alpha_{ij})\dot{\varepsilon}_{eff}^{pl} \qquad (4.8)$$

where, C_k and γ_k are material parameters for each back stress α_{ij}. These parameters can be obtained by calibration using cyclic test data. Indeed, C_k is the initial kinematic hardening moduli, and γ_k is a parameter defining decreasing rate of the kinematic hardening with plastic strain. The recall term $(\gamma_k\alpha_{ij}\,\dot{\varepsilon}_{eff}^{pl})$ introduces the nonlinearity to the evolution law proposed by Lemaitre and Chaboche (1990). It should be noted that when $\dot{\varepsilon}_{eff}^{pl}$ approaches infinity, the back stress α_{ij} approaches the saturation back stress α^s $(\alpha^s = \frac{C_k}{\gamma_k})$.

The illustration of the nonlinear kinematic hardening model is presented in Figure 4.1, where Figure 4.1a represents the relation between the von Mises stress and plastic strain. As evident in Figure 4.1b, as the position of the yield stress centre moves relative to the initial yield surface σ_{yi} centre (while the size of the yield surface remains unchanged as a result of ignoring isotropic hardening effect), the back-stress tensor (α_{ij}) also translates from the centre of the initial yield surface to the centre of the current yield surface, which is capturing kinematic hardening effect. According to the evolution law for the kinematic hardening component (Equation 4.8), the back stress tensor is contained within the cylinder of radius equal to $\sqrt{2/3}\alpha^s$, where $\sqrt{2/3}\alpha^s = \sqrt{\frac{2}{3}}\frac{C_k}{\gamma_k}$, and the stress point should lie within a cylinder of radius $\sqrt{2/3}\sigma^s$, where σ^s is the maximum stress at large plastic strains, known as saturation condition.

Stress (σ)

Maximum yield stress at saturation

$\sigma = \sigma^s$

σ_{yi} $\sigma_{yi} \leq \sigma^s$

$\alpha + \sigma_{yi} \leq \sqrt{2/3}\,\sigma^s$

$\sigma = \sigma_{yi}$

α $\alpha \leq \sqrt{2/3}C/\gamma$

$\sigma = 0$

Plastic strain (ε^{pl})

Large plastic strain (saturation condition)

(a)

σ_1

Initial yield surface $\sqrt{2/3}\,\sigma_{yi}$

Limit yield surface $\sqrt{2/3}\sigma^s$

New yield surface $\sqrt{2/3}\,\sigma_y$

Limiting location of back stress (α_{ij})

α_{ij}^{dev}

σ_2

$\dfrac{\partial f}{\partial \sigma}$

σ_3

$\sqrt{2/3}\,\sigma_y$
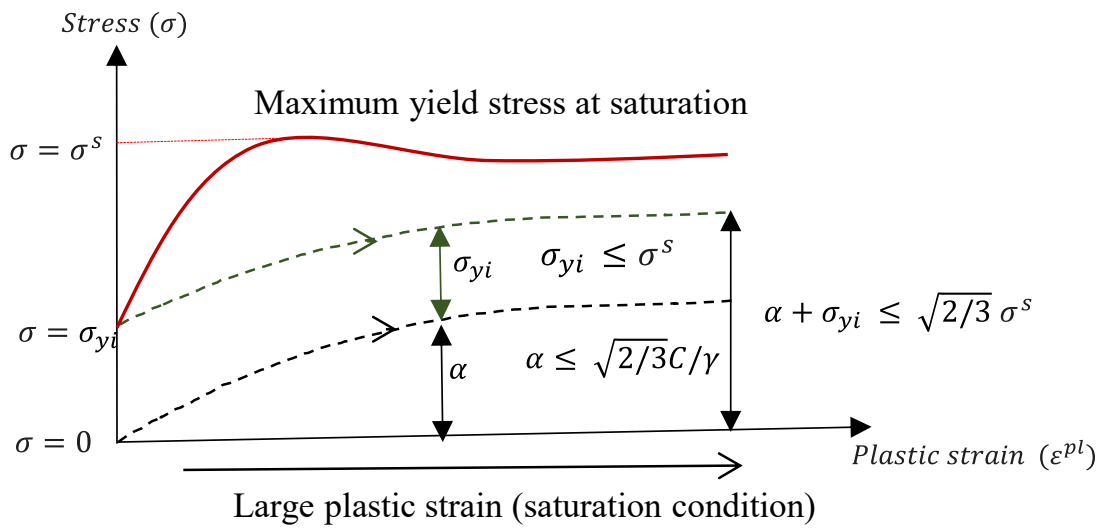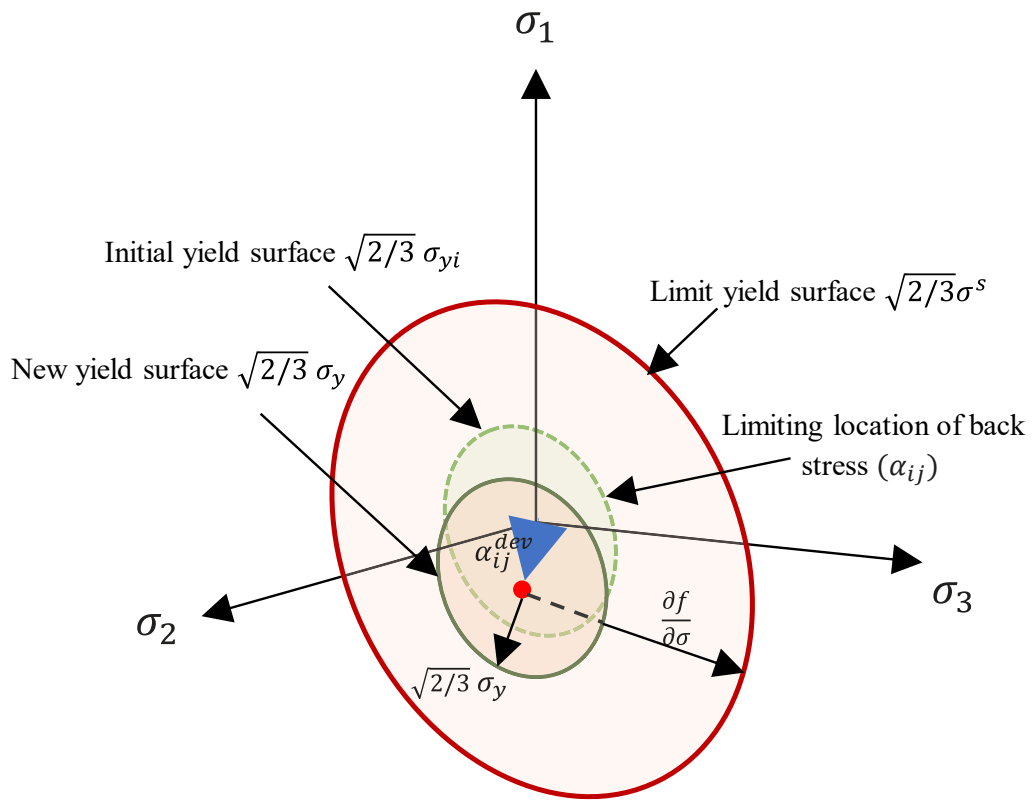
(b)
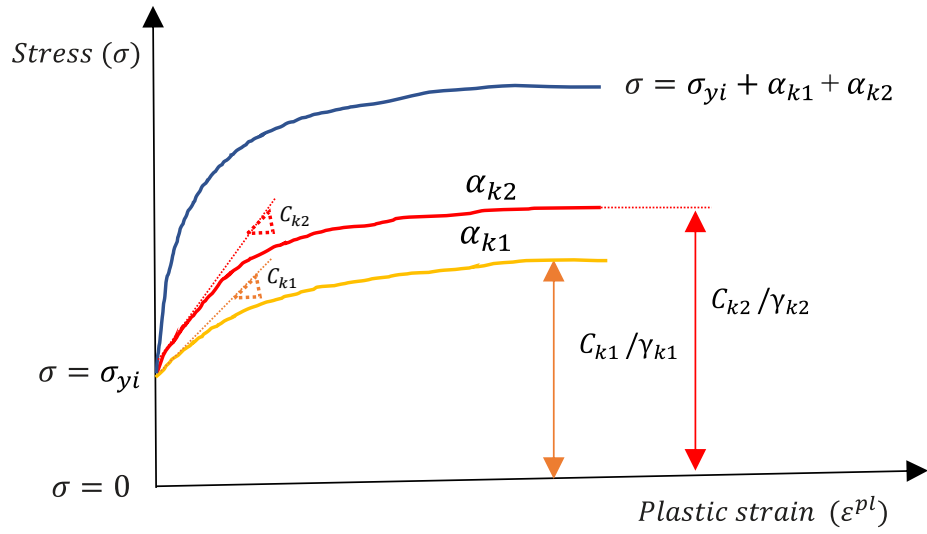
(c)

Figure 4.1 Explanation of the nonlinear kinematic hardening (NKH) model implemented in this study, (a) one-dimensional representation of the hardening nonlinear kinematic rule and the generalised stresses with respect to plastic strain (b) three-dimensional representation of the kinematic hardening effect in translation the yield stress surface in the stress space (c) back stresses parameters in case of two back stresses as adopted in this chapter.

As mentioned earlier the deviatoric part of the nonlinear kinematic hardening law can affect the material behaviour. Thus, for each deviatoric back stress tensor, the martial parameters σ_{yi}, γ_k, and C_k can be calibrated from cyclic stress strain stabilize cycle. Depending on the degree of nonlinearity, more than one back stress may be needed to capture the nonlinear behaviour and hysteresis damping precisely. In those cases, each introduced back stress covers different range of equivalent plastic strains, and the overall back stress can be computed via summation of back stresses as in Equation (4.9):

$$\alpha = \sum_{k=1}^{N} \alpha_k \qquad (4.9)$$

Figure 4.1c illustrates application of two back stress parameters as used in this study, where the accumulative yield stress is the summation of all back stresses and the initial yield stress.

4.4 Numerical modelling

4.4.1 Benchmark model considering stiffness degradation and hysteretic SDHD damping (FLAC3D)

FLAC3D (Itasca, 2011) is a numerical modelling software package specifically focusing on geotechnical analyses and it can reasonably analyse soil dynamic response (e.g., Lu et al. 2016; Zhang et al. 2015; Alsaleh and Shahrour 2009). Thus, a FLAC3D model was developed as the benchmark to compare with the predictions of seismic wave propagation obtained from NKH constitutive model programmed in ABAQUS.

Three different site classes (i.e. Site Classes C, D and E) according to IBC (2012) were utilised to study a broad range of seismic site responses. In this study, a uniform site condition (i.e. a single layer soil deposit) was considered. Table 4.1 lists the adopted soil properties corresponding to different site classes. As shown in Figure 4.2, a $30 \times 30 \times 30$ m soil deposit was modelled using $1 \times 1 \times 1$ m zones and in total, 13831 brick-type solid zones were used.

Table 4.1 Adopted soil characteristics of different site classes.

Site Class (IBC, 2012)	Shear wave velocity, V_s (m/s)	Maximum dynamic shear modulus, G_{max} (MPa)	Soil density, ρ_{soil} (kg/m³)	Poisson's ratio, ν	Reference
C	564	675	2124		Galal and Naimi (2008)
D	270	136	1877	0.25	
E	160	43	1714		
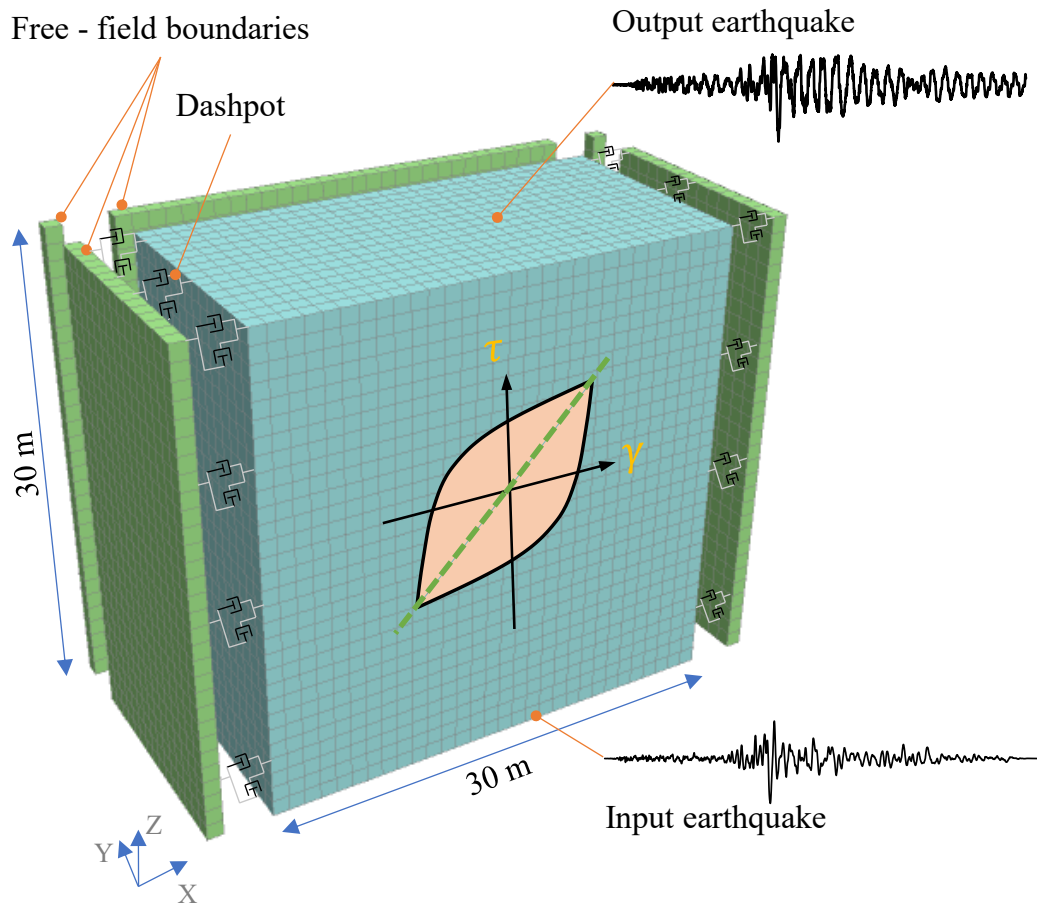
Figure 4.2 Model geometry (half model) and analysis demonstration implemented in FLAC 3D.

4.4.1.1 Simulation of dynamic soil behaviour

Under earthquake load, soil exhibits nonlinear and hysteresis behaviour. Ambrosini (2006) highlighted the importance of adopting appropriate soil constitutive model in seismic analysis. As shown in Figure 4.3, the soil response subjected to cyclic load can be described using the soil secant shear modulus (G_{sec}) and the corresponding damping ratio (ξ) of a hysteresis loop (Kramer 1996). According to Das (1983), G_{sec} and ξ can be determined via Equations (4.10) and (4.11), respectively.

$$G_{sec} = \frac{\tau_c}{\gamma_c} \tag{4.10}$$

$$\xi = \frac{W_D}{4\pi W_S} = \frac{1}{2\pi}\frac{A_{loop}}{G_{sec}\gamma_c^2} \tag{4.11}$$

where the parameters of these equations explained previously in chapter 2 (see Equations 2.3 and 2.14).
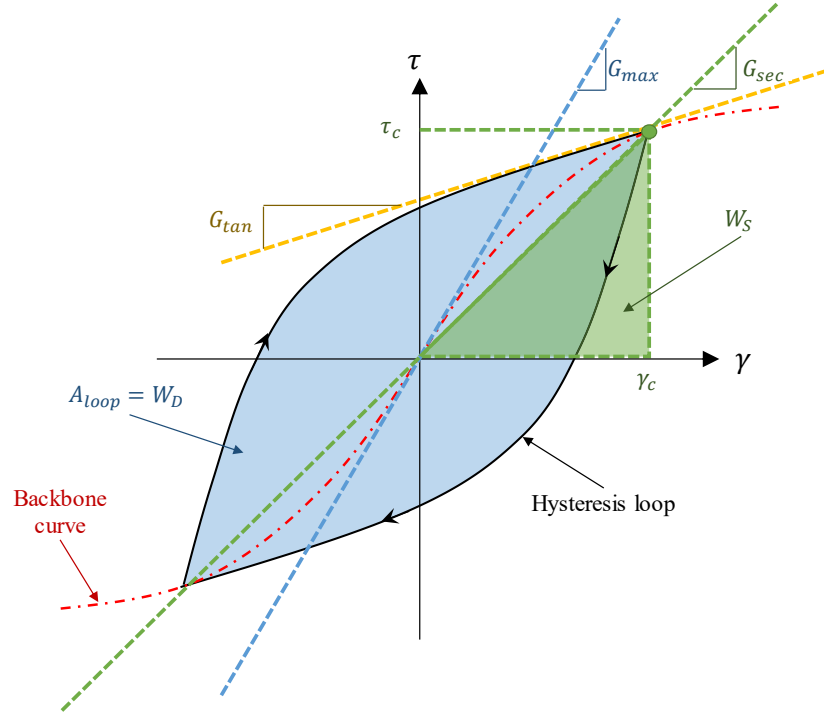
Figure 4.3 Hysteresis loop of soil.

In order to represent dynamic features of the soil in nonlinear analysis, as shown in Figure 4.3, the backbone curve representing the change of G_{sec} with cyclic shear strain level should be considered, as well as the corresponding damping due to the reduction of soil shear modulus. Figure 4.4 shows the considered modulus reduction and corresponding damping ratio curves based on Sun et al (1988).

In this study, Hardin-Drnevich function (Hardin et al. 1972) was applied in the numerical model to correlate G_{sec} to γ_c using Equation (4.12).

$$G_{sec} = \frac{1}{1+\frac{\gamma_c}{\gamma_{ref}}} \tag{4.12}$$

where γ_{ref} is the reference shear strain when the ratio between the secant shear modulus (G_{sec}) and the initial dynamic shear modulus (G_{max}) reached 0.5. According to Itasca (2011), the corresponding damping ratio (ξ) for Hardin-Drnevich function can be obtained using the following equation:

$$\xi = \frac{2}{\pi} \left\{ 2 \frac{1 + {\gamma_c}/{\gamma_{ref}}}{\left({\gamma_c}/{\gamma_{ref}}\right)^2} \left[{\gamma_c}/{\gamma_{ref}} - \ln\left(1 + {\gamma_c}/{\gamma_{ref}}\right)\right] - 1 \right\} \tag{4.13}$$

It should be noted that in this study stationary hysteretic mechanism was considered, which means that the shear stress in the model only depended on cyclic strain and not on the number of cycles. As shown in Figure 4.4, the modulus reduction and damping ratio curves can be reasonably duplicated using Hardin-Drnevich function with $\gamma_{ref} = 0.234$. The calibrated value of $\gamma_{ref} = 0.234$ resulted in the best match for backbone curves with coefficient of determination R^2 equal to 0.88 and 0.80 for the modulus reduction curve and damping ratio as evident in Figure 4.4, respectively.
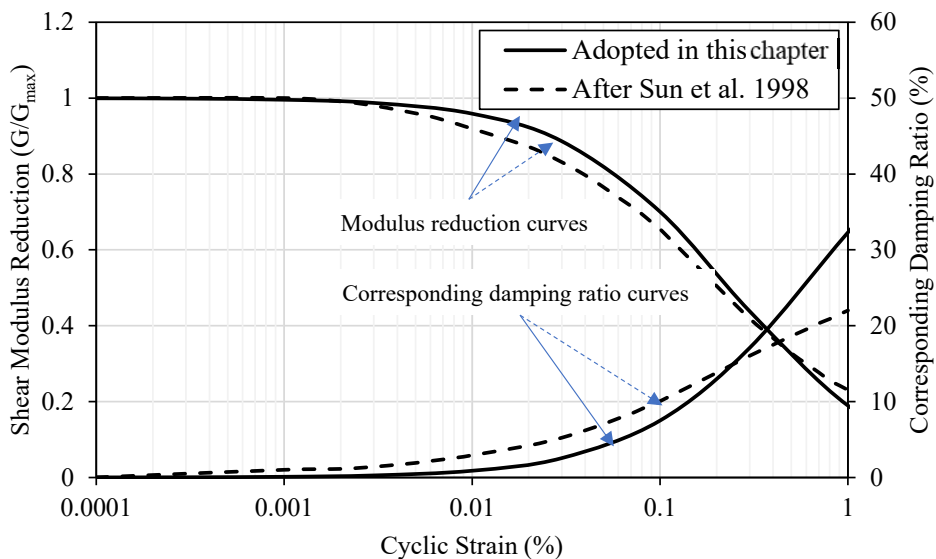
Figure 4.4 Adopted modulus reduction and the corresponding damping ratio curves used in this study.

4.4.1.2 Boundary conditions

In this study, two different sets of boundary conditions were applied so that reasonable and accurate analysis could be carried out. For the static analysis generating the initial in-situ stress condition and soil deformation due to gravity in the soil deposit, the side boundaries were restrained to vertical movement parallel to the gravity load action, while the model base was fully fixed.

According to Semblat (2010), it is essential that the side boundaries of the numerical model can reflect free-field motions for dynamic analysis. As shown in Figure 4.2, free-field boundaries were modelled around the soil deposit to carry out seismic analysis. The free-field boundary condition was achieved by coupling solid zones with free-field zones using dashpots. Indeed, the dashpots simulated quiet boundary condition and the free-field zones generated forces to cancel the unbalanced forces acting on the soil deposit boundaries due to wave propagation; this adopted force condition can be expressed as follows:

$$F_{boundary} = F^{ff} - \rho C_b A^{ff}(v^z - v^{ff}) \qquad (4.14)$$

where F^{ff} is free-field regions forces to stability the side boundary force from the outward waves, ρ is the mass density of the lateral boundaries, C_b is the wave speed, A^{ff} is the free-field zone area, and v^z and v^{ff} are the velocities of solid zones at side boundaries and coupled free-field zones, respectively. As a result, waves propagating vertically with no distortion at the boundaries, while the outward waves did not reflect back into the model, simulating the boundless condition at the boundaries.

On the other hand, a rigid boundary was adopted at the model base simulating bedrock. According to previous research studies (e.g. Dutta and Roy 2002; Spyrakos et

al. 2009), a rigid boundary is appropriate to model large dynamic impedance (e.g. low-shear-wave-velocity sediments sitting on high-shear wave-velocity bedrock).

4.4.1.3 Considered earthquakes

As summarised in Table 4.2, two near-field earthquakes (i.e. 1994 Northridge and 1995 Kobe) and two far-field earthquakes (i.e. 1940 El-Centro and 1979 Imperial Valley) were utilised to conduct nonlinear time history analysis. The earthquake records were picked from the Pacific Earthquake Engineering Research Centre PEER (2014), and as shown in Figures 4.5 and 4.6, the selected earthquakes could cover a wide range of frequencies, peak ground acceleration (PGA), and duration.

Table 4.2 Adopted earthquake records in this chapter.

Earthquake*	Country	Year	Magnitude (Rw)	Mechanism	Station
Northridge	United state	1994	6.7	Reserve	MWD station 655
Kobe	Japan	1995	6.9	Strike-slip	CUE station
El Centro	United state	1940	6.9	Strike-slip	USGS station 0117
Imperial Valley	United state	1979	6.5	Strike-slip	USGS station 5066
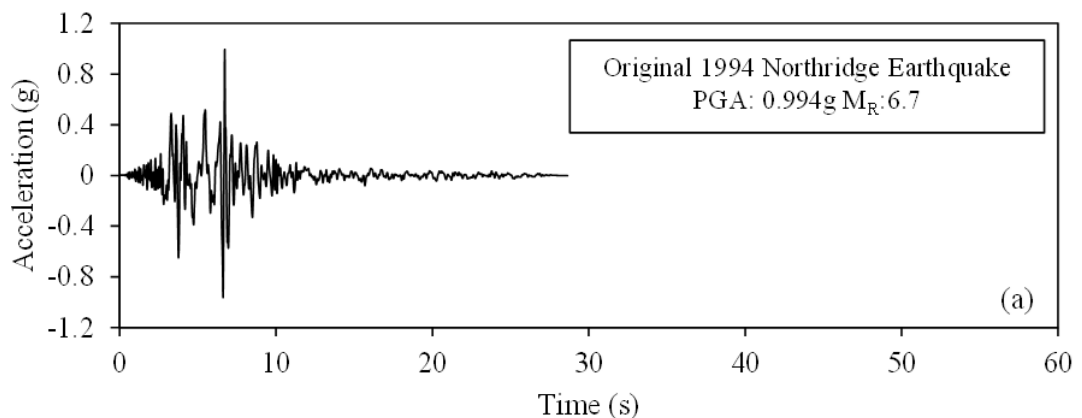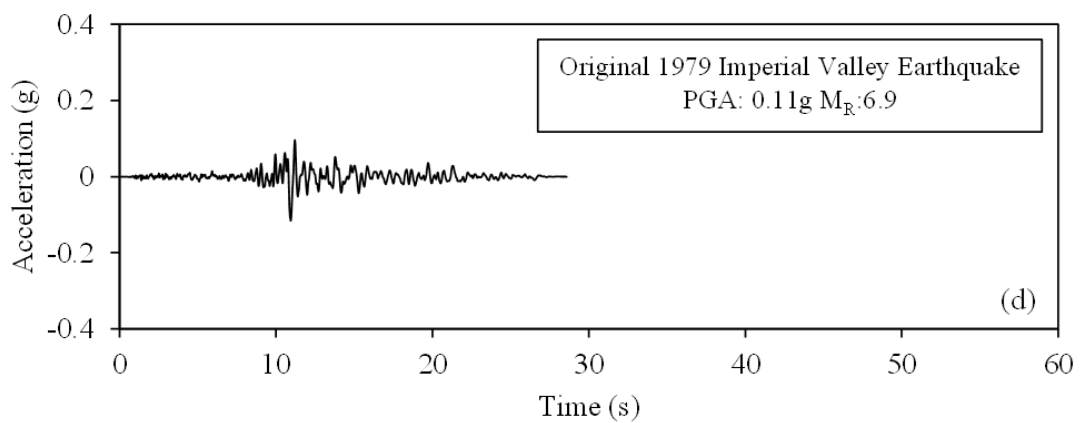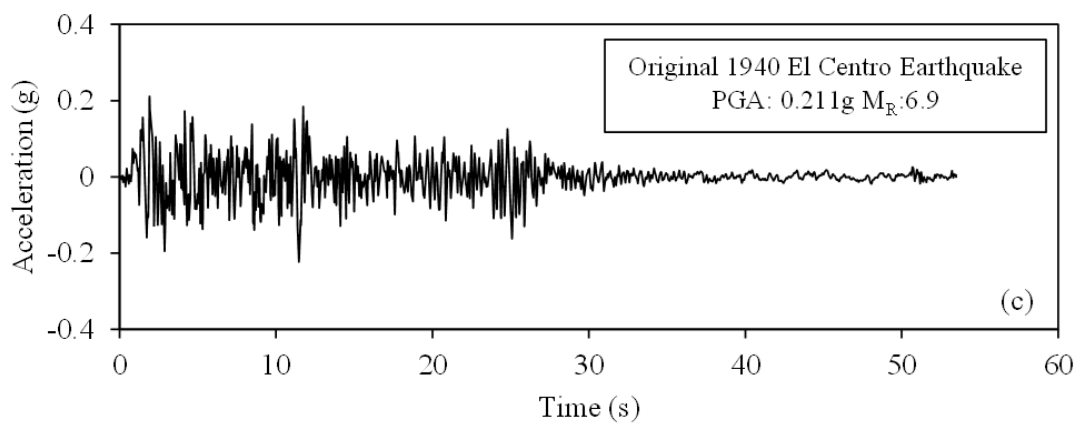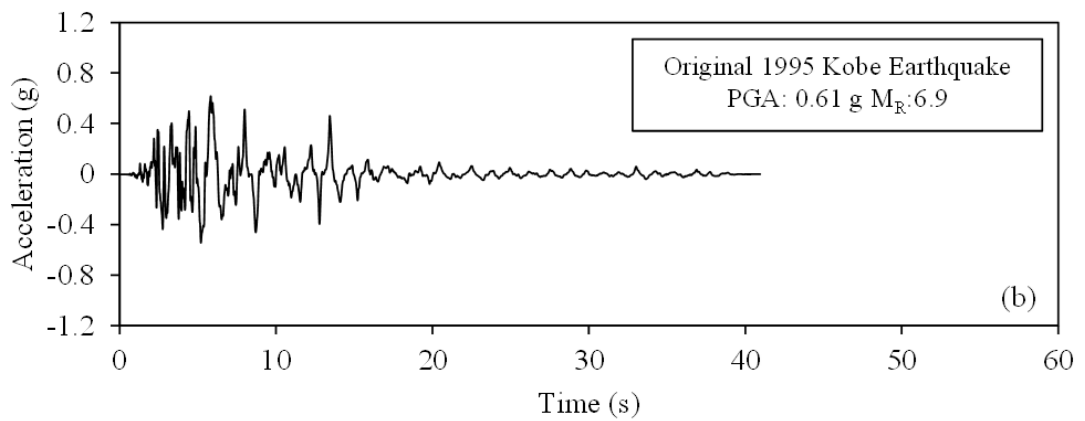
Figure 4.5 Considered earthquakes: (a) Original 1994 Northridge Earthquake, (b) Original 1995 Kobe Earthquake, (c) Original 1940 El Centro Earthquake and (d) Original 1979 Imperial Valley Earthquake.

(a)

Original 1994 Northridge Earthquake
PGA: 0.994g M_R:6.7

(b)

Original 1995 Kobe Earthquake
PGA: 0.61g M_R:6.9

(c)

Original 1940 El Centro Earthquake
PGA: 0.211g M_R:6.9
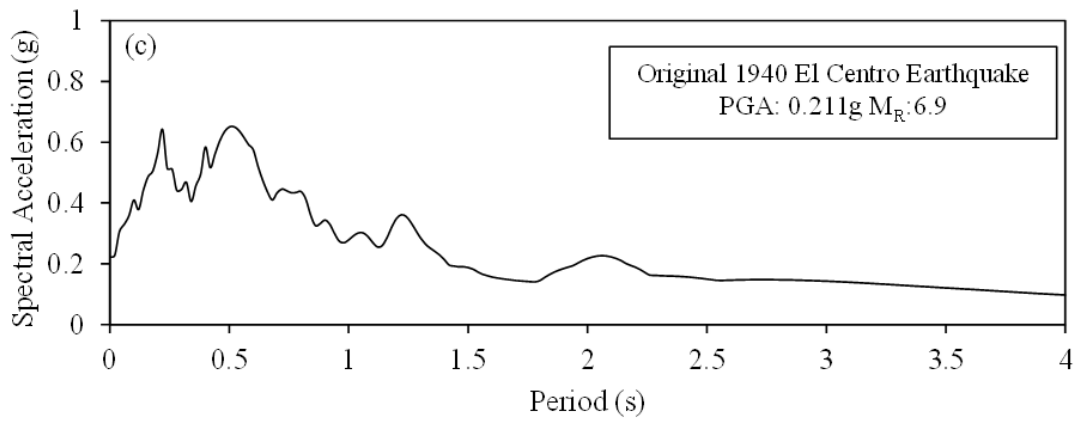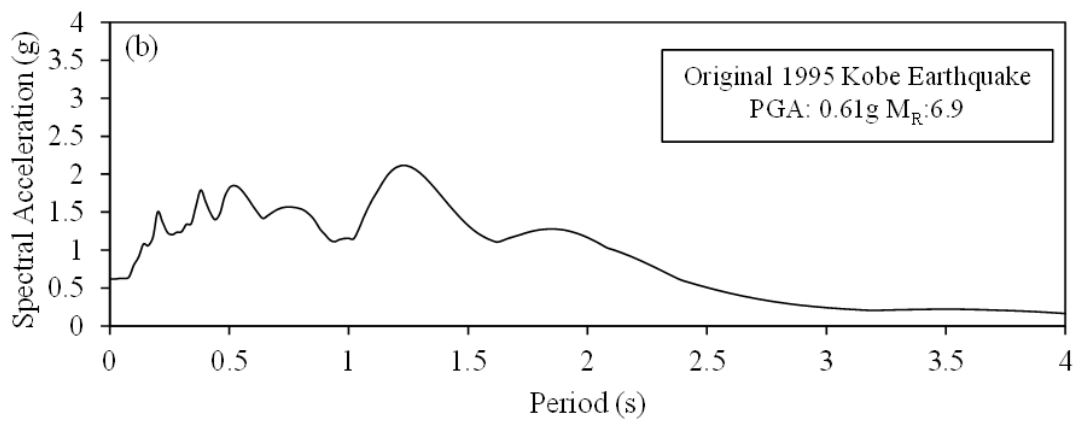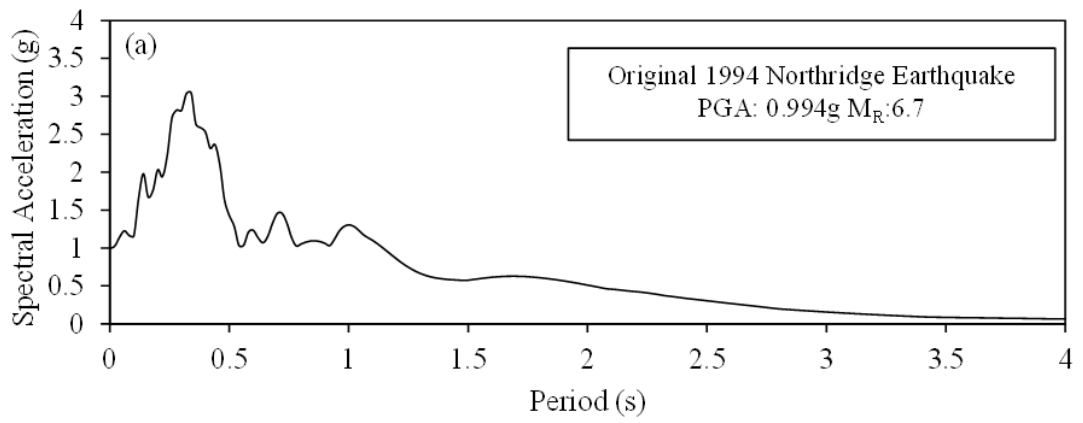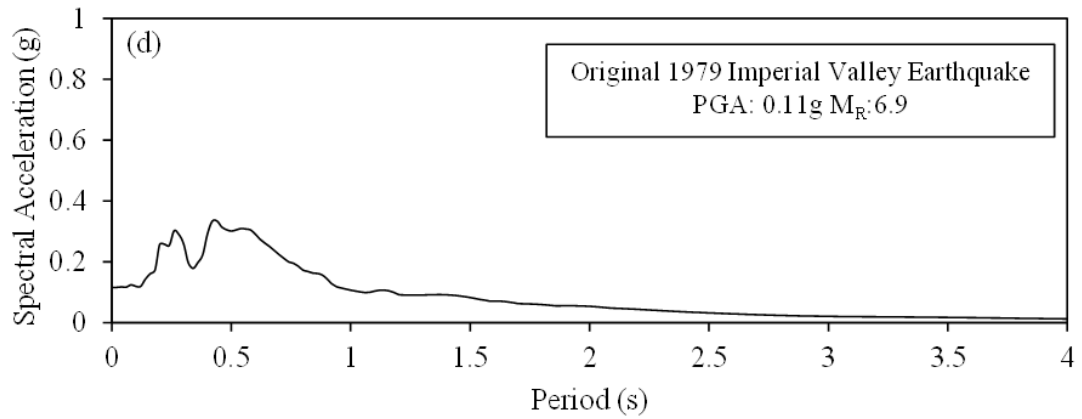
Figure 4.6 Response spectra considering 5% structural damping: (a) Original 1994 Northridge Earthquake, (b) Original 1995 Kobe Earthquake, (c) Original 1940 El Centro Earthquake and (d) Original 1979 Imperial Valley Earthquake.

To conduct the ground response spectrum analysis, each original earthquake input motion, to be applied at the based on the model where the bedrock was located, was scaled to three different target response spectrums. Indeed, the adopted response spectrum was obtained based on NZS1170.5 (2004) procedures to reflect events of different annual exceedance probability (AEP) (i.e., 1/50, 1/500 and 1/2500) at strong rock site (i.e. simulating bedrock motion). Referring to Figure 4.7, the shape of target spectrum was defined by the response spectrum acceleration factor *C(T)* using Equation (4.15).

$$C(T) = C_h(T)ZR_f N_{(T,D)} \tag{4.15}$$

where $C_h(T)$ is spectral shape factor which depends on the site subsoil class and structure period (*T*), *Z* is the hazard factor equal to 0.6 for Otira city in New Zealand based on the available site hazard map. R_f is the return period factor which was taken as 1.8, 1.0 and 0.35, for the annual probability of exceedance (APE) values of 1/50, 1/500 and 1/2500, respectively. These three target response spectra represented the common seismic demand levels in performance-based design framework, namely, Maximum Considered Earthquake (MCE), Design Level Earthquake (DLE), and Service Level Earthquake

(SLE). In addition, $N_{(T,D)}$ is a factor related to near fault properties, taken to be 1 in this study. In this study SeismoMatch (2016) software was used to obtain the scaled earthquake records to match the target response spectra. to avoid displacement drift at the end of the input earthquakes a baseline correction is necessary (Melgar et al. 2013). Therefore, the corrected acceleration time histories of scaled earthquakes were induced at the bedrock level (model base) to perform time history analysis.
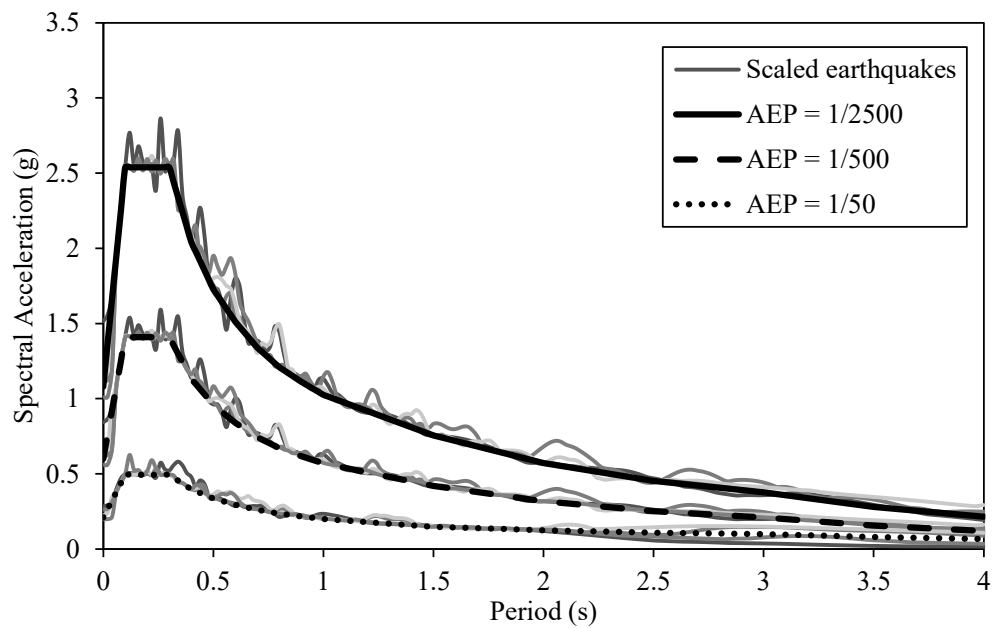
Figure 4.7 Scaled earthquakes reflecting different AEP at strong rock site.

4.4.2 Finite element model adopting NKH model (ABAQUS)

4.4.2.1 Model Parameters calibration

As explained earlier, the adopted nonlinear kinematic hardening NKH model requires input parameters σ_{yi}, γ_k, and C_k for each back stress. These parameters can be obtained by using input cyclic triaxial shear test data corresponding to the stress-strain data points for the stabilised cyclic curve. In this study, backbone curve, proposed by Sun et al. (1988) and adopted in the benchmark exercise in FLAC 3D model, was used as presented in Figure 4.4. Since this backbone curve captures the variation of modulus reduction ratio

(G/G_{max}) and damping ratio (ξ) with cyclic shear strain (γ) for cohesive soils, obtained from cyclic simple shear and resonant column test results, it can be used for seismic site response evaluations for cohesive soils.

Hardin-Drnevich function (Hardin et al. 1972) was also adopted to obtain a mathematical formulation to fit the backbone laboratory measurements using the Equations (4.12) and (4.13). Since the kinematic hardening model adopted in this study for cyclic behaviours of soils required the stabilised shear stress-strain cycle, Masing (1926) rule presented in Equation (4.16) was used to obtain a full loop of cyclic shear stress - strain response for the soil. In this study it is assumed that the stabilised cyclic loading - unloading curve is reached at cyclic shear strain value of 2% beyond which the shear modulus remains unchanged (McDowell 1992; Hennessey et al. 2017).

$$\tau - \tau_{rev} = \frac{G_{max}\ (\gamma - \gamma_{rev})}{1 + \left(\frac{|\gamma - \gamma_{rev}|}{2 * \gamma_{ref}}\right)} \tag{4.16}$$

where, τ_{rev} and γ_{rev} are the shear stress and cyclic shear strain at the reversal point, respectively.

As mention earlier, in this study, three different homogenous soil deposits with different shear stiffnesses (represented by the shear wave velocities V_s) and densities were used, namely, the very stiff Site Class C, stiff Site Class D and soft Site Class E according to IBC (2012). These three soils deposits were used by Galal and Naimi (2008) as benchmark exercise to examine the soil - structure interaction effect on the performance of the concrete moment resisting building frames under seismic effect. The adopted soil mechanical properties for these soil deposits are summarized and represented in Table 4.1, which are same as what was used in the benchmark FLAC 3D model report in the previous section.

To calibrate the nonlinear kinematic hardening parameters, a discrete set of shear yield stress and plastic shear strain data points, corresponding to the stabilised cyclic shear stress - strain curve, obtained from the Hardin-Drnevich model with Masing (1926) rule, were directly adopted. These data points start from the re-yielding point (τ_e, γ_e) to the reversal point in upper part of the hysteresis curve, as shown in Figure 4.8 as an example. It should be mentioned that in the adopted kinematic hardening model, the relationship between shear stress (τ_i) and accumulated plastic shear strain (γ_i^{pl}) at any point on the upper stabilised curve is as below:

$$\gamma_i^{pl} = \gamma_i - \frac{\tau_i}{G_{max}} - \gamma_p^0 \tag{4.17}$$

where, τ_i and γ_i are the total shear stress and strain for Point i, and $\gamma_p^0 = \gamma_e - \frac{\tau_1}{G_{max}}$, which is the plastic shear strain at the re-yielding point (τ_e, γ_e) as shown in Figure 4.8. Indeed, by programming a subroutine, a regression analysis was conducted to determine the nonlinear kinematic hardening model constants based on the shear - stress strain data points. Referring to Equation (4.9), by adopting several back stresses and calibrating the parameters, a larger strain range can be covered resulting in more accurate predictions. Thus, in this study two back stresses were adopted which resulted in more reliable predictions.
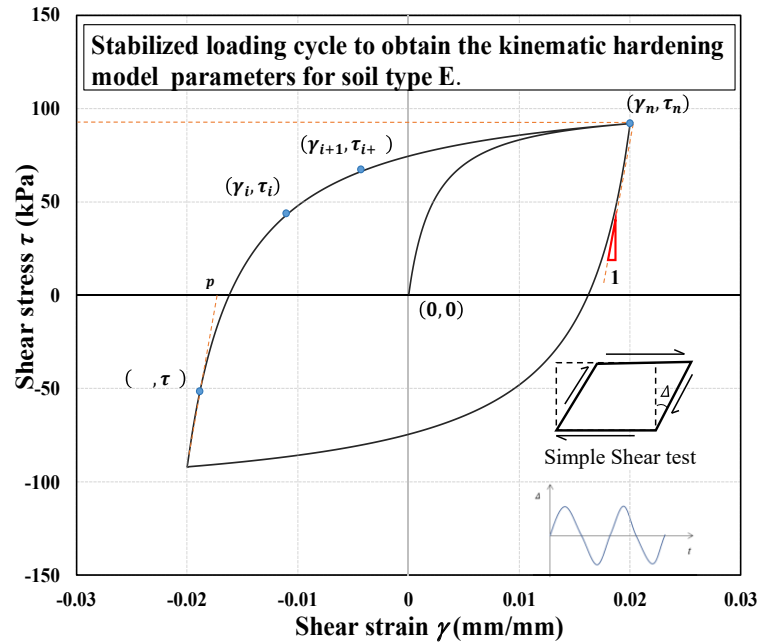
Figure 4.8 Stabilised loading cycle based on Hardin/Drnevich (1972) model with Masing (1926) rule for Soil E with V_s 160 m/s.

The obtained parameters were then used to perform strain-controlled shear tests by simulating one soil element. Figure 4.9 illustrates the comparison of the calibrated kinematic hardening model adopted in this study versus the results from Sun et al. (1988), while adopting Masing (1926) rule to obtain closed loading-unloading cyclic loops for the different stiffness values of the clay soils. As evident, the predictions adopting kinematic hardening model are reasonable, confirming capability and suitability of the adopted nonlinear kinematic hardening model to simulate the cyclic response of clayey soils using the calibrated parameters. Indeed, as the shear wave velocity (soil shear stiffness) increased from Site Class E to C, the stress amplitude also increased from 100 kPa to 1500 kPa for the same strain amplitude, respectively. The two calibrated back stress parameters for each soil type are summarized in Table 4.3. In the next stage, these calibrated soil parameters were used for the site response analysis to be explained in the next section.

(a)

(b)
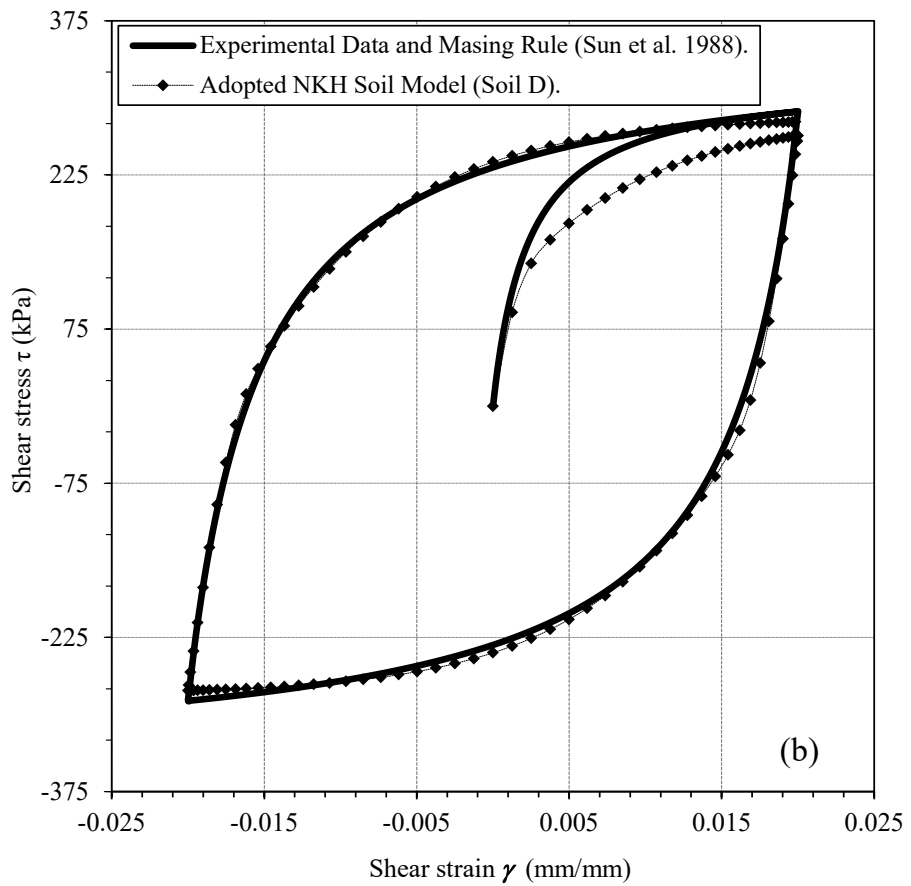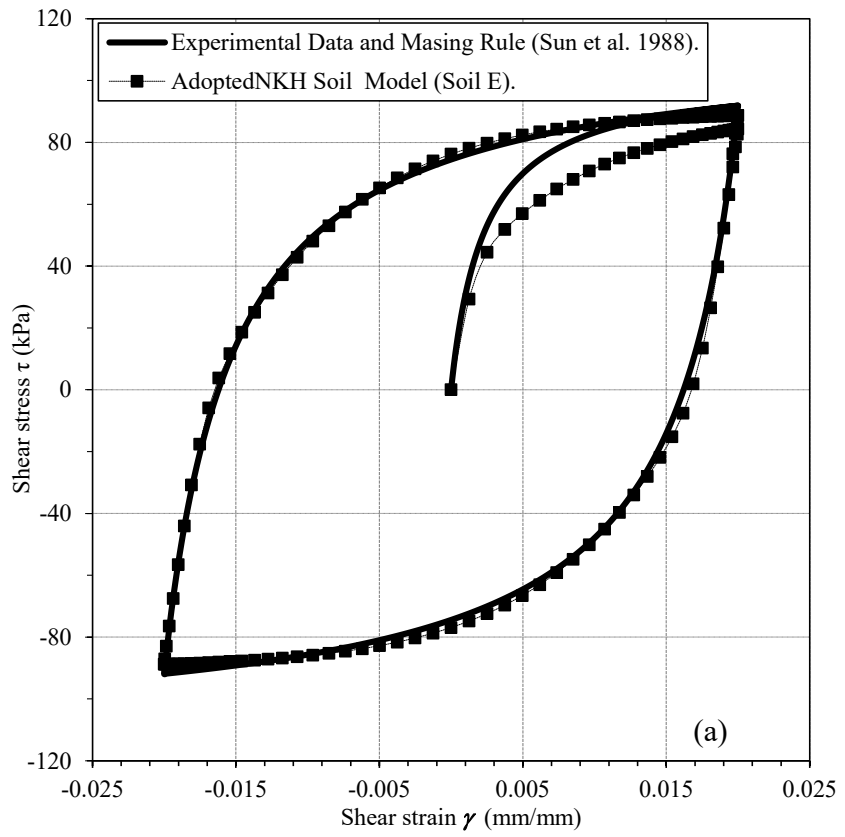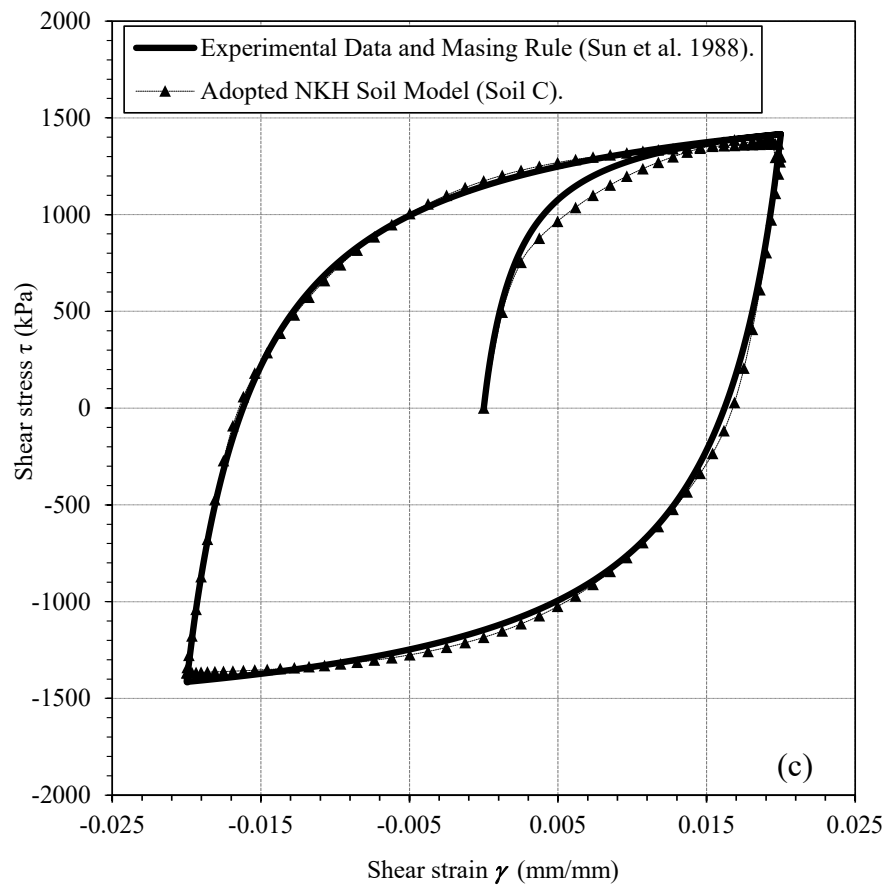
Figure 4.9 Comparison between the calibrated kinematic hardening models adopted in this study with the laboratory measurements obtained from Sun et al. (1988) (a) soil E, (b) soil D, and (c) soil C.

Table 4.3 Soil properties and the calibrated nonlinear kinematic hardening model parameters.

Soil properties	Symbol	Soil C	Soil D	Soil E
Density (kg/m^3)	ρ_{soil}	2124	1877	1714
Shear wave velocity (m/s)	V_s	564	270	160
Small strain shear modulus (MPa)	G_{max}	675.63	136.83	43.87
Poisson's Ratio	v		0.25	
Initial yield stress (kPa)	Y	28.9	1.877	1.879
Calibrated initial kinematic hardening modulus (MPa)	C_{k1}, C_{k2}	270, 297	54.4, 60.1	17.6, 19.3
Calibrated hardening modulus degradation rate	γ_{k1}, γ_{k2}	2200, 2440.5	1869, 2100.5	1534, 1700
1st and 2nd mode natural period for 30m deep deposit	s	0.21, 0.07	0.44, 0.148	0.75, 0.25

4.4.2.2 *Model Geometry, boundary conditions and earthquake records*

Time history analyses were carried out, and the result of the nonlinear kinematic hardening soil model adopting ABAQUS (version 2018), were verified against with stiffness degradation with hysteretic damping soil model implemented in FLAC3D software. For the sake of consistency both ABAQUS and FLAC 3D models had the same geometry and mesh size, and the same acceleration time history records were applied at the base and comparable free field boundaries implemented in both models (see Figures 4.2 and 4.10).
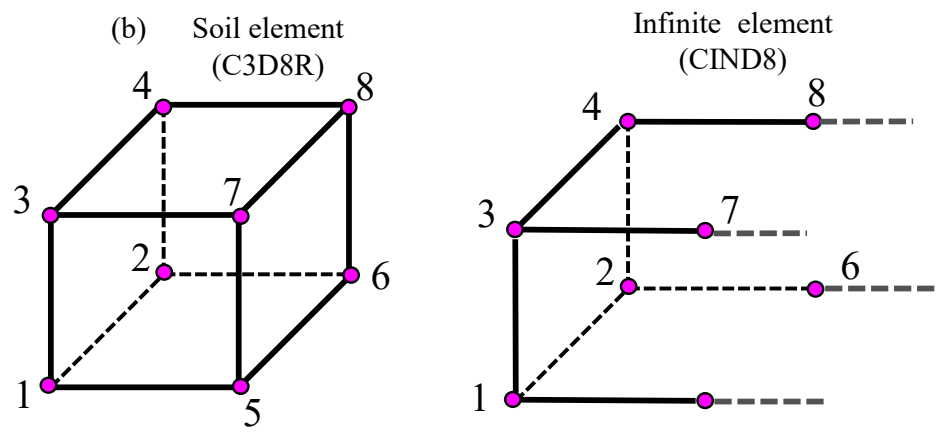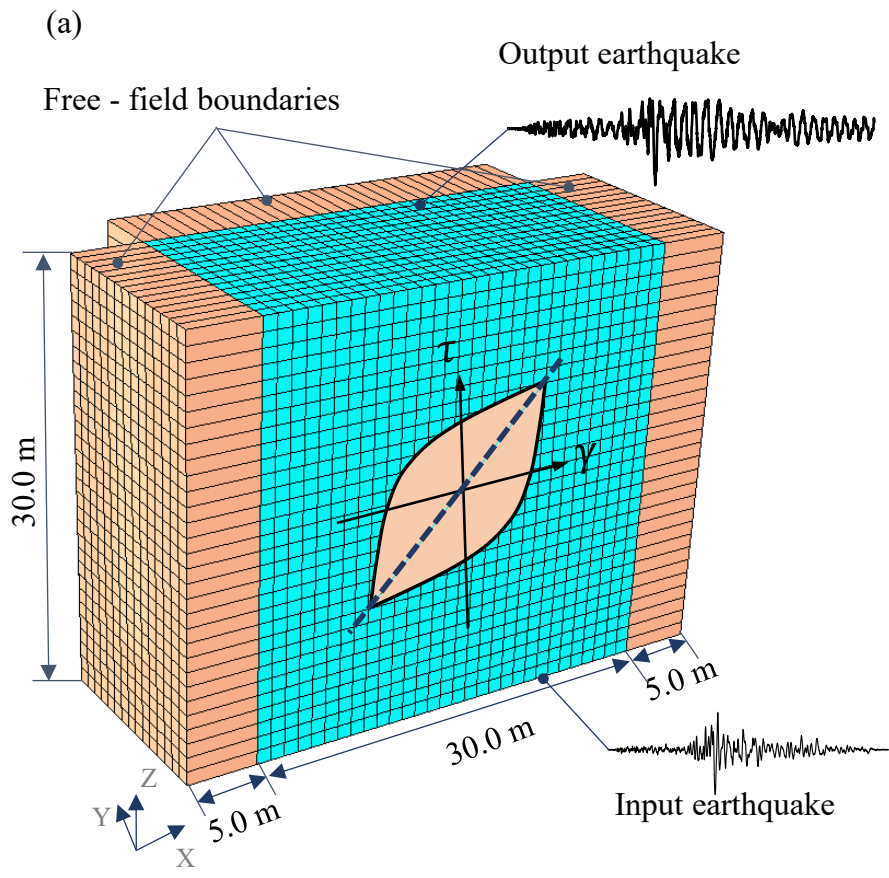
Figure 4.10 Soil model adopted in this study (a) model geometry (half model) demonstration implemented in ABAQUS; (b) representation of different elements implemented in the finite element model, namely, soil element (C3D8R) and infinite element (CIN3D8).

As Figure 4.10 shows, $30 \times 30 \times 30$ m soil deposit was modelled using $1 \times 1 \times 1$ m zones in ABAQUS, resulting in 13831 linear brick solid elements (C3D8R). Similar to the FLAC 3D benchmark model, for the static analysis generating the initial in-situ stress condition due to gravity in the soil deposit in ABAQUS, the geostatic condition of the soil medium was defined through predefined stresses, while the side boundaries were restrained to vertical movement parallel to the gravity load action, and the model base was fully fixed. Then, for dynamic analysis, the seismic excitation was applied in the horizontal direction (i.e. X-axis) at the base of the model using implicit integration scheme (i.e Newmark's method). It should be note that in the ABAQUS model, the one way 8 nodes infinite solid elements CIN3D8 were used at the lateral boundaries to represent the far-field soil, as these infinite elements could model the initial static equilibrium conditions (Zienkiewicz et al. 1983), while could also absorb the energy from the unbounded soil area under dynamic loading (Lysmer and Kuhlemeyer 1969). These boundaries could perfectly absorb all types of waves (e.g. body waves and surface waves) at all angles of incident and frequencies propagating outward from the side boundaries (Nielsen 2006). Therefore, these infinite elements were implemented to allow the vertical wave propagation through the soil medium, while preventing reflection of the side waves back into the model. The dynamic response of these infinite elements is governed by the following equation of motion:

$$\rho_{inf}\, \ddot{u}_i = G_{inf}\, \frac{\partial^2 u_i}{\partial x_i \partial x_j} + (\lambda + G_{inf}) \frac{\partial^2 u_j}{\partial x_i \partial x_j} \tag{4.18}$$

while the damping ratios of the adopted infinite boundaries in the normal and shear directions are described by Equation (4.19):

$$d_p = G_{inf} \frac{\lambda_{inf} + 2G_{inf}}{c_p};$$ (4.19a)

$$d_s = \rho_{inf} c_s$$ (4.19b)

where ρ_{inf} is the representative density of unbounded soil area, G_{inf} and λ_{inf} are Lame's constants of the unbounded soil area, c_p and c_s are the velocities of the compression and shear waves, respectively, d_p and d_s are the damping parameters of the infinite element in the normal and shear directions, respectively, u_i and u_j are the particle displacements, x_i and x_j are the positions of nodes i and j, respectively.

As the seismic input motions are propagated through the soil deposit, the dynamic features of the soil play a key role in the ground surface response in term of response spectra, acceleration amplification, and damping. Therefore, in this study local site effect, which relates to both the soil dynamic properties and the nature of the input seismic wave, alerting the structural response, is assess. In the following sections, the results of the nonlinear kinematic hardening NKH model programmed in ABAQUS are assessed against benchmark FLAC 3D model in terms of shear stress – strain responses, acceleration time history and acceleration response spectrum.

4.5 Results and discussion

In this section, the time history analysis results in terms of the shear stress - strain response in the middle of the soil deposit, and the acceleration response spectrum, and acceleration time history at the ground surface are presented and discussed for both adopted constitutive models in FLAC 3D and ABAQUS. The analyses were carried out for three Site Classes C, D, and E, with corresponding shear wave velocities V_s equal to 564 m/s, 270 m/s, and 160 m/s with other characteristics as reported in Table 4.3,

subjected to different seismic motions scaled to three seismic demand levels and the acceleration response spectrums were extracted and compared for each soil deposit.

4.5.1 Shear stress - strain response of soil

To assess the seismic behaviour of the soil and capture the nonlinear characteristics of the soil response, the shear stress - strain curves were extracted and compared at 15.0 m depth of the soil model for both NKH (ABAQUS) and SDHD (FLAC 3D) soil models subjected to four original earthquake records. It should be note that assessing the stress - strain response at the mid-depth of soil deposit seems to be more suitable compared with the ground surface level where the minimal shear strains were experienced. Figures 4.11 – 4.14 report the samples of stress - strain curves for Site Classes C, D, and E under the effect of original 1994 Northridge, 1995 Kobe, 1940 El Centro, and 1979 Imperial Valley earthquakes, respectively.

As Figure 4.11 shows, the shear stress - strain responses for Site Class C (i.e. the stiffer soil deposit with V_s =564 m/s) experienced the higher shear stresses and lower shear strains compared to Site Class D (Figure 4.11b), and Site Class E (Figure 4.11c). Indeed, the maximum experienced shear stresses decreased from 800 kPa to 200 kPa and 80 kPa, when the soil shear wave velocity decreased from Site C to D and E (i.e. corresponding to reduction in the stress by 52%, and 72% respectively) for original 1994 Northridge earthquake. Moreover, the maximum shear strain experienced by the soil increased from 0.002%, to 0.0042% and 0.006% for Site Classes C to D and E, respectively, under the 1994 Northridge earthquake. It should be noted that comparable results were reported in the literature (Nakamura et al. 2014; Rayamajhi et al 2014) where the soil with lower shear velocity develop less shear stresses during earthquakes. Referring to Figures 4.11 – 4.14, the area under the hysteresis loops were larger for Site

111

Class E (softer soil) and decreased toward Site Class C (harder soil), which means the softer soil (i.e. Site E with Vs =160 m/s) damped more seismic energy than Site Class D and C. In general, the predicted shear stress- strain curves from NKH soil model in ABAQUS were in good agreement with those of SDHD soil model in FLAC 3D for different soil deposits and under the different earthquakes.
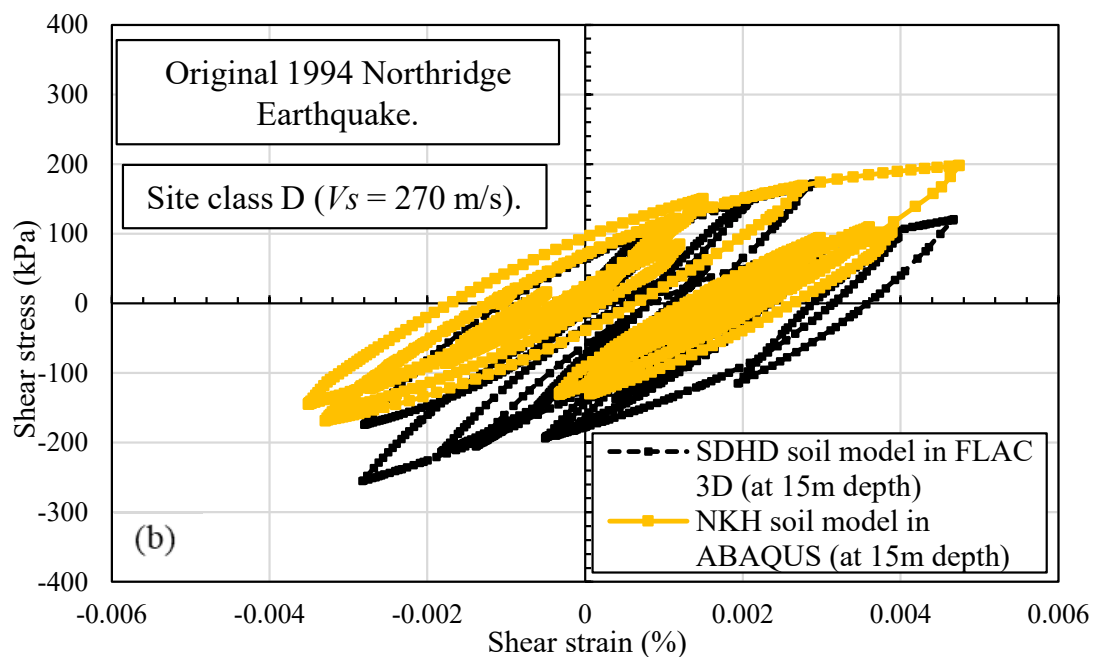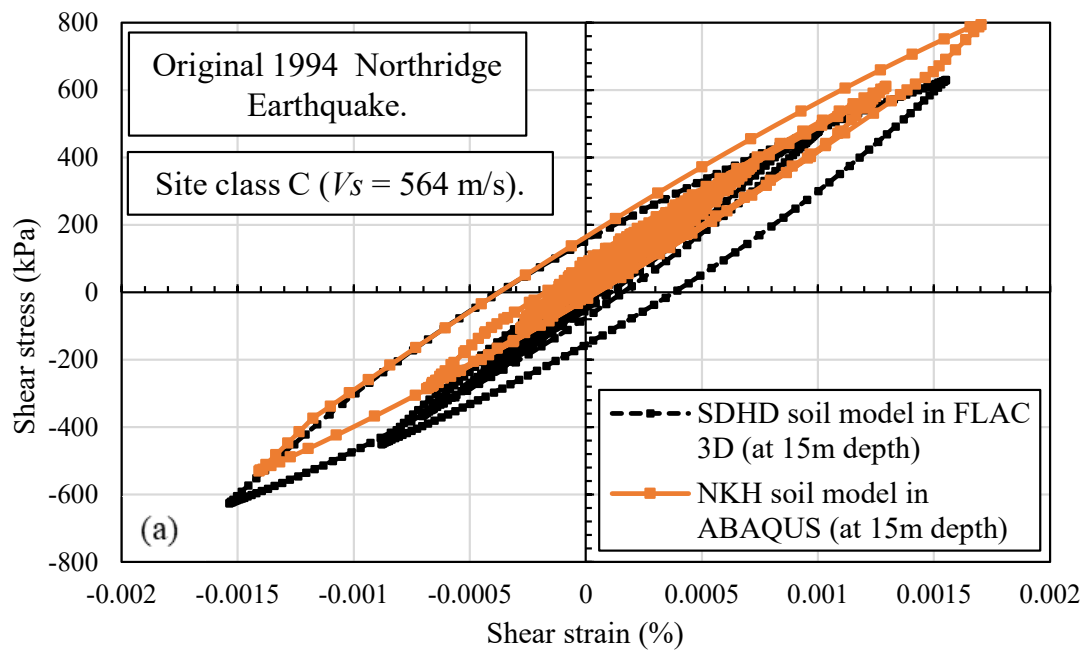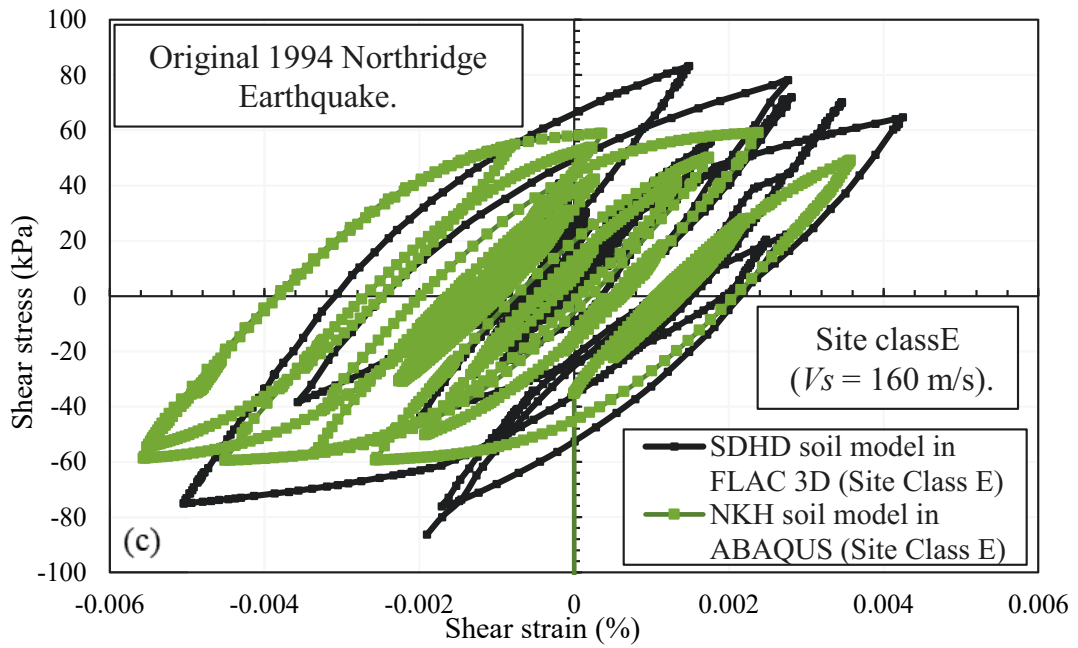
Figure 4.11 Comparison between shear stress strain record at 15 m depth between SDHD soil model in FLAC 3D and NKH soil model for (a) site class C, (b) site class D and (c) site class E under original 1994 Northridge earthquake.
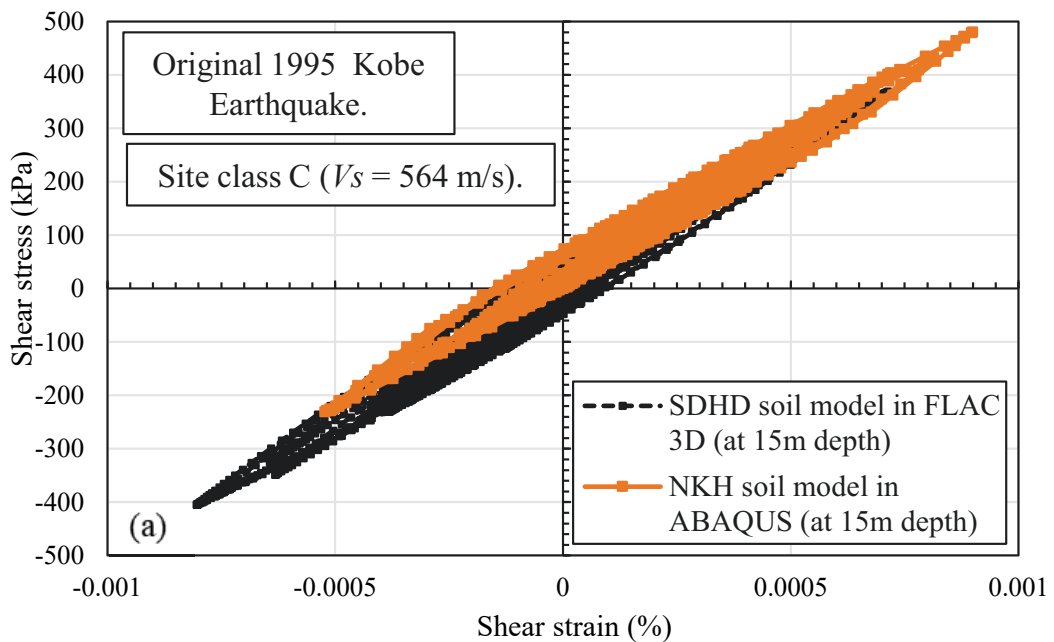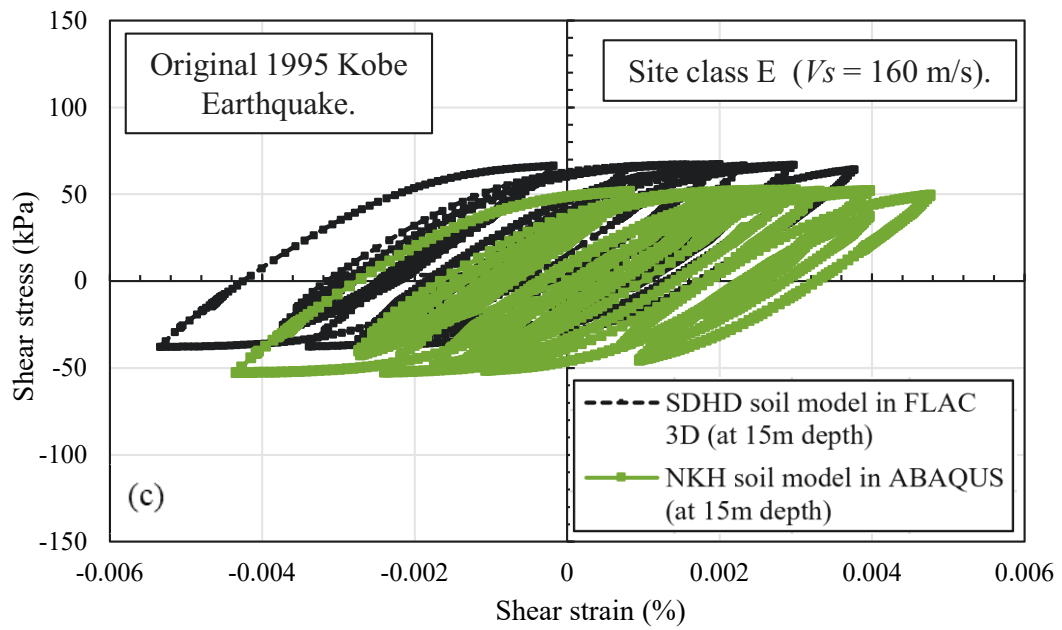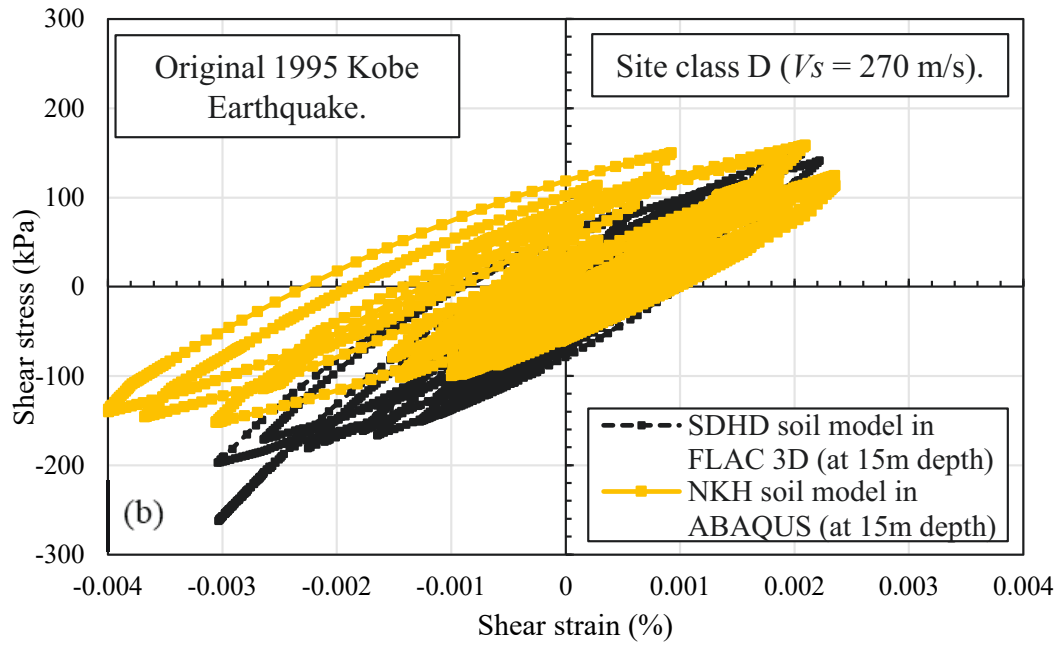
Figure 4.12 Comparison between shear stress strain record at 15 m depth between SDHD soil model in FLAC 3D and NKH soil model for (a) site class C, (b) site class D and (c)

site class E under original 1995 Kobe earthquake.

(a)

(b)
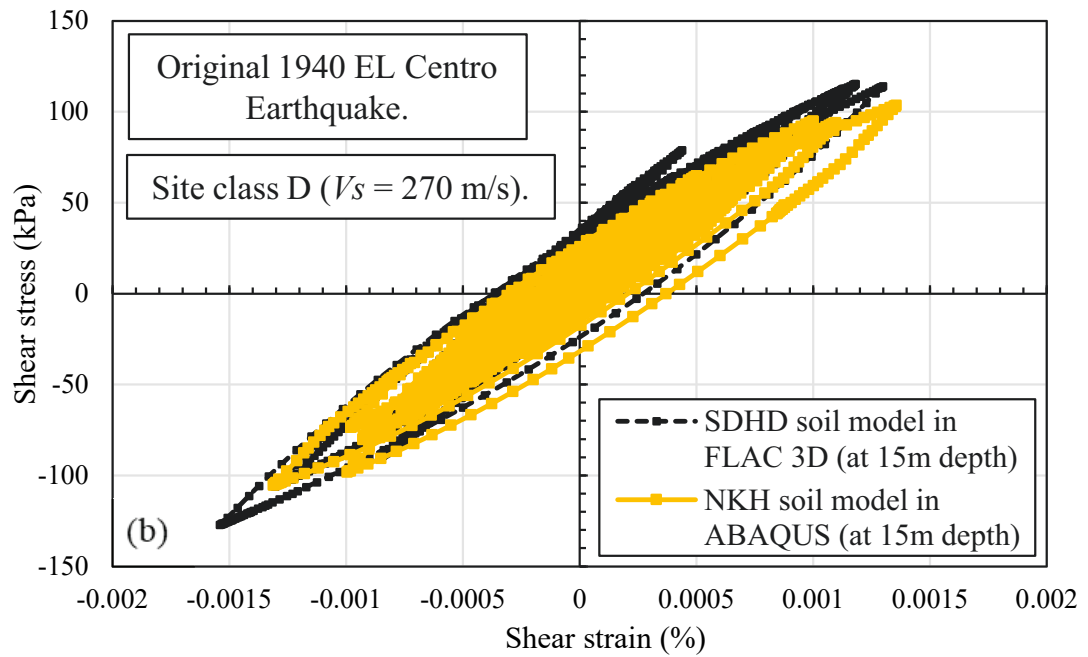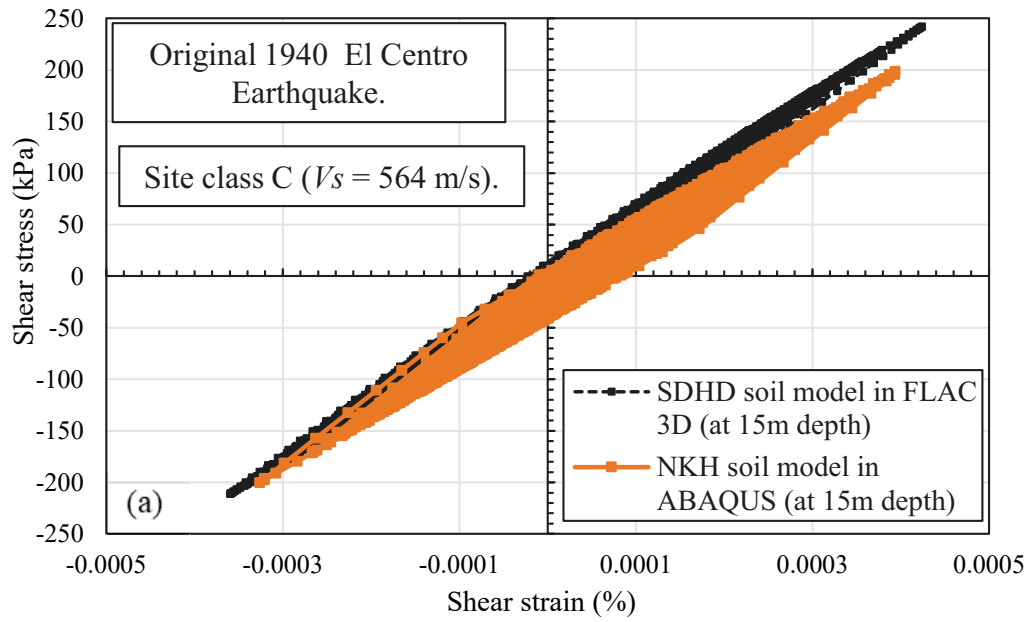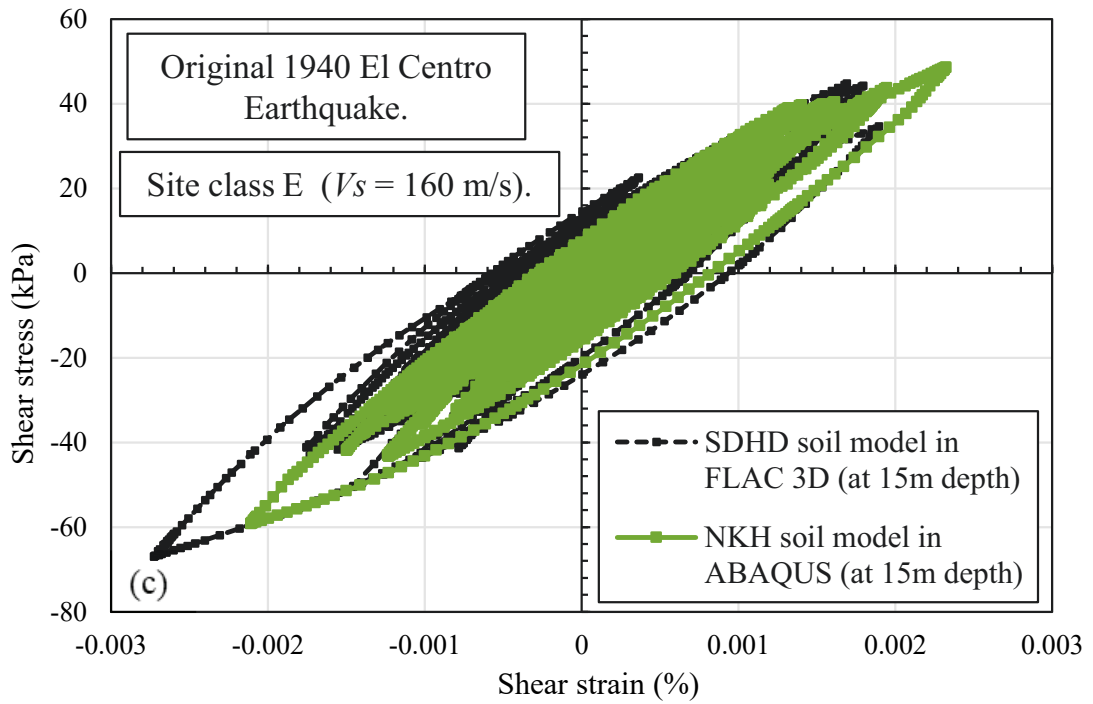
Figure 4.13 Comparison between shear stress strain record at 15 m depth between SDHD soil model in FLAC 3D and NKH soil model for (a) site class C, (b) site class D and (c) site class E under original 1960 El Centro earthquake.
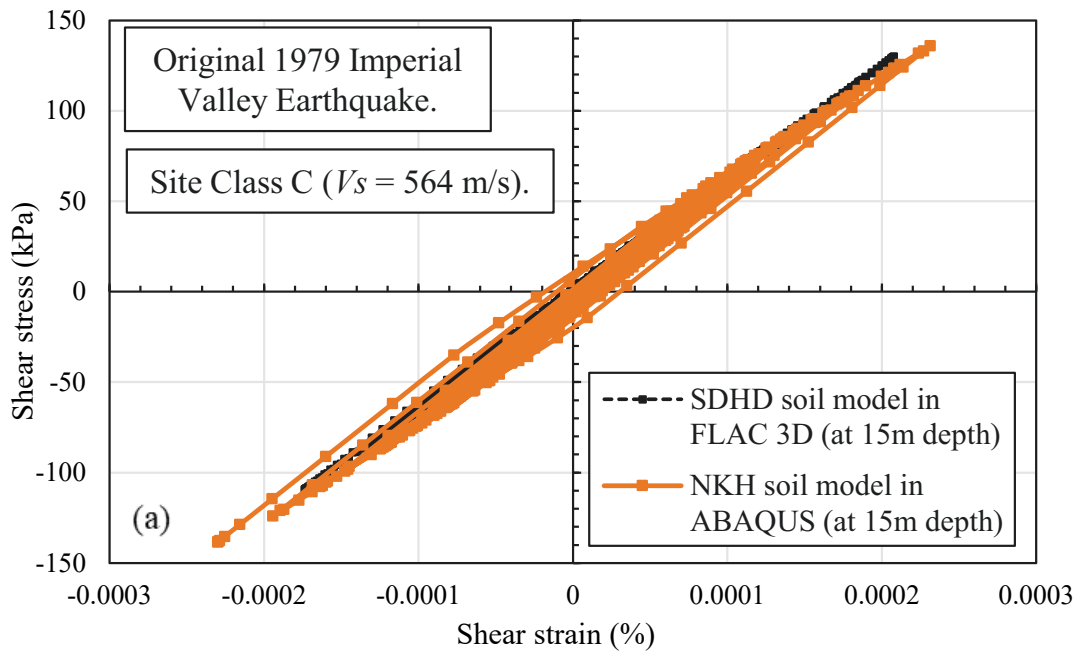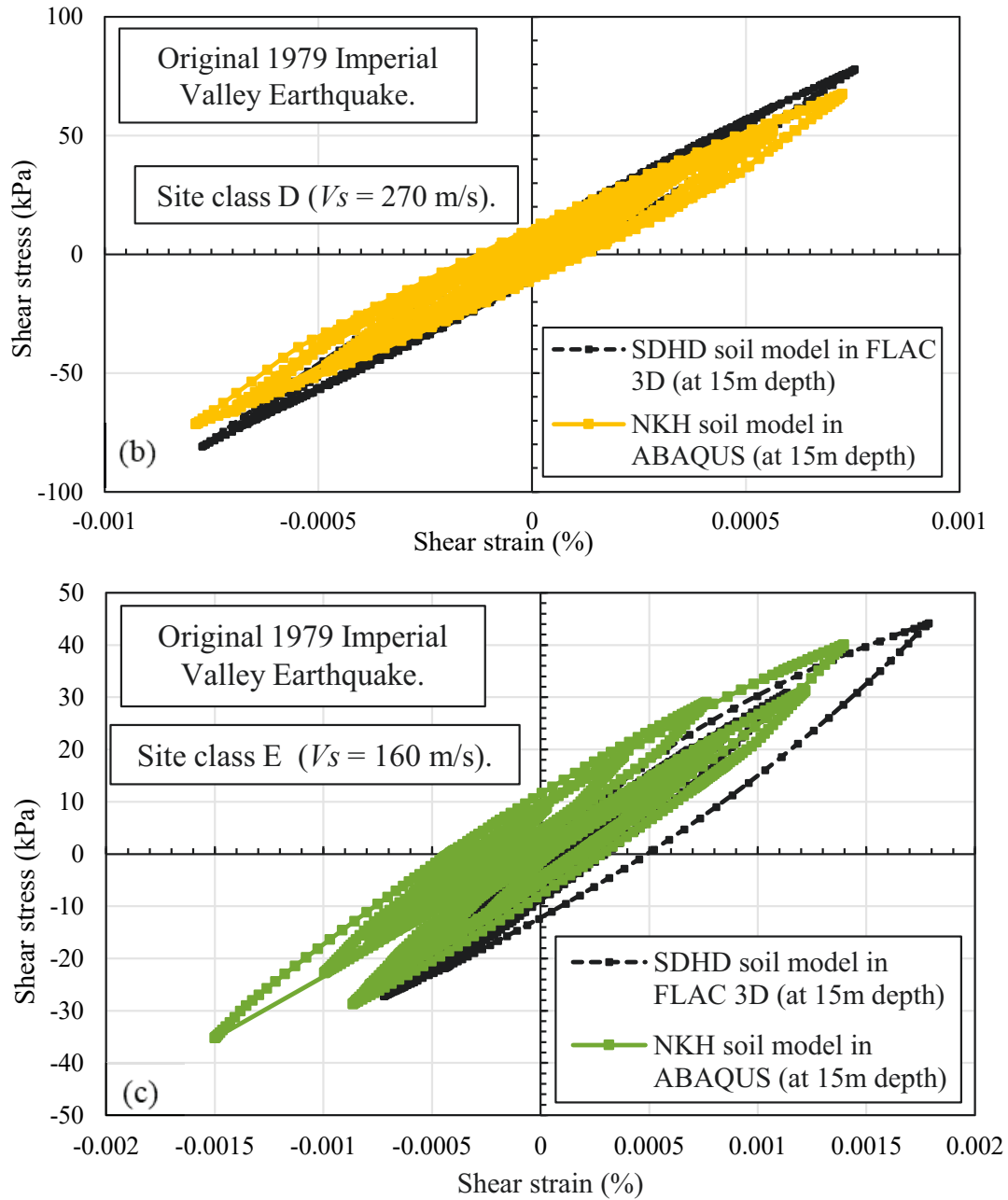
Figure 4.14 Comparison between shear stress strain record at 15 m depth between SDHD soil model in FLAC 3D and NKH soil model for (a) site class C, (b) site class D and (c) site class E under original 1979 Imperial Valley earthquake.

4.5.2 Acceleration time history predictions

Figures 4.15 – 4.18 compare the samples of recorded acceleration time histories at the ground surface using two adopted constitutive models for three Site Classes C, D and E, under original 1994 Northridge, 1995 Kobe, 1940 El Centro and 1979 Imperial

valley earthquakes, respectively. In general, amplification of Peak Ground Acceleration (PGA) were evident as the seismic wave propagated from the bedrock to the surface. Referring to Figure 4.15b as an example corresponding to 1994 Northridge earthquake for Site Class C (stiff soil with V_s = 564 m/s), the acceleration amplitude for the most part of the earthquake duration is amplified, particularly, for the absolute PGA it found to be amplified by factor of 2.07, (e.g. absolute PGA increased from 0.99g to 2.05g for 1994 Northridge earthquake). For Site Class D (V_s =270 m/s) and 1994 Northridge earthquake (Figure 4.15c), the acceleration reported at the ground surface increased, with the average amplification factor of 1.19 for the high amplitude range between 3 s and 10 s (e.g. PGA increased from 0.99g to 1.19g). Finally, for Site Class E (V_s=160 m/s), the amplification was at the later parts of the earthquake record (e.g. 15 - 25 s) with average factor 1.1 along the later parts of the 1994 Northridge earthquake (Figure 4.15d), while in the early stages of earthquake (e.g. 3-10 s), minor acceleration amplification (i.e. amplification factor of about 1.08) was observed and the PGA values remained almost the same. Comparing the observations in Figure 4.15 with the observations for the three site classes under the 1995 Kobe earthquake as reported in Figures 4.16 shows that the reported acceleration at ground surface amplified by a factor of about 2.0 for Site Class C (V_s = 564 m/s), where the PGA for the original earthquake which was 0.61g increased to 1.21g as represented in Figure 4.16b. For Site Class D (V_s=270 m/s), the PGA increased from 0.61g to 1.07g (i.e. amplification factor 1.75 in Figure 4.16c), and for Site Class E (V_s=160 m/s), while PGA did not change much, a notable amplification was observed for lower ground accelerations at the later stages of earthquake (i.e. after 15 s) as reported in Figure 4.16d.
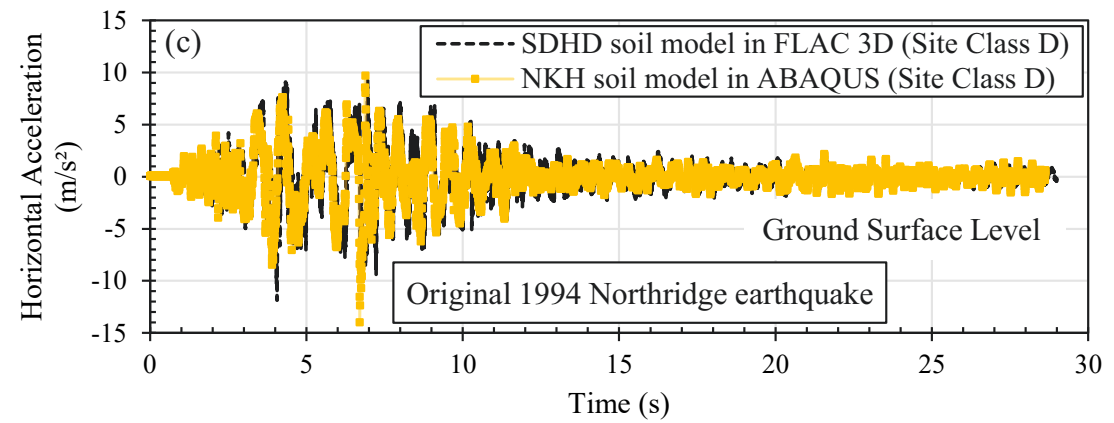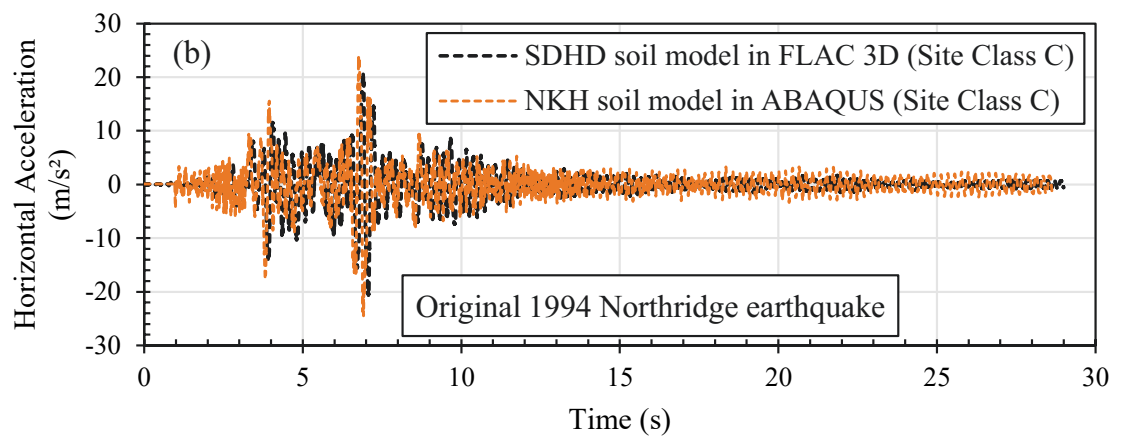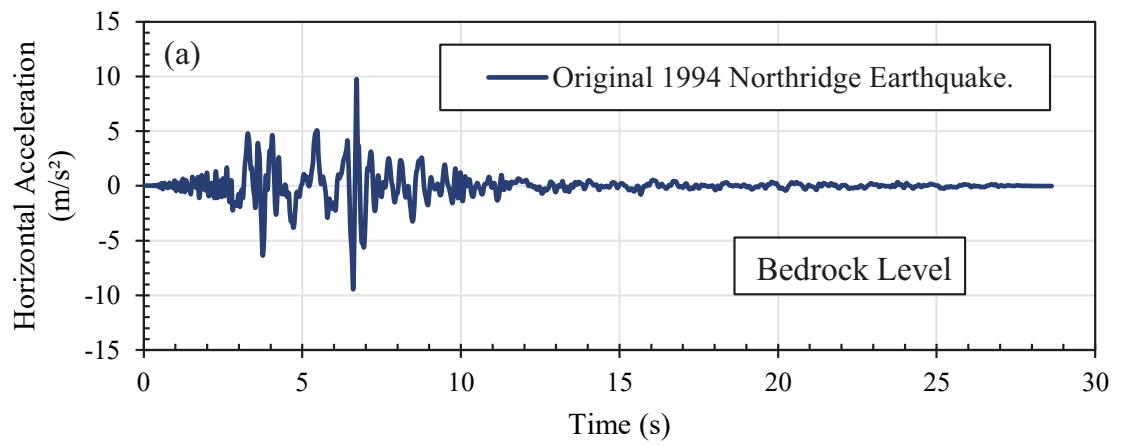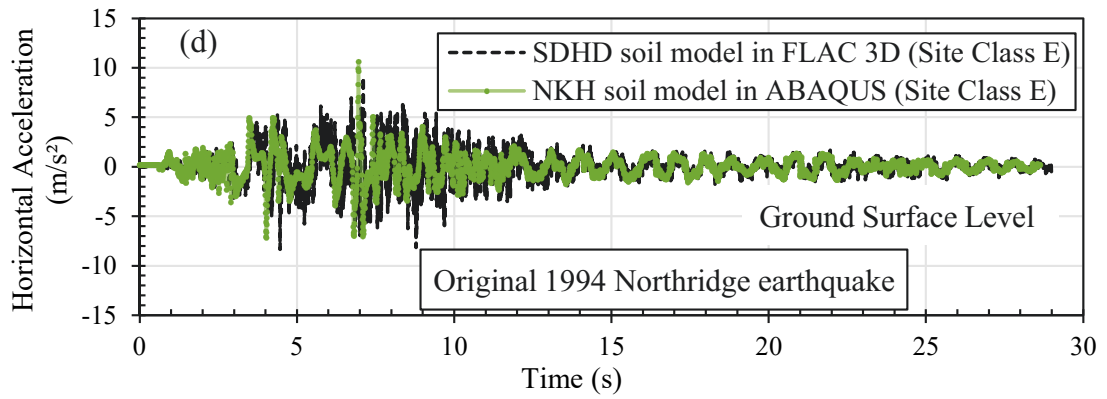
Figure 4.15 Horizontal acceleration time history for (a) Bedrock Level for Original 1994 Northridge Earthquake, and Comparison between acceleration time histories at ground surface of stiffness degradation with hysteresis damping and nonlinear kinematic hardening soil models for (b) site class C, (c) site class D and (d) site class E under Original 1994 Northridge earthquake.
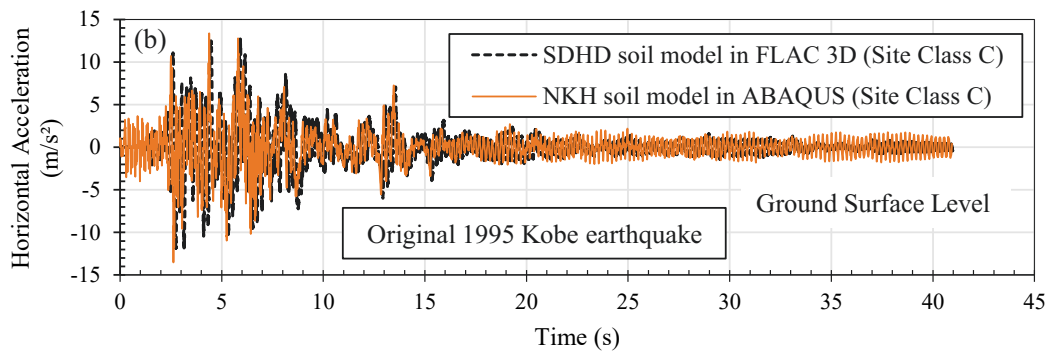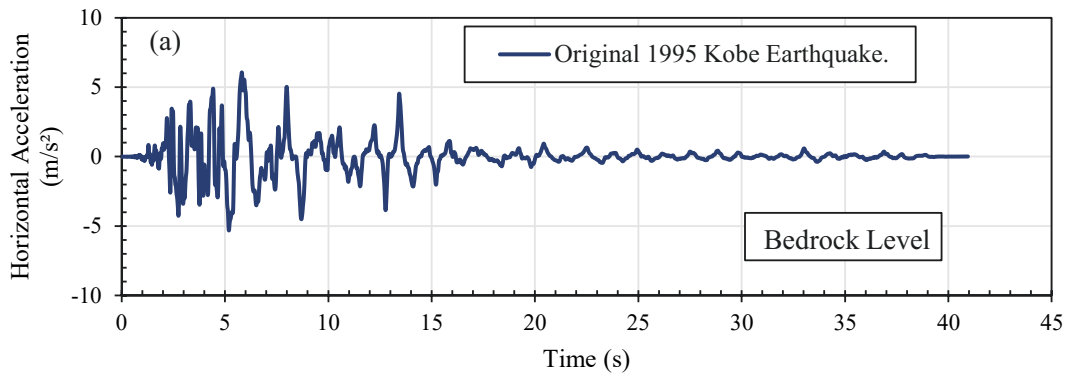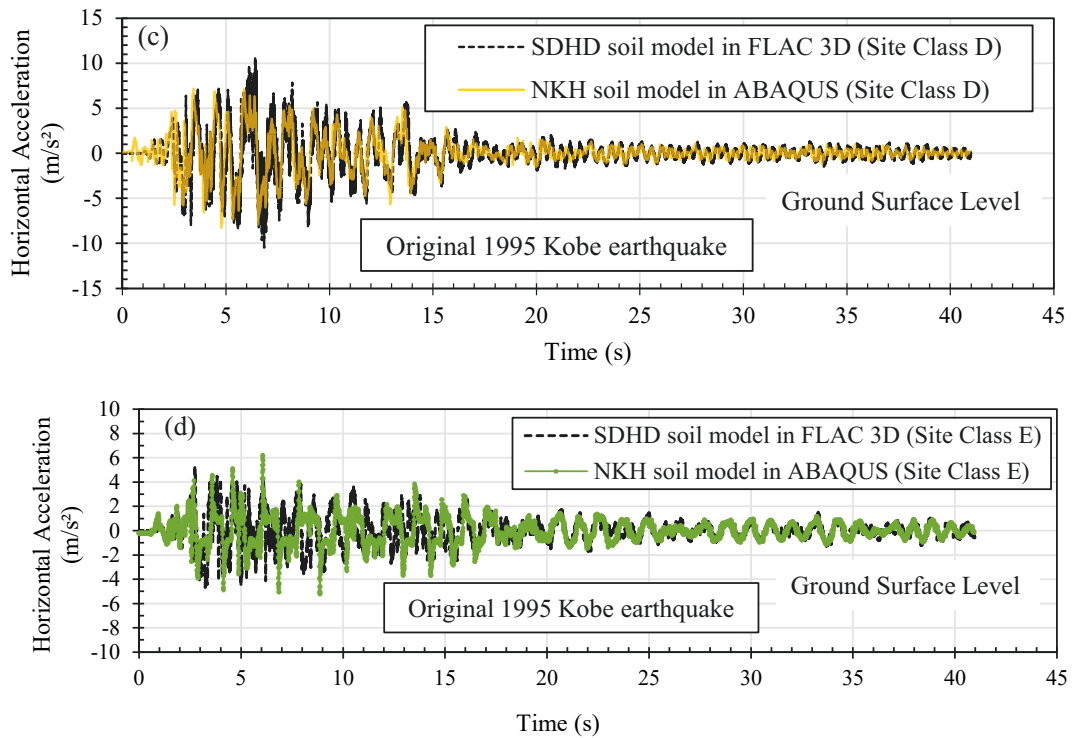
Figure 4.16 Horizontal acceleration time history for (a) Bedrock Level for Original 1995 Kobe Earthquake, and Comparison between acceleration time histories at ground surface of stiffness degradation with hysteresis damping and nonlinear kinematic hardening soil models for (b) site class C, (c) site class D and (d) site class E under Original 1995 Kobe Earthquake.

On the other hand, subjected to far field 1940 El Centro in Figure 4.17 and 1979 Imperial Valley in Figure 4.18 higher amplification in the absolute of the PGA amplitude was observed. For example, for 1940 El Centro earthquake with intermediate frequency, the PGA amplified by factor of 3.54, 2.13, and 1.3 for Site Class C, D, and E, respectively, when the wave seismic wave travel from the bed rock to the ground surface. For 1979 Imperial valley the PGA amplified by 3.7, 2.7, and 2.1 for Site Classes C, D and E, respectively. Moreover, for near field large earthquakes including 1994 Northridge and 1995 Kobe earthquakes, the extent of amplification of PGA was less compared to far field earthquakes including 1940 El Centro and 1979 Imperial Valley, particularly, for Site Classes D and E. These observations are in a good agreement with those made by other researcher such as Khaheshi Banab et al. (2012) and Zalachoris and Rathje (2015) who

showed that for high intensity near field earthquakes loading the soil experienced higher nonlinear response in term of shear strain and damping, that reduced the ground response amplification. As evident in the results reported in Figures 4.15 – 4.18, the predictions from NKH soil model in ABAQUS and SDHD soil model in FLAC 3D are generally in a good agreement. However, some minor disparities were observed where NKH soil model in comparison to SDHD soil model showed over prediction of the PGA values for the very stiff and stiff soils (Site Class C with $V_s = 564$ m/s and Site Class D with $V_s = 270$ m/s) for near field earthquakes.
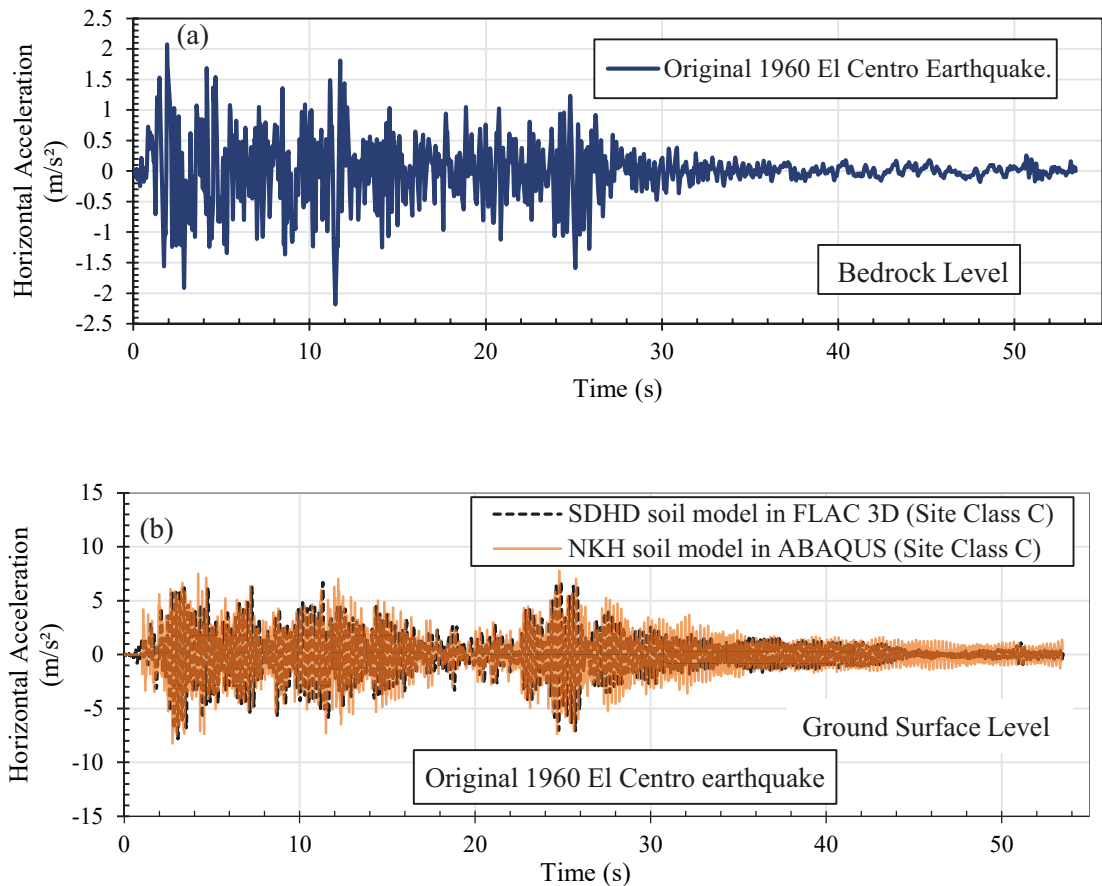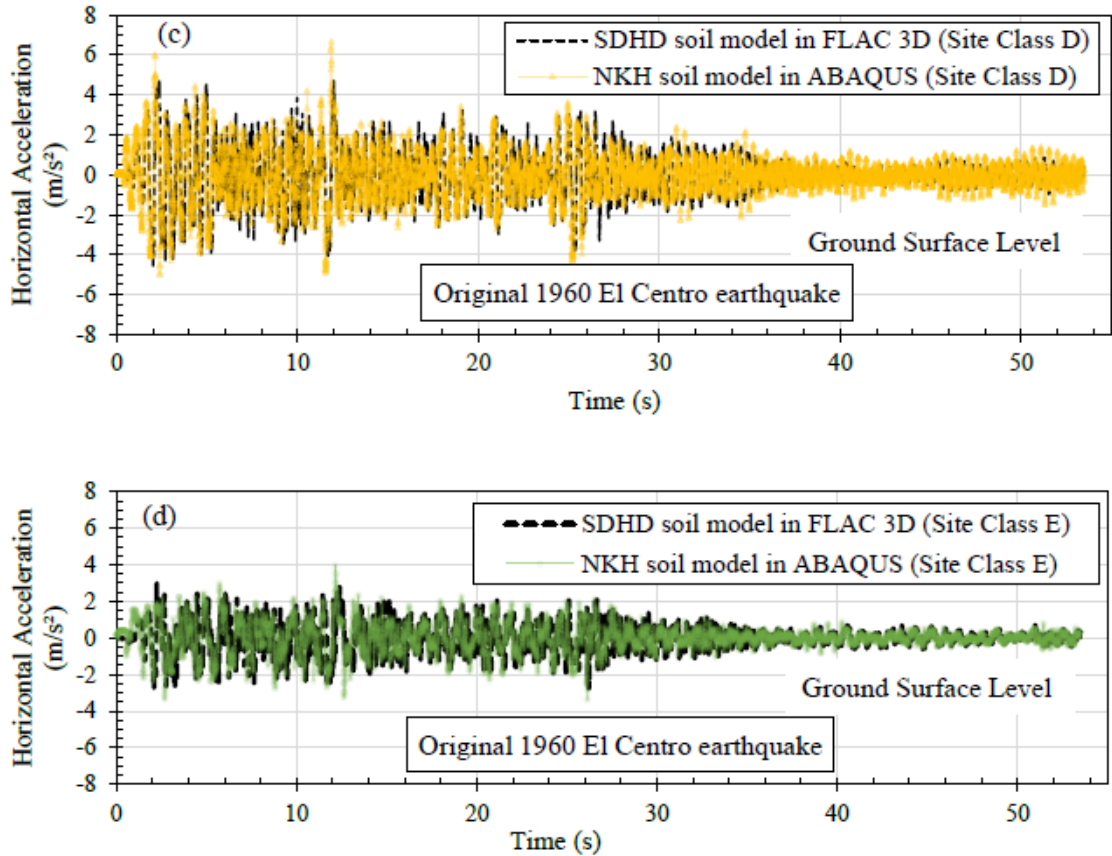
Figure 4.17 Horizontal acceleration time history for (a) Bedrock Level for Original 1960 El Centro Earthquake, and Comparison between acceleration time histories at ground surface of stiffness degradation with hysteresis damping and nonlinear kinematic hardening soil models for (b) site class C, (c) site class D and (d) site class E under Original 1960 El Centro earthquake.
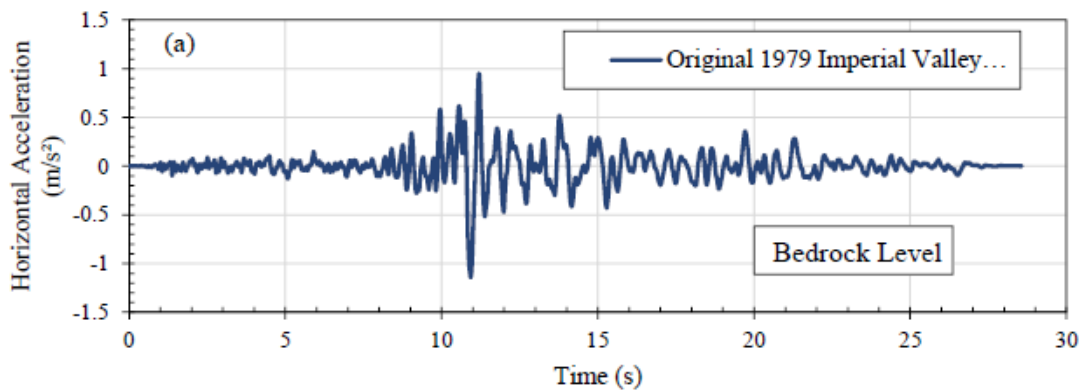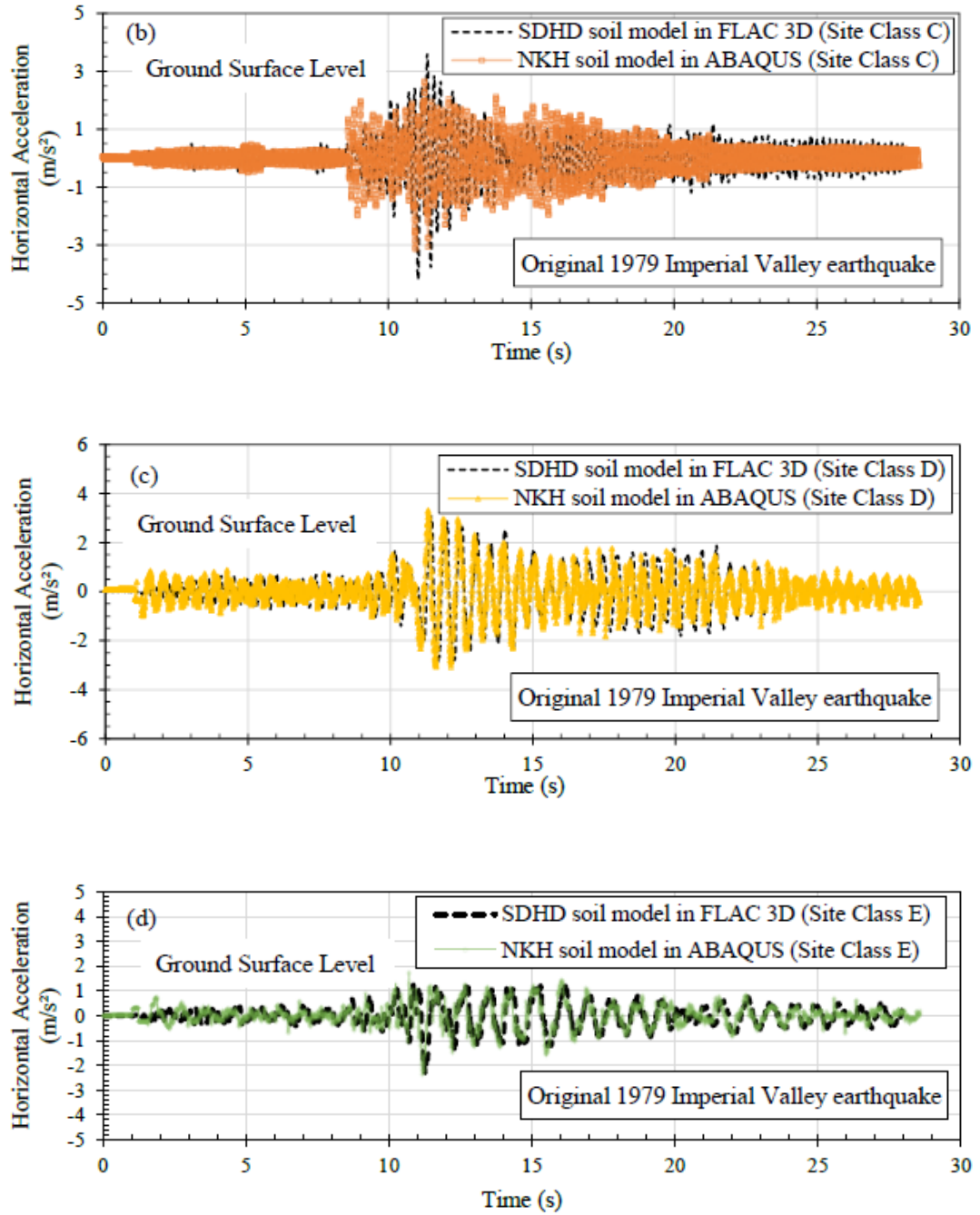
Figure 4.18 Horizontal acceleration time history for (a) Bedrock Level for Original 1979 Imperial Valley Earthquake, and Comparison between acceleration time histories at ground surface of stiffness degradation with hysteresis damping and nonlinear kinematic hardening soil models for (b) site class C, (c) site class D and (d) site class E under Original 1979 Imperial Valley earthquake.

4.5.3 Acceleration response spectrum

The acceleration response spectrum of the recorded motions at the ground surface

was extracted and reported for Site Classes C, D and E in Figure 4.19 subjected to original

1994 Northridge (Figure 4.19a), 1995 Kobe (Figure 4.19b), 1940 El Centro (Figure

4.19c), and 1979 Imperial Valley (Figure 4.19d) earthquakes, respectively. Referring to

Figure 4.19a, the acceleration response spectrum S_a under 1994 Northridge earthquake

observed to be the highest for Site Class C, in the short period ranges (i.e. 0.05- 0.35 sec),

and for T > 0.5 sec, Site Class D resulted in the highest S_a. In addition, the maximum

acceleration response spectrum value (Sa_{max}) reported to be 9.89g around T = 0.25 sec

corresponding to Site Class C, compared with the input original bedrock earthquake

record with S_{amax} was 3.1g (i.e. the S_{amax} amplified by factor 3.2). To explain this

observation, it good to highlight that the acceleration response spectrum S_a depends on

the local site characteristics, such as soil stiffness and thickness, and the earthquake

intensity. Referring to Kramer (1996), the fundamental natural periods of vibration of

the soil deposit can be determined based on soil shear wave velocity and soil deposit

depth. Table 4.3 summarises the 1st and 2nd mode natural periods of the soil deposits with

adopted in this study. For Site Classes C, D and E, the 1st mode natural periods of the soil

deposit were determined to be T = 0.21 sec, 0.44 sec and 0.75 sec, respectively, and

therefore, referring to Figure 4.19, the period corresponding to the peak spectral

acceleration S_{amax} shifted to longer periods. The other observed local spikes in the

acceleration response spectrum particularly in shorter period ranges also corresponded to

the 2nd mode natural periods in the range of 0.07 – 0.25 sec for different site classes.

Indeed, the high reported S_{amax} values for Site Class C with V_s= 564 m/s S_{amax} were equal

to 9.89g, 6.8g, 5.36g and 2.6g for 1994 Northridge, 1995 Kobe, 1940 El Centro and 1979

Imperial Valley earthquakes, corresponding to amplification factor equal 3.2, 3.1, 8.6,

and 6.38, respectively. This observation was due to the fast that the dominant frequencies

of the earthquakes were closest to natural period of vibration of this soil deposit, resulting

in the largest amplification and possibly resonance. Indeed, other researchers (Tucker et al. 1984; Riepl et al. 1998) also report significant earthquake amplification in low period range as a result of seismic waves passing through stiff soil deposit, particularly for far field earthquake motion. Indeed, the effect of far field earthquakes loading (i.e. El Centro and Imperial Valley earthquakes) is also reported for Site Class D; where the S_{amax} amplification factor values were 1.1, 1.28, 4.53 and 4.92 for 1994 Northridge, 1995 Kobe, 1940 El Centro and 1979 Imperial Valley earthquakes, respectively. However, for soft Site Class E with Vs =160 m/s the amplification on the S_{amax} value observed for only the far field earthquakes; where the S_{amax} amplification factor values were 0.91, 0.5, 1.77 and 2.4 for 1994 Northridge, 1995 Kobe, 1940 El Centro and 1979 Imperial Valley earthquakes, respectively. Referring to Figure 4.19, despite some disparities in very low period range (i.e. T < 0.2 s), acceleration response spectra adopting NKH soil model in ABAQUS and SDHD soil model in FLAC 3D are in good agreement.
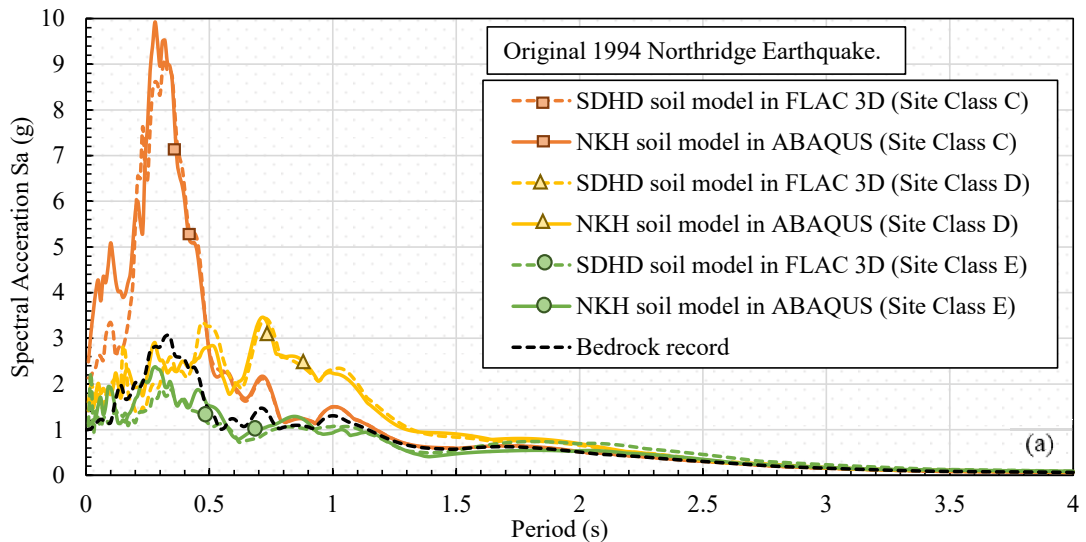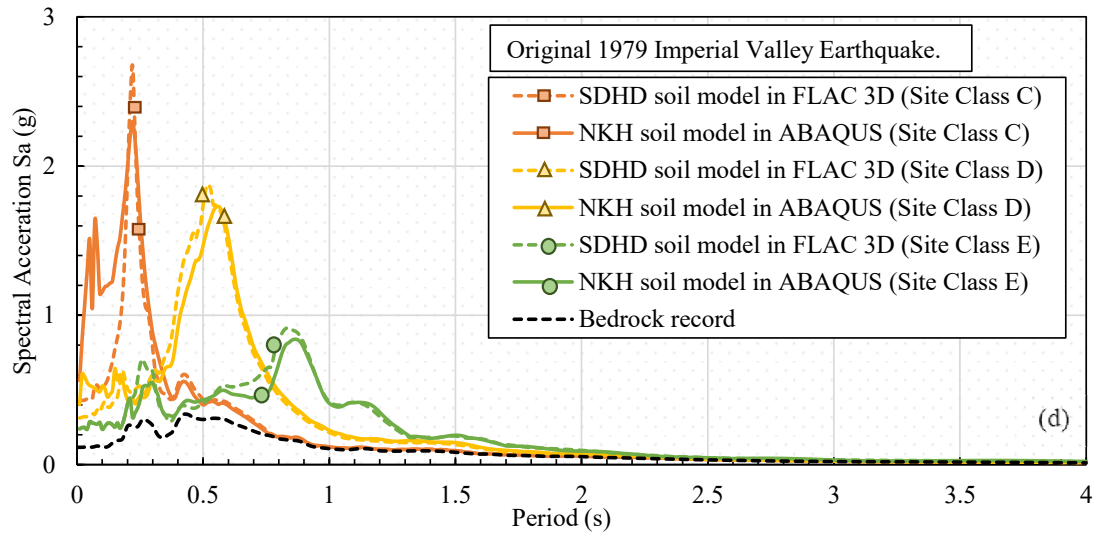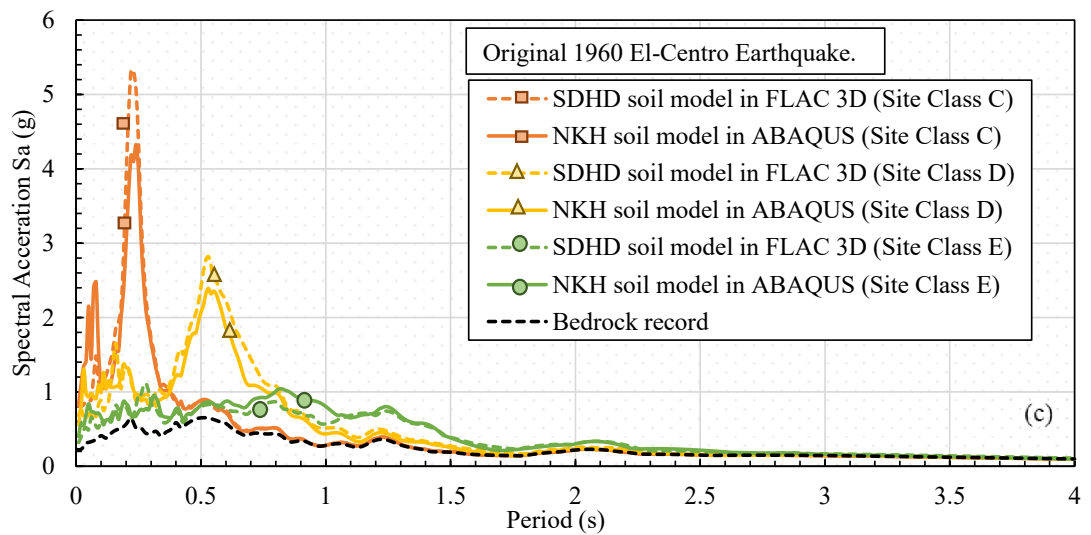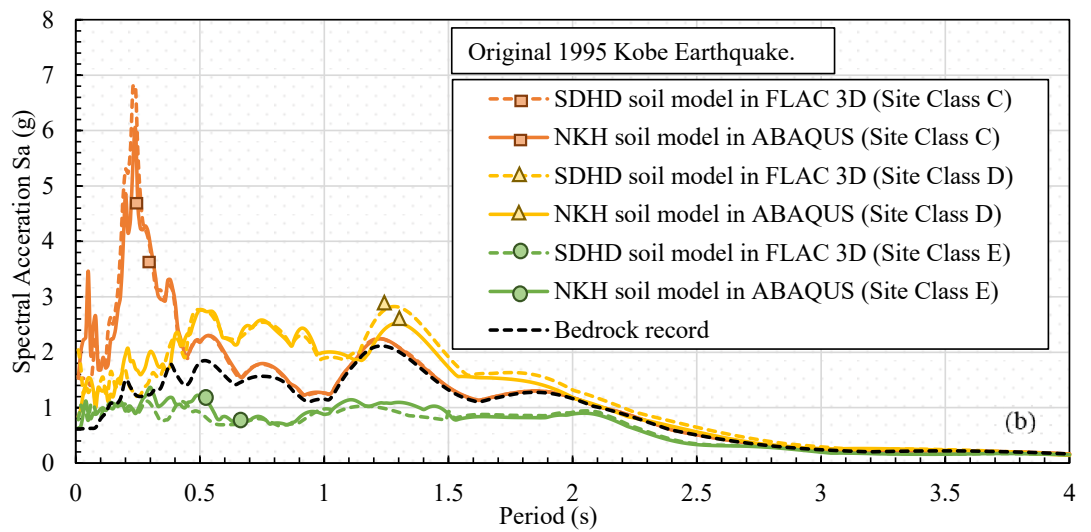
Figure 4.19 Comparison of acceleration response spectra for the recorded ground motions

on the soil surface of stiffness degradation with hysteresis damping and nonlinear kinematic hardening soil models for Site class C, D and E under (a) 1994 Northridge earthquake, (b)1995 Kobe earthquake, (c) 1940 El Centro earthquake, and (d) 1979 Imperial Valley earthquake.

4.5.4 Assessment of NKH model for different hazard levels

Figures 4.20 – 4.22 show the acceleration ground response spectra for Site Classes C, D, and E under three hazard levels by scaling 1994 Northridge, 1995 Kobe, 1940 El Centro and 1979 Imperial Valley earthquakes. The adopted three scaling levels reflect events of different annual exceedance probability (AEP) (i.e., 1/50, 1/500 and 1/2500), where these three target levels represented the common seismic demand levels in performance-based design framework, namely, Maximum Considered Earthquake (MCE), Design Level Earthquake (DLE), and Service Level Earthquake (SLE). Figure 4.20 reports the acceleration response spectrum S_a of Site Class C under three hazard levels for different earthquakes. In general, the maximum spectral accelerations were observed in the period range of 0.1 s to 0.3 s. Referring to Figure 4.20a for 1994 Northridge earthquake, it can be observed that for the SLE (AEP = 1/50), the maximum spectral acceleration S_{amax} amplified from 0.53g in the scaled earthquake rerecord (see Figure 4.20a and Figure 4.7) to 4.1g, corresponding to the amplification factor of 7.8, while for DLE and MCE the corresponding amplification factors were 5.5 and 4.4, respectively. As the S_{amax} amplified from 1.42g to 7.8g for DLS earthquake level and the corresponding values for MCE were 2.5g for the bedrock scaled earthquake level to 11g at ground surface level.   The Corresponding maximum spectral accelerations for 1995 Kobe earthquake passing through Site Class C (Figure 4.21b) were 9.8, 6.7 and 4.23, for SLE, DLE and MCE, respectively. For 1940 El Centro earthquake (Figure 4.20c) and 1979 Imperial Valley earthquake (Figure 4.20d), a higher S_{amax} amplification factors of

[10.8,7.7 and 5.4] and [11.2,6.64, and 4.5] were observed for seismic hazard levels [SLE, DLE and MCE] respectively. This observation highlighted the paramount importance of conducting site specific response analysis particularly for far field earthquakes propagating through stiff soil deposits (e.g. Site Class C with V_s =564 m/s).
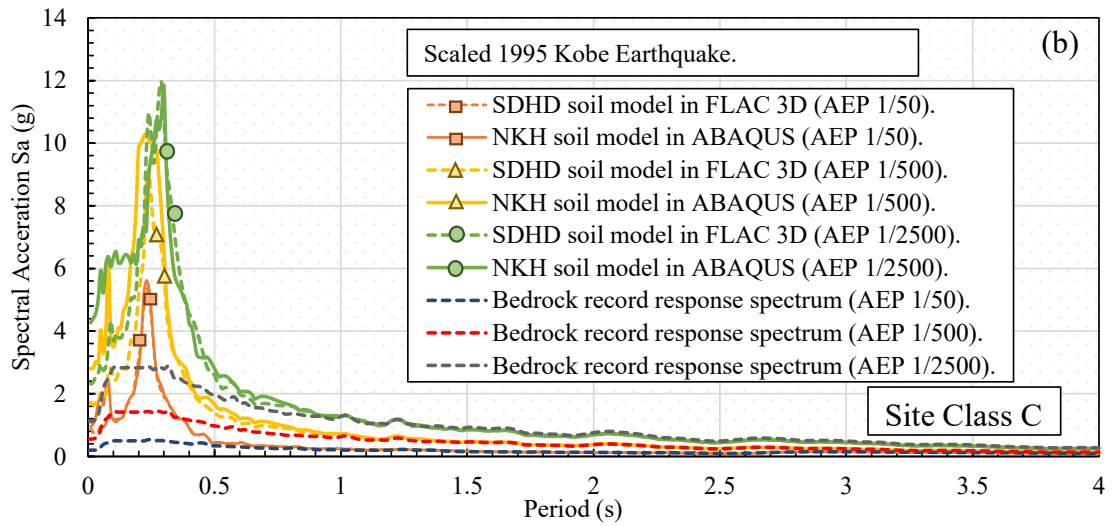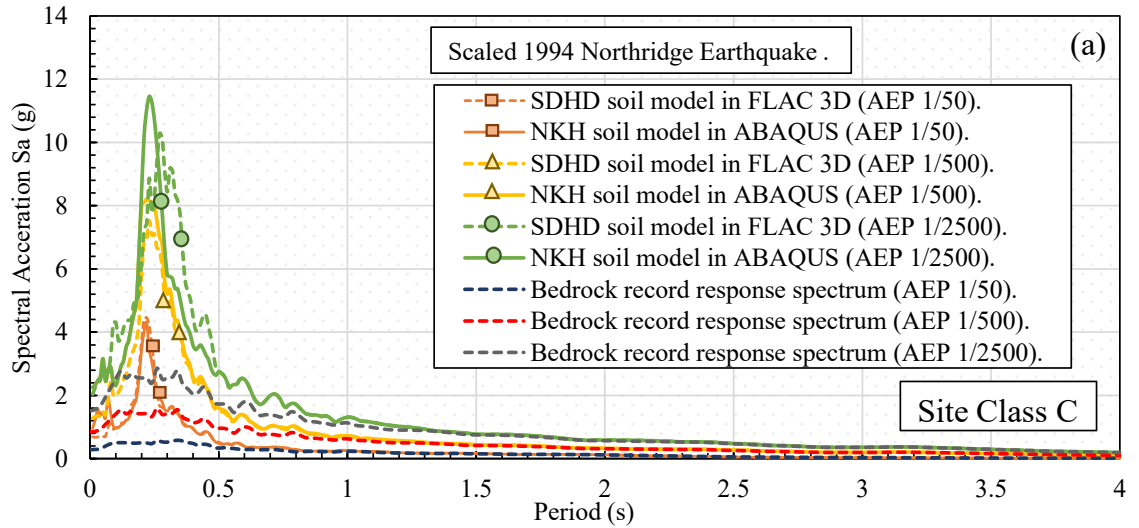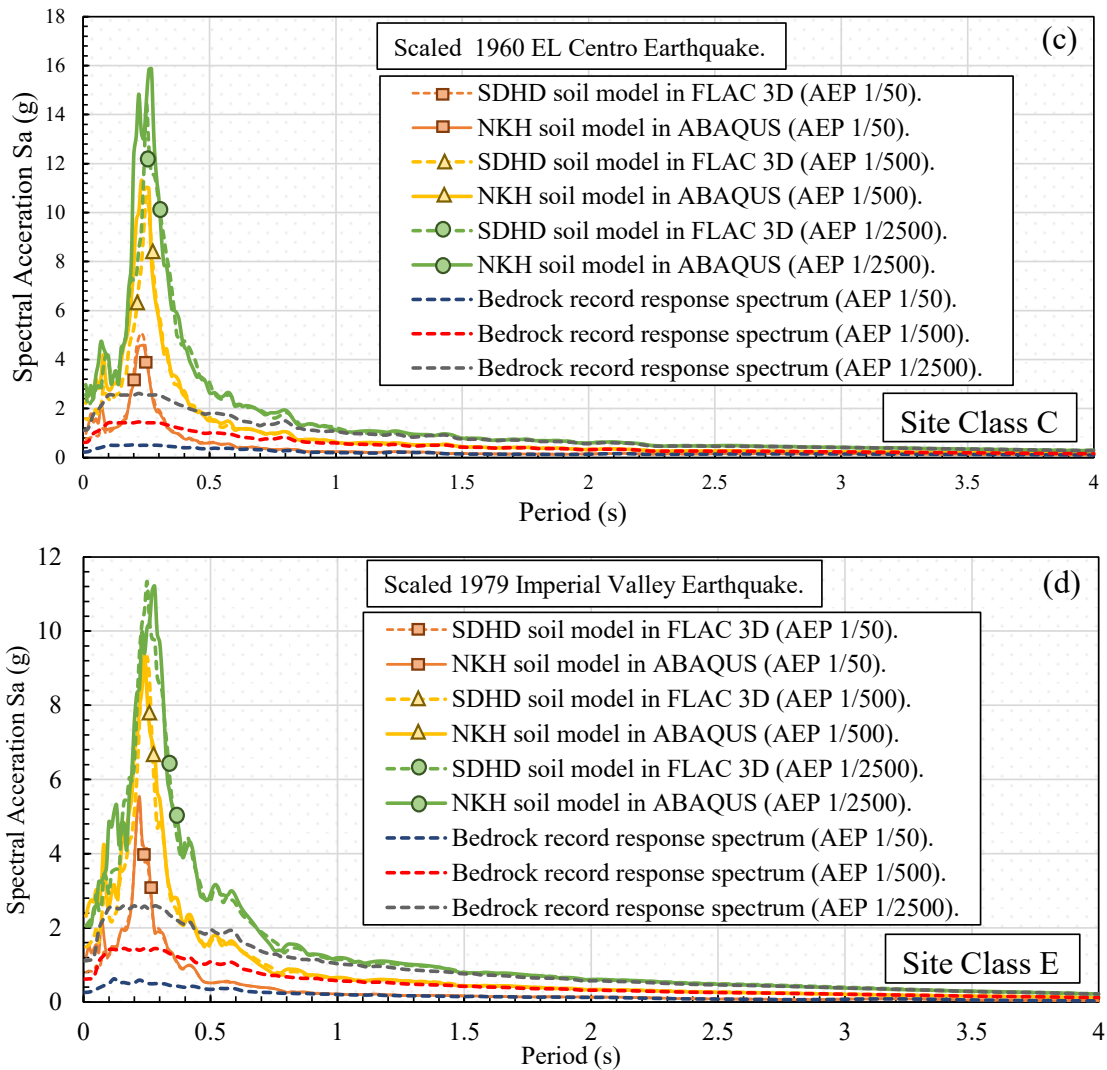
Figure 4.20 Comparison of acceleration response spectra for the three recorded ground motion levels on the soil surface of stiffness degradation with hysteresis damping and nonlinear kinematic hardening soil models for Site class C under (a) 1994 Northridge earthquake, (b)1995 Kobe earthquake, (c) 1940 El Centro earthquake, and (d) 1979 Imperial Valley earthquake.
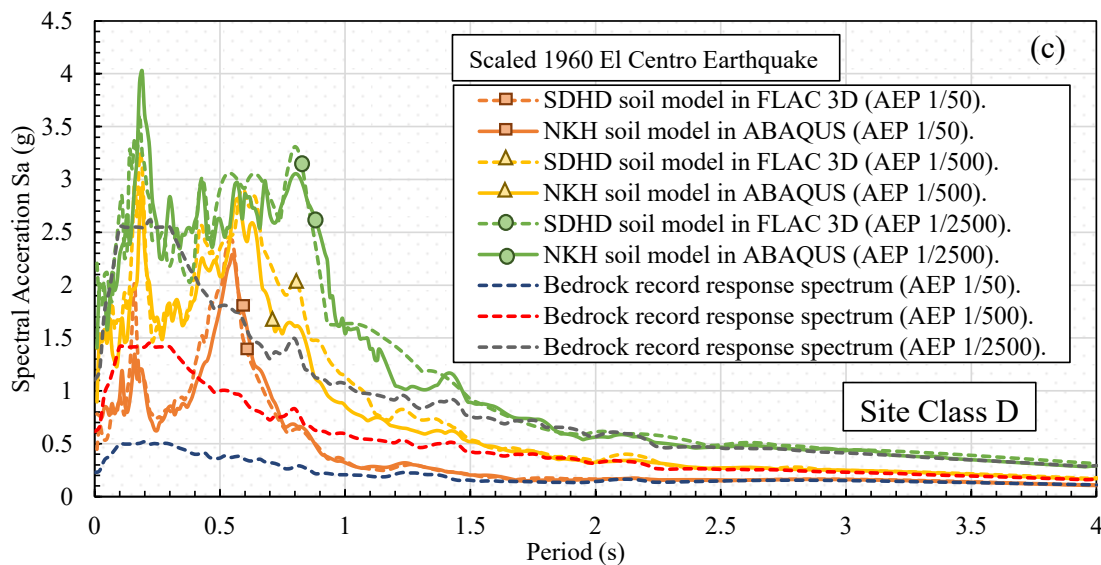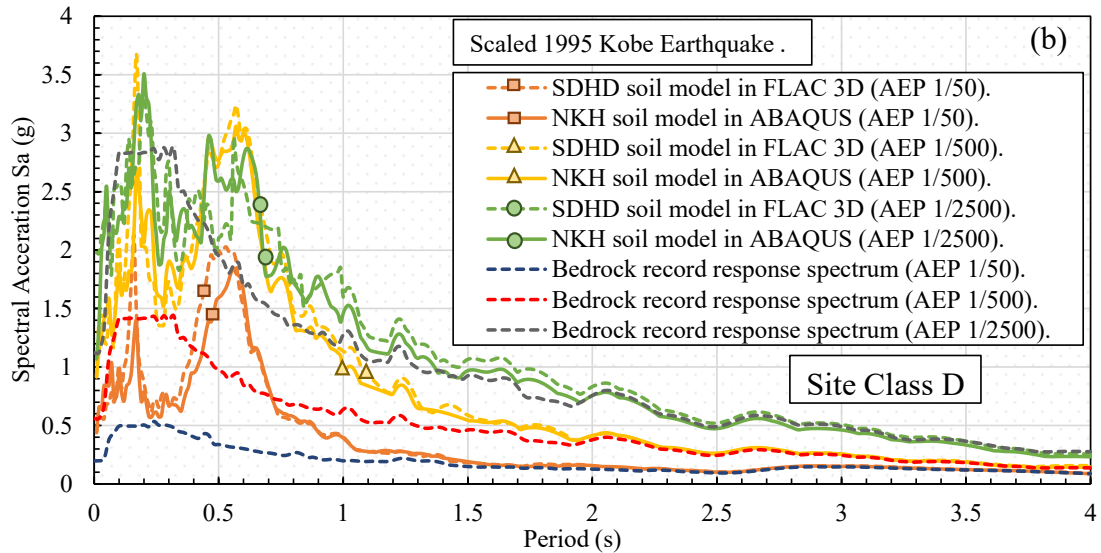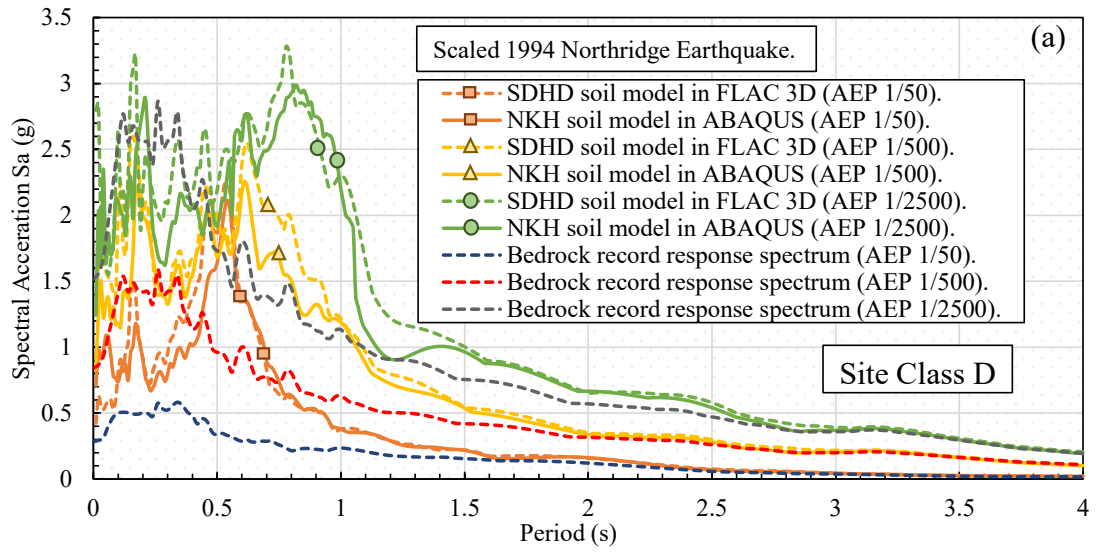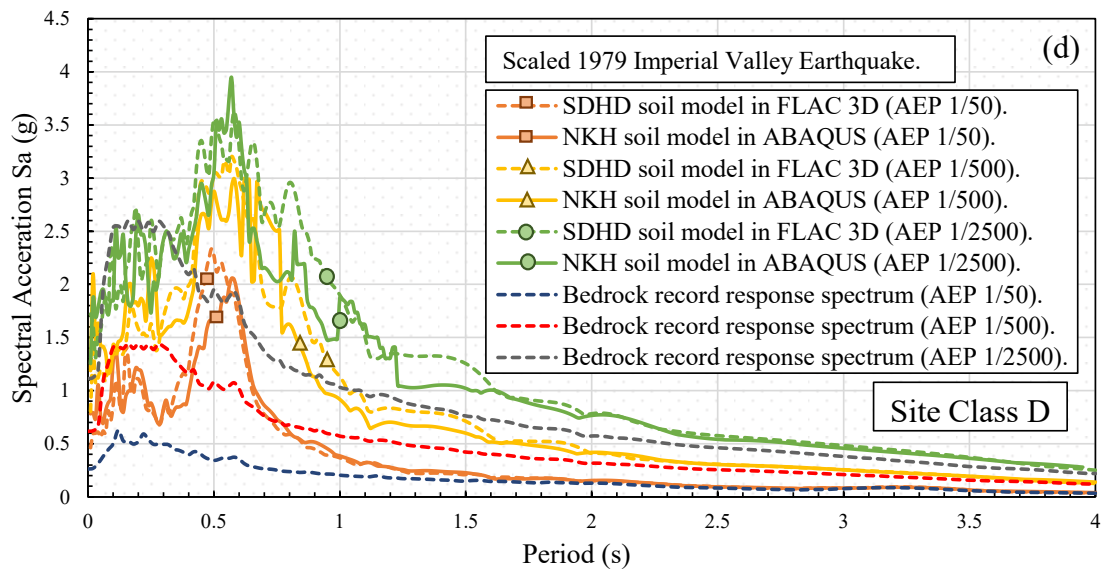
Figure 4.21 Comparison of acceleration response spectra for the three recorded ground motion levels on the soil surface of stiffness degradation with hysteresis damping and nonlinear kinematic hardening soil models for Site class D under (a) 1994 Northridge earthquake, (b)1995 Kobe earthquake, (c) 1940 El Centro earthquake, and (d) 1979 Imperial Valley earthquake.

Figure 4.21 presents the acceleration response spectrum results for Site Class D under different scaled earthquakes, and in general the maximum spectral accelerations were observed in the period T < 1.0 s. Referring to Figure 4.21, for the two near field earthquakes, propagating through Site Class D, namely, 1994 Northridge in Figure 4.21a, and 1995 Kobe earthquake in Figure 4.21b, the maximum amplification factors for SLE, DLE and MCE hazard were [4.03,1.97, and 1.24] and [3.7,2.0, and 1.25], respectively. The corresponding maximum amplification factors for the adopted far field earthquakes, namely, 1960 El Centro in Figure 4.21c, and 1979 Imperial Valley earthquake in Figure 4.21d, were 4.7 and 3.9 for SLE earthquake level, 2.4 and 2.35 for DLE earthquake level, and 1.5 and 1.53 for MCE earthquake level, respectively. Mostly, for Site Class D with V_s =270 m/s the amplification in Sa value reported in far field earthquakes were slightly higher than near field earthquakes, and for all earthquakes scaled levels the amplification observed along the most of period range.

Reducing the Site Class stiffness resulted in decreasing the *Sa* amplification, and even for some earthquakes period range no amplification was observed. For example, referring to Figure 4.22a for 1994 Northridge earthquake for Site Class E, the spectral acceleration S_a reduced in the low period range (i.e. T < 0.5 sec). For the near field earthquakes including 1994 Northridge and 1995 Kobe earthquakes (Figures 4.22a and 4.22b), S_{amax} amplification factors of [2.3, 1.5, and 0.96] and [1.96, 1.74, and 1] were observed for seismic hazard levels [SLE, DLE and MCE] respectively. Moreover, referring to Figures 22c and d, for two near field earthquakes namely 1940 El Centro and 1979 Imperial Valley earthquakes, propagating through Site Class E, the corresponding maximum amplification factors were 2.55 and 1.96 (SLE), 1.51 and 1.52 (DLE), and 1.15 and 1.07 (MCE). It can be perceived that, the amplification factors of S$_{amax}$ was increased when the soil stiffness decreased, particularly, for far field earthquakes and MCE level. as evidence Figure 4.22 summarises the seismic demand levels for Site Class E (i.e. softer Site Class with *Vs*= 160 m/s) under different scaled earthquakes.
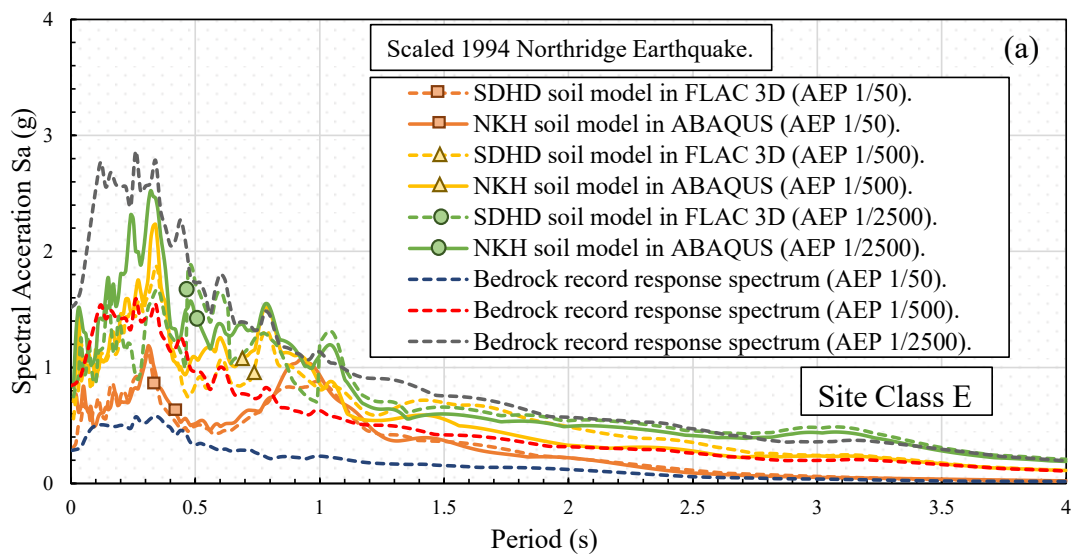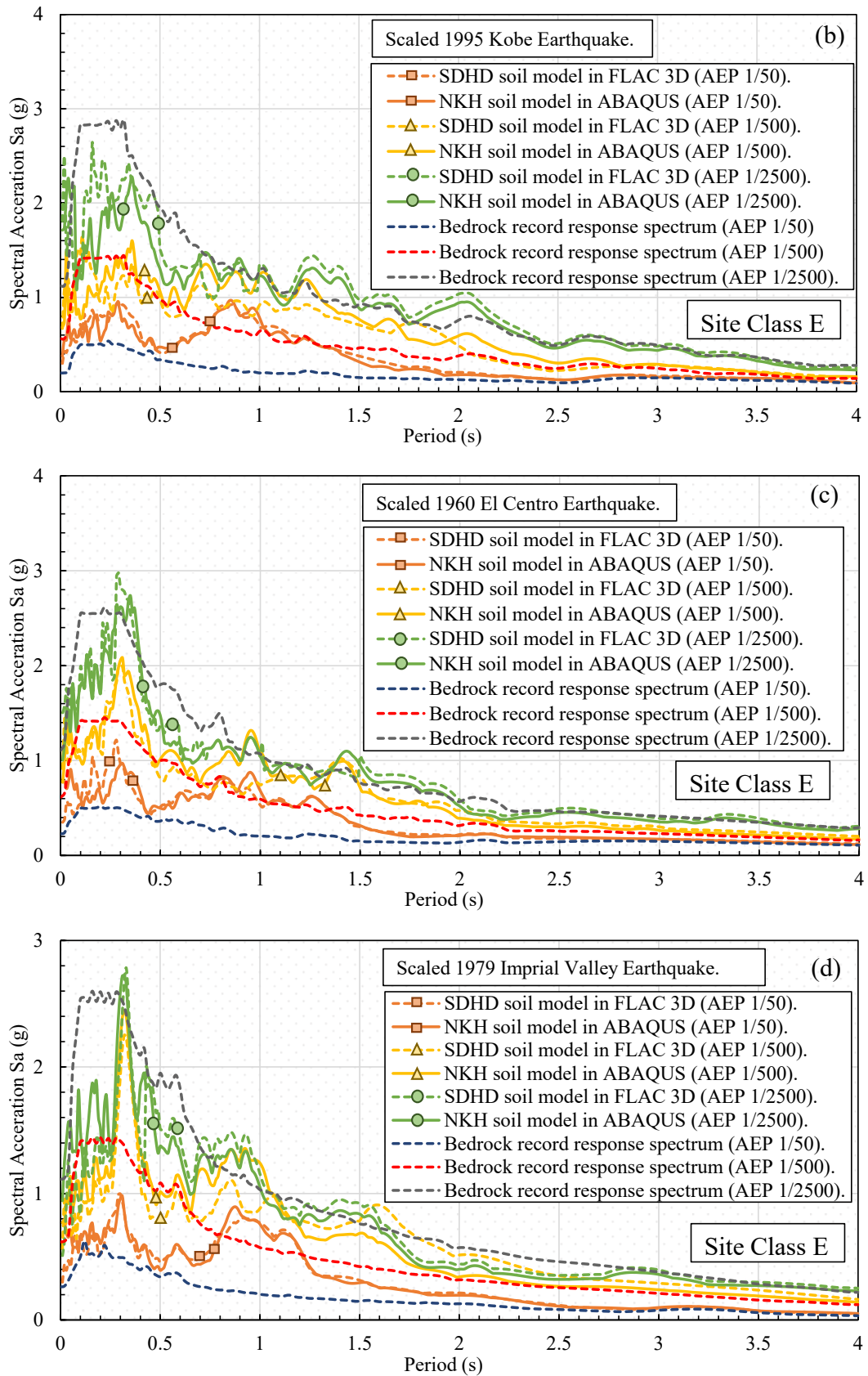
Figure 4.22 Comparison of acceleration response spectra for the three recorded ground motion levels on the soil surface of stiffness degradation with hysteresis damping and nonlinear kinematic hardening soil models for Site class E under (a) 1994 Northridge

earthquake, (b)1995 Kobe earthquake, (c) 1940 El Centro earthquake, and (d) 1979 Imperial Valley earthquake.

In general, results of acceleration response spectra for various earthquakes and scaled to different levels show that predictions from NKH soil model in ABAQUS and SDHD soil model in FLAC 3D are in good agreement.

4.6 Summary

The performance of the nonlinear kinematic hardening (NKH) soil model was assessed by comparing the predictions adopting the NKH model programmed in ABAQUS against the well-known stiffness degradation and hysteresis damping (SDHD) soil model available in FLAC 3D. The results demonstrated the NKH model capability in capturing the soil dynamic behaviour for the seismic wave propagation problems. Using a fully nonlinear time-domain analysis, both NKH and SDHD models showed that reducing soil stiffness (i.e. shear wave velocity) resulted in higher shear strains in the soil and increased hysteresis damping due to more seismic energy dissipation for all adopted earthquakes. For both adopted far-field earthquakes, numerical modelling results revealed horizontal earthquake amplification as the seismic wave propagated from the bedrock to the ground surface. Moreover, an extended duration of acceleration amplification for earthquakes with lower dominant frequencies (such as 1994 Northridge) were observed. Both NKH and SDHD soil models demonstrated that the dynamic properties of the soil deposit and the peculiarities of bedrock earthquake records had an impact on ground surface vibration. It is also important to note that both the NKH and SDHD numerical predictions highlighted the importance of hazard level on site-amplification factors. Thus, the earthquake scaling by matching the target response spectrum could alert earthquake characteristics and seismic site responses.

CHAPTER 5   SEISMIC RESILIENCE OF EXTRA-LARGE LNG TANK BUILT ON LIQUEFIABLE SOIL DEPOSIT CAPTURING SOIL-PILE-STRUCTURE INTERACTION

5.1   General

Assessment of seismic resilience of critical infrastructure such as liquefied natural gas (LNG) storage tanks, is critical to ensure availability and security of services during and after occurrence of large earthquakes. In many projects, it is preferred to build energy storage facilities in coastal areas for the ease of sea transportation, where weak soils such as soft clay and loose sand with liquefaction potential may be present. In this study, three-dimensional finite element model is implemented to examine the seismic response of a 160,000 m^3 full containment LNG tank supported by 289 reinforced concrete piles constructed on liquefiable soil overlaying the soft clay deposit. The seismic soil-structure interaction analysis was conducted through direct method in the time domain subjected to the 1999 Chi-Chi and the 1968 Hachinohe earthquakes, scaled to Safe Shutdown Earthquake (SSE) hazard level for design of LNG tanks. The analyses considered different thicknesses of the liquified soil deposit varying from zero (no liquefaction) to 15 m measured from the ground surface. The key design parameters inspected for the LNG tank include the acceleration profile for both inner and outer tanks, the axial, hoop and shear forces as well as the von Mises stresses in the inner tank wall containing the LNG, in addition to the pile response in terms of lateral displacements, shear forces and bending moments.

5.2   Introduction

Liquid storage tanks have traditionally played a major role in the distribution of water, chemicals and refined petroleum products. In particular, during the past 30 years, the demand on the Liquefied Natural Gas (LNG) tanks has increase significantly (Animah and Shafiee 2020). As the LNG is cleaner and a cheaper fuel for power generation than oil and coal, it is considered as a transition and rather environmentally friendly energy fossil fuel source. While large water storage reservoirs near cities and populated areas are in demand for a constant supply of water., oil and liquefied natural gas storage tanks are generally located in refineries, terminals and ports to reduce the transportation cost and stay away from populated areas for safety reasons (Solakivi et al. 2019).

Indeed, natural gas is primarily made of methane, and to reduce the storage space, it is liquefied and stored at atmospheric pressures while operating at temperatures around -166 C^{o}. LNG tanks are usually built in areas near the shorelines to increase the flexibility of LNG transportation and reduce the traveling and storage cost. These tanks have capacities ranging from 160,000 m^3 to 225,000 m^3 corresponding to diameters of 80 m to 100 m and heights from 30 m to 50 m (Nagashima et al. 2011; Calderón et al. 2016). Thus, the foundation soil may not be capable of bearing the load of such heavy structure, and usually deep foundations are used to support these tanks built on weak soils near ports. Pile foundations are commonly used to support these types of extra-large tanks to carry the entire load and control the settlement (Hor et al. 2017). Indeed, when utilising the pile foundation, the LNG tank load is transferred to the piles through rigid reinforced slab at the base of the tank, which acts as a load distribution mat.

The LNG industry is growing quickly and many LNG tanks are constructed in seismically active coastal regions; hence, potential damage or leak due to cracking

triggered by earthquake can result in the catastrophic environmental and safety threatening events (Zhang et al. 2011; Zhai et al. 2019). The LNG tanks should be designed wisely for safe and secure energy storage, and to meet the stringent requirements, the liquid inside the tank is usually contained within a steel container with high ductility material to ensure high performance subjected to low temperatures. Researchers have found that the inner container performance could be enhanced by using 9% nickel steel inner tank, surrounded by insulation materials (Chung et al. 2019). Moreover, for external protection and vapour containment, prestressed concrete outer tanks are usually used (Zhai et al. 2019). This type of tank, with inner steel tank and outer concrete tank with insulation material in between, is known as full containment tank, which is the most commonly used tank in practice to store LNG.

The seismic performance of LNG storage tanks is particularly significant, over and above the economic value of the structure, due to the need to remain operational after a major earthquake. (Di Sarno 2020). Any potential hazard associated with the failure of tanks containing highly flammable resources may lead to significant uncontrolled fires, whereas any potential spill of this content could cause significant damage to the environment and affect populated areas. (Zhang et al. 2018). Therefore, the need for quite advanced experimental, analytical and numerical investigations to assess the seismic response of such structures, is quite evident.

Under earthquake loading, the dynamic behaviour of LNG tank is quite complicated due to SFSI and FSI effects. Under dynamic loading, the LNG exerts additional hydrodynamic forces on to the tank walls. These hydrodynamic forces have two components; in the first component, portion of the liquid is accelerated with the tank walls and acts as added mass (or impulsive force), while in the second component, the upper portion of liquid sloshes generating surface waves (i.e. convective force), and the

characteristics of these waves are affected by ground displacement rather than ground acceleration (Christovasilis and Whittaker 2008). Many researchers studied the FSI effects on liquid storage tanks under dynamic loading (e.g. Housner 1957; Veletsos and Tang 1987; Haroun and Housner 1981; Malhotra et al. 2000) and proposed a simple mechanical model to capture the FSI, where the two hydrodynamic forces can be represented by concentrated forces attached to the tank wall with appropriate links. Indeed, the simplified analytical models are adopted in several well-established design codes such as API 650 (2007) and NZSSE (2009). Later, Virella et al. (2006) enhanced the simplified mechanical models to capture FSI by replacing the hydrodynamic concentrated forces with distributed forces along the tank wall as adopted in Eurocode (2008).

Evidently, the SSI could greatly alert the dynamic behaviour of the superstructures and their supporting foundation system, and indeed the contribution of SSI is significantly increased when the superstructure is constructed on soft soil deposits in seismically active areas (Gazetas and Mylonakis 1998; Stewart et al. 2000; Mylonakis and Gazetas 2000; Trifunac 2000; Carbonari et al. 2008; Padrón et al. 2009; Gičev and Trifunac 2012; Asimaki et al. 2019; Elwardany et al. 2019; Cavalieri et al. 2020; Brunelli et al. 2021). Medina et al. (2013) assessed the SSI effects on seismic characteristics of pile supported structures including period of vibration and damping implementing substructure analysis method. The results highlighted the importance of pile characteristics on the response of both high and short buildings. Zimmaro and Ausilio (2020) investigated the dynamic properties and seismic behaviour of earth fill dam foundations using modal and seismic hazard analyses, and showed that the substantial underestimation of the fundamental period of the dam could be observed when the SSI effects was ignored.

Similarly, since the SSI can significantly affect the seismic response of large

capacity structures like LNG tanks, several researchers investigate SSI effects on the seismic response of LNG tanks (Willford et al. 2010; Ruiz and Gutiérrez 2015; Tajirian et al. 2019). For example, Sun and Cui (2015) studied the seismic response of the base-isolated LNG tank considering the SSI effect using a simplified mechanical model and elastic soil foundation. Their results illustrated the importance of SSI on selecting the best isolation system. Son and Kim (2019) highlighted the importance of SSI effects on the seismic response of LNG tank subjected to vertical earthquake component. Moreover, Hokmabadi et al. (2019) considered the impact of SSI on the seismic response of a large LNG tank sitting on the improved ground, and highlighted the importance of conducting rigorous numerical modelling to optimise the seismic design of LNG tanks.

One of the furthermost causes of damage to structures under seismic shaking is the liquefaction of saturated sand. Loose sand tends to bond under the cyclic loading imposed by earthquake shaking, that can cause increase in excess pore water pressure if the soil is saturated and unable to drain during earthquake. This results in reduction in soil effective stress and consequently substantial loss of soil strength and stiffness (Booth and Fenwick 1994; Bhattacharya and Madabhushi 2008). Several infrastructures and buildings suffered severe damages from soil liquefaction in the past earthquakes such as the 1964 Niigata, the 1971 San Fernando, the 1989 Loma Prieta and the 1995 Kobe earthquakes (Abdoun and Dobry 2002; Brandenberg et al. 2018; Jiménez et al. 2019; Zimmaro et al. 2020).

The liquefaction hazard should be evaluated in the seismic design of the projects. This includes undertaking liquefaction assessment to identify layers with liquefaction potential under the design earthquakes. The consequences of onset of potential liquefaction should be assessed and addressed in the design. From authors design experience, ground improvement techniques (e.g. deep cement mixing, jet grouting, stone

columns) or pile foundations are common solutions to mitigate the liquefaction hazard in the design of large LNG tanks. While ground improvement techniques are considered to be more economical in many cases, their application depends on site ground conditions, extent of the liquefiable hazard, and project specific requirements. On the other hand, pile foundations offer a robust solution for the design of large LNG tanks and have been adopted in many projects.

The seismic response of large LNG tanks founded on potentially liquefiable soil needs a precise consideration of soil-pile-structure interaction. This is not only required for the design of pile elements, but the impact of soil liquefaction on the overall response of the LNG tanks is crucial and should be well understood. Many studies had highlighted the potential failure of pile foundation in liquefiable soils due to buckling instability, bending, shear or settlement failures of piles during earthquakes (e.g. Tokimatsu et al. 1996; Dash et al. 2009; Haldar and Babu 2010; Zhuang et al. 2015). However, there is very limited research available in the literature on the response of LNG tanks founded on pile foundation in potentially liquefiable soil deposits. Thus, in this study, the effect of the depth of liquefied soil deposit on the seismic response of LNG tank supported by pile foundation will be examined using three-dimensional finite element analysis. Results of this study can be used to assess the seismic efficiency of end-bearing pile foundation to support extra-large LNG tanks on liquefiable soils without ground improvement.

5.3 Overview of adopted LNG tank and soil profile

In this study, a 160,000 m^3 full containment LNG tank is used to perform the seismic analysis. The adopted LNG tank is an example of extra-large tank constructed in highly to moderately seismic regions. This tank consists of an open top 9% Ni steel inner tank and an outer reinforced concrete (RC) tank with fixed roof, sitting on end-bearing

pile raft foundation system. Figure 5.1 shows the overview of the structural and geometrical features of the adopted LNG tank. The total height of the outer RC tank is 51.20 m, the outer tank wall is 42.27 m high, the inner tank wall is 40.0 m high and the LNG design level in the inner tank is 36.0 m. The inner 9% Ni steel tank wall thickness is varying from 40.0 mm (bottom) to 10.0 mm (top), and the outer tank wall thickness is 800 mm. Figure 5.1b illustrates the layout of 289 reinforce concrete piles, while Figure 5.1c shows the details of the piles supporting the raft foundation (i.e. tank slab).

Figure 5.2 shows the adopted soil profiles in this study to assess the impacts of depth of liquefiable soil on the seismic response of the LNG tanks. Figure 5.2a shows the adopted benchmark scenario in which the LNG tank sitting on soft clay soil deposit (non-liquefiable) with the average shear wave velocity $V_s = 225$ m/s for the top 15.0 m of soil deposit, and $V_s = 270$ m/s from 15.0 m to 30.0 m depth. This benchmark subsoil profile (Scenario I) is classified as site Class C (Soft Soil Site) according to AS/NZS1170.4 (2004). It should be note that it is assumed that the soil deposit is underlain by Sandstone rock with shear wave velocity in excess of 760 m/s and the unconfined compressive strength greater than 50 MPa. To assess impacts of presence of liquefiable soil deposit on the seismic response of LNG tank system, three other scenarios with different depths of liquefiable soil are considered as in Figure 5.2, namely Scenario II (5 m deep liquefied soil), Scenario III (10 m deep liquefied soil) and Scenario IV (15 m liquefied soil). Further details about adopted properties of the liquefied soil deposits are provided in the next section.

Outer Reinforced concrete tank diameter 80.0 m

Inner steel tank diameter 78.0 m

Reinforced concrete roof thickness 0.45 m

Inner tank wall thickness (10 mm top to 40 mm bottom)

Outer tank 51.0 m

Inner tank wall 40.0 m

LNG level 36.0 m

160,000 m³ LNG

Outer tank wall thickness 0.8 m

Reinforced concrete slab thickness 1.5 m

Pile length 30.0 m

289 Reinforced concrete Pile ϕ1.20 m

4.50 m

(a)

143
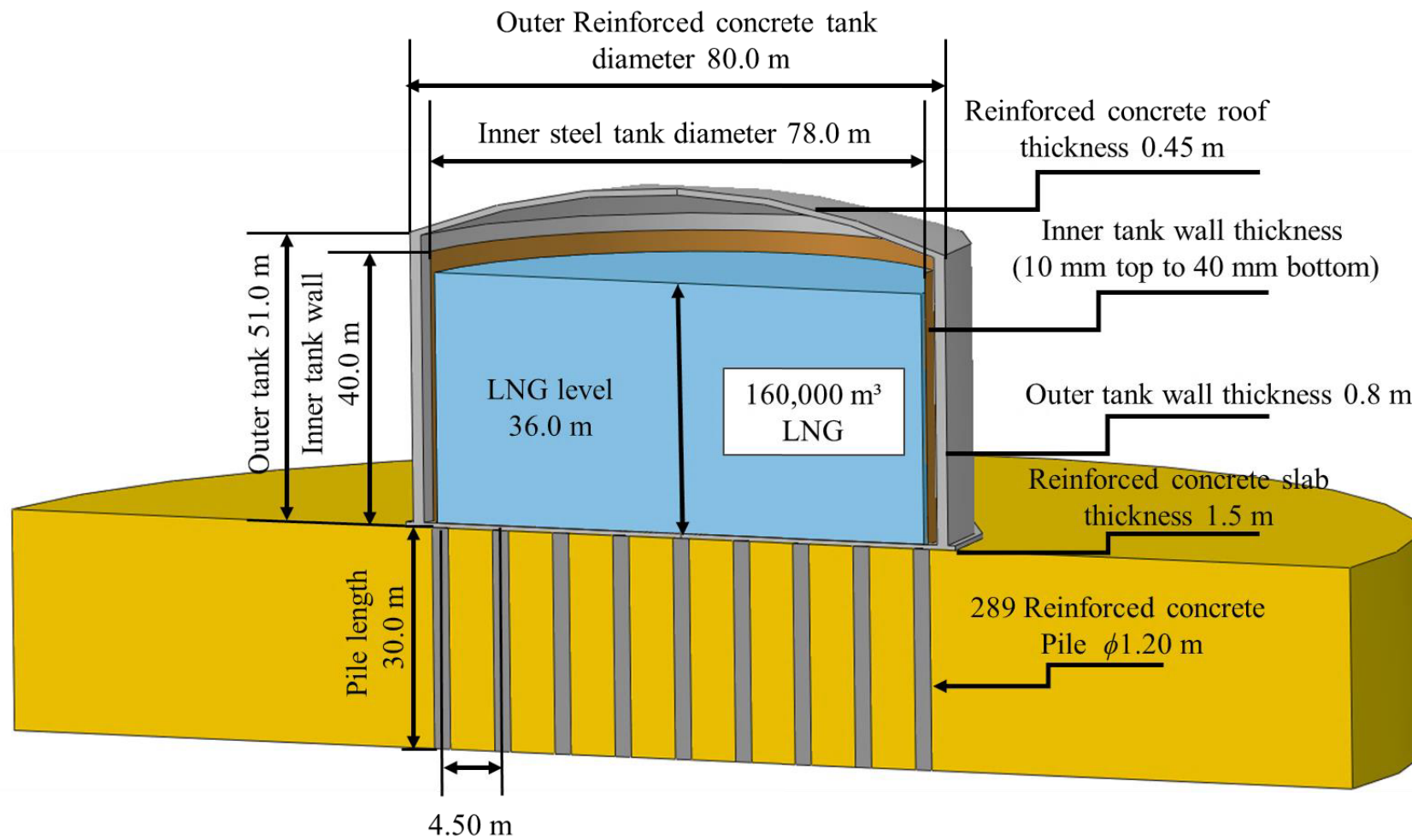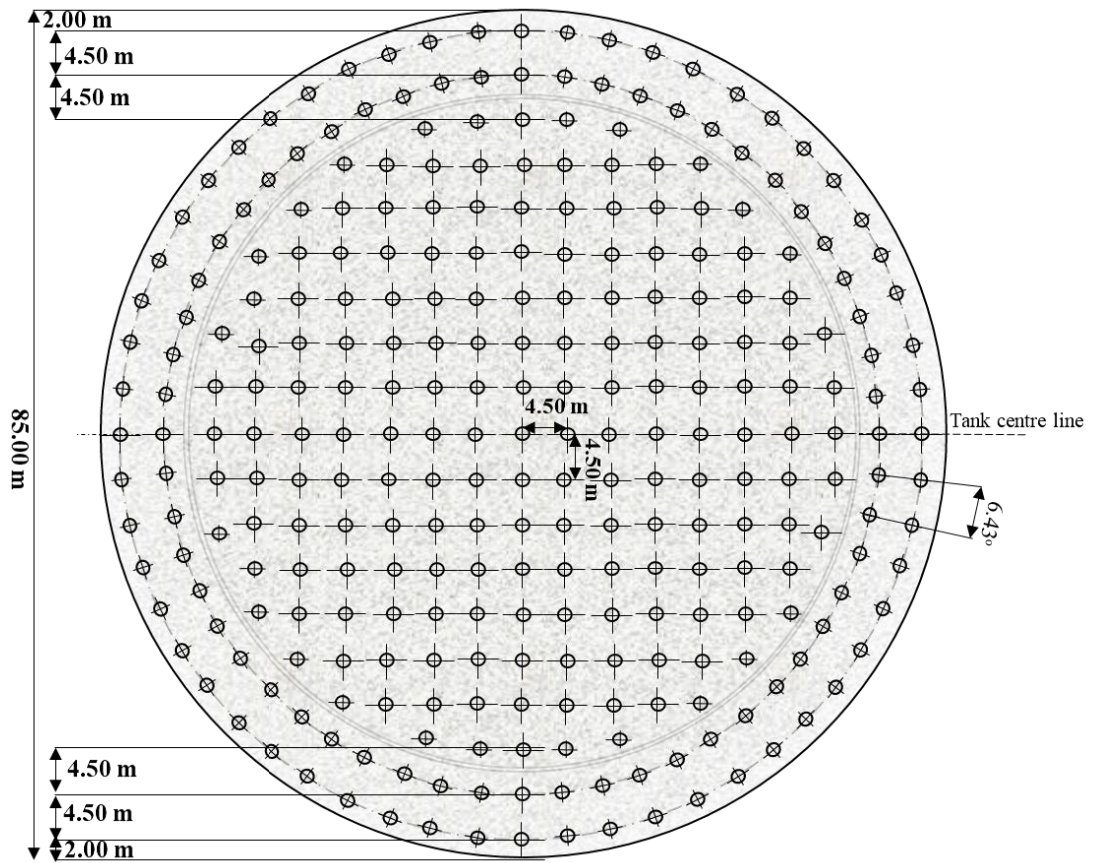
(b)
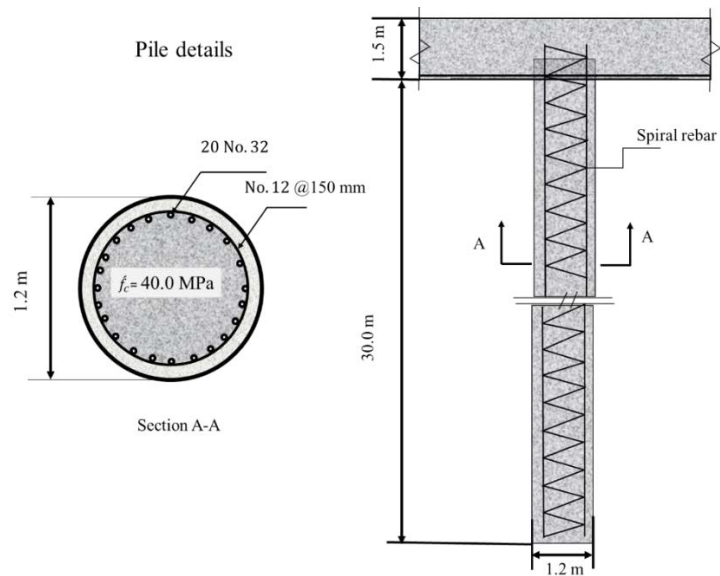
(c)

Figure 5.1 The LNG tank adopted in this study (a) LNG tank configuration including the superstructure and foundation details; (b) the plan view of the arrangement 289 piles supporting the LNG tank and (c) end bearing pile details.

(a) Soil layers properties for Scenario I

Shear wave velocity (m/s)

Soil depth (m)

Soft clay layer 1
ρ_{clay}=1650 kg/m³

Soft clay layer 2
ρ_{clay}=1950 kg/m³

(b) Soil layers properties for Scenario II

Shear wave velocity (m/s)

Soil depth (m)

Liquefied layer 1
ρ_{liq}=1650 kg/m³

Soft clay layer 1
ρ_{clay}=1650 kg/m³

Soft clay layer 2
ρ_{clay}=1950 kg/m³

(c) Soil layers properties for Scenario III

Shear wave velocity (m/s)

Soil depth (m)

Liquefied layer 1
ρ_{liq}=1650 kg/m³

Liquefied layer 2
ρ_{liq}=1650 kg/m³

Soft clay layer 1
ρ_{clay}=1650 kg/m³

Soft clay layer 2
ρ_{clay}=1950 kg/m³

(d) Soil layers properties for Scenario IV

Shear wave velocity (m/s)

Soil depth (m)

Liquefied layer 1
ρ_{liq}=1650 kg/m³

Liquefied layer 2
ρ_{liq}=1650 kg/m³

Liquefied layer 3
ρ_{liq}=1650 kg/m³

Soft clay layer 1
ρ_{clay}=1950 kg/m³

Figure 5.2 Soil profile scenarios used in the study (a) Scenario I (benchmark case - non-liquefied soil); (b) Scenario II with 5.0 m deep liquefied soil; (c) Scenario III with 10.0 m deep liquefied soil and (d) Scenario IV with 15.0 deep liquefied soil.

145

5.4   Details of numerical modelling

In this study, the three dimensional finite element analysis was conducted using ABAQUS (2018) software, where the superstructure, pile foundation and the soil were simulated using fully nonlinear direct method (Kramer 1996), where the LNG tank, foundation and the soil were treated with the same rigour. Taking the advantage of the fact that the problem is symmetric about the line of symmetry parallel to the direction of the applied earthquake, only half of the model was simulated in this study as shown in Figure 5.3.

5.4.1   Modelling of the inner and outer tanks and pile foundation

The inner 9% Ni steel and outer reinforced (RC) concrete tanks were modelled using S4R shell elements. Additionally, the steel reinforcements in the RC tank wall, roof and slab were modelled as uniaxial reinforcement layers embedded in the shell element, similar to the technique used by other researchers to simulate axial and circumferential steel rebars (e.g. Nateghi and Yakhchalian 2011; Hafez 2012; Zhai et al. 2018).

5.4.1.1   *Modelling of Outer Reinforced Concrete Tank*

The concrete damage plasticity (CDP) model was implemented in this study to model the outer concrete containment of LNG tank under the seismic loading. As explained by several researchers (Zhai et al. 2018; Hafez 2012; Dulinska and Jasinska 2014), this model is suitable to capture the concrete behaviour under dynamic loading particularly for thin wall structures such as concrete tanks and pipes. Indeed, this model adopts plasticity-based damage for the concrete, assuming two failure mechanisms, namely the tensile cracking and compressive crushing to represent the inelastic behaviour of concrete. The development of yield surfaces was controlled by two hardening variables,

namely the tensile plastic strain ($\bar{\varepsilon}_t^{pl}$), and the compressive plastic strain ($\bar{\varepsilon}_c^{pl}$). where f_{b0} and f_{c0} are the biaxial and uniaxial compressive yield strengths, respectively. Moreover, $\bar{\sigma}_c$ and $\bar{\sigma}_t$ are the effective compressive and tensile stresses respectively (i.e. the stresses determined based on undamaged elastic stiffness). K_c is the ratio of the second stress invariants on tensile and compressive meridians, which explains the shape of the yield surface. Since the CDP model adopts non-associated flow rule the yield surface differs from the "potential plastic flow", which utilises the Drucker-Prager hyperbolic function to formulate the flow potential function Q as follows:

$$Q = \sqrt{(\epsilon \, \sigma_{t0} \tan \psi \,)^2 + \bar{q}^2} - \bar{p} \tan \psi \tag{5.1}$$

where, σ_{t0} is the tensile stress at failure (i.e. tensile strength), ϵ is the eccentricity of plastic potential surface, and ψ is the dilation angle measured in $\bar{q} - \bar{p}$ space.

The degradation of concrete strength and stiffness in this adopted CDP model is captured via tension and compression damage parameters (d_t and d_c), where these model parameters refer to the weakened concrete characteristics during unloading response as a result of cracking and crushing impacting the initial elastic stiffness (i.e. E_0). Indeed, the damage of the concrete under the tensile and the compressive stresses is characterized by damage plasticity theory developed by Lubliner et al. (1989) and Lee and Dale (1998), so the adopted stress-strain relation under uniaxial tension and compression loading can be presented as follows:

$$\sigma_t = (1 - d_t)E_0 \, (\varepsilon_t - \bar{\varepsilon}_t^{pl}) \tag{5.2}$$

$$\sigma_c = (1 - d_c)E_0 \, (\varepsilon_c - \bar{\varepsilon}_c^{pl}) \tag{5.3}$$
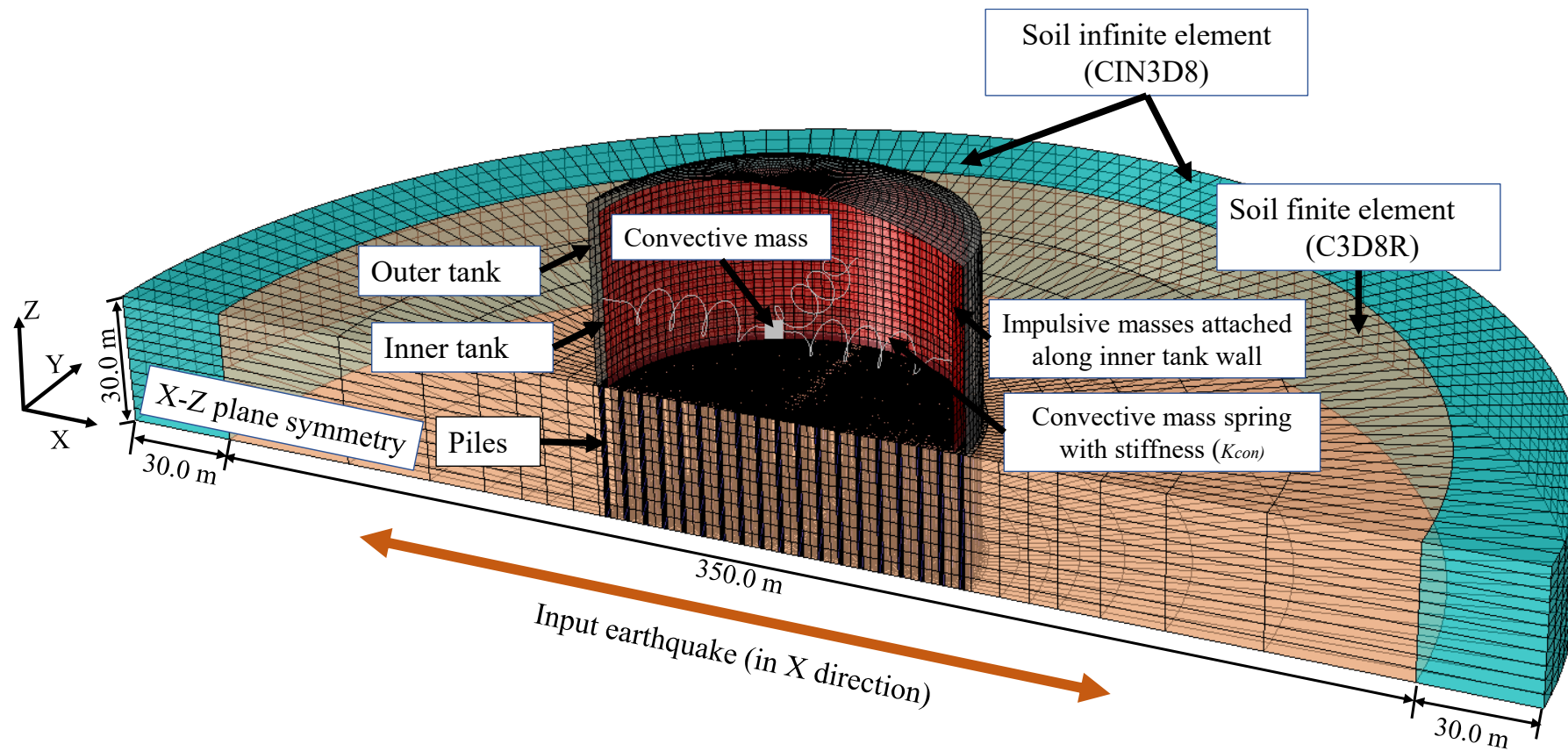
Figure 5.3 The adopted finite element model used in this study for homogenous clay soil case and the modelling element details of the developed soil structure system.

where, the subscripts t and c refer to tension and compression, respectively, and E_0 refers to the initial stiffness of the concrete under compression and tension before any yielding occurs. The damage or degradation parameters (i.e. d_t and d_c) impacting the concrete stiffness can take a value from zero, where there is no loss in stiffness, to one, which represents the total damage state of the concrete.

Similar to many previous studies (e.g. Miglietta et al. 2016; Murray et al. 2018), the impacts that reinforcing bars would have on the concrete behaviour were modelled by introducing tension stiffening into the tension softening section of concrete damage plasticity model to simulate the load transfer across cracks through the rebar. As Wahalathantri et al. (2011) explained, by introducing tension stiffness, strain softening behaviour of the cracked concrete would be revised. The key parameter required to formulate the tension stiffening is the cracking strain $\bar{\varepsilon}_t^{cr}$, which is calculated by subtracting the elastic strain corresponding to the undamaged material from the total strain (ε_t).

$$\bar{\varepsilon}_t^{cr} = \varepsilon_t - \frac{\sigma_t}{E_0} \tag{5.4}$$

As discussed by Wahalathantri et al. (2011) and reported in ABAQUS (2018), the cracking strain ($\bar{\varepsilon}_t^{cr}$) and plastic strain ($\bar{\varepsilon}_t^{pl}$) are correlated as:

$$\bar{\varepsilon}_t^{pl} = \bar{\varepsilon}_t^{cr} - \frac{d_t}{(1-d_t)}\frac{\sigma_t}{E_0} \tag{5.5}$$

Nayal and Rasheed (2006) reviewed different tension stiffening models, then developed a model based on the stress-strain relation established by Gilbert and Warner (1978), that considersthe tension stiffening, softening and local bond slip effects. This model captures the primary and secondary cracking phenomena on the stress - strain graph. Wahalathantri et al. (2011) modified the model to be consistent with the general formulations on CDP model available in ABAQUS. Figure 5.4 represents the modified tension stiffening model

implemented in this study. Indeed, the stress-strain relation is linear till reaching the tensile strength σ_{t0} (MPa), where it can be determined according to ACI 318-08 (2014) as below:

$$\sigma_{t0} = 0.62\sqrt{f'_c} \tag{5.6}$$

where f'_c is the concrete compressive strength in (MPa). The axial strain corresponding to peak tensile strength σ_{t0} is called critical tensile strain ε_{cr}. Then there is a rather abrupt drop in the state of stress to point $(1.25\varepsilon_{cr}, 0.77\sigma_{t0})$. The primary cracking stage ends at $(4\varepsilon_{cr}, 0.45\sigma_{t0})$, while the secondary cracking stage stopes at $(8.7\varepsilon_{cr}, 0.10\sigma_{t0})$ as shown in Figure 5.4a.

(a)

(b)
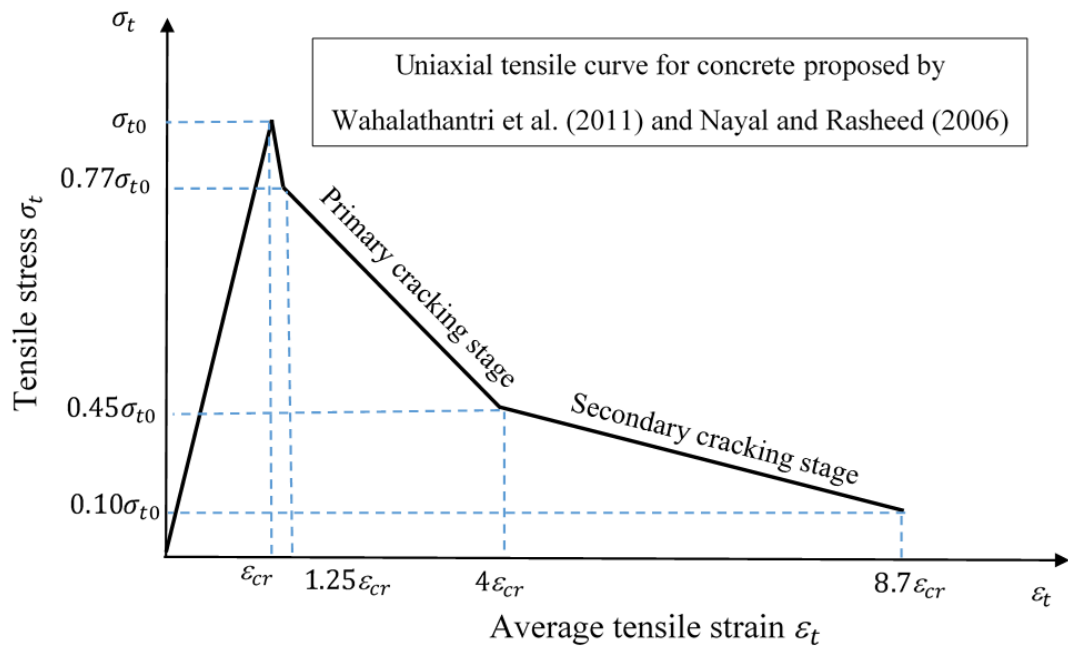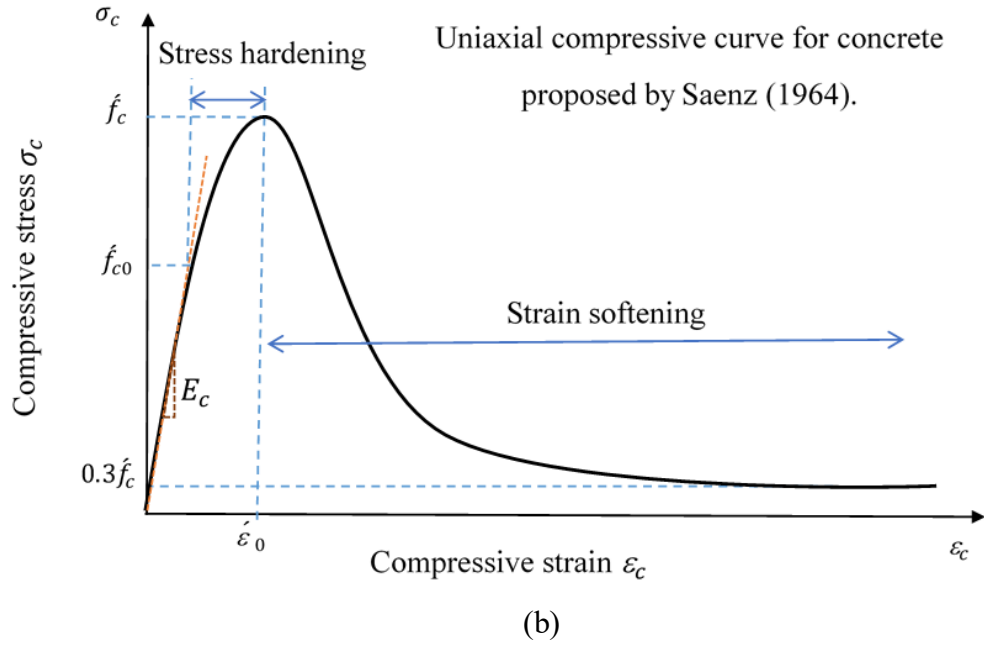
Figure 5.4 Concrete damage plasticity models used in this study (a) modified tension stiffening model and (b) uniaxial compressive stress- strain curve for concrete.

However, to capture the compressive stress-strain curve of the concrete following the initial elastic response, the compressive stress data are input in terms of the inelastic crushing strain $\bar{\varepsilon}_c^{in}$ which is defined as:

$$\bar{\varepsilon}_c^{in} = \varepsilon_c - \frac{\sigma_c}{E_0} \tag{5.7}$$

while the plastic strains $\bar{\varepsilon}_c^{pl}$ required for evolution of the yield surface were calculated based on the recommendation by Genikomsou and Polak (2015) as follows:

$$\bar{\varepsilon}_c^{pl} = \bar{\varepsilon}_c^{in} - \frac{d_c}{(1-d_c)} \frac{\sigma_c}{E_0} \tag{5.8}$$

To define the compressive stress - strain curve of concrete to be used for the calibration of the CDP model parameters, data and approach provided by Saenz (1964), shown in Figure 5.4b, were utilised in this study. It should be noted that many other researchers (e.g. Asran et al. 2016; Tahnat et al. 2018; and Sakr et al. 2019) had validated and utilised the compressive stress - strain relationship developed by Saenz (1964) for various grades of concrete..

151

For the concrete *C45* grade (i.e. f'_c = 45 MPa) adopted in this study for the outer RC containment, the modulus of elasticity of concrete (MPa) was determined based on ACI 318-08 (2014) as $E_c = 0.043 * \rho_c^{1.5}\sqrt{f'_c}$, where ρ_c is concrete density (kg/m³) taken as 2500 kg/m³ in this study. The basic parameters of grade *C45* concrete corresponding to the calibrated CDP model are summarised in Table 5.1. In addition to these parameters, variations of the compressive yield stress and the stiffness degradation with inelastic strains (i.e. $\sigma_c - \bar{\varepsilon}_c^{in}$ and $d_c - \bar{\varepsilon}_c^{in}$), as well as variations of the tensile yield stresses and the stiffness degradation with cracking strains (i.e. $\sigma_t - \bar{\varepsilon}_t^{cr}$ and $d_t - \bar{\varepsilon}_t^{cr}$), illustrated in Figure 5.5, were adopted as the input parameters in this study. Indeed, Figure 5.5 shows the comparison of the typical *C45* concrete response obtained from Saenz (1964) and Wahalathantri et al. (2011) for compression and tension, respectively and calibrated CDP model predictions adopting model parameters reported in Table 5.1. A reasonable agreement is observed, which is confirming the suitability of adopted concrete model parameters in this study.
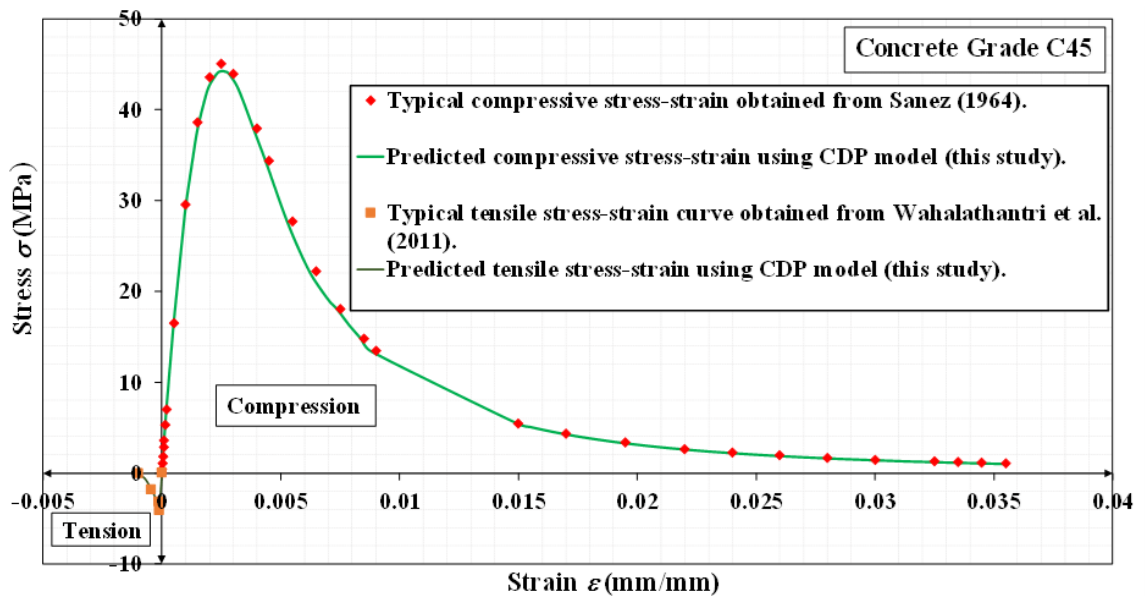
Figure 5.5 Calibration of the CDP model parameters used in this study.

Table 5.1 Parameters used in this study to simulate the *C45* concrete adopting CDP model.

Property	Symbol	Value	Reference
Density (kg/m^3)	ρ_c	2500	Ruiz and Gutiérrez (2015)
Poisson's Ratio	ν	0.2	Ruiz and Gutiérrez (2015)
Modulus of Elasticity (GPa)	E_c	36.057	ACI 318 (2014)
Dilation angle	ψ	36°	Kmiecik and Kamiński (2011)
Eccentricity	ϵ	0.1	Vermeer and De Borst (1984)
Ratio of biaxial to uniaxial compressive yield strengths	f_{b0}/f_{c0}	1.16	Kupfer et al. (1969)
Ratio of the tensile to the compressive meridian	K_c	0.667	Oller (2014)

The steel reinforcement bars in the outer concrete tank were Grade 60 (f_y =420 MPa) referring to ASTM A615 (2018), and were embedded in concrete in both vertical and circumferential directions with reinforcement content ratio 1% in both directions. The rebars were modelled as an equivalent smeared layer with a constant thickness determined based on the rebar size and spacing, while adopting rebar layered shell option available in ABAQUS, particularly customised for reinforced concrete simulation as mention earlier. In this study, it is assumed that the rebar layers were completely bonded to the concrete and the linear kinematic model explained earlier was used to model the steel reinforcement bars, with adopted model parameters summarised in Table 5.2. It should be noted that the outer reinforced concrete tank has a fixed reinforced concrete roof, and in this study the roof material is assumed to be same as the tank wall with same reinforcement ratios.

Table 5.2 Reinforcing bar parameters adopted in this study to simulate steel Grade 60.

Parameter	Symbol	Value	Reference
Tensile strength (MPa)	f_{ult}	620	
Tensile yield stress (MPa)	f_y	420	ASTM A615 /
Elongation (%)	δ	9	A615M-18e1
Linear kinematic hardening modulus (MPa)	C_r	2222	(2018);
Young's Modulus (GPa)	E_r	206.56	
Density (kg/m³)	ρ_r	7850	Hawileh et al.
Poisson's Ratio	v	0.3	(2009)

5.4.1.2 *Modelling of Reinforced Concrete Piles*

For the simulation of concrete piles, concrete grade *C40* ($f'_c = 40$ MPa) was used in this study. The hybrid modelling procedure was used to capture the elastic-plastic response of the piles by implementing the "moment-curvature relationship" for the reinforced concrete pile section, where a 2-node linear beam element (B31) was circumscribed by solid eight-node brick elements (C3D8R) to model the pile. The soil brick elements were defined with a nominal flexural stiffness. Considering the pile geometrical characteristics and reinforcement content, the bending moment-curvature relationship of the piles was established as in Figure 5.6 using SAP2000 software, and assigned to the beam element in the centre of concrete pile. It should be noted that other general beam section details including the Young's modulus of 30.1 GPa, the Poisson's ratio of 0.3, and the mass density of 2500 kg/m³ were assigned to the pile element.
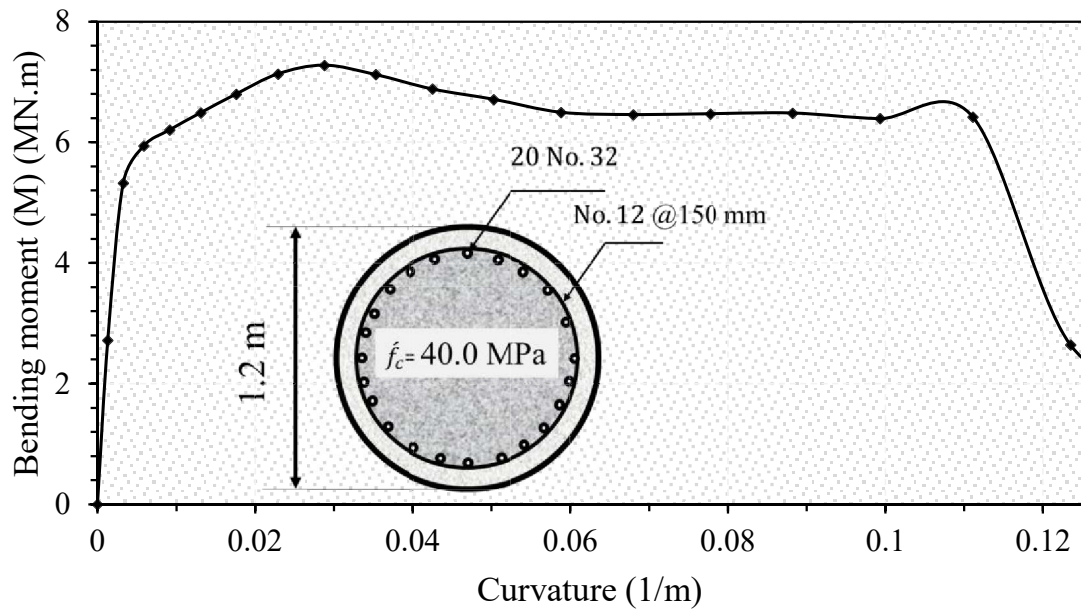
Figure 5.6 Moment-curvature response of the concrete reinforced pile section adopted in this study with the pile cross section details.

5.4.1.3 Modelling of inner 9% Ni steel tank

The linear kinematic hardening model was considered in this study to model the inelastic behaviour of the inner steel tank made of 9% Ni steel, recognized by the ASTM A353 (2014) for cryogenic service temperatures, while considering linear elastic behaviour when the stress state is within the yield surface. The linear kinematic hardening model was used in several previous research studies for seismic analysis of steel structures (e.g. Zakavi et al. 2014; Mizuno et al. 2014). The adopted constitutive model to simulate the metal inelastic behaviour under cyclic loading, adopts von Mises yield surface as defined in Equation (5.9). In this model, the equivalent Mises stress (i.e. $f(\sigma - \alpha)$) is defined with respect to kinematic shift stress (also known as the back-stress α) which describes the translation of the yield surface in the stress space. It should be noted that in Equation (5.9), the yield stress σ_y defines the size of yield surface which separates elastic and elastoplastic responses.

155

$$F = f(\sigma - \alpha) - \sigma_y = 0 \qquad\qquad (5.9)$$

where σ_y is the yield stress and $f(\sigma - \alpha)$ is the equivalent Mises stress with respect to the back stress, α, which determines the kinematic evolution of the yield surface in the stress space. The adopted linear kinematic hardening model in this study assumes associated plastic flow rule which is acceptable for metals subjected to cyclic loading (Chun et al. 2002; Hashiguchi and Ueno 2017; Koo et al. 2019). The evolution of the hardening law adopted in this study follows the linear Ziegler (1959) hardening law as formulated below:

$$\dot{\alpha} = C_s \frac{1}{\sigma_y} (\sigma - \alpha) \dot{\bar{\varepsilon}}^{pl} \qquad\qquad (5.10)$$

where $\dot{\bar{\varepsilon}}^{pl}$ is the equivalent plastic strain rate, C_s is the kinematic hardening modulus for steel which remains constant in this model, and σ_y is the equivalent stress denoting the size of the yield surface which remains constant and equal to yield stress at zero plastic strain ($\sigma|_0$). In this model the kinematic hardening parameter is obtained to be a "purely kinematic" following the linear Ziegler (1959) hardening law, and the "relaxation term" (or the recall term $\gamma_k \alpha \dot{\bar{\varepsilon}}^{pl}$ mentioned in Equation 5.23) is omitted since γ_k is assumed to be equal to zero.

As explained by Driver et al. (1998), the linear kinematic hardening model adopted here takes the Bauschinger effect into consideration. In other words, the model allows the straining in one direction (e.g. tension of compression) decrease the yield stress in the opposite direction (i.e. compression and tension correspondingly). Figure 5.7 illustrates the adopted stress-strain behaviour considering the linear kinematic hardening model with hysteresis effects to simulate response of 9% Ni steel. Indeed, the stress-strain relation follows linear elastic behaviour with initial stiffness E_s until the yield condition

at point $(\sigma_y, \varepsilon_y)$ is reached. Then the stress-strain relationship continues with a post-yield modulus E_t. As shown in Figure 5.7 and Figure 5.8, it should be noted that the post yield modulus is different from the plastic modulus; the post yield modulus refers to the slope of the total strain and stress, while the plastic modulus (i.e C_s) is the slop of the plastic strain versus stress. Furthermore, the inelastic material properties must be entered into ABAQUS as "Cauchy stress" σ_{true} and "true logarithmic strain" ε_{true} values, that can be considered from the nominal stress- strain values $(\sigma_{eng}, \varepsilon_{eng})$ using Lubliner (1990) equations:

$$\sigma_{true} = \sigma_{eng}(1 + \varepsilon_{eng}) \tag{5.11}$$

$$\varepsilon_{true} = ln(1 + \varepsilon_{eng}) \tag{5.12}$$

The inelastic input parameters for this model into ABAQUS are only two data pairs, the yield stress at zero plastic strain $\sigma|_0$, and the yield stress σ_y at finite plastic strain ε^{pl}; which are used to determine the linear kinematic hardening modulus (i.e. plastic modulus) from the following relation:

$$C_s = \frac{\sigma - \sigma|^\circ}{\varepsilon^{pl}} \tag{5.13}$$

The linear kinematic hardening model parameters for 9% Ni steel used in this study is summarized in Table 5.3.

σ_y : Yield stress.

ε_y: Yield strain.

E_s : Initial stiffness.

E_t : Post- yield modulus.
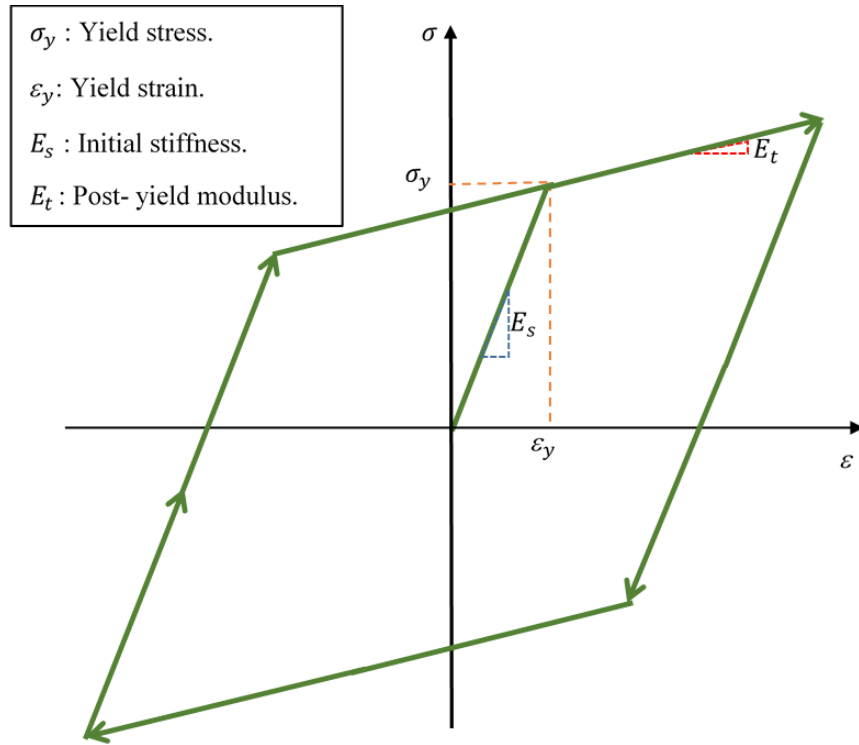
Figure 5.7 Hysteresis linear kinematic hardening model adopted.

$d\sigma$: Total stress increment value.

$d\varepsilon$: Total strain increment value.

$d\varepsilon^p$: Plastic portion of the strain increment.

$$E_t = \frac{d\sigma}{d\varepsilon} \ , \ C_s = \frac{d\sigma}{d\varepsilon^p} \ , \ C_s = \frac{E_s * E_t}{E_s - E_t}$$
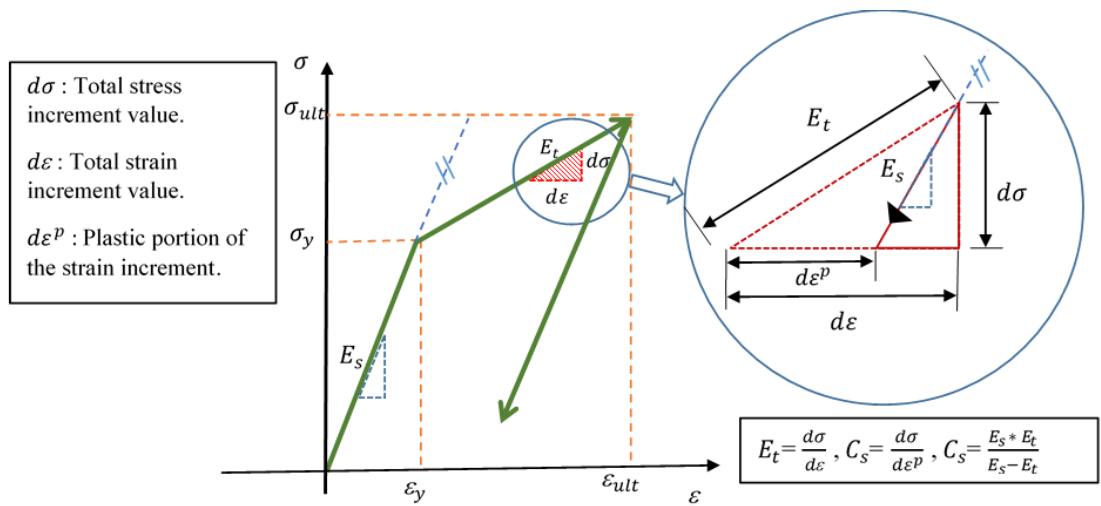
Figure 5.8 The relation between the initial stiffness, tangent modulus and initial kinematic hardening modulus of the steel.

Table 5.3 Linear kinematic hardening model parameters for inner 9% Ni steel tank used in this study.

Property	Symbol	Value	Reference
Ultimate stress (MPa)	σ_{ult}	662	
Yield stress (MPa)	σ_y	515	El-Batahgy
Elongation (%)	δ	28	et al. (2018)
Linear kinematic hardening modulus (MPa)	C_s	275	
Young's Modulus (GPa)	E_s	205	
Density (kg/m^3)	ρ_{steel}	7850	Aggen and
Poisson's Ratio	ν	0.29	Allen (2018)

5.4.2 Modelling of the Fluid-Structure Interaction

The hydrodynamic forces exerted from the accelerated fluid to the tank walls are commonly considered in two main modes of vibration; one is due to the rigid movement of the fluid which is called the impulsive force, while the other mode is due to surface waves and sloshing of the liquid, called convective force. In practical analysis and design, these forces are represented using simplified mechanical spring-mass models (Houser 1957), where these two forces are modelled as concentrated equivalent masses attached to the tank wall via link or spring elements with appropriate stiffness. Further developments were done by Virella et al. (2006) by adopting distributed masses, also recognized by Eurocode-8 (2006), which is known as a rigorous and a sound alternative model to Houser (1957) simplified mechanical model. In Virella et al. (2006) model, instead of using one concentrated mass to represent the impulsive force, the mass is spread along the tank wall in several segments as added masses. Indeed, usually these distributed

masses are linked to the wall nodes via rigid springs. In general, the Virella et al. (2006) replaced the hydrodynamic concentrated forces of Houser (1957) mechanical model with equivalent distributed pressure along the tank wall.

In this study, the FSI is considered by combining the Houser (1957) spring-mass model and the distributed pressure method of Virella et al. (2006). Indeed, the concentrated convective mass was used to model the convective force based on Houser (1957) and API-650 (2007), while the impulsive mass model based on Virella et al. (2006) and Eurocode-8 (2006) pressure distribution method was used to simulate the impulsive force. The adopted techniques deem suitable since the convective mode is generally uncoupled and independent from the impulsive mode, and can have less impact on the overall response of the liquid storage tank under horizontal loading, and many previous studies ignored the convective mode of liquid when adopting the add-mass approach for the sake of simplicity (e.g. Virella et al. 2006; Buratti and Tavano 2014).

As mentioned above, the convective force was modelled using spring - mass model, including the first convective mode of vibration only for the single convective mass (i.e. M_{con}) attached to the inner tank at a height of H_{con} (the centre of action or effective height of the convective mass) via springs with a stiffness equal to $K_{con,}$ where in this study the springs were used to connect the convective mass to the tank wall in the horizontal direction (i.e. earthquake acceleration direction). The required parameters to capture the convective hydrodynamic effect were determined using the equations 3.4 to 3.7 (explained in chapter 3), where these equations obtained from API-650 (2007).

For the impulsive mass modelling, Eurocode-8 (2006) was used, in which the distribution "spatial-temporal" of the impulsive hydrodynamic pressure (p_{imp}) were determined by equations 3.1 to 3.3 (as explained in chapter 3) to obtain the distributed impulsive masses m_{imp}. Indeed, Equation (3.3) was used to calculate the equivalent mass

at each segment of tank wall, which was 1.0 m segment along the tank wall in this study. As recommended by Virella et al. (2006), a convenient alternative to avoid attaching lumped masses via rigid link elements, is including these extra masses by increasing the wall density in each segment, which was used in this study to reduce the computational time.

5.4.3 Modelling of the soil deposit

5.4.3.1 *Modelling of clay soil deposit*

The nonlinear kinematic hardening model, was implemented in this study to model the cyclic behaviour of clay (non-liquefiable soil) under seismic loading. This pressure-independent plasticity model based on von Mises yield criteria, and associated flow rule, can be considered as appropriate model for nonlinear cyclic behaviour of pressure independent material, such as clay under undrained condition (Zhang and Tang 2007). As explained by George et al. (2016) and Zhu (2019), the key parameters of this model are Young's modulus, Poisson's ratio, and stress - strain curve of stabilised loading cycle obtained from the triaxial shear test. Based on the modification work done by Armstrong and Frederick (1966) on the original model which was proposed by Lemaitre and Chaboche (1994), the yield surface of the adopted nonlinear kinematic hardening constitutive model is defined according to Equation (5.9), while the equivalent Mises stress can be defined by the following relation:

$$f(\sigma - \alpha) = \sqrt{\frac{3}{2}(S - \alpha^{dev}):(S - \alpha^{dev})} \tag{5.14}$$

where S is the deviatoric stress tensor, and α^{dev} is the deviatoric part of back stress tensor. In the adopted model, an associated flow rule is adopted to obtain the required kinematic hardening flow rule as reported by Zhu (2019). The hardening rule of this model is a mixed nonlinear isotropic-kinematic hardening making it suitable for capturing the cyclic

behaviour of soils as explained by Elia and Rouainia (2016) and Mucciacciaro and Sica (2018). Indeed, the nonlinear kinematic hardening parameter defines the change of the yield surface in stress space through the back stress (α), as it is described by the superposition of pure kinematic and relaxation (source of the nonlinear behaviour) terms, while the isotropic hardening parameter defines the modification of the equivalent stress controlling the size of the yield surface (σ_y) as a function of plastic distortion. The isotropic hardening behaviour adopted in this study follows a simple exponential law as reported by ABAQUS (2018) and Zhu (2019) and presented in Equation (5.15), and data fitting can be utilised to obtain the model parameters by directly introducing data points for the yield surface size and plastic strains.

$$\sigma_y = \sigma|_0 + Q_\infty(1 - e^{-b\bar{\varepsilon}^{pl}}) \tag{5.15}$$

where $\sigma|_0$ is the yield stress at zero plastic strain and Q_∞ and b are parameters need to be defined for each soil, corresponding to the maximum change in the size of the yield surface, and the parameter defining the degree at which the size of the yield surface variations as plastic straining progresses, respectively. It should be noted that when the equivalent stress denoting the size of the yield surface keeps unchanged (*i.e.* $\sigma_y = \sigma|_0$), the general combined nonlinear isotropic-kinematic hardening model reduces to only nonlinear kinematic hardening model, which is adopted in this study.

The evolution of the kinematic component for the yield surface on the stress space based on Ziegler (1959) kinematic hardening law is presented below:

$$\dot{\alpha}_k = C_k \frac{1}{\sigma_y} (\sigma - \alpha)\dot{\bar{\varepsilon}}^{pl} - \gamma_k \alpha \dot{\bar{\varepsilon}}^{pl} \tag{5.16}$$

where (α_k) is the back-stress tensor, C_k and γ_k are material parameters for each back stress α_k, which are obtained through calibration using cyclic test data. Indeed, C_k is the

initial kinematic hardening moduli, and γ_k controls the degree at which the kinematic hardening moduli decreases with the plastic strains for each back stress α_k. It should be noted that the recall term $\gamma_k \alpha \dot{\bar{\varepsilon}}^{pl}$ introduces the nonlinearity to the evolution law proposed by Chaboche and Lemaitre (1990).

Moreover, each back stress is covering a different range of equivalent plastic strains, so the overall back stress is computed by summation of back stresses:

$$\alpha = \sum_{k=1}^{N} \alpha_k \tag{5.17}$$

The kinematic and isotropic hardening components are illustrated in Figure 5.9a for uniaxial loading, while Figure 5.9b illustrates the same for more generalised stresses for multiaxial loading. It is evident that the kinematic hardening component implies that the back stress is limited inside a cylinder of radius $\sqrt{\frac{2}{3}}\alpha^s$, where α^s is the value of α at large plastic strains (known as saturation condition), while the stress points lie within a cylinder with radius $\sqrt{\frac{2}{3}}\sigma_{max}$ (represented in Figure 5.9) since the yield surface remains bounded.

(a)

σ_3

Limit surface
$\sqrt{2/3}\sigma_{max}$

Limiting location of back
stress (α_k) $\sqrt{2/3}\frac{C_k}{\gamma_k}$

σ_2

α^{dev}

$\frac{\partial F}{\partial \sigma}$

σ_1

Yield surface

$\sqrt{2/3}\sigma_0$
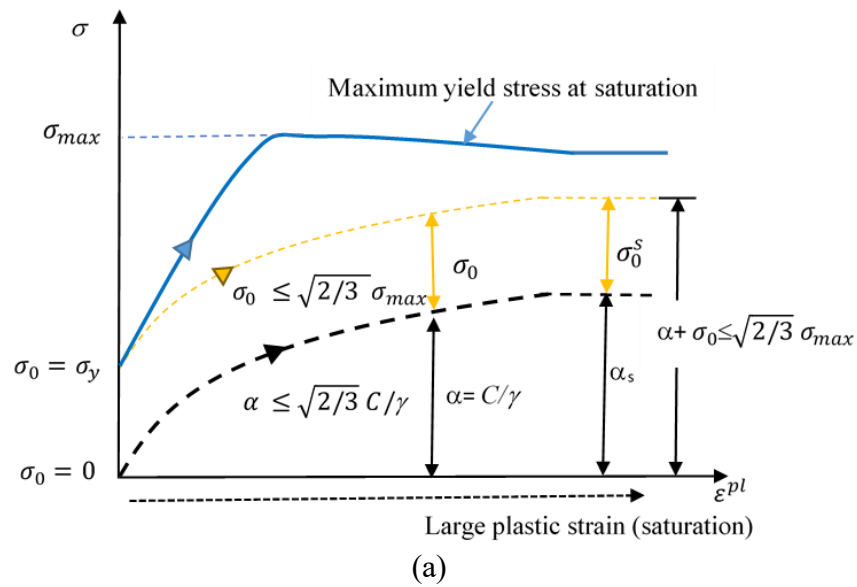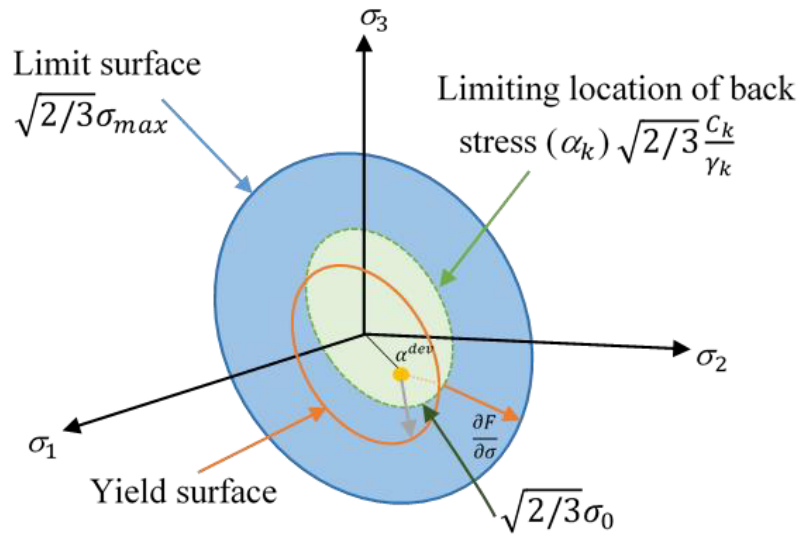
(b)

Figure 5.9 Soil nonlinear kinematic model (a) One-dimensional illustration of the hardening in the nonlinear kinematic model; (b) the generalised stresses for multiaxial loading in three-dimensional illustration of the hardening in the nonlinear kinematic model.

As explained above, the adopted nonlinear kinematic hardening model requires input parameters C_k and γ_k, or directly input triaxial shear test data corresponding to the stress-strain data points for stabilised cyclic curve. In this study, the soil properties, corresponding to the site class C and the density and shear wave velocity taken from in-situ tests are ρ_{clay}=1650 kg/m³ and 1950 kg/m³, with V_s=225 m/s and 270 m/s, for the top 15 m and the second 15.0 m, respectively. The maximum shear modulus (G_{max}) of the adopted soil was obtained from the following relationship:

$$G_{max} = \rho_{soil} * V_s^2 \tag{5.18}$$

As shown in Figure 5.10, Sun et al. (1988) summarised backbone curves for practical application in seismic site response analysis for cohesive soils. The backbone curves adopted in this study capture the variations of modulus reduction ratio (G/G_{max})

164

and damping ratio (ξ) with cyclic shear strain (γ) for cohesive soils obtained from cyclic simple shear and resonant column test results. To obtained an analytical formulation fitting the backbone laboratory measurements, Hardin and Drnevich (1972) model, as shown below, was adopted in this study.

$$\tau = \frac{G_{max}}{1 + \dfrac{\gamma}{\gamma_{ref}}} \tag{5.19}$$

$$\xi_{damping} = \xi_{max}(1 - \frac{G}{G_{max}}) \tag{5.20}$$

where τ is the shear stress, ξ is the damping ratio, G is secant shear modulus, γ is the cyclic shear strain of the soil, and γ_{ref} is Hardin and Drnevich (1972) constant to get a best fit for backbone curves for modulus reduction and damping ratio. The calibrated value of γ_{ref} = 0.234 resulted in the best match for backbone curves with coefficient of determination R^2 equal to 0.88 and 0.80 for the modulus reduction curve and damping ratio, respectively, as evident in Figure 5.10.
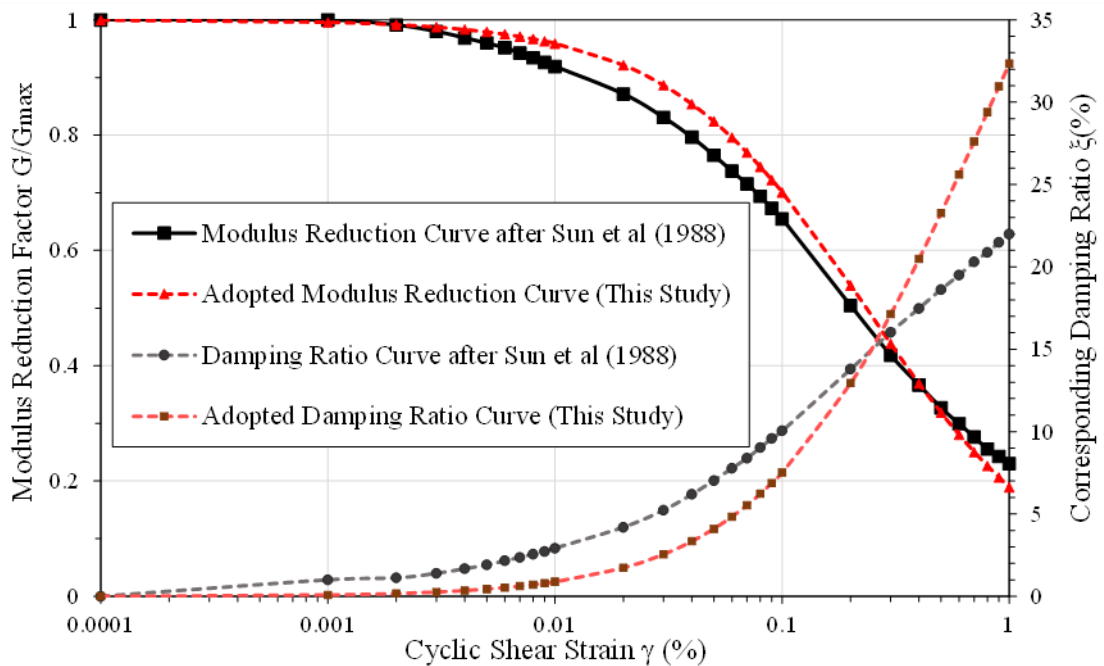
Figure 5.10 Implemented fitting curve for cohesive soil.

Since the kinematic hardening model adopted in this study for cyclic behaviours of soils required the stabilised stress-strain cycle, Masing (1926) rule presented in Equation (5.21) was used to obtain the cyclic shear stress - strain behaviour. In this study, it is assumed that the stabilised cyclic loading - unloading curve is reached at cyclic shear strain value of 2% beyond which the shear modulus remains unchanged.

$$\tau - \tau_{rev} = \frac{G_{max} \; (\gamma - \gamma_{rev})}{1 + (\frac{|\gamma - \gamma_{rev}|}{2 * \gamma_{ref}})} \qquad (5.21)$$

where τ_{rev} and γ_{rev} are the shear stress and cyclic shear strain at the reversal point. The stabilised loading cyclic was used to obtain the kinematic hardening parameters by inputting the shear stress and plastic shear strain data points from the re-yielding point to the reversal point. Indeed, using an ABAQUS subroutine, a curve fit analysis was conducted to determine the combined hardening constants based on the shear - stress strain data points. Referring to Equation (5.17), by adopting several back stresses and calibrating the parameters, a larger strain range can be covered resulting in more accurate predictions. Thus, in this study two back stresses were adopted which resulted in more reliable predictions. Table 5.4 summarises soil properties and the calibrated kinematic hardening model parameters adopted in this study.

Figure 5.11 illustrates the comparison of the calibrated kinematic hardening model adopted in this study versus the laboratory measurements obtained from Sun et al. (1988) experiments while adopting Masing (1926) rule to obtain closed loading-unloading cyclic loop. As evident, the predictions adopting kinematic hardening model are in good agreement with the experimental data, confirming the suitability of the adopted nonlinear kinematic hardening model and calibrated parameters to simulate the cyclic response of

adopted soft clay deposits.

Table 5.4 Clay soil properties and calibrated nonlinear kinematic hardening model parameters.

Soil properties	Symbol	Value for Soft clay layer 1	Value for Soft clay layer 2
Density (kg/m³)	ρ_{clay}	1750	1950
Undrained shear strength (kPa)	Cu	18.5	24
Shear wave velocity (m/s)	V_s	225	270
Small strain shear modulus (MPa)	G_{max}	88.1	142.1
Poisson's Ratio	v	0.3	0.49
Calibrated initial kinematic hardening modulus (MPa)	C_{k1} , C_{k2}	26.1, 250	45.9, 280
Calibrated hardening modulus decreasing rate	γ_{k1} and γ_{k2}	1150, 1450	1170.36, 1600

(a) Clay Layer 2
$\rho_{clay} = 1650 \text{ kg/}m^3$
$Vs = 225$ m/s
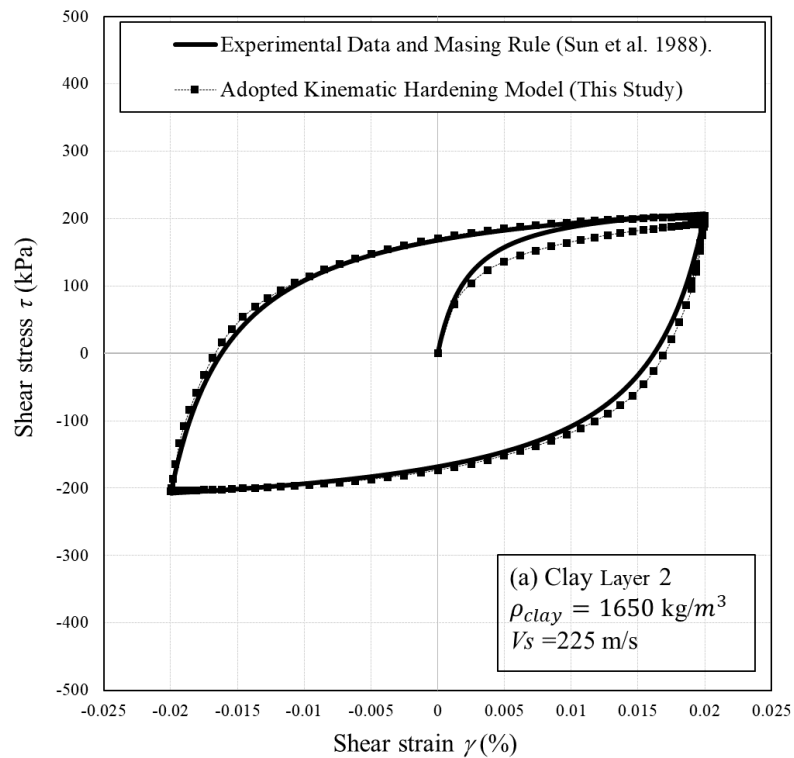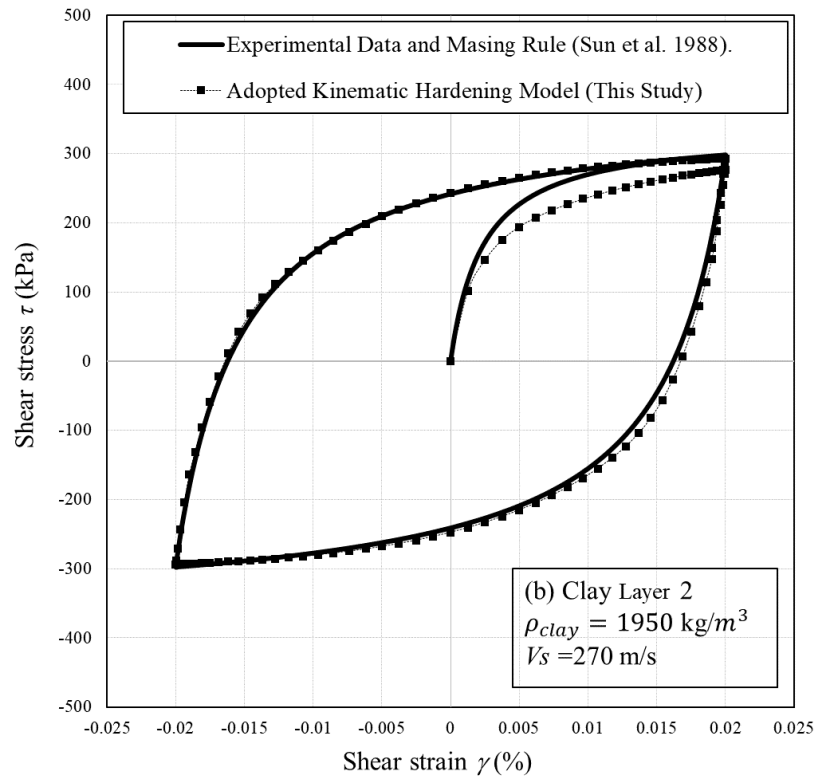
Figure 5.11 Comparison of cyclic stress-strain predictions adopting the calibrated kinematic hardening model and corresponding experimental data for clayey soils (a) clay soil layer 1 (from 0.0 m to 15.0 m depth) and (b) clay soil layer 2 (from 15.0 m to 30.0 m depth).

5.4.3.2 *Modelling of liquefied soil deposit*

Large pore water pressures can be generated in saturated loose granular soils under undrained conditions during strong earthquake, resulting in a reduction in effective stresses and, as a result, a significant loss in strength and stiffness. The presence of groundwater, the particle size distribution of the soil, the in-situ relative density of the soil, the effective confining stress, and the amplitude and duration of ground vibrations are factors that influence the beginning of liquefaction.

The current state-of-the-practice approach commonly adopted in projects has been used to obtain the post-liquefaction properties of the liquified layers for modelling. The adopted approach is in accordance with Idriss and Boulanger (2008), where the residual shear resistance of liquefied sand, *Sr*, were estimated based on back analysis of several

field case histories. Idriss and Boulanger (2008) correlated the residual shear strength with the ground in-situ penetration test measurements (SPT or CPT). In this study, the correlation (Equation 5.22) based on equivalent clean sand corrected SPT value, (N1)60cs−Sr, is adopted for condition in which the effects of void redistribution are considered negligible:

$$S_r/\acute{\sigma}_{vc} = \left(\frac{(N_1)_{60cs-Sr}}{16} + \left(\frac{(N_1)_{60cs-Sr}-16}{21.2}\right)^3 - 3.0\right) \leq \tan\acute{\phi} \tag{5.22}$$

where S_r/σ'_{vc} is residual shear strength ratio, σ'_{vc} is effective vertical stress pre-liquefaction, and φ' is effective friction angle of the liquefiable layer (before onset of liquefaction). The idea of correlating residual strength with (N1)60cs−Sr was initially proposed by Seed (1987) and considered logical on the basis of critical-state concepts and established correlations between the overburden correlated penetration resistance and in-situ relative density (Idriss and Boulanger, 2018).

Table 5.5 summarizes the post-liquefaction soil properties used in this study. The damping behaviour of the liquefied soil was captured using Rayleigh damping formulation via Rayleigh damping coefficients $\alpha_{damping}$ and $\beta_{damping}$, calculated based on the first and second mode natural frequency of the liquefied soil deposit and 20% damping ratio for the liquefied soil referring to Poulos (2017), Boulanger et al. (2014) and Lombardi and Bhattacharya (2014). Rayleigh damping coefficients adopted in this study for different liquefied soil thicknesses are presented in Table 5.5.

Table 5.5 Post-liquefaction residual properties for sand.

Soil properties	Symbol	Liquified soil layer 1 Value	Liquified soil layer 2 Value	Liquified soil layer 3 Value
Density (kg/m^3)	ρ_{liq}		1650	
Friction angle (Degree)	Φ		0	
Poisson's Ratio	v		0.49	
Equivalent *SPT* value	$(N_1)_{60cs-S}$		14	
Residual Shear Stress Ratio (based on Idriss and Boulanger, 2008)	Sr/σ'_{vo}		0.12	
Effective Stress at mid. of liquefiable layer (kPa)	$\sigma'v$	40	121	202
Residual Shear Strength (kPa)	S_r	4.85	14.5	24.3
Residual Shear Stiffness (kPa)	$G_{liq.}$	243	728	1213
Residual Shear Wave Velocity (m/s)	$V_{s(liq.)}$	12	21	27
Adopted Rayleigh damping parameters	α	0.659	1.21	1.72
	B	0.062	0.033	0.0218

5.4.4 Modelling of interfaces, boundary conditions and the adopted earthquakes

To include the SSI effect and capturing the possible separation or sliding between the subsoil and the piles, and between the subsoil and the foundation raft (i.e. outer tank slab), interfaces were defined between the mentioned surfaces. For the normal response of interacting surfaces, the hard contact algorithm was used by defining the relationship between the contact pressure (*p*) and the overclosure (*h*) between the master and slave surfaces. Indeed, the pressure was transferred between interacting surfaces when the overclosure between them was zero (i.e. *h* = 0). In this adopted hard contact model,

penalty algorithm, based on stiff approximation of contacting surfaces, was implemented to avoid over-constraining issue in the modelling, and thus a minor penetration for the interacting surfaces, was allowed. Moreover, for the tangential interaction between the interacting surfaces, the "Coulomb frictional model" via penalty option was implemented, where the comparative movement in the contacting surfaces was controlled by defining a critical shear stress between them ($\tau_{critical} = \mu. P$), which is proportional to the contact pressure through the friction coefficient (μ), where the relative movement can occur when the shear stress between the contacting surfaces exceeds the critical shear stress (i.e. the frictional resistance between the surfaces). The friction coefficients (μ) between the clay subsoil and the raft surfaces, and between the subsoil and pile surfaces were considered to be 0.4 and 0.35, respectively (Rasouli and Fatahi 2021; Agalianos et al. 2020). It should be noted that frictionless interfaces were used between the liquefied soil and foundation elements. Moreover, the rigid connection between the pile head and the raft foundation was imposed via the tie constraint condition available in ABAQUS.

The numerical analyses for the tanks – foundation - soil system was performed in two steps; the initial step, which was static analysis, considered the gravity loads for the entire system, followed by the second step which was application of earthquake acceleration at the model base in X-direction only adopting dynamic implicit stepping technique. During the static analysis, the bottom of the soil deposit was fixed in all directions, and the vertical movements were allowed on the side boundaries, while the displacements normal to the side boundaries were disallowed. During the dynamic analysis, the infinite boundaries were introduced on the side boundaries replacing the initial roller boundaries. The adopted one way 8 nodes infinite elements CIN3D8 (see Figure 5.3) are appropriate solid elements representing the far-field soil, capturing the initial static equilibrium conditions (Zienkiewicz et al. 1983) and absorbing the energy

from the unbounded soil area under dynamic loading (Lysmer and Kuhlemeyer 1969). During the dynamic analysis the response of these elements are isotropic linear elastic and represent the infinite model where the normal waves are not allowed to be reflected and the damping of the normal velocity of these boundaries are governing by the following equations:

$$\rho c_p = \rho \sqrt{\frac{\lambda + 2G}{\rho}} \qquad (5.23)$$

$$\rho c_{sv} = \rho \sqrt{\frac{G}{\rho}} \qquad (5.24)$$

where c_p and c_{sv} are the compressive and shear wave velocities of the soil, ρ is the mass density of the material, and λ and G are Lamé's constants. It should be noted that the adopted infinite elements eliminate energy transmission for plane waves crossing the boundary, while the wave propagation upward will not be distorted.

For the input seismic excitations, one near-field earthquake 1999 Chi-Chi earthquake and one far-field earthquake, 1968 Hachinohe earthquake, were used to study the dynamic response of the LNG tank. In general, the seismic design of LNG tanks follows the same scenario of nuclear power plants by applying the two earthquake levels, namely the Operating Basis Earthquake (OBE) and Safe Shutdown Earthquake (SSE). Under OBE, the LNG storage system needs to remain fully operational with no damage, while subjected to SSE, no leakage of LNG should occur. In this study, the response of LNG tank system subject to SSE was assessed.

To minimise the scatter in the response of earthquake engineering demand parameters, the seismic input motions are suggested to be scaled using spectral matching method (Guzel 2019). The spectral matching which to match a target response spectrum using SeismoMatch software (SEISMOSOFT 2016).

To simulate earthquake wave transmitted from bedrock (i.e. high shear wave velocity) via assessed ground condition to the LNG tank, the response spectra of input motions were scaled to the target response spectrum representing Site Class A (i.e. strong rock site) from AS/NZS1170.5 (2004) as shown in Figure 5.12. The shape of target spectrum is defined by the response spectrum acceleration factor $C(T)$ using Equation (5.25).

$$C(T) = C_h(T)ZR\left\{1 + (N_{max} - 1)\left[\frac{20 - D_k}{18}\right]\right\} \tag{5.25}$$

where $C_h(T)$ is spectral shape factor which depends on the site subsoil class and structure period (T), Z is the hazard factor equal to 0.4 for Wellington city in New Zealand based on the available site hazard map. R is the return period factor taken as 1.8 (i.e. annual probability of exceedance (APE) of 1/2500) for the SSE earthquake level for tank containing hazardous liquid based on importance level of 4 and design working life of 100 years taken from AS/NZS1170.5 (2004). N_{max} and D_k are factors related to near fault properties, where N_{max} is the maximum near fault factor and taken to be 1 in this study; and D_k is the shortest distance between the site and the nearest fault which was considered to be 2 in this study.

A specified period range, the minimum and maximum periods of 0.4 seconds and 1.5 second, respectively which covers the period range of soil-structure system under seismic load, was defined to perform spectral matching. Figure 5.13 shows the original and scaled accelerogram. It should be noted that baseline correction was conducted after the selected accelerogram being spectral matched. The scaled accelerogram was applied at the base of the soil-structure model to perform dynamic analysis.
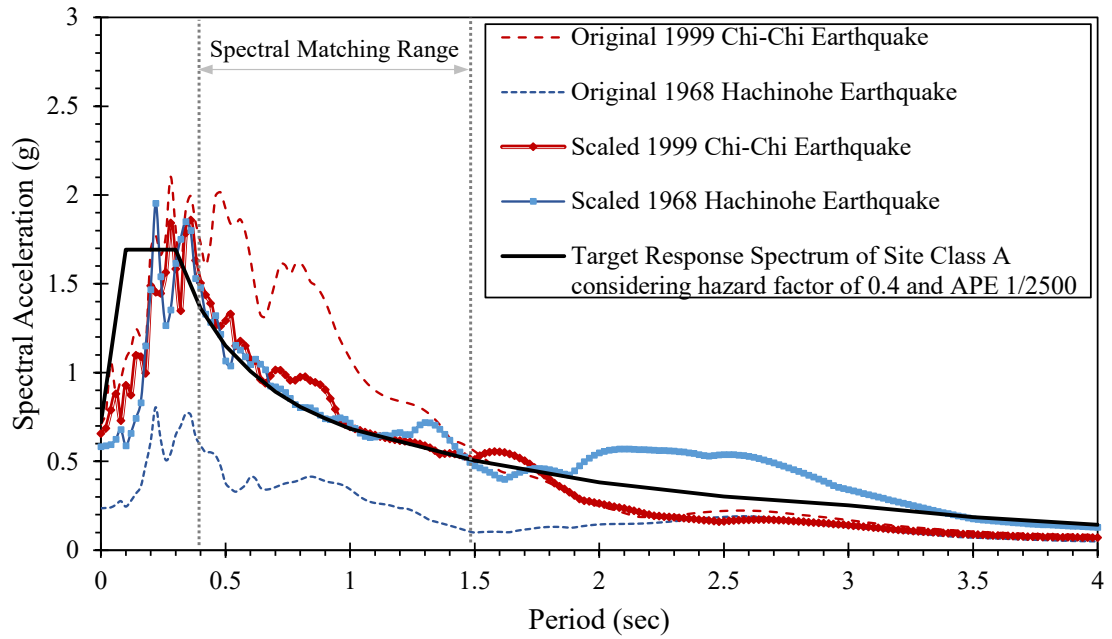
Figure 5.12 The target acceleration response spectra and the original with the scaled acceleration response spectrum for the applied earthquake.
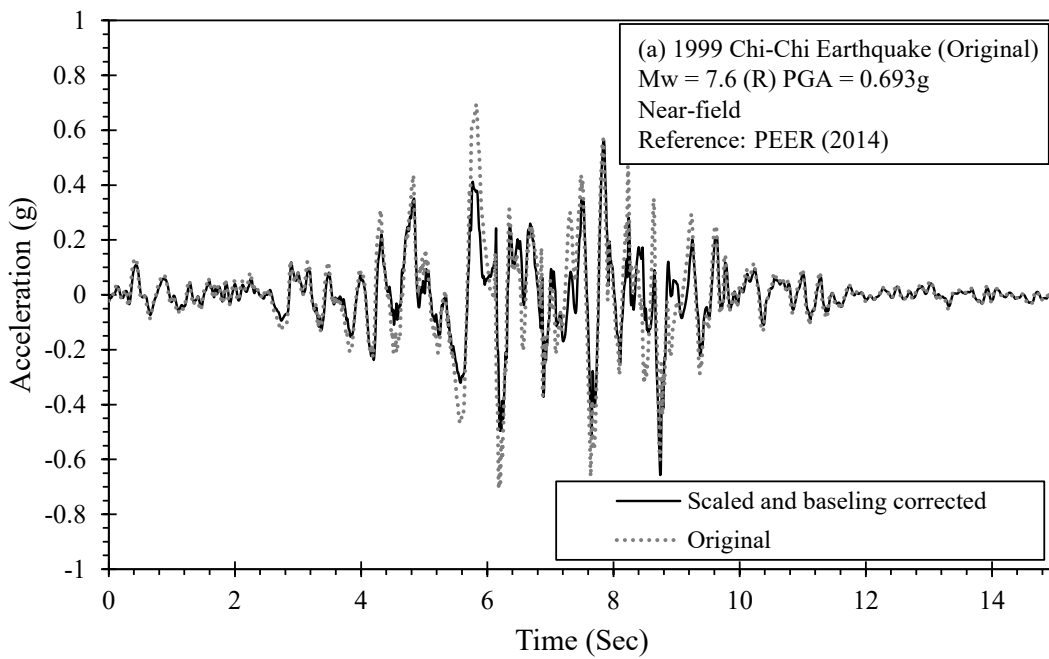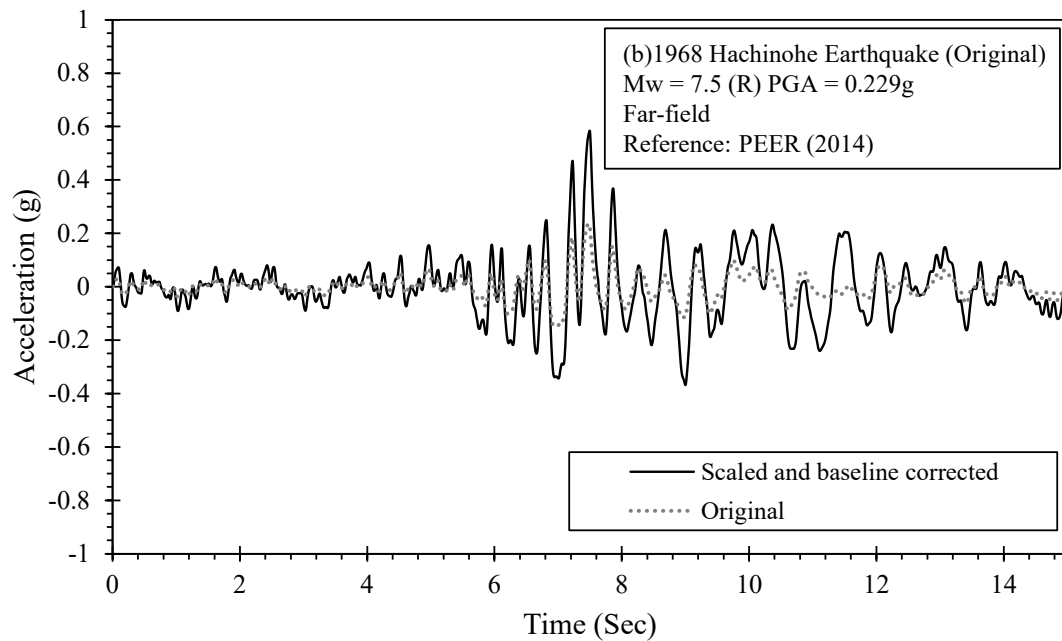
Figure 5.13 Earthquake records scaled and used from: (a) 1999 Chi-Chi earthquake; (b) 1968 Hachinohe earthquake.

5.5 Results and discussion

In this section, the results of free vibration and time history analyses are presented to assess the dynamic response of LNG tank system while capturing effect of soil liquefaction on the seismic response of the pile foundation and the superstructure. Initially, the free vibration analysis results are presented, and then numerical predictions from the nonlinear time history analysis under the 1999 Chi-Chi and the 1968 Hachinohe earthquakes are presented and discussed.

5.5.1 Free vibration analysis

In this study, the modal analysis was performed for the LNG tank using Block Lanczos algorithm. Firstly, the modal analysis on the fixed base tank (no foundation movement) was conducted as a reference to highlight importance of SSI when compared with other cases capturing the soil and foundation movements. Since the impulsive and

convective hydrodynamic forces were modelled using added mass and spring-mass methods, respectively, the first impulsive and convective modes of the LNG were captured in the numerical model and the corresponding predicted natural periods were compared with the analytical formulations available in API-650 (2007) as explained previously in equations 3.10 and 3.11. It should be mentioned that the density of LNG assumed to be 480 kg/m^3.

Table 5.6 summarise the FEA predictions and the analytical calculations for the natural period of inner LNG tank. Moreover, Figures 5.14a and 5.14b show the vibration mode shapes for both impulsive and convective first modes. It can be noticed that the first impulsive mode shape is the beam type mode, where the liquid and the tank wall vibrated similar to a cantilever beam as a result of rigid movement of the impulsive LNG mass attached to the tank wall. In addition, the convective mass vibrated in the horizontal direction since it was tied to the tank wall via springs controlling the stiffness of the vibrating mass. Figure 5.14c represents the first mode shape for outer concrete tank, and it is evident that the first mode shape corresponded to tank roof. Moreover, Table 5.6 verifies the suitability of the proposed mechanical model to simulate FSI in the three-dimensional finite element model used in this study, since a good agreement was observed between the natural periods obtained from the 3D numerical and the analytical formulations in API-650 (2007).
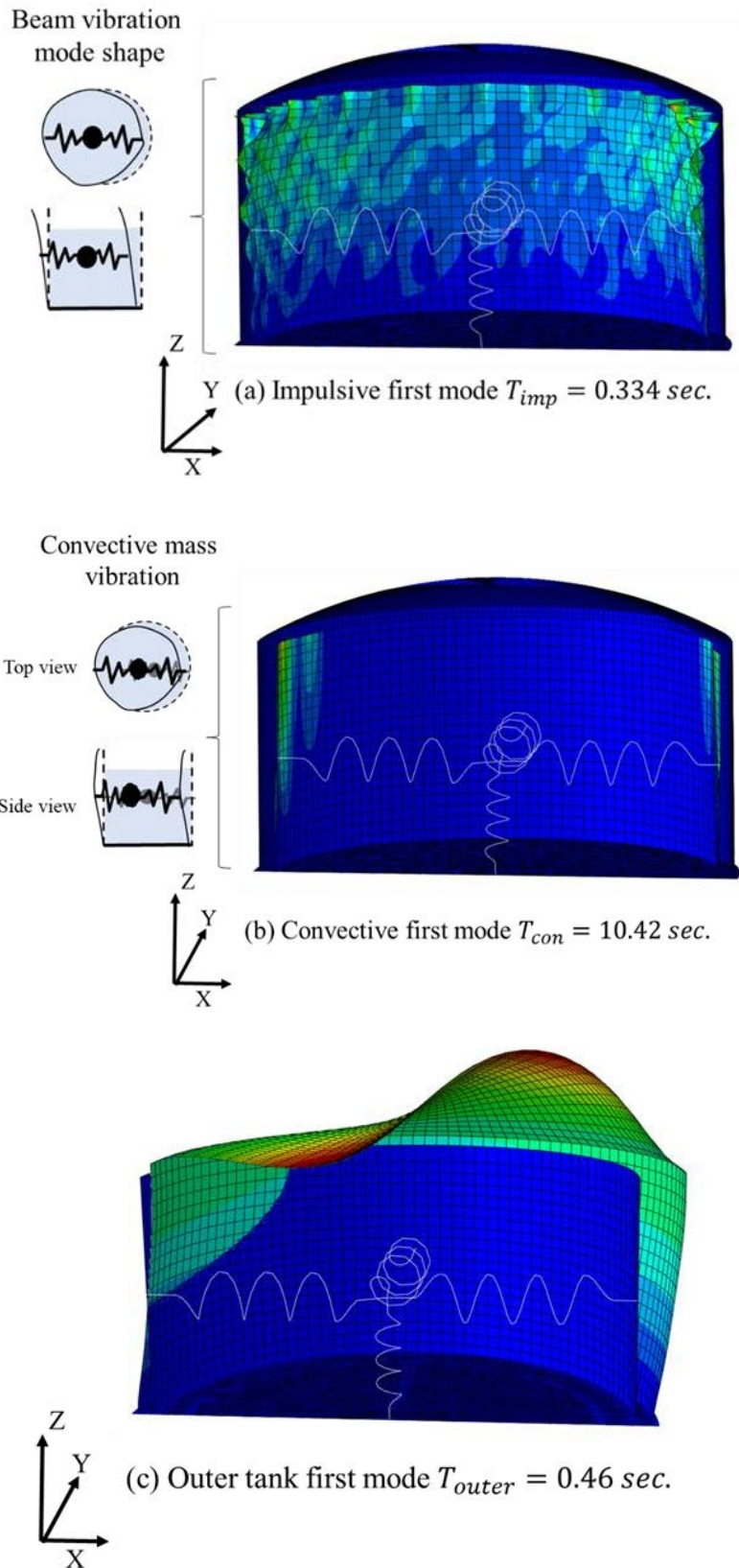
Figure 5.14 Fixed based LNG tank free vibration mode shapes for the Inner and outer tanks; (a) Impulsive (b) convective modes for the proposed mechanical model used in this study, and (c) the outer tank first mode shape.

Table 5.6 The fundamental periods of vibration obtained from numerical model and analytical solution.

Method of calculation	FEM Calculation (this study)	API-650 (2007) Approximation
Impulsive fundamental period T_{imp} (sec)	0.334	0.354
Convective fundamental period T_{con} (sec)	10.42	9.67
Outer tank fundamental period T_{outer} (sec)	0.146	-

The effects of the soil liquefaction on the dynamic properties of LNG tank reinforced by end-bearing pile foundation namely frequency and damping are also discussed. Table 5.7 summarise the results of the modal analysis conducted to obtain LNG tank natural period for different depths of liquefied soil deposit varying from zero (no liquefaction) to 15 m. In general, the vibration characteristics of pile foundation impact the response of the entire LNG tank system. Indeed, Table 5.7 show that the natural period of the LNG tank system increased significantly when the soil deposit liquefied; for example, the fundamental period of the LNG tank excluding soil liquefaction was 0.46 sec, while when the top 5 m of soil liquefied, the fundamental natural period increased by 69% to 0.78 sec. This is due to the fact that loss of soil stiffness around the piles supporting the LNG tank as a result of liquefaction increased the overall structural flexibility and thus altered the dynamic characteristics of the LNG tank system significantly. Further increasing the depth of liquefied soil to 10 m and 15 m, enlarged LNG tank natural period by 104% (to 0.94 sec) and 154% (to 1.17 sec sec) comparing to the LNG tank on non-liquefiable soil, respectively. Figure 5.15 shows the corresponding fundamental vibration mode shapes for LNG tank. When the soil deposit liquefied, the mode shape was governed by the vibration of the section of the pile embedded in the liquefied soil layer which deform more compared with the pile in the non-liquefied soil deposit. In general, when the soil liquefied and the liquefaction extended deeper, the

dynamic properties of the LNG tank alerted significantly, which could trigger different responses for different parts of the LNG tank system. However, for the convective mass mode, it can be notice that increasing the depth of the liquefied soil deposit slightly decrease the natural period since the convective mass system was already more flexible due to the presence of springs attaching the mass to the wall, in contrast to the rigid connection between the impulsive mass and the tank wall.

(a) Fundamental vibration mode shape for LNG tank for non-liquefied soil deposit.

(b) Fundamental vibration mode shape for LNG tank with 5.0 m liquefied soil depth.

(c) Fundamental vibration mode shape for LNG tank with 10.0 m liquefied soil depth.

(d) Fundamental vibration mode shape for LNG tank with 15.0 m liquified soil depth.
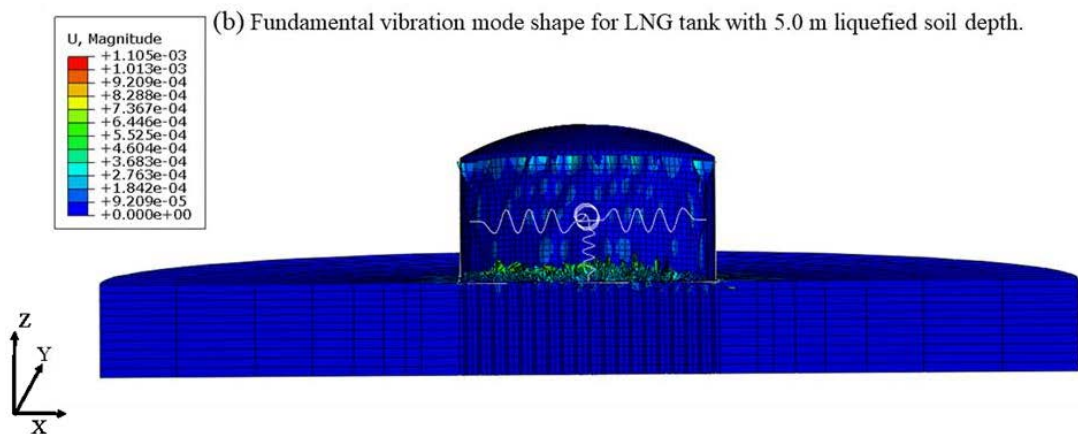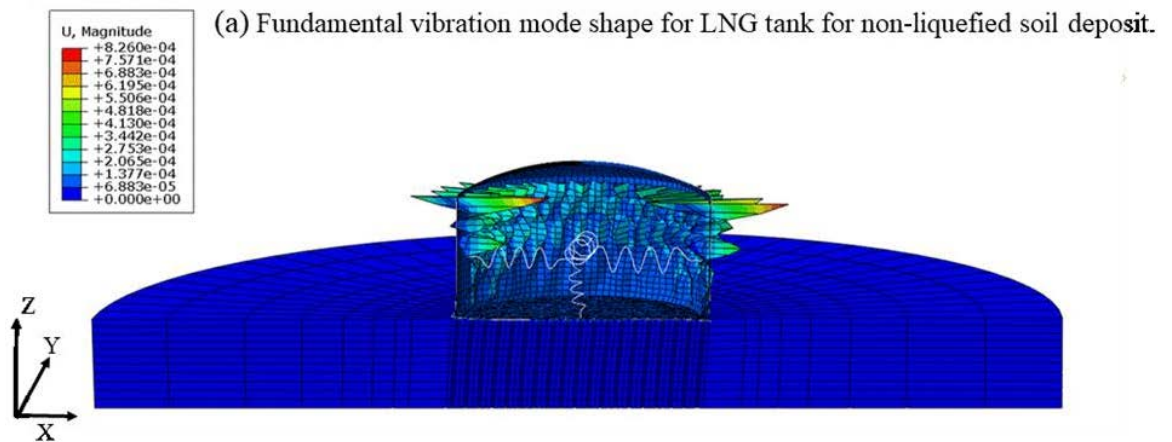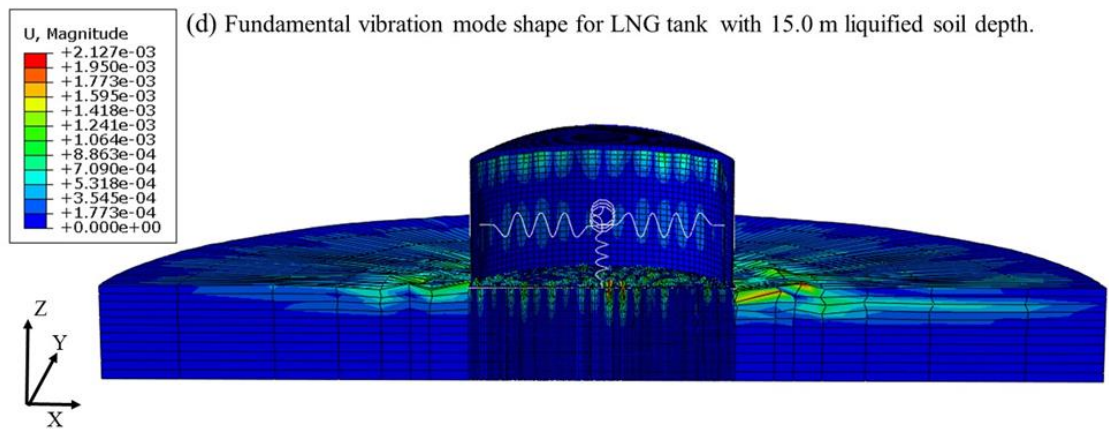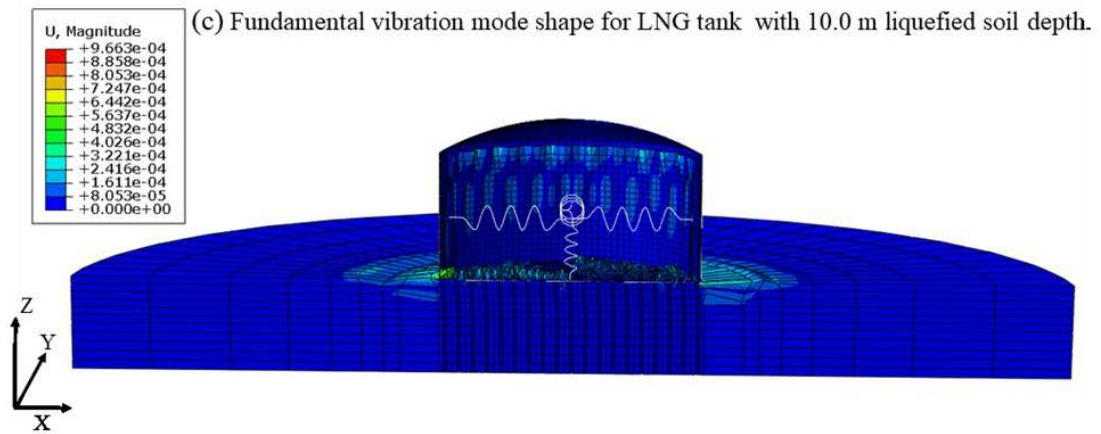
Figure 5.15 The deformation value (U) of the fundamental vibration mode shape for LNG tank with different soil deposit condition: (a) LNG tank on end-bearing piled foundation with non-liquefied soil deposit, (b) LNG tank on end-bearing piled foundation with 5.0 m liquefied soil deposit, and (c) LNG tank on end-bearing piled foundation with 10.0 m liquefied soil deposit, (d) LNG tank on end-bearing piled foundation with 15.0 m liquefied soil deposit.

Table 5.7 Differences of natural frequencies of LNG tank with diverse sub soil conditions.

Sub soil condition	LNG tank natural period							
	Convective mode period (sec)		Impulsive mode period (sec)		Outer tank mode period (sec)		Pile foundation system period (sec)	
	First mode (T_1)	Second mode (T_2)	First mode (T_1)	Second mode (T_2)	First mode (T_1)	Second mode (T_2)	First mode (T_1)	Second mode (T_2)
Fixed base condition	10.24	5.33	0.334[*]	0.21	0.146	0.128	-	-
Scenario I (Non-liquefied, T_{s1})	10.238	5.32	0.51	0.395	0.248	0.24	0.46[*]	0.32
Scenario II (5 m deep liquefied soil, T_{s2})	10.16	5.2	0.78	0.67	0.56	0.53	0.78[*]	0.67
Scenario III (10.0 m deep liquefied soil, T_{s3})	9.78	4.82	0.94	0.91	0.627	0.613	0.94[*]	0.89
Scenario IV (15.0 m deep liquefied soil, T_{s4})	9.5	4.23	1.17	1.08	0.74	0.72	1.17[*]	1.0

* The fundamental natural period (sec)

5.5.2 Nonlinear time history results

The seismic analyses for the LNG tank on the different sub soil scenarios as shown in Figure 5.2 were conducted in time domain for two spectral matched earthquake records, namely, the 1999 Chi-Chi and the 1968 Hachinohe earthquakes. The seismic outcomes were extracted and compared in terms of the response spectrum, tanks maximum acceleration profile, inner tank wall maximum structural response, and the pile seismic response (i.e. lateral displacements, shear forces and bending moments developed along the pile).

5.5.2.1 *Response spectrum*

Figure 5.16 displays the acceleration response spectra at the ground surface (i.e. the raft level of LNG tank) for four soil deposit scenarios with different depth of liquefied soil. The induced motion in the soil gets modified as it propagates through the soil deposit from the bedrock level to ground surface, which is known as the site effect. The extent of the site effect depends on the geometrical and mechanical characteristics of the soil deposit and the applied earthquake. Indeed, Figure 5.16a shows the amplification of the 1999 Chi-Chi earthquake input motion from the bedrock to the ground surface for the no liquefaction scenario, where the peak ground acceleration (PGA) for the input motion at the bedrock level was 1.85g and increased to 3.5g on the ground surface (i.e. almost twice amplification). Similar observations could be made in Figure 5.16b for the 1968 Hachinohe earthquake where the PGA amplified from 1.95g (bedrock level) to 4.1g (ground surface level). However, the acceleration response spectra decreased when the soil liquefaction occurred, as a result of energy dissipation within the liquefied soil layer. As also evident in Figure 5.16, increasing the thickness of the liquefied soil layer from 5.0 m to 15.0 m incrementally resulted in continuous increase in the dissipation of the seismic wave as evident in the corresponding reduction in the PGA measured on the

ground surface. However, the presence of liquefied soil deposit amplified the spectral acceleration in the long period rang and shifted the peak response spectrum towards the long period rang. These observations are comparable with the results reported by Youd and Carter (2005) and Gingery et al. (2015). Indeed, Youd and Carter (2005) studied five real liquefied sites and found that the liquefaction induced softening reduced the spectral acceleration in the short period (i.e. period range less than 1.0 sec), while in long period range (i.e. period range more than 1.0 sec), the amplification of the spectral acceleration was observed due to the ground oscillations in this range. Referring to Figure 5.16, it can be observed when the thickness of the liquefied soil increased, the extent of soil softening was more, alerting the vibration characteristics of the soil deposit, filtering the high frequency components of the input motions, and delaying the transition of the seismic motion to the ground surface.
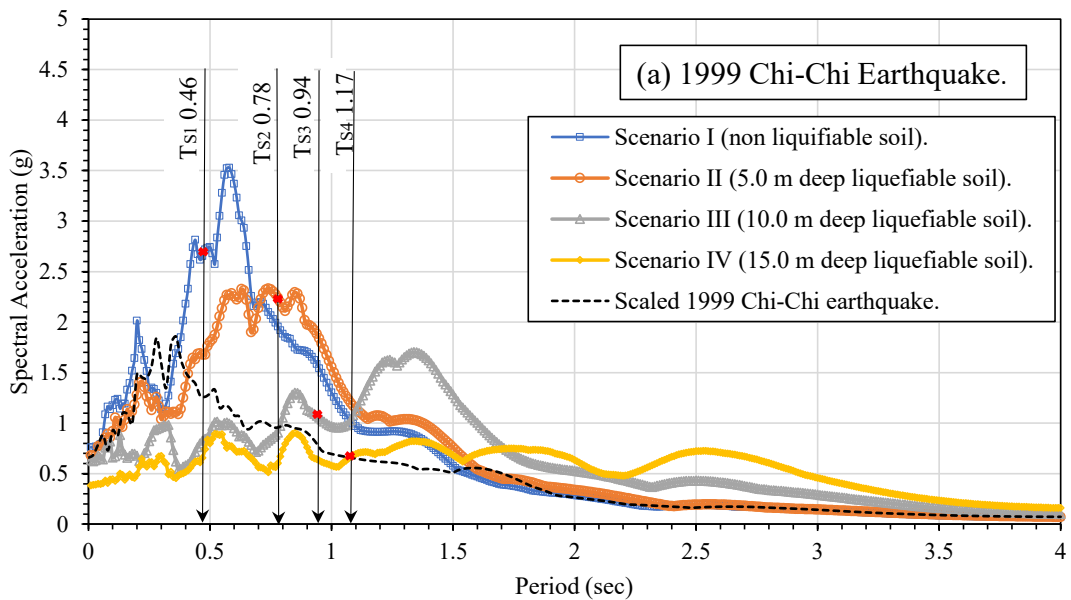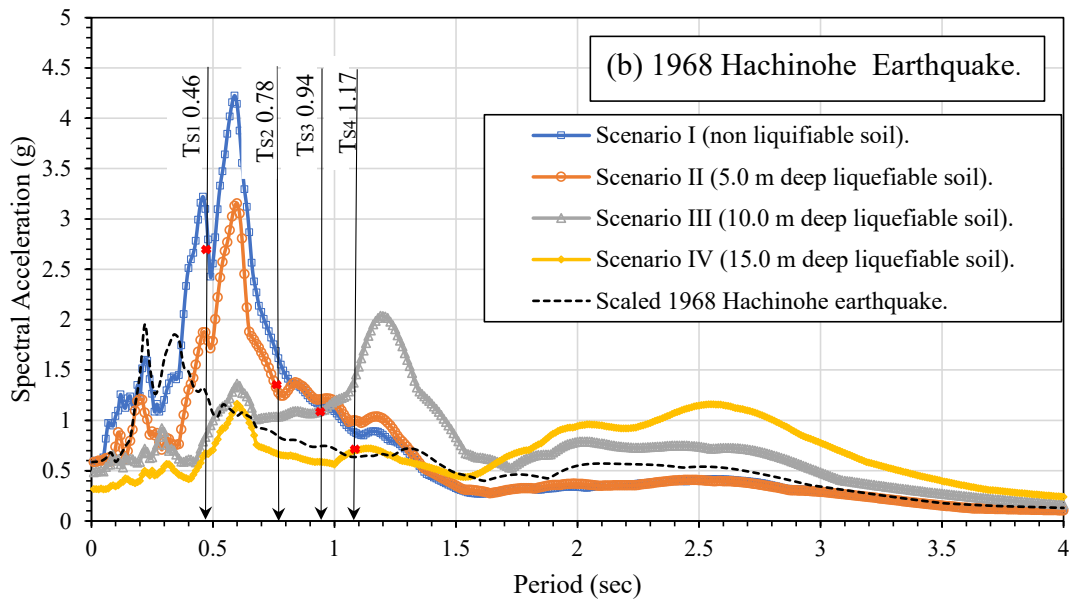
Figure 5.16 Response spectrum derived from the motion of foundation slab with 5% damping ratio under (a) 1999 Chi-Chi Earthquake, and (b) 1968 Hachinohe Earthquake.

5.5.2.2 *Maximum tank acceleration profile*

Figure 5.17 shows the horizontal acceleration time history record of the outer tank roof for different soil conditions. It is evident that the maximum horizontal acceleration occurred at different times for each soil condition scenario under same earthquake; for example, for non-liquefied soil deposit, the maximum horizontal acceleration was observed at t = 6.0 sec and t = 7.4 sec under the 1999 Chi-Chi and the 1968 Hachinohe earthquakes, respectively. However, the maximum horizontal accelerations were observed at t= 6.2 sec, 7.5 sec and 7.8 sec when the liquefied soil deposit increased to 5.0 m, 10 and 15.0 m under the 1999 Chi-Chi earthquake (Figure 5.17a). The corresponding values under the 1968 Hachinohe earthquake were t = 7.8 sec, 8.3 sec, and 10.8 sec, respectively (Figure 5.17b). This can be explained by referring to the Figure 5.16 where the liquefied soil layer changed the amplitude and frequency content of the seismic load. In addition, the profiles of the seismic acceleration developed along the inner and outer tank walls are reported in Figure 5.18 and Figure 5.19, respectively, where the

acceleration profile was extracted along the tank wall when the maximum acceleration occurred at the top of the tank walls in X direction (i.e. at polar coordinate where $\theta = 0°$ and parallel to the direction of applied earthquake). Referring to Figure 5.18a and as expected, the maximum acceleration profile was observed in non-liquefied soil case (i.e. Scenario I), where the maximum recorded acceleration at the top of the outer tank wall was 2.3g, and decreases gradually to 1.62g, 0.98g and 0.92g in the presence of 5.0 m (Scenario II), 10.0 m (Scenario III) and 15.0 m (Scenario IV) thick liquefied soil deposit, respectively. Similarly, Figure 5.18b shows the maximum acceleration of the outer tank wall under the effect of the 1968 Hachinohe earthquake, where the maximum acceleration values of 1.83g, 1.78 g, 0.82 g, and 0.52 g were observed for Scenarios I to IV, respectively.

185
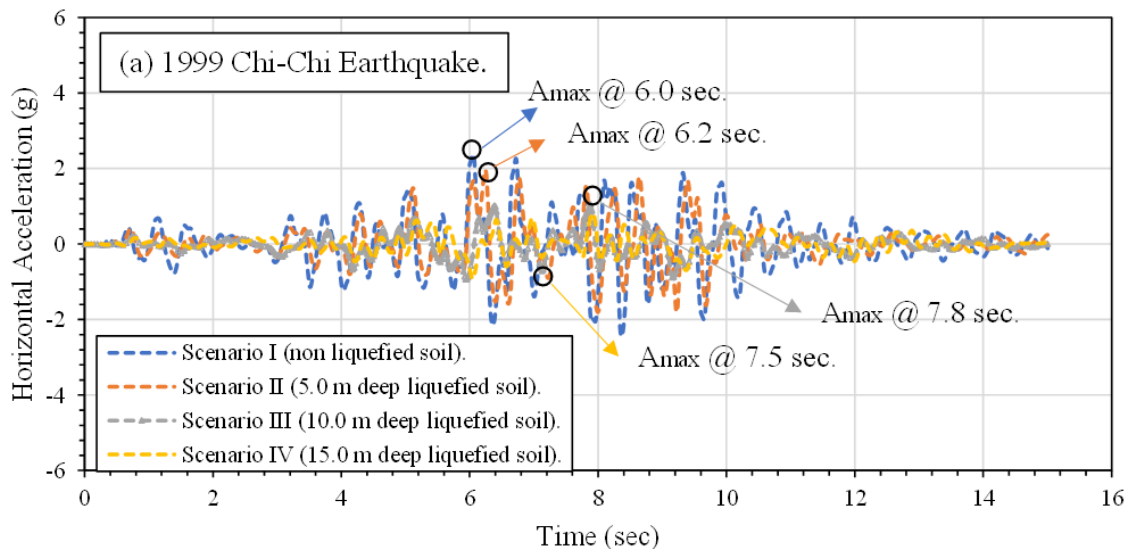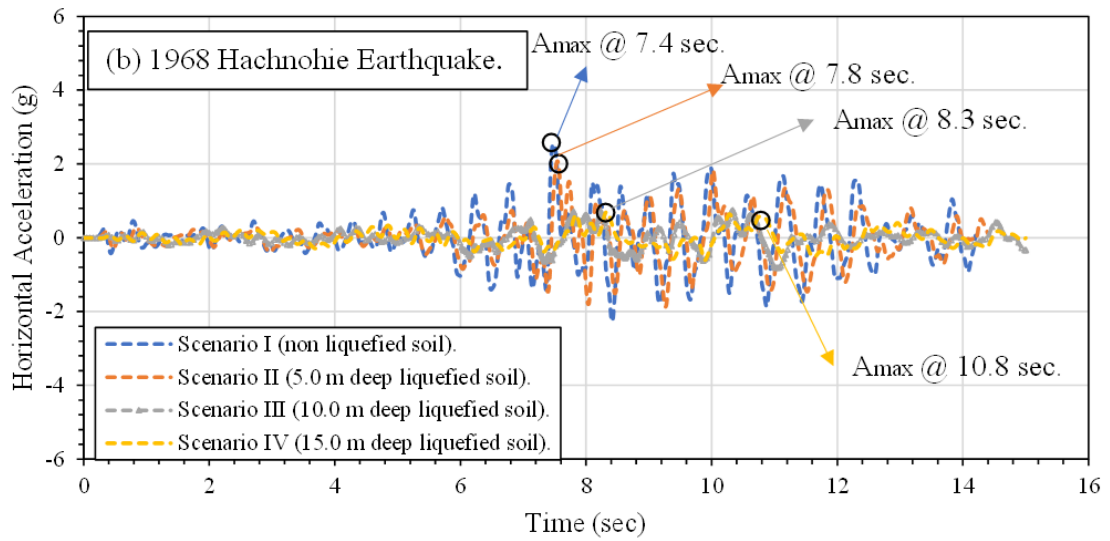
Figure 5.17 Horizontal acceleration record of outer tank roof for different foundation options subjected to (a) 1999 Chi-Chi Earthquake, and (b) 1968 Hachinohe Earthquake.
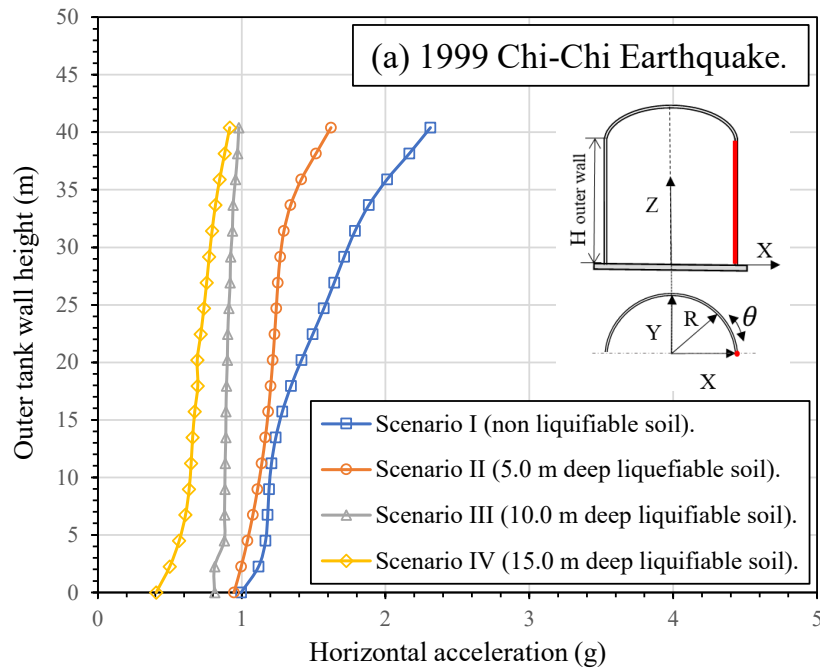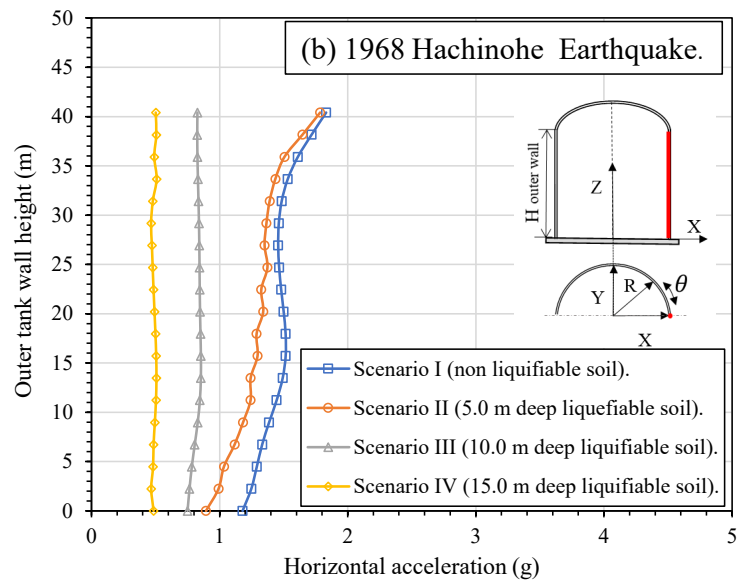
Figure 5.18 Maximum horizontal acceleration profile along outer tank wall for different foundation options subjected to (a) 1999 Chi-Chi Earthquake, and (b) 1968 Hachinohe Earthquake.

Figure 5.19 shows the maximum acceleration for the inner steel tank wall under the 1999 Chi-Chi (Figure 5.19a) and the 1968 Hachinohe (Figure 5.19b) earthquakes. As evident, the acceleration along the inner tank wall experienced significant fluctuations in Z direction (i.e. tank wall elevation highlighting the impacts of seismic FSI as a result of impulsive and convective hydrodynamic forces applied on the tank wall. For both earthquakes, presence of thicker liquefied soil deposit reduced the seismic acceleration induced at the tank base, as well as along the tank wall. Besides, it can be seen that at the location where the convective mass was connected to the wall (i.e. H = 20.0 m), the peak acceleration for the LNG tank under Scenarios III and IV behaved quite differently to Scenario I and II, as the horizontal acceleration increased at convective mass level when the soil liquefied, while an opposite trend was observed for the non-liquefied soil deposit. Indeed, as the liquefied soil thickness increased, the frequency of the seismic load experience by the inner tank decreased, contributing to the increase in the convective mass acceleration, similar to observations made by Kianoush and Ghaemmaghami (2011).
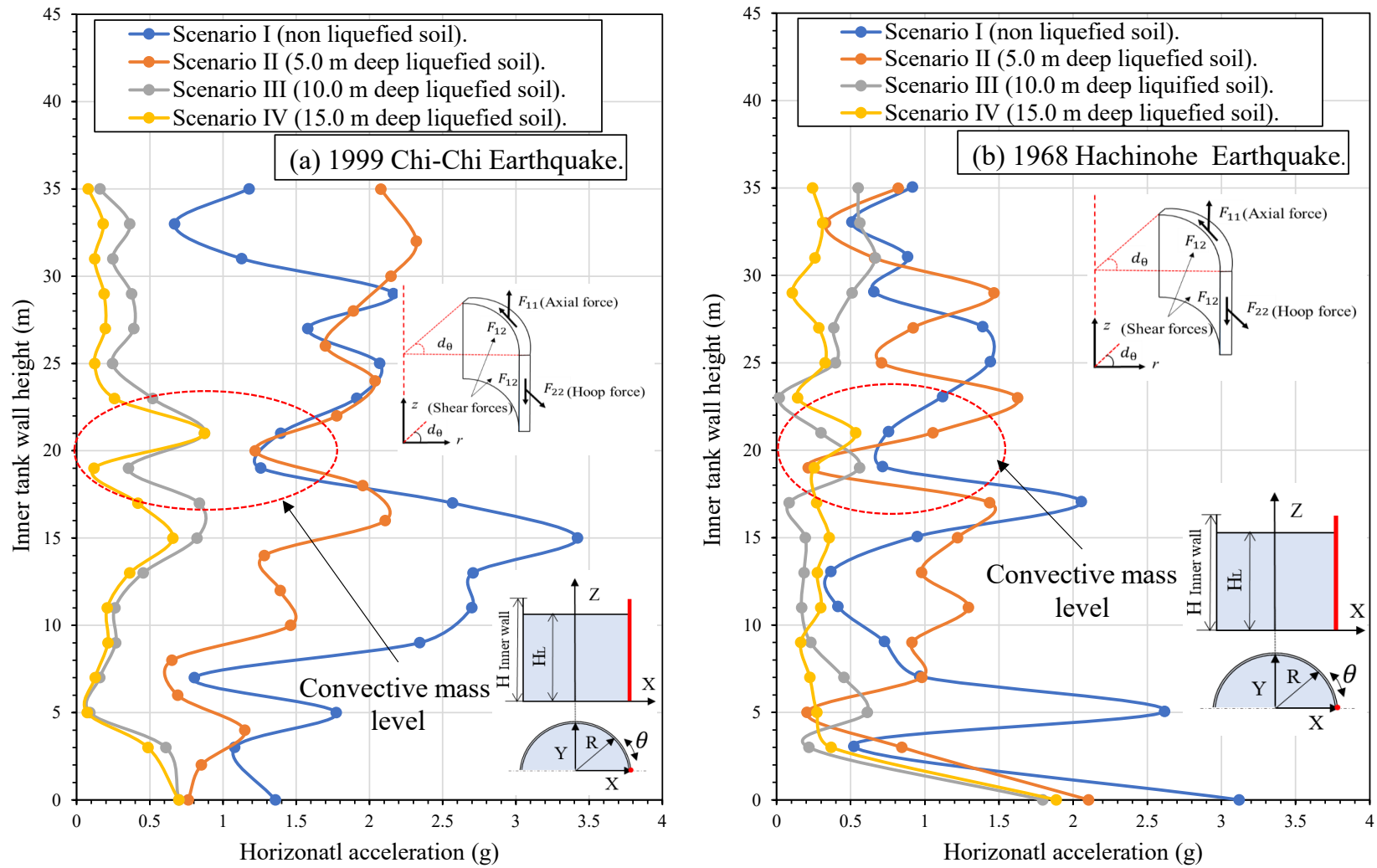
Figure 5.19 Maximum horizontal acceleration profile along Inner tank wall for different foundation options subjected to (a) 1999 Chi-Chi Earthquake, and (b) 1968 Hachinohe Earthquake.

5.5.2.3 *The structural response of the LNG tanks*

The maximum structural response of the inner steel tank under the applied earthquakes in terms of generated forces and displacements along the tank wall are reported and discussed in this section. Assessing the impacts of the soil liquefaction surrounding the piles on the resilience of the steel tank against different failure modes is very crucial. Indeed, the hydrodynamic forces applied to the inner tank as a result of earthquake result in amplified hoop and axial forces in the steel tank wall and potentially cause the inner tank shell buckling. In fact, the shell buckling is the main failure mode for ground supported steel tanks (Brunesi et al. 2015; Dogangun et al. 2009). The failure of steel tanks subjected to the hydrodynamic forces, can be due to elastic or elastoplastic buckling. The elastoplastic buckling occurs when the axial compression and the circumferential hoop stresses (due to the self-weight and hydrostatic and hydrodynamic pressures) exceed the yield limit, often near the based on the tank, and result in an outward bulge appearing which is known as elephant's foot buckling mode. The diamond-shaped buckling mode, which is an elastic buckling often happens at small values of hoop stresses, where inward hydrodynamic suction at the base level of the tank wall or at upper level of the tank wall (corresponding to secondary diamond shape buckling mode) exceed the outward hydrostatic pressure. Indeed, the distribution of the hydrodynamic forces along the tank wall plays a critical role in formation of diamond-shaped buckling, even if stresses remain in the elastic range. Thus, the axial force (F_{11}) and the hoop force (F_{22}) for circumferential unit width of the tank and radial displacements of the inner tank wall are presented and discussed for various foundation conditions.

Figure 5.20 shows the time history of the horizontal displacement of the inner tank top, indicating that the maximum lateral displacements of the inner tank were observed at different times for different soil deposit scenarios. Figure 5.20a indicates that the

189

maximum horizontal displacement of the inner tank under 1999 Chi-Chi earthquake occurred at t = 9.4 sec, 9.3 sec, 10.0 sec and 10.4 sec, for Scenarios IV, III, II, and I, respectively. The corresponding value under the 1968 Hachinohe earthquake were t = 11.0 sec, 10.1 sec, 10.0 sec and 13.0 sec, respectively (Figure 5.20b). It can be noticed that increasing the thickness of the liquefiable soil deposit increased the lateral displacement amplitude and the maximum lateral deformation of the superstructure.
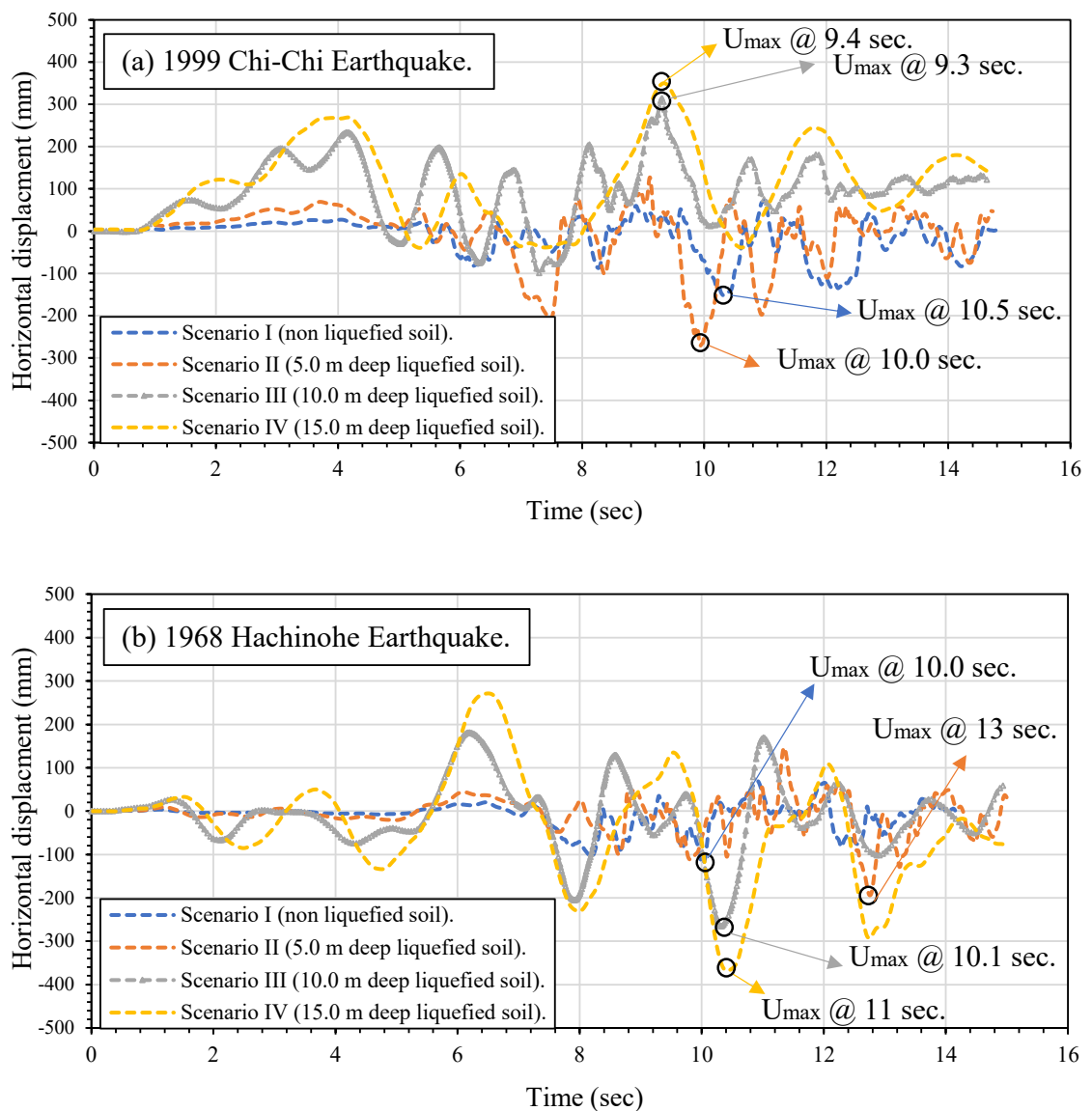
Figure 5.20 Horizontal displacement record of Inner tank top for different foundation options subjected to (a) 1999 Chi-Chi Earthquake, and (b) 1968 Hachinohe Earthquake.

Figure 5.21 shows the distribution of the hoop forces (F_{22}) within the inner tank shell under 1999 Chi-Chi and 1968 Hachinohe earthquakes when the maximum deformation of the tank was recorded. The distribution of the hoop forces along the inner steel tank wall is in a line with the horizontal accelerations recorded for the inner steel tank wall (see Figure 5.19). The maximum hoop forces in the upper portion of the tank wall for the soil deposit Scenarios I and II, exceeded those of Scenarios III and IV. Indeed, since the impulsive mode periods for Scenarios I and II (i.e. 0.51 sec and 0.78 sec as in Table 5.7), were located in the shorter period range of the acceleration response spectrum (Figure 5.16), the amplification of seismic forces was observed. However, the lengthened impulsive mode periods for Scenarios III and IV (i.e. 0.94 sec and 1.17 sec as in Table 5.7) were located in longer period range with decreased spectral accelerate range, which resulted in reduced the seismic forces due to impulsive mass. It is noticed that the maximum hoop forces for the tank built on non-liquefiable soil deposit subjected to the 1999 Chi-Chi earthquake (refer to Figure 5.21a) and the 1968 Hachinohe earthquake (Figure 5.21b) were 1.3 MN/m and 2.87 MN/m, respectively.

On the other hand, Figure 5.22 shows the maximum axial forces (F_{11}) along the inner tank wall at $\theta = 0°$ for different soil deposits considered (i.e. Scenarios I to IV) when the maximum horizontal displacement of the tank was observed. It is evident that the axial forces in the inner tank generally increased from the top to the bottom along the inner steel tank wall with the maximum observed at Z/H =0.10 - 0.375 (or Z/H_L = 0.12 - 0.44). In addition, referring to Figure 5.22, the maximum axial forces in the inner tank wall decreased with the increasing depth of the liquefied soil. For example, under 1999 Chi-Chi earthquake, when the depth of liquefied soil was increased from zero to 5.0 m, the axial force reduced by 21%, and increasing the depth of liquefied soil layer to 10.0 m and 15.0 m reduced the axial force by 42% and 50%, respectively (Figure 5.22a).
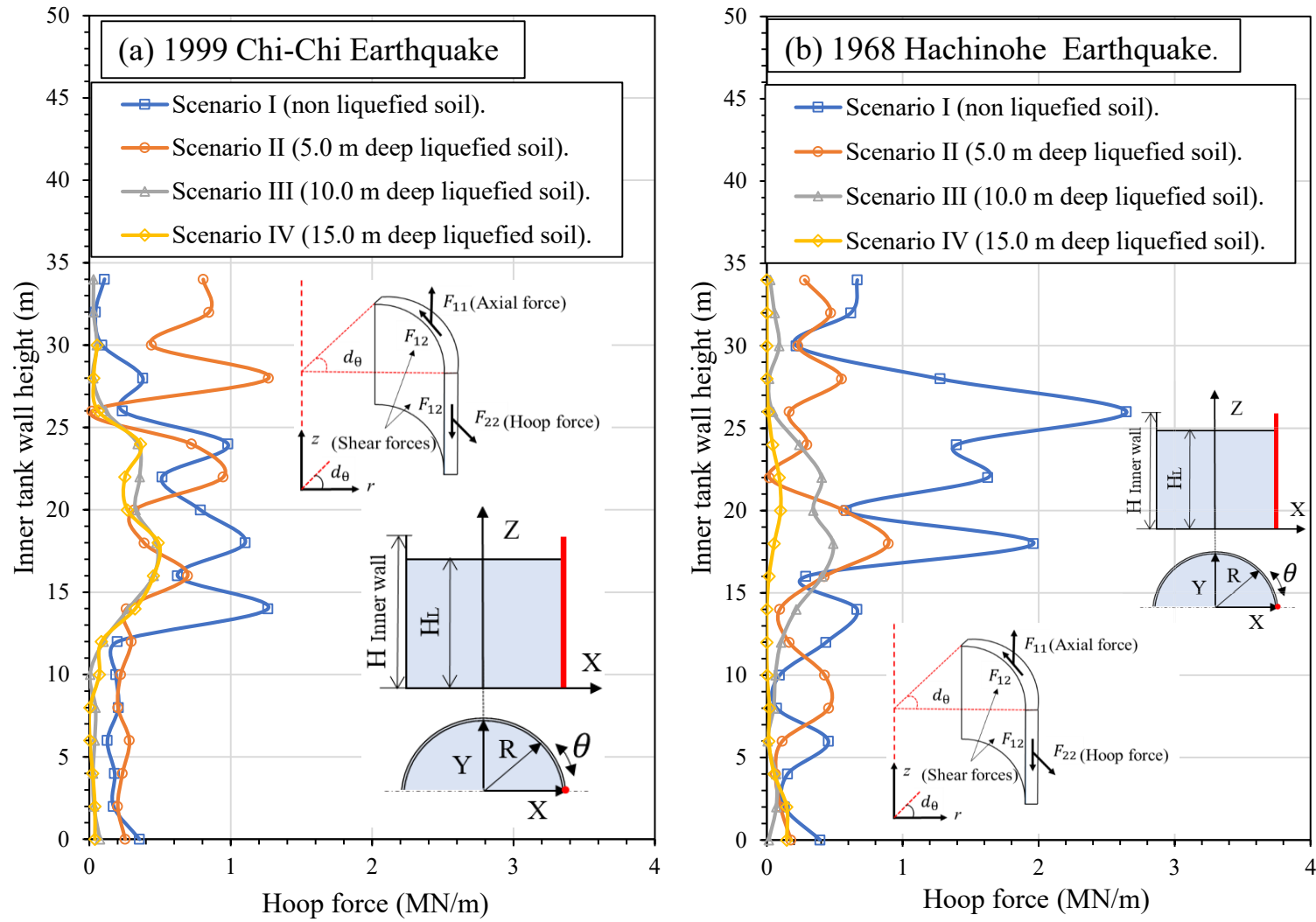
Figure 5.21 Distribution of the hoop forces in the tank wall at $\theta = 0\,^\circ$: to (a) 1999 Chi-Chi Earthquake, and (b) 1968 Hachinohe earthquake.
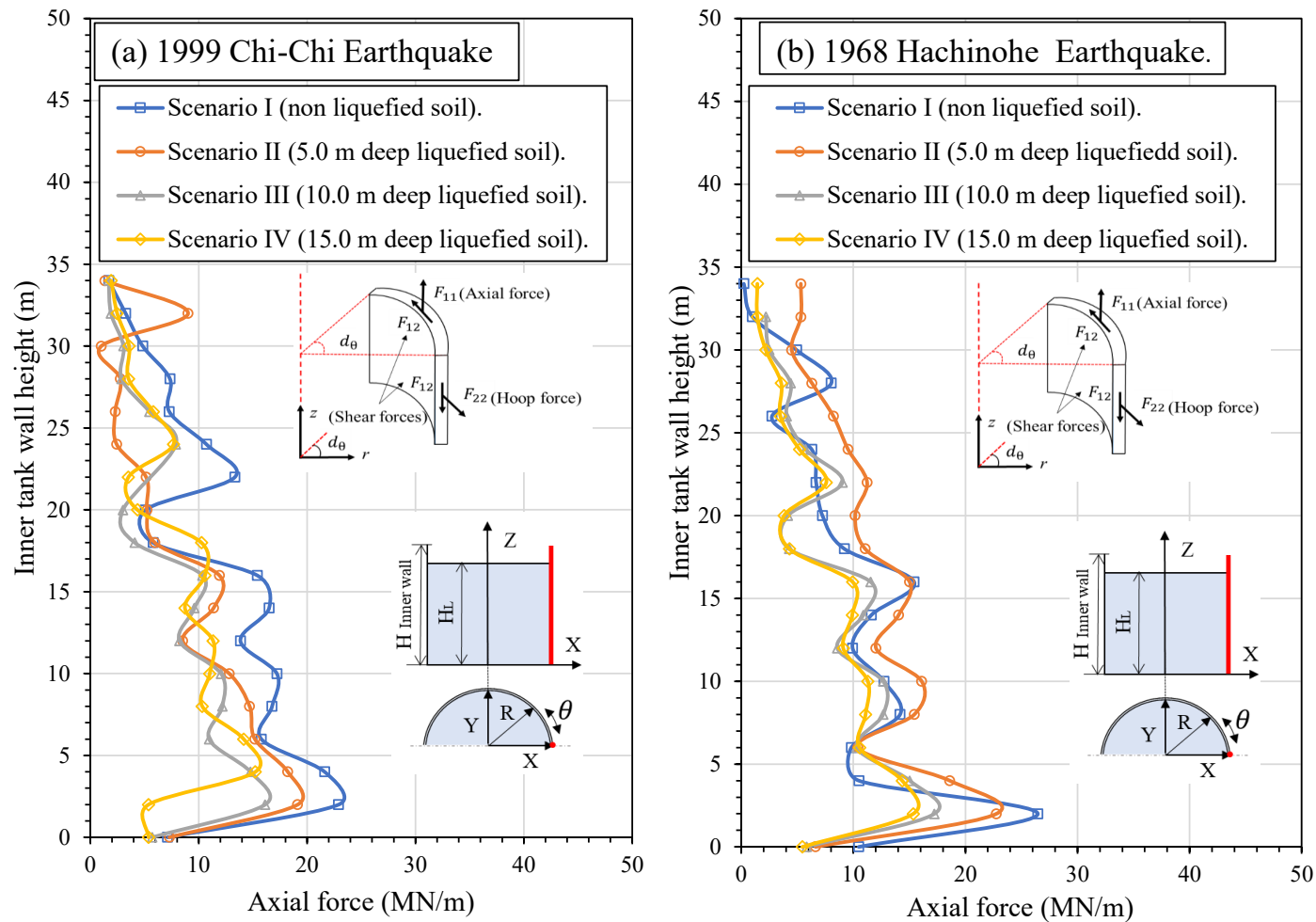
Figure 5.22 Distribution of the axial forces in the inner tank wall at θ = 0°: to (a) 1999 Chi-Chi Earthquake, and (b) 1968 Hachinohe earthquake.

Figure 5.23 captures the distribution of the shear forces along the inner steel tank wall when the maximum lateral displacement was observed (as indicated in Figure 5.20). It is evident that for both earthquakes, the maximum shear forces were observed at the base of the inner tank wall where the maximum axial forces were reported. Moreover, a second local peak of the shear force was recorded near the middle of the tank wall (i.e. $Z/H = 0.45$ or $Z/H_L = 0.52$ in the vicinity of the location where the convective mass was attached to the wall, at which significant variation of the hoop forces were also reported. As evident in Figure 5.23, among the soil deposit scenarios considered, the non-liquefiable soil deposit (Scenario I) resulted in the maximum mobilised shear forces in the inner tank under both earthquakes.
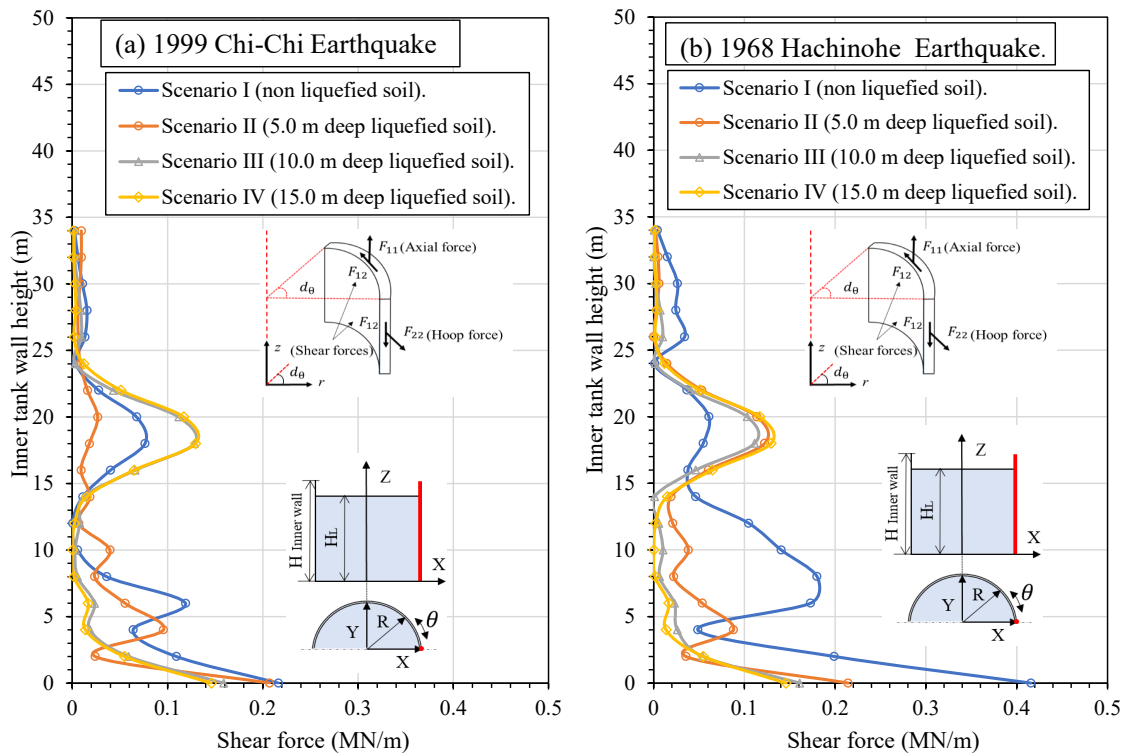
Figure 5.23 Distribution of the shear forces in the inner tank wall at $\theta = 0°$: to (a) 1999 Chi-Chi Earthquake, and (b) 1968 Hachinohe earthquake.

Figure 5.24 shows the radial displacements along the inner tank wall when the maximum lateral displacement was reported (as indicated in Figure 5.20). It is evident

that the most significant radial displacement gradient (or section rotation) was observed in vicinity of the mid-height of the inner tank, where the second peak of the shear forces were observed. Indeed, the convective hydrodynamic force applied at the mid height of the inner tank wall could alert the structural response of the inner tank. As discussed earlier, increasing the liquefied soil depth resulted in changing the seismic waves, mainly by reducing the frequency, resulting in the reduction in the impulsive forces, and in contrary amplification of the convective forces. This observation highlights the importance of including the convective mass in the seismic analysis of the LNG tanks, especially, where the presence of the liquefiable soil deposit can increase the flexibility and natural period of the soil-structure system significantly. This can result in amplified radial displacement of the LNG tank system which can in turn introduce more convective hydrodynamic forces to the system.
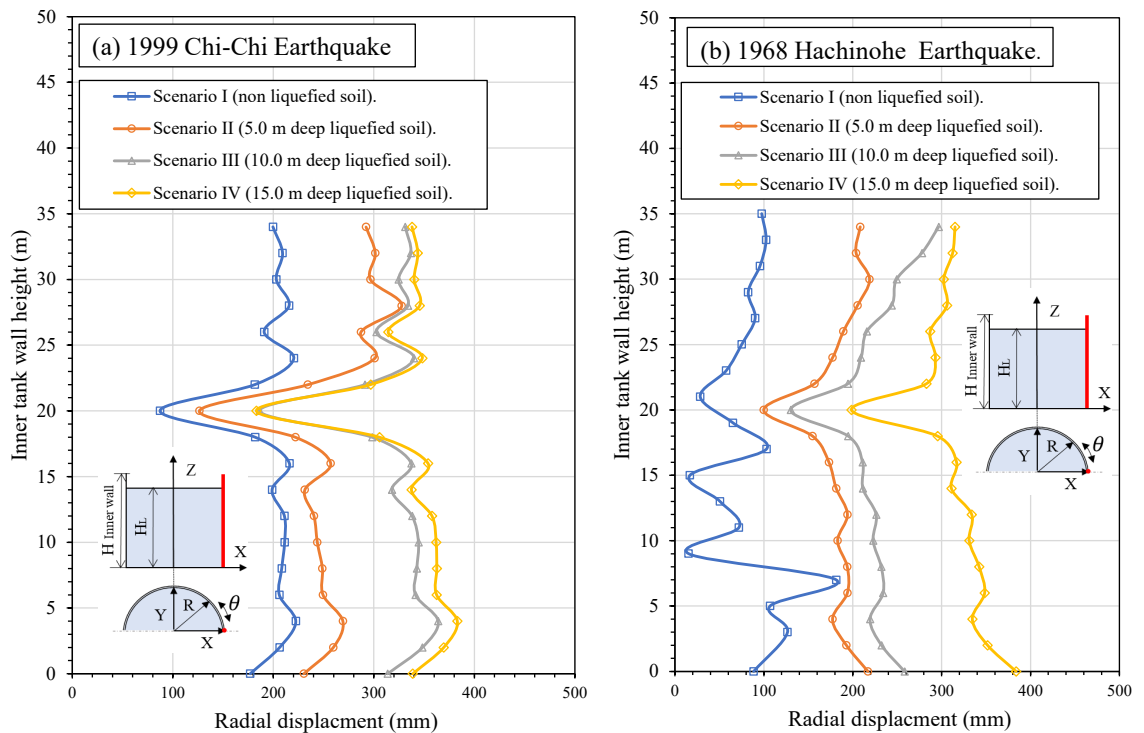
Figure 5.24 Distribution of the Radial displacement in the inner tank wall at θ = 0˚: to (a) 1999 Chi-Chi Earthquake, and (b) 1968 Hachinohe earthquake.

Figure 5.25 presents the maximum von Mises stresses generated in the inner tank wall under the 1999 Chi-Chi (Figure 5.25a) and the 1968 Hachinohe (Figure 5.25b) earthquakes. The results show that the maximum induced von Mises stresses corresponded to the LNG tank built on the non-liquefiable soil deposit (i.e. Scenario I) for both earthquakes, where the maximum induced plastic strains reached 0.29% and 0.89% for the 1999 Chi-Chi earthquake (Figure 5.26a) and the 1968 Hachinohe (Figure 5.26b) earthquakes, respectively. The above observations show that for the LNG tank on the non-liquefiable soil deposit, elastic-plastic buckling may happen in the upper section of the tank where plastic deformations are observed as a result of the von Mises stresses exceeding the yield stress. However, when soil liquefaction occurs, due to period lengthening and significant soil damping, stresses in the inner tank may reduce below the yield limit, while more concentrated stresses may be observed in the lower section of the tank near the base, where potential elephant foot buckling failure may occur.

(a) 1999 Chi-Chi Earthquake.
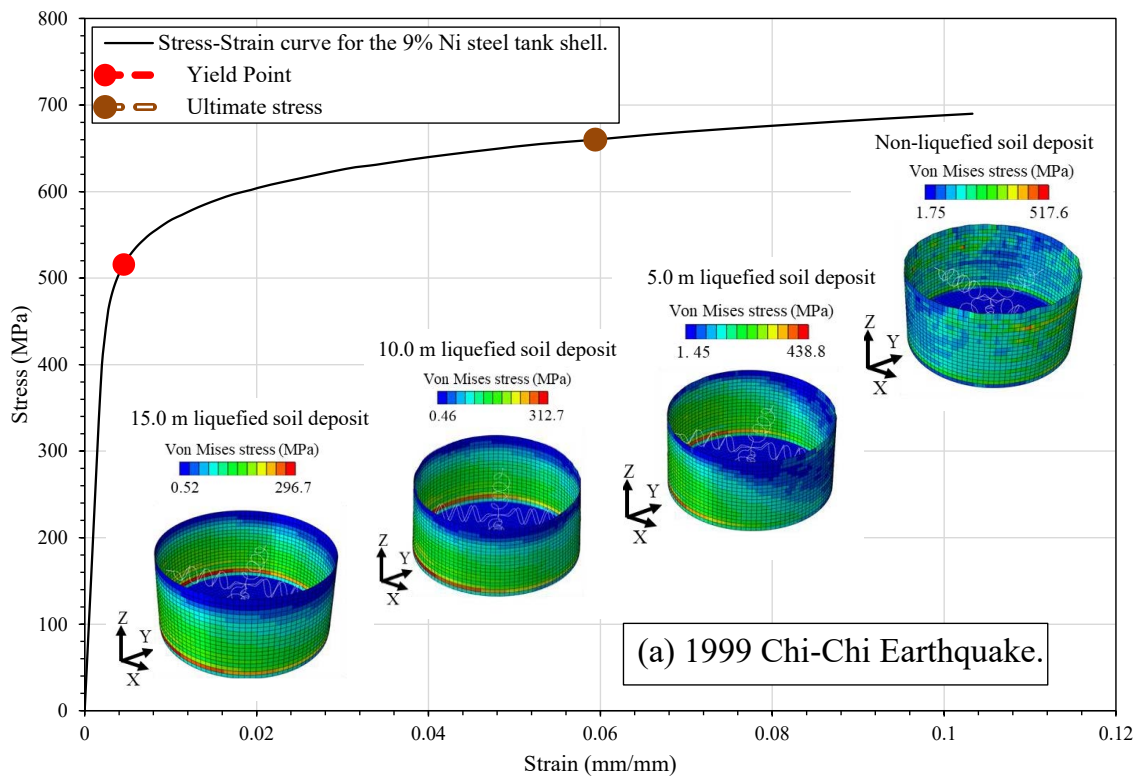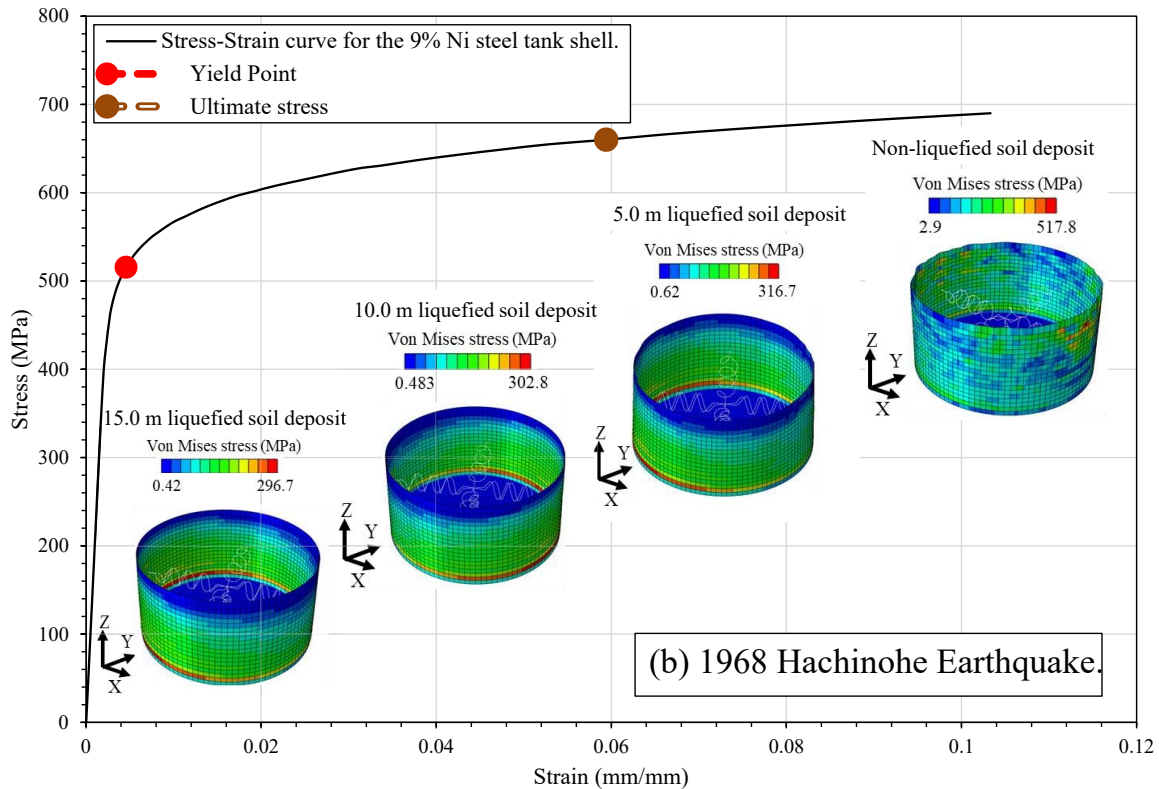
Figure 5.25 The maximum von Mises stress on the inner 9% Ni steel tank wall and the location of the maximum stress on the stress- strain under (a) 1999 Chi-Chi Earthquake, (b) 1968 Hachinohe earthquake.

Figure 5.27 and 5.28 present the maximum von Mises stresses generated in the outer tank wall under the 1999 Chi-Chi and the 1968 Hachinohe earthquakes, respectively. It should be mentioned here that since no failure was observed in the inner tank under any analysed scenarios, no leakage of LNG from the inner tank was considered, and thus LNG was not in the direct contact with the outer tank wall in this study. It is evident that the non-liquefied soil deposit scenario (Scenario I) led to the maximum generated von Mises stresses in the outer tank wall. According to Figure 5.27, the maximum von Mises stress decreased from 25.9 MPa to 19.9 MPa when the top 5.0 m of soil deposit had liquefied under 1999 Chi- Chi earthquake, while when the liquefied soil layer extended to 10.0 m and 15.0 m, the maximum von Mises stresses reduced to 18.4 MPa and 10.9 MPa respectively. It can be seen that the maximum stresses in the outer tank were generated at the connection between the tank wall and the roof for both earthquakes. Moreover, referring to Figure 5.28, the maximum von Mises stresses

decreased by 5%, 4% and 19% when the liquefied soil depth increased from zero to 5.0 m, 10.0 m and 15.0 m respectively. These results are in a line with the maximum acceleration reported for the outer tank as in Figure 5.17 and 5.18.

(a) Non-liquified soil deposit under 1999 Chi-Chi Earthquake.

Von Mises stress (MPa)

1.75   517.6

Principle plastic strain (%)

0.0   0.278

Input earthquake (in *X* direction)

Input earthquake (in *X* direction)
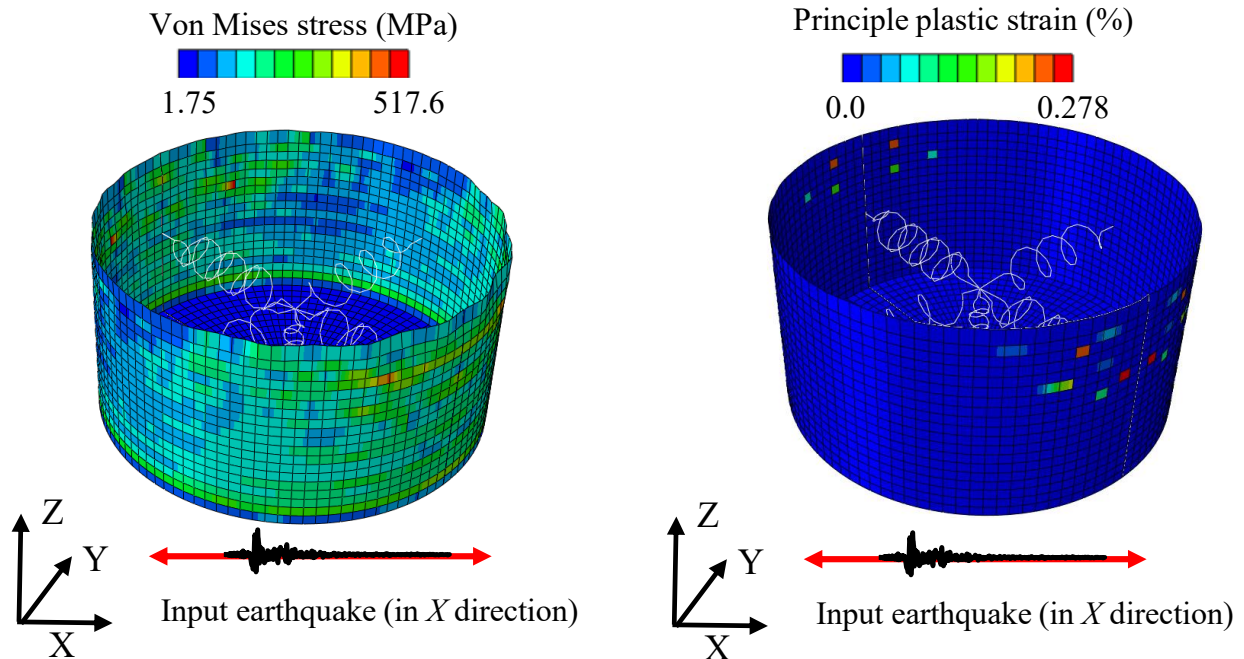
(b) Non-liquified soil deposit under 1968 Hachinohe Earthquake.

Von Mises stress (MPa)

2.6   517.8

Principle plastic strain (%)

0.0   0. 89

Input earthquake (in *X* direction)

Input earthquake (in *X* direction)
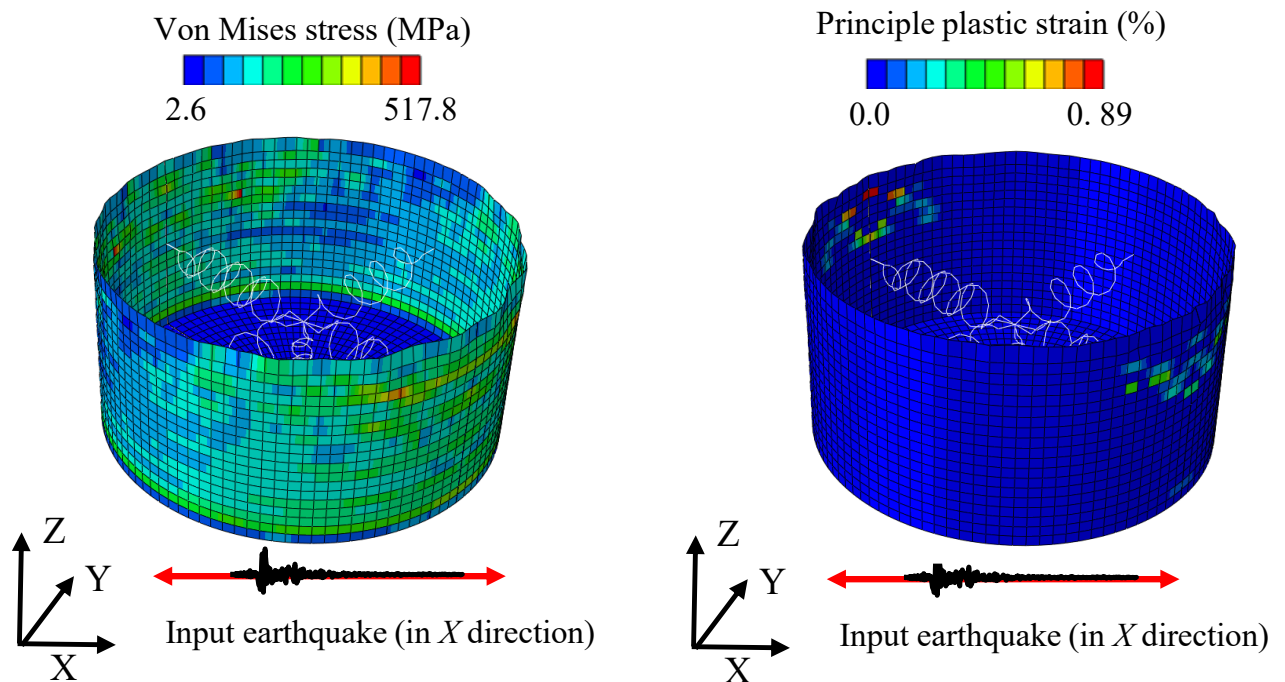
Figure 5.26 The maximum von Mises stress on the inner 9% Ni steel tank wall and the corresponding plastic strain at the end of the earthquake of (a) 1999 Chi-Chi Earthquake, (b) 1968 Hachinohe Earthquake.

198

(a) Non-liquified soil deposit under Von Mises stress (MPa)

0.3   25.9

Maximum von Mises stress at t= 6.2 sec.

(b) Liquified soil depth 5.0 m. Von Mises stress (MPa)

0.28   19.9

Maximum von Mises stress at t= 6.5 sec.

(c) Liquified soil depth 10.0 m. Von Mises stress (MPa)

0.28   18.4

Maximum von Mises stress at t= 7.7 sec.

(d) Liquified soil depth 15.0 m. Von Mises stress (MPa)

0. 126   10.9

Maximum von Mises stress s at t= 7.9 sec.

Z Y   1999 Chi-Chi Earthquake.

X

Input earthquake (in X direction)
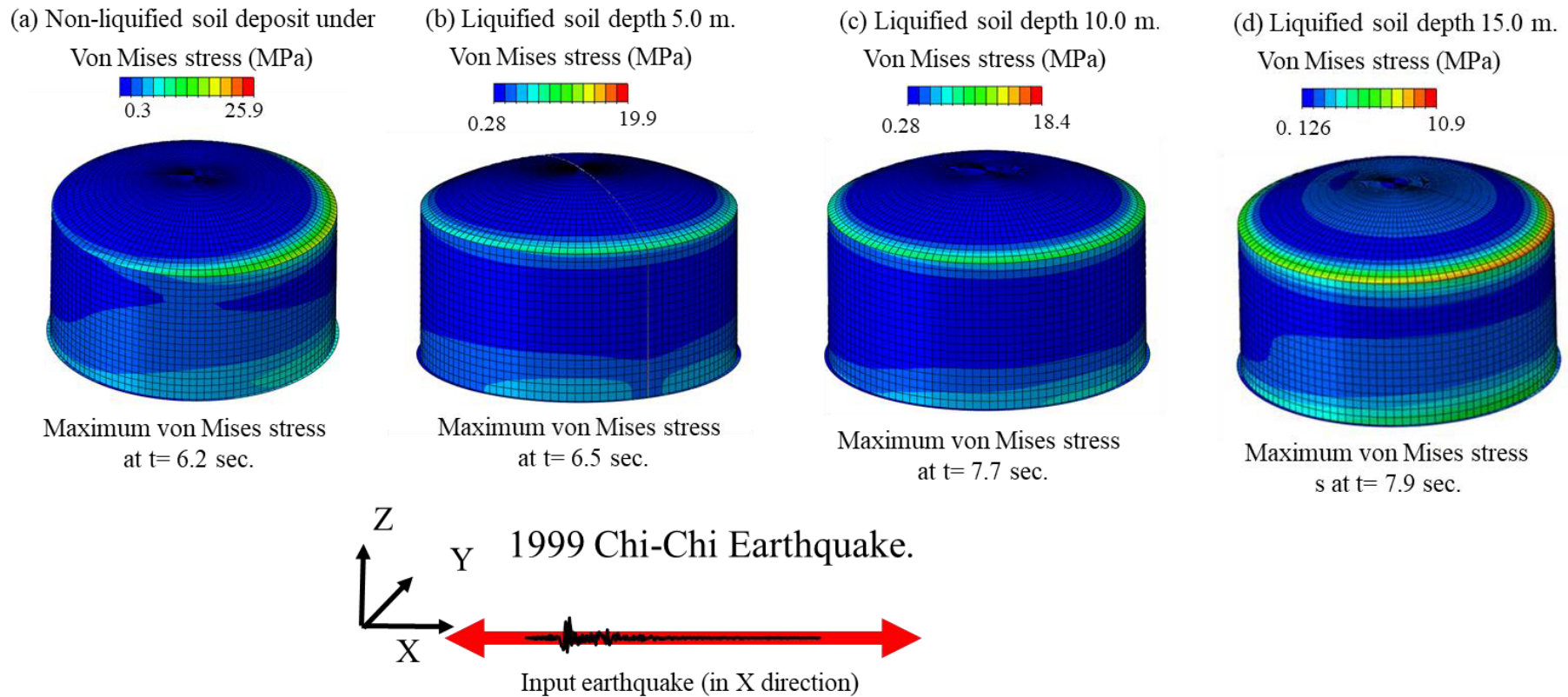
Figure 5.27 The maximum von Mises stress on outer concrete tank under the effect of 1999 Chi-Chi Earthquake for different soil deposit scenarios namely, (a) non-liquified soil deposit, (b) 5.0 m liquified soil depth, (c) 10.0 m liquified soil depth and (d) 15.0 m liquified soil depth.

(a) Non-liquified soil deposit under
Von Mises stress (MPa)

0.3   20.9

Maximum von Mises stress
at t= 7.2 sec.

(b) Liquified soil depth 5.0 m.
Von Mises stress (MPa)

0.12   19.9

Maximum von Mises stress
at t= 7.5 sec.

(c) Liquified soil depth 10.0 m.
Von Mises stress (MPa)

0.21   19.2

Maximum von Mises stress
at t= 8.2 sec.

(d) Liquified soil depth 15.0 m.
Von Mises stress (MPa)

0. 16   16.9

Maximum von Mises stress
s at t= 8.2 sec.

Z
Y
X
1968 Hachinohe Earthquake.

Input earthquake (in X direction)
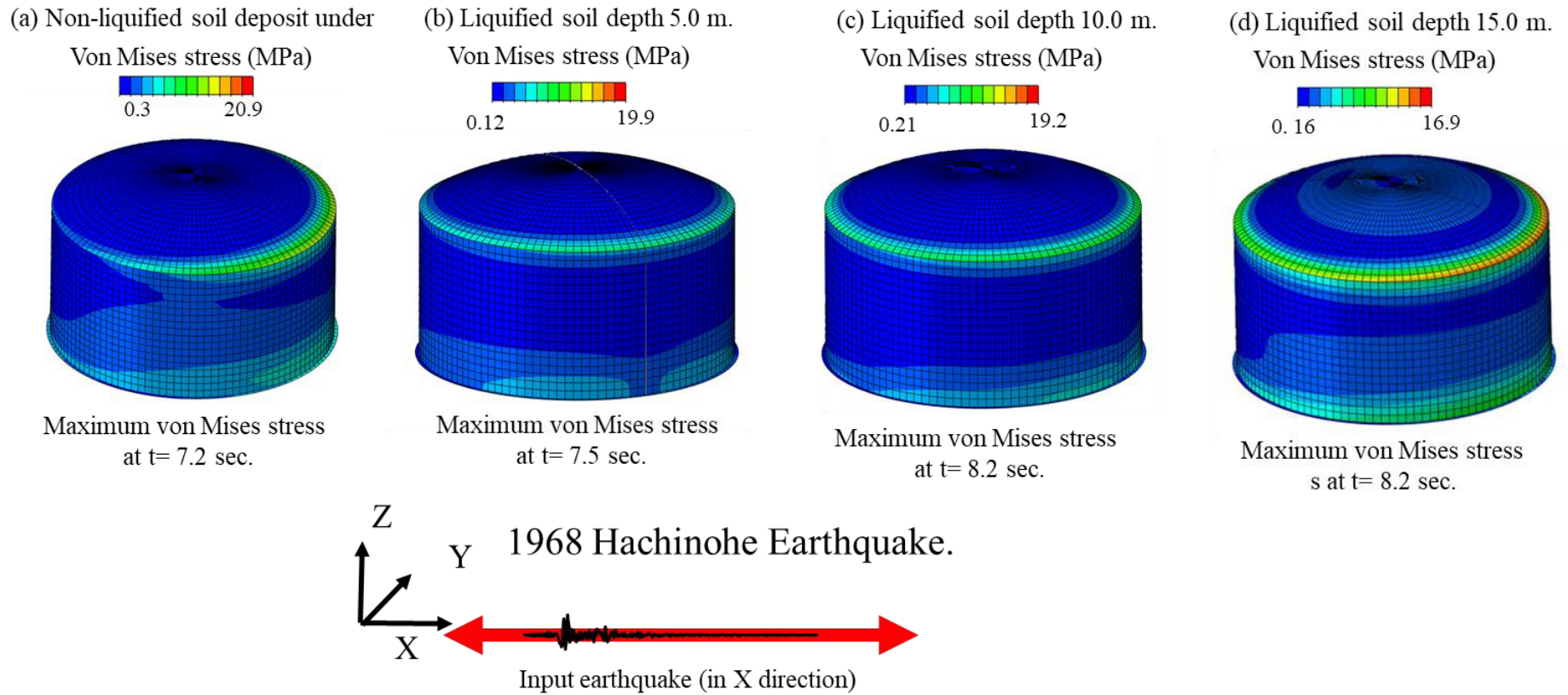
Figure 5.28 The maximum von Mises stress on outer concrete tank under the effect of 1968 Hachinohe Earthquake for different soil deposit scenarios namely, (a) non-liquified soil deposit, (b) 5.0 m liquified soil depth, (c) 10.0 m liquified soil depth and (d) 15.0 m liquified soil depth.

5.5.2.4   *Seismic response of pile foundation*

To examine the impacts of liquefiable soil deposit on the piles supporting the LNG tank performance, the pile in the outermost ring of piles in *Y* direction as shown in Figure 5.29 was selected. This pile was selected because it is under the outer tank wall and resists the highest shear forces, lateral displacement and overturning effects (Tajirian et al. 2019). Referring to Figures 5.29 – 5.31, the lateral displacement, shear force, and bending moment profiles along the pile length were reported when the maximum response (i.e. displacement) at the pile head was observed.

Referring to Figure 5.29, as the liquefied soil depth increased, the lateral pile displacement also increased. Indeed, since the liquefied soil layer lost the stiffness and shear strength significantly, the ground displaced more laterally and piles experienced larger deflections. According to Figure 5.29a, the maximum lateral deflection of the pile head increased from 72 mm to 150 mm, 272 mm and 330 mm when the liquefiable soil depth increased from 0 (non-liquefiable soils deposit Scenario I) to 5.0 m (Scenario II), 10.0 m (Scenario III), and 15.0 m (Scenario IV) under the 1999 Chi-Chi earthquake, respectively. The corresponding lateral displacements for the 1968 Hachinohe earthquake were 80 mm (Scenario I), 155 mm (Scenario II), 243 mm (Scenario III) and 410 mm (Scenario IV), respectively (see Figure 5.29b).

Figure 5.30 and 5.31 show the shear force and bending moment envelopes along the pile length. In general, once the seismic wave affected the superstructure, the inertial forces transferred from the superstructure to the pile heads and ultimately to the soil deposit. After the liquefaction occurred, more lateral displacement was developed in the vicinity of the ground surface which induced more bending moments near the top of the piles. Therefore, the piles behaved like rather unsupported column in that section. As the liquefied soil depth increased, the pile head displacement increased and subsequently the

shear forces increased as in Figure 5.30.

Similar to shear forces, the bending moments developed at the pile head amplified as the depth of liquefied soil increased. As Figure 5.31 shows, in Scenario I, where the soil deposit was non-liquefiable, the maximum bending moment was observed at the pile head, while for other scenarios where soil liquefaction occurred, local amplified bending moments were observed well below the ground surface. In addition, the higher values of bending moment and shear forces were observed at the border between the liquefied and non-liquefied soil layers where abrupt the soil stiffness change was observed. These results are comparable with observations made by Rostami et al. (2017) and Dobry et al. (2003) where plastic hinges were generated in the piles at the boundary between the liquefied and non-liquefied soil layers. However, for heavy superstructure such as LNG tanks, the maximum bending moments are expected to occur at the pile head due to the large inertial forces, which could exceed the bending moments observed at the boundary between the liquefied soil layer and non-liquefied soil layer. In this study when over one third of the entire soil was liquefied soil (i.e. Scenarios III and IV), the bending moments in the pile exceeded the yield stress. For example, as shown in Figure 5.31, the generated bending moments in the piles for Scenario III were 6.6 MN.m (1999 Chi-Chi earthquake) and 6.5 MN.m (1968 Hachinohe earthquake) which exceeded the yield moment of pile M_{yield} = 5.8 MN.m, resulting in formation of plastic hinges in the piles. Similarly, the corresponding bending moment generated at the pile head for Scenario IV for both earthquakes reached the ultimate moment capacity of the pile $M_{ultimate}$ = 7.5 MN.m resulting in the bending failure of the piles.
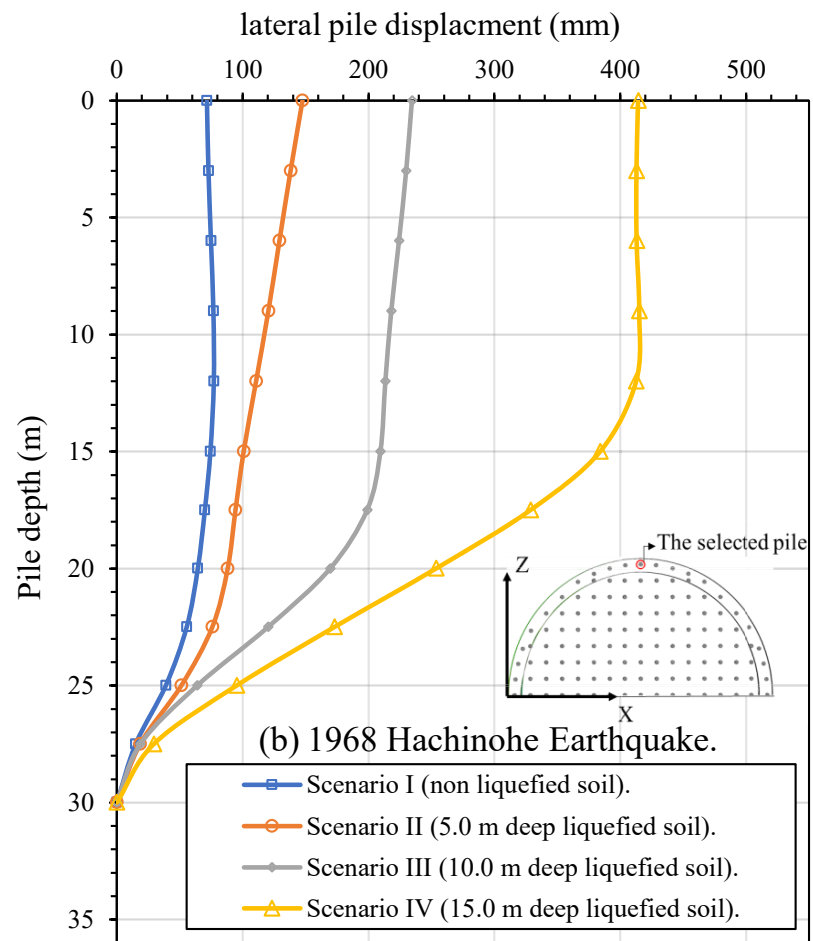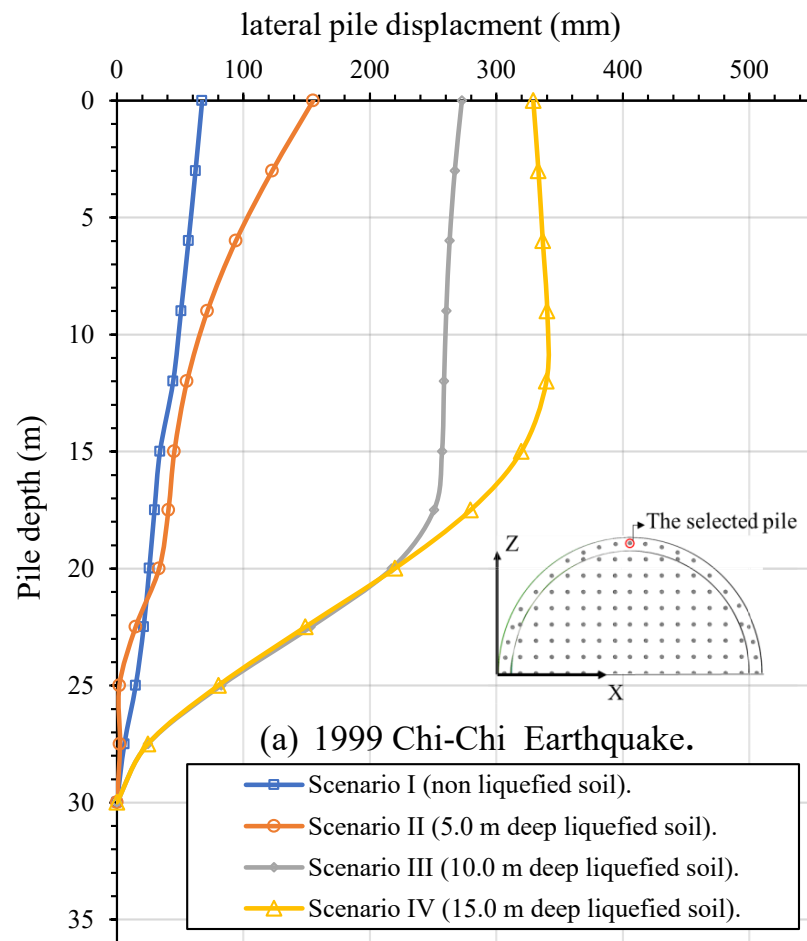
Figure 5.29 Maximum lateral pile displacement for different soil deposit scenarios along the pile length subjected to (a) 1999 Chi-Chi Earthquake, (b) 1968 Hachinohe earthquake.
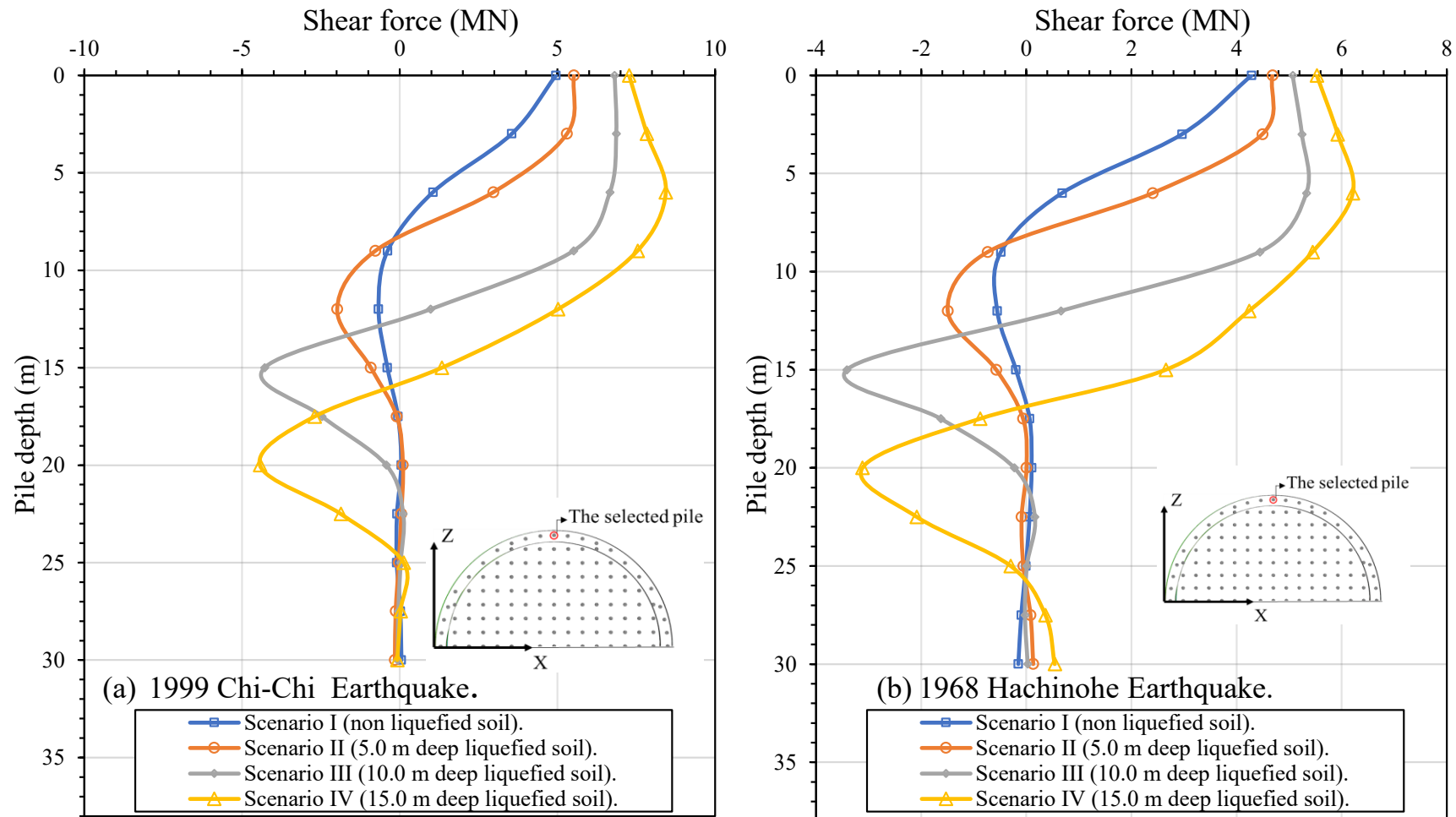
Figure 5.30 Maximum shear force profile imposed on the pile for different soil deposit scenarios along the pile length subjected to (a) 1999 Chi-Chi Earthquake, (b) 1968 Hachinohe earthquake.
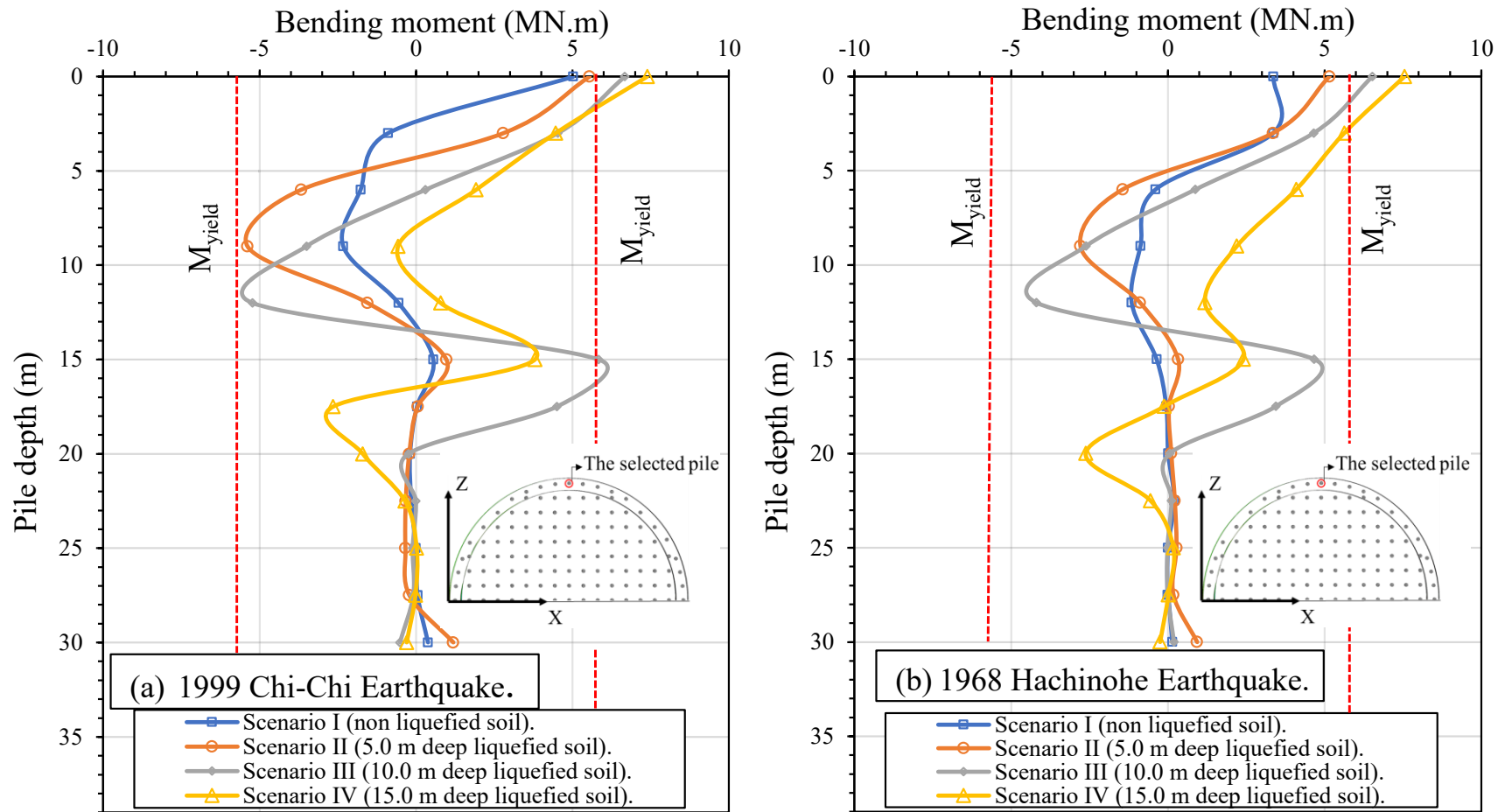
Figure 5.31 Maximum bending profile imposed on the pile for different soil deposit scenarios along the pile length subjected to (a) 1999 Chi-Chi Earthquake, (b) 1968 Hachinohe earthquake.

The variations of soil stiffness and strength with depth can influence the inertial and kinematic interactions impacting the seismic response of piles and resulted reported in Figures 5.29 – 5.31 illustrate these effects for pile foundation used in this study. The observed inertial interaction stemmed from the movement of the tank generating more seismic response in the upper part of the piles due to the rigid linking between piles and foundation cap, and the forces decayed rapidly with depth in the case of non-liquefiable soil (Scenario I) as evident in Figures 5.30 and 5.31.

When the soil deposit liquefied (i.e. Scenarios II to IV), although the impact of inertial interaction on piles reduced (i.e. less base shear transferred tothe superstructure as revealed in Figure 5.23), the seismic response of piles increased in the upper part of the piles (see Figures 5.30 and 5.31). This is due to the fact that the kinematic interaction between the piles and the surrounding soil became more significant. Indeed, kinematic interaction is caused by the inability of a foundation to match the deformation of the surrounding soil (Kramer 1996). The presence of liquefied soil layer (Scenarios II to IV) introduced larger difference between the stiffnesses of the piles and the nearby soil compared to Scenario I. Consequently, the incapability of the piles to follow the adjacent soil distortion was more substantial resulting in more kinematic interaction induced loads (i.e. shear forces and bending moments). It can be concluded that when the liquefaction occurred in the shallow depth only, the kinematic interaction had a dominant impact on the pile response over inertial interaction. Indeed, with the increase in the thickness of the liquefied layer, the loads developed in the piles due to kinematic interaction increased and extended deeper, while the loads due to inertial interaction decreased.

5.6   Summary

Three-dimensional numerical models were developed using ABAQUS (version 2018) to evaluate the impact of liquefiable soil deposit depth on the seismic resilience of LNG tanks. The multi-interaction mechanisms, including SFSI and FSI effects, were taken into account in this study using direct technique analysis. The free vibration analysis was performed using the Block Lanczos algorithm to investigate the effect of the liquefiable soil deposit depth on the dynamic properties of LNG tanks. In addition, the nonlinear time history analysis was conducted for LNG tanks under the effect Safe Shutdown Earthquake (SSE) hazard level. Material and geometric nonlinearities of the SFSI system were considered wisely. Soil properties implemented in this study was taken from field and laboratory tests. For the clay soil layer, the verified and calibrated NKH soil model was adopted. For the liquefiable soil deposit, post-liquefaction parameters were obtained from the existing literature, and the damping behaviour of the liquefied soil was captured using Rayleigh damping formulation via Rayleigh damping coefficients. The CDP model was used for the outer RC tank with emended reinforced layers option. The linear kinematic hardening rule was used for the inner steel tank inelastic cyclic response. The hybrid modelling technique was used for reinforced piles to capture the elastic-plastic response of the piles by implementing the moment-curvature relationship.

The analyses considered different thicknesses of the liquefied soil deposit varying from zero (no liquefaction) to 15 m measured from the ground surface. The results revealed the importance of damping effect of the partial liquefied soil layer on the performance of a large pile group (e.g. 229 piles for LNG tank) and how increasing the depth of the liquefied soil deposit decreased the seismic forces generated in the superstructure. The predictions showed that the von Mises stresses in the inner steel tank

exceeded the yield stress for non-liquefied soil deposits. The elastic-plastic buckling was initiated in the upper section of the tank, where plastic deformations were detected due to excessive von Mises stresses. However, when soil liquefaction occurred, although von Mises stresses in the inner tank shell remained below the yield limit, localised stress concentrations were observed in the lower section of the tank near the base, increasing the risk of the elephant foot buckling. The results for pile foundations represented how the lateral displacements, shear forces, and bending moments in the piles increased with increasing depth of the liquefied soil.

Moreover, the results indicated the severe risk of extended liquefied soil depth as the lateral displacements of piles increased and amplified bending moment were recorded near the pile head. This observation was more significant when liquefied soil depth exceeded one-third of the entire soil deposit; hence, the bending moment at the pile head exceeded the yield moment capacity of the pile, and subsequent plastic hinges were formed. Indeed, when the thickness of the liquefied soil was more than half of the entire soil depth, the mobilised bending moments in the piles exceeded the ultimate moment capacity of the pile, resulting in failure of the piles. Moreover, the results showed that the inertial interaction had a dominant impact on the pile response. With increasing the thickness of the liquefied layer, the forces developed in the piles due to the kinematic interaction increased, while the inertial interaction induced forces decreased.

CHAPTER 6   CONTEMPORARY PROBLEMS FOR LNG CONTAINMENT ON RIGID BASE CONDITION

6.1   General

This chapter investigates the effect of different tank conditions for LNG storage containments, impacting the dynamic characteristics and seismic performance under the design earthquakes. In particular, the seismic vulnerability of the inner steel LNG tanks with varying height (H) to diameter (D) aspect ratios are investigated. Moreover, the effect of the wall support condition of the secondary RC tank (i.e. both hinged and fixed wall support conditions) is investigated using time history dynamic analysis.

6.2   Impacts of steel LNG tank aspect ratio on seismic vulnerability subjected to near-field earthquakes

6.2.1   Introduction

The global demand for Liquefied Natural Gas (LNG) has been continuously increasing with average yearly growth of approximately 6.6% in the last twenty years. Several factors derive the demand expansion globally, including conversion to cleaner and cheaper fuels for power generation as compared to coal and fuel oil. This leads to an increasing need for smart and affordable storage solutions. Full-containment above-ground LNG tanks have been one of the most common storage options. A full-containment LNG tank consists of (i) an inner cylindrical tank normally open-top steel tank made of cryogenic steel (9% Ni) to fulfil ductility requirements at the operating temperature and (ii) an outer reinforced concrete tank to ensure structural resistance to withstand the external hazards.

The fundamental period range for common LNG tanks are usually between 0.1 sec and 0.5 sec which coincides with the peak of the design response spectrum for most of earthquake ground motions. As such, LNG tanks can absorb significant energy during earthquake events. The safety of these tanks against earthquake excitations is crucial as the environment and economic losses can be significant in case of any damage or failure.

The seismic design of the LNG tanks normally follows the similar standpoint to the nuclear power plants by implementing the two earthquake level scenarios, namely the Operating Basis Earthquake (OBE) and Safe Shutdown Earthquake (SSE) scenarios with no leakage permitted at SSE level (Willford et al. 2010). The main difference between the seismic design of the liquid storage tanks and other civil structures is the hydrodynamic loadings and interaction between the tank structure and the contained liquid which makes tanks (Hokmabadi et al. 2014), particularly inner steel tanks with relatively thin walls, vulnerable to failure or damage (e.g. the thin-walled buckling failure mode).

Dynamic buckling phenomenon in steel tanks under seismic effect is generally identified as elastic or elastic-plastic buckling. Many studies showed the elastic-plastic buckling as an outward bulge close to the tank base when the axial compression due to overturning moment and the circumferential hoop stresses, which results from both the hydrostatic and hydrodynamic pressures at the bottom of the tank, exceed the yield limit. This outward bulging occurs at tank base identified as elephant's foot buckling mode. Indeed, the diamond-shaped buckling mode, which is an elastic buckling happens usually at small values of hoop stresses, as the inward hydrodynamic suction at the base level of the tank wall or at upper level of the tank wall (i.e. secondary diamond shape buckling mode) goes beyond the outward hydrostatic pressure (Brunesi et al. 2015).

The FSI concept has been studied by several researchers such as Housner (1957)

and Veletsos and Yang (1976) where the hydrodynamic pressure from the liquid was deemed to be decomposed of impulsive and convective liquid mode. The impulsive portion is due to the liquid coincidentally vibrating with the tank wall, while the convective portion is due to the upper portion of liquid sloshing as waves at the surface of liquid. These two forces can be combined in a simple mechanical model to represent the dynamic response of liquid storage tanks as reported by Haroun and Housner (1981) and Malhotra et al. (2000).

Several research studies and experiments have been carried out on the dynamic behaviour of liquid storage tanks, some of these studies have been conducted on the inner steel LNG tank to assess the effect of the hydrodynamic forces and enhance their seismic performance. For example, compared the seismic behaviour of the LNG tank using the finite element analysis (FEA) method and the simplified mechanical model, usually used for preliminary seismic analysis and design of liquid storage tank. The results demonstrated that the mechanical models could be used with confidence for the preliminary analysis and design of conventional and isolated LNG tanks (Christovasilis and Whittaker 2008). In addition, Zhou et al. (2018) investigated the effects of base isolation on the seismic response of LNG tanks with different filling liquid levels using finite element analysis (FEA) technique, and their numerical results shown that the lead rubber bearings were very effective in avoiding the significant portion of seismic forces transferring to the tanks and thus enhancing the seismic responses of the LNG tanks.

This study investigates the impact of the aspect ratio (i.e. tank height to diameter H/D) on the seismic response of the 9% Ni steel inner LNG tank under near-field earthquake excitations. For this purpose, three-dimensional finite element simulation using ABAQUS software, capturing material and geometric nonlinearities, were adopted. The FSI effect was considered utilizing the added-mass technique. The seismic response

of different tanks is presented and discussed.

6.2.2 Details of adopted storage tanks

To demonstrate the height to diameter (*H/D*) aspect ratio effect on the seismic response of the inner 9% Ni steel LNG tank, three geometric configurations were used in this study (see Figure 6.1). The considered tanks were anchored vertical cylindrical ground supported tanks, with the constant diameter of 30.5 m (representing typical modular inner LNG tank size), and different *H/D* ratios of 0.95 (Tank A), 0.63 (Tank B), and 0.40 (Tank C) corresponding to tall, medium and broad tanks as classified by (Virella et al. 2006),respectively. The filling level of the LNG liquid height was considered to be 90% of each tank height, which represent the full condition with 10% of freeboard. The structural design of tanks (i.e. wall thicknesses) follows API-650 (2007) (i.e. American Petroleum Institute) fulfilling the seismic design requirements for fully anchored tanks in high seismic regions.
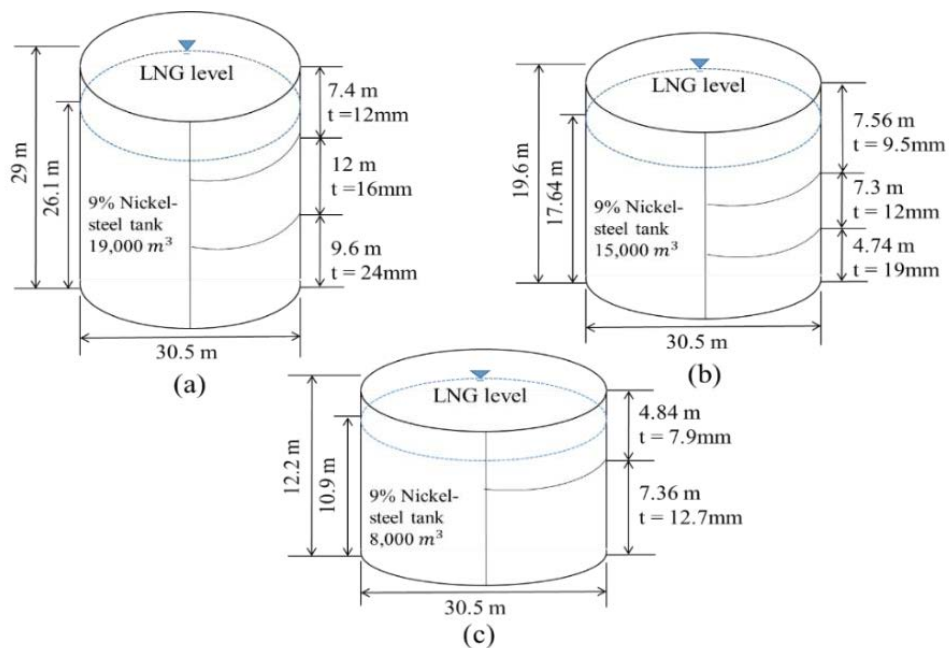
Figure 6.1 The considered tank models, (a) tall Tank A with *H/D*=0.95, (b) medium Tank B with *H/D*=0.63, and (c) broad Tank C with *H/D*=0.40.

6.2.3 Fluid-Structure Interaction effects

The seismic analysis of liquid storage tanks generally should capture the liquid hydrodynamic forces applied on the tank wall. Evaluation of hydrodynamic forces, given the complex nature of the FSI phenomenon, have been previously investigated via simplified mechanical models, which assume that the loads applied from the liquid to the storage tank walls can be represented in two parts, namely the convective and impulsive forces. The convective component (sloshing mode) relates to the oscillation in the higher region of the stored liquid, while the impulsive component (rigid movement of liquid) corresponds to the dynamic pressure of the coincidental movement of the liquid and tank walls subject to dynamic loadings.

According to Eurocode-8 (2008), the distribution of the impulsive component of the hydrodynamic pressure (p_{imp}) and the pressure distribution coefficients can be obtained using Equations 3.1-3.2, which explained previously in chapter 3. The pressure distribution coefficients defined in Equation (3.2) for each of the tank models for $\theta = 0°$ are presented in Figure 6.2 To find the overall seismic response of the storage tanks, including the FSI, only the impulsive portion of the liquid is considered in the current study, as this portion is the major one accelerates with the tank wall and generates hydrodynamic forces as reported by previous studies (Zhou et al. 2018; Buratti and Tavano 2014).
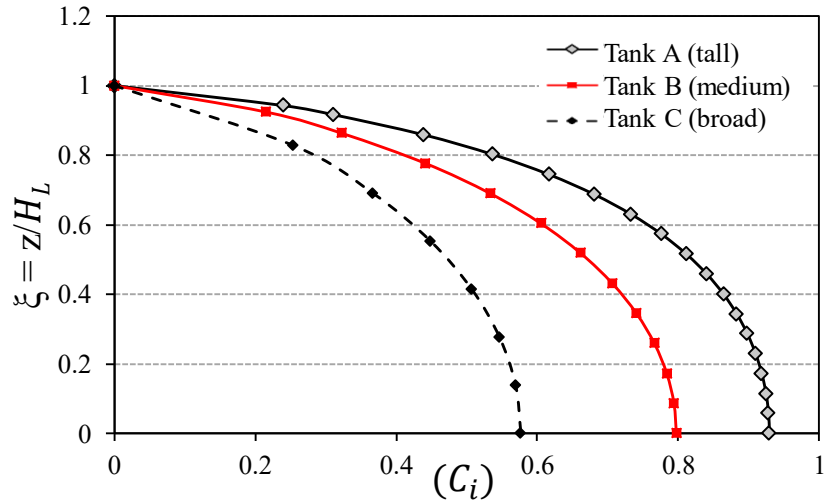
Figure 6.2 Impulsive pressure along tank wall.

6.2.4 Finite element model of the tank-liquid System

The nonlinear dynamic analysis of the LNG tank-liquid system carried out using the finite element analysis software ABAQUS (version 2018). The inner steel tank was modelled using shell elements (S4R) with four-nodes, doubly curved quadrilateral finite membrane strain formulations. The 9% Ni steel material which is recognized by the ASTM A36 (2018) for cryogenic service temperatures, with the yield stress (f_y) and ultimate strength (f_{ult}) of 245 and 360 MPa, respectively, was used in this study. Additionally, elastic modulus and the strain hardening modulus were considered to be 205 GPa and 3888 MPa, respectively. The 9% Ni steel material behaviour was modelled using the kinematic hardening rule with von Mises yield criteria to capture the metal inelastic behaviour under seismic loading.

The LNG liquid was modelled using the lumped added-mass method for the dynamic analysis. In which impulsive portion of the liquid can simultaneously accelerate or decelerate with a tank wall, which reproduces the impulsive pressure. The adopted added-mass technique in this study is a comprehensive alternative to Housner (1957) traditional method of the single masses mechanical model used for dynamic analysis for

214

liquid storage tanks. Accordingly, the impulsive hydrodynamic pressure was modelled using a series of added masses attached to the tank nodes via rigid springs. Each lumped mass m_i calculated from the pressure defined using Equation (3.1) and attached to the corresponding node, in this method the height of the tank was separated into some segments and the area of the pressure affect the curve for each segment was divided by the normal acceleration of the wall Ag (t). The lumped masses are in same vertical distribution as the impulsive pressure (Figure 6.3a), and they have a uniform distribution around the circumference (Figure 6.3b) same procedure proposed by (Virella et al. 2006).

The attached masses in ABAQUS were modelled using specific connector elements named MPC type LINK, which simulates a unidirectional rigid spring between two nodes. This ignores the vertical and tangential acceleration along the tank wall, while the springs provide radial added inertia effects perpendicular to shell surface. In addition, fixed base condition used for tank base.

(a) The normal masses along the cylinder height.

(b) The normal masses along tank circumference.
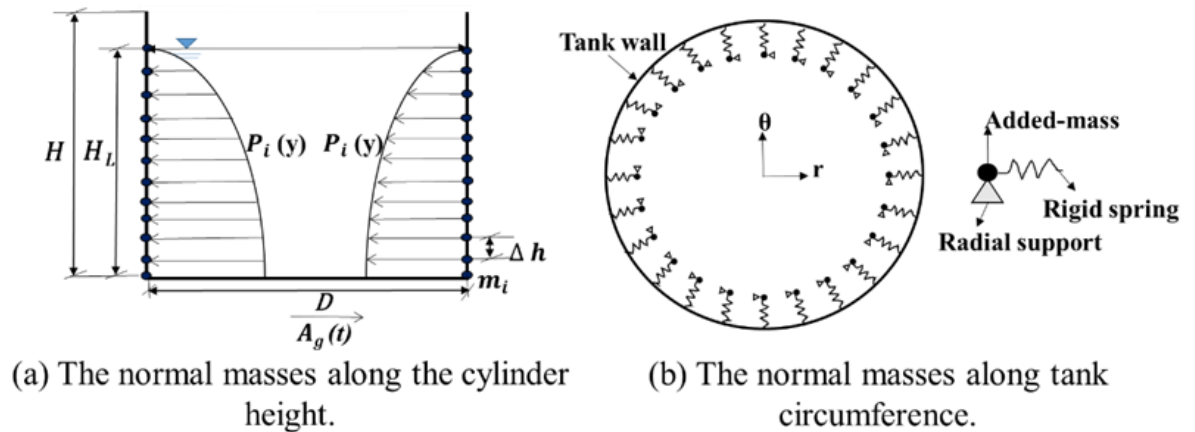
Figure 6.3 Mass-spring modelling technique used in this study to capture impulsive fluid - structure interaction, the normal masses (a) along the cylinder height, (b) along tank circumference.

Figure 6.4 illustrates the developed finite element models for different tank aspect ratios. The finite element analysis was conducted for each tank in three steps; the first step was the modal analysis to obtain the natural frequency and compare it with the

analytical formulations available in API-650 (2007). The second step was to establish the initial equilibrium under the gravity load including the hydrostatic load on the tank wall and base. Finally, the earthquake excitation was applied at the tank base in one horizontal direction (no vertical ground motion was considered) to conduct the non-linear dynamic time-history analysis capturing both material and geometric nonlinearities. It is assumed that the LNG tank was sitting on competent hard rock site, and two benchmark near-field earthquake records were selected in this study, these earthquakes selected by several researchers (e.g. Xu and Fatahi 2019) to denote maximum measured level of earthquakes. The 1994 Northridge and 1995 Kobe earthquakes, were used in this study as shown in Figure 6.5. Each running analysis took around 8 hours to complete with model size (10 Giga-bytes), therefore, fast computation facilities were used to conduct this time-history analysis.
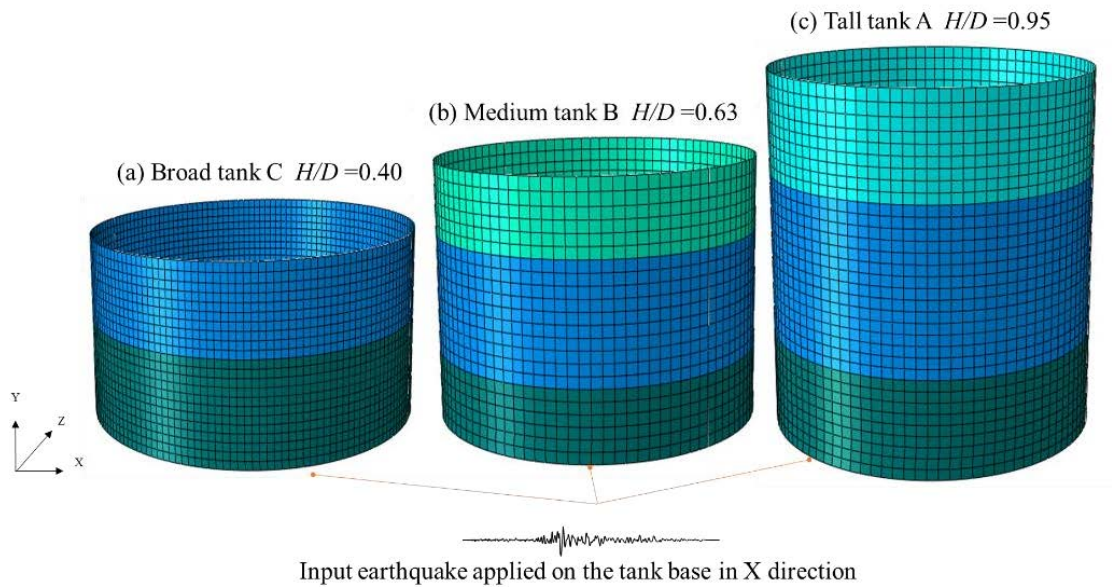
Figure 6.4 Finite element models for different tanks adopted in this study (a) Broad tank C, (b) Medium tank B, and (c) Tall tank A.
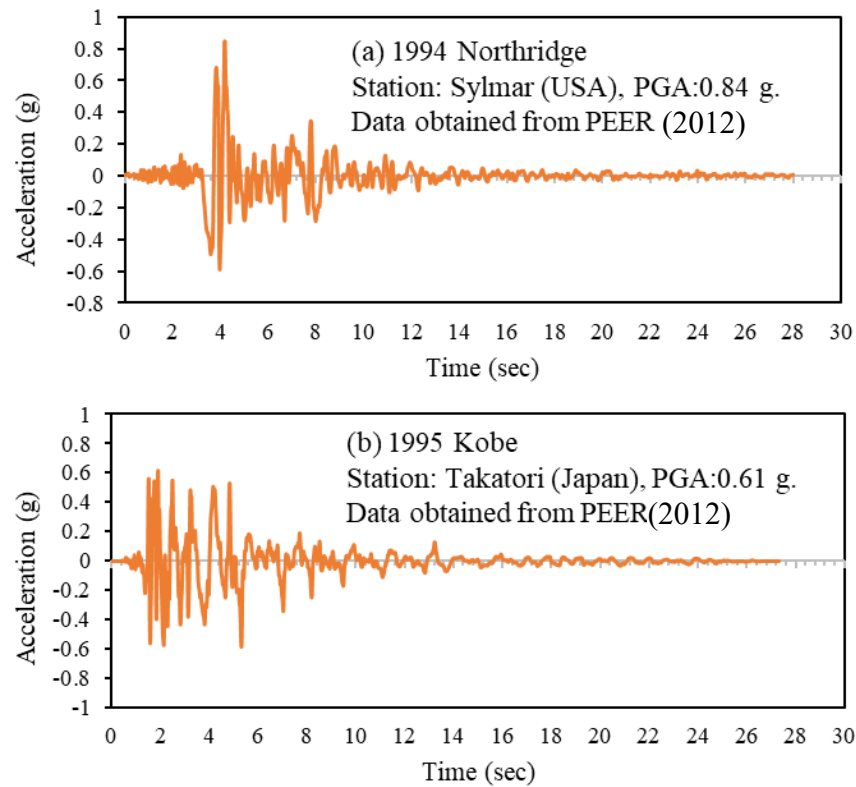
Figure 6.5 Adopted earthquake time histories of the ground accelerations, (a) 1994 Northridge earthquake and (b) 1995 Kobe earthquake.

6.2.5 Results and discussion

The results of free vibration analysis and nonlinear time-history analysis for three adopted LNG tanks aspect ratios under 1994 Northridge and 1995 Kobe Earthquake records are presented below.

6.2.5.1 Free vibration analysis

Modal analysis was performed on the three tanks models Type A (tall), Type B (medium) and Type C (broad) to find the fundamental impulsive period of each tank. Then the natural period obtained from the FEA was compared with the analytical solution presented in API-650 (2007) for the fundamental impulsive mode period as explained previously in chapter 3 using Equation (3.11).

In Table 6.1, the results of FEA calculated by eigenvalue modal analysis using Block

Lanczos algorithm is compared with those obtained from API-650 code. The results show that the natural period obtained by FEA is in a good agreement (lowe than 3% variance) with the analytical formulations proving the reliability of the implemented numerical model with spring-added mass technique to simulate the liquid-tank interaction.

Table 6.1 Comparison between fundamental periods of vibration (T_i) for filled tank obtained from FEA and API-650 (2007).

Tank Model	T_i (sec) - 3D FEA	T_i (sec) - API 650
Tall Tank A ($H/D = 0.95$)	0.217	0.220
Medium Tank B ($H/D = 0.63$)	0.145	0.150
Broad Tank C ($H/D = 0.40$)	0.098	0.096

Figure 6.6 summarises the schematic deformed shapes of tanks corresponding to the fundamental modes of vibration. It can be noticed that for tall Tank A (with H/D=0.95) the fundamental impulsive mode is comparable with a bending mode of a cantilever beam. However, for medium Tank B and broad Tank C ($H/D = 0.63$ and 0.40, respectively) the bulge shape deformation near the mid-height of the wall is apparent. Which implies that the cross- section area at the tank mid-height is vulnerable to higher deformation during horizontal excitation due to impulsive mass effect.

(a) Tank C T_i =0.098 sec.   (b) Tank B T_i =0.145 sec.   (c) Tank A T_i =0.217 sec.
Fundamental natural period of the impulsive mode
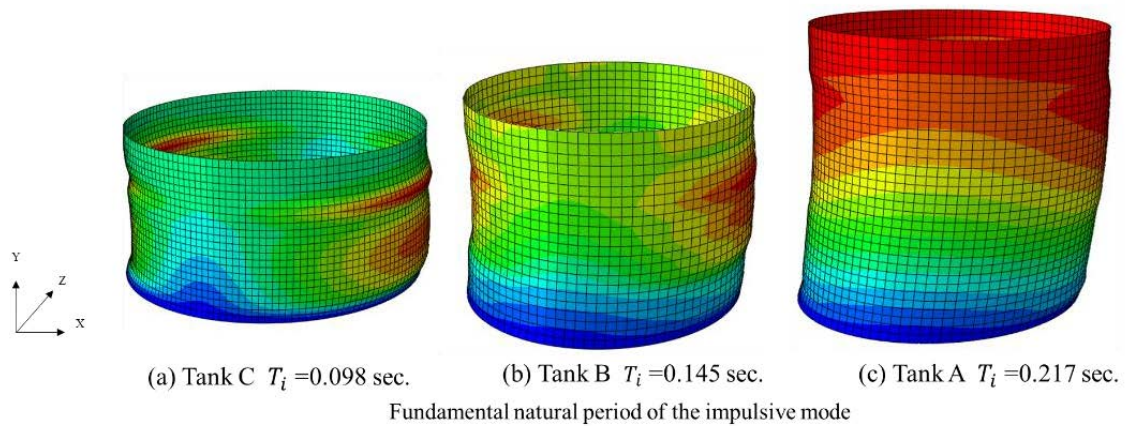
Figure 6.6 Fundamental natural period of the impulsive mode for (a) Tall tank A, (b) Medium tank B, and (c) Broad tank C.

6.2.5.2 *Non-linear dynamic time-history analysis*

The nonlinear time-history analysis was performed on the LNG inner steel tank with different aspect ratios, subjected 1994 Northridge and 1995 Kobe earthquakes. Figure 6.7 shows the acceleration response spectra of these earthquakes, as well as the fundamental periods of vibration for three tanks used. The acceleration response spectra is communally used in the seismic analysis as it is interrelated to the maximum superstructure response under the earthquake load (Xu and Fatahi 2018). As evident, the fundamental periods of vibration for all selected tanks are located in the short period range of the response spectrum.
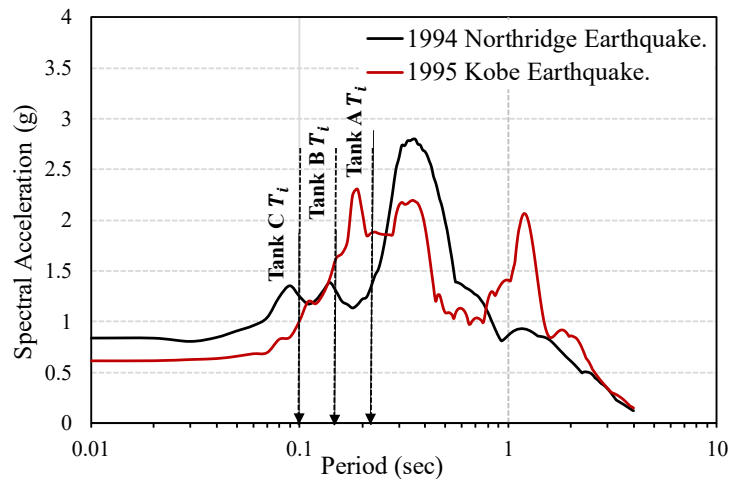
Figure 6.7 Acceleration response spectra for the selected earthquakes.

To verify the accuracy of the nonlinear time-history analysis employing three-dimensional finite element modelling, the seismic response for these tanks were compared with Eurocode-8 (2006) formulations. In particular, the base shear forces and the overturning moments were computed and compared. According to Eurocode-8 (2006), the base shear force (Q) and bending moment (M) for the liquid storage tank considering impulsive liquid-wall interaction only, can be calculated using the following equations:

$$Q = (m_i + m_w) * S_a (T_{imp})$$ (6.1)

$$M = (m_i * h_i + m_w * h_w) * S_a (T_{imp})$$ (6.2)

where, m_i is the impulsive mass component; h_i is the height where the impulsive hydrodynamic wall pressure was applied; m_w is the tank wall mass; h_w is the height of the centre gravity of tank wall; S_a (T_{imp}) is the impulsive spectral acceleration obtained from the acceleration response spectrum (i.e. Figure 6.7). Figure 6.8 and Figure 6.9 present the maximum base shear forces and bending moments obtained from the analytical solution and the FEA predictions having reasonable agreement (less than 16% difference). However, it is obvious that increasing the aspect ratio H/D from 0.63 to 0.95 (medium tank to tall tank) increase the base shear forces significantly, which correspond to 72% and 58% increases for the 1994 Northridge and the 1995 Kobe earthquakes, respectively. Furthermore, as a result of increasing the H/D from 0.63 to 0.95 (medium tank to tall tank), overturning moments increased by 58% and 52% under the effects of the 1994 Northridge and the 1995 Kobe earthquakes, respectively.

The conducted nonlinear time-history analysis allows for seismic response comparison of the LNG inner tanks with different aspect ratios. The maximum structural response of the LNG tank walls under the applied earthquakes was reported and compared. The axial force (F_{11}) and the hoop force (F_{22}) for circumferential unit width of the tank (Figure 6.10) and radial displacements of the wall are of particular interest and discussed below.
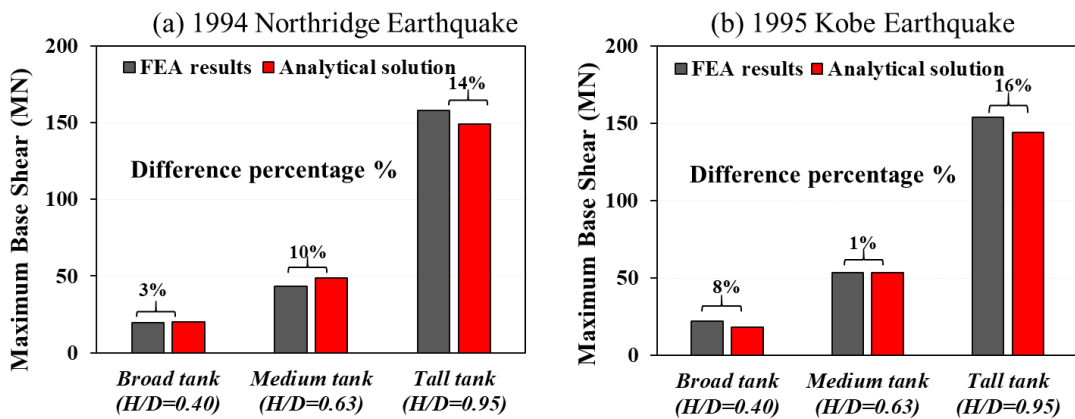
Figure 6.8 The maximum base shear force obtained from the analytical solution and 3D FEA, (a) 1994 Northridge Earthquake and (b) 1995 Kobe Earthquake.
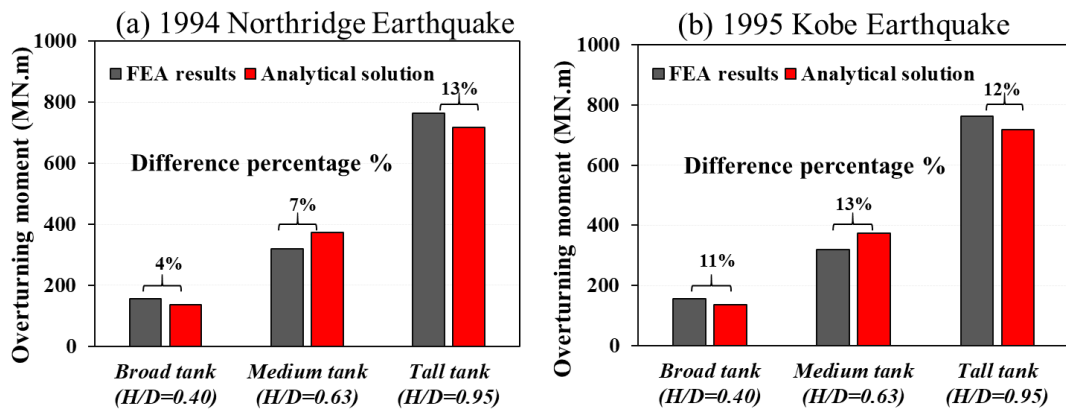
Figure 6.9 The maximum overturning moment obtained from the analytical solution and 3D FEA, (a) 1994 Northridge Earthquake and (b) 1995 Kobe Earthquake.
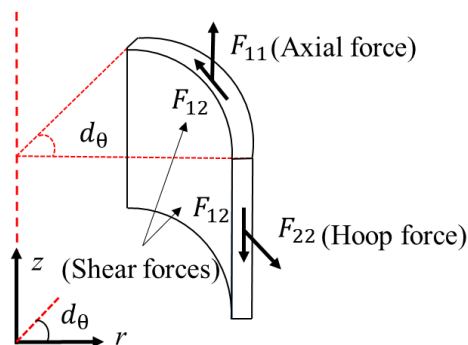
Figure 6.10 Illustration of different force components in the LNG tank wall.

Figure 6.11 shows distribution of maximum hoop forces for tall, medium and broad tanks under 1994 Northridge and 1995 Kobe earthquakes. For the sake of more

meaningful comparison, the hoop forces were plotted against the normalized liquid level (i.e. z/H_L, where z is the elevation measured from the tank bottom and H_L is the Liquid height). The maximum hoop forces were observed at polar coordinate $\theta = 0°$ on the X-axis of the tanks and occurred at t = 4.2 sec under 1994 Northridge and t = 5.8 sec under 1995 Kobe earthquake. It can be seen that, irrespective of the tank aspect ratio, the maximum hoop forces were all located at the bottom section of the wall, which shows the higher tendency of the lower levels of the tank wall experiencing bulge if the stresses exceed the yield stress limit. Referring to Figure 6.11, the maximum hoop forces increased with increasing aspect ratio, with approximately 20% increase when H/D increased from 0.40 to 0.63, and 25% when H/D increased from 0.63 to 0.95. This is due to the fact that both impulsive hydrodynamic force and hydrostatic force increases with the tank height.
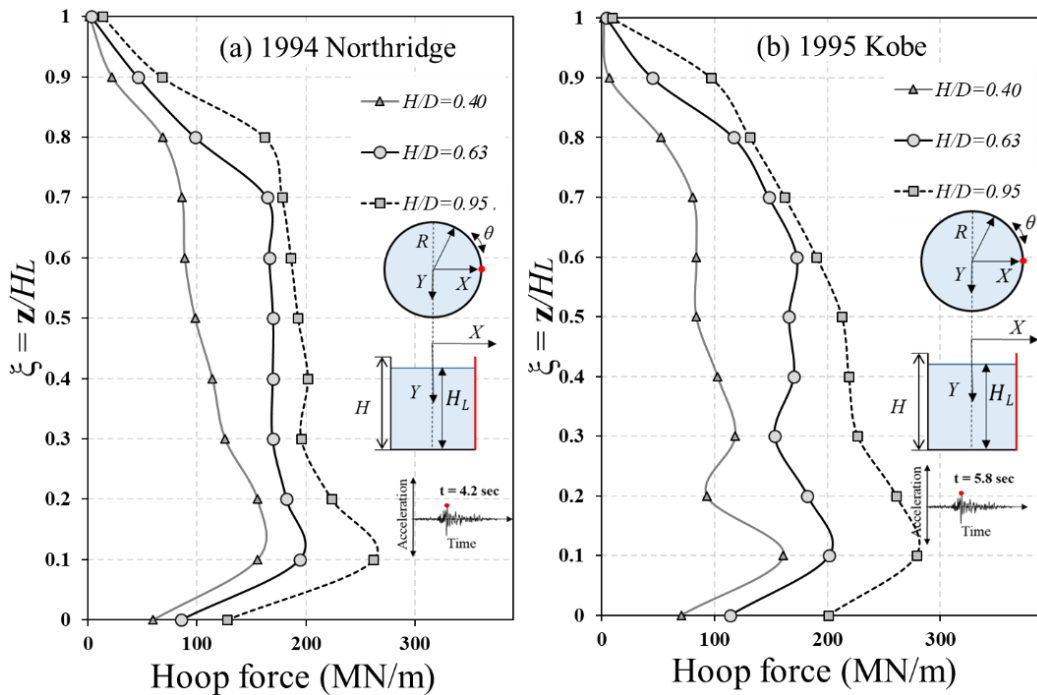
Figure 6.11 Distribution of hoop forces in the tank wall at $\theta = 0°$, (a) 1994 Northridge Earthquake and (b) 1995 Kobe earthquake.

Similar observations could be made for the maximum axial forces, which occurred

at $\theta = 0°$ on the X-axis for all tanks (Figure 6.12). However, in comparison to hoop forces, the axial forces show more consistent incrementation pattern from the liquid level to the tank base. Referring to Figure 6.12, the maximum axial forces increased with the aspect ratio (or the tank height), where 31% and 64% increase was observed when H/D increased from 0.40 to 0.63, and from 0.63 to 0.95, under the 1994 Northridge, respectively. It can be noted that the corresponding observed amplifications in the maximum axial forces under the 1995 Kobe earthquake were 50% and 60%, respectively.

The combined effects of the axial and hoop forces on the tank response can be observed in the radial displacements predicted along the tanks wall. Figure 6.13 shows the radial displacement of the wall subjected to adopted earthquake records. In general, the peak radial deformations were observed at the bottom portion of the tanks, while relatively smaller variations at the middle and upper portions of the tanks were observed. These observations are in line with other researchers (e.g. Buratti and Tavano 2014 and Brunesi et al. 2015) findings on elephant's foot buckling failure mode development for tanks. Furthermore, referring to Figure 6.13, it can be noted that Tank B with H/D =0.63 showed another peak at the upper portion which could potentially impose the risk of local buckling. This observation is aligned with the reported deformation shape from modal analysis (Figure 6.6b) showing bulge shape deformation near the mid-height of the wall.
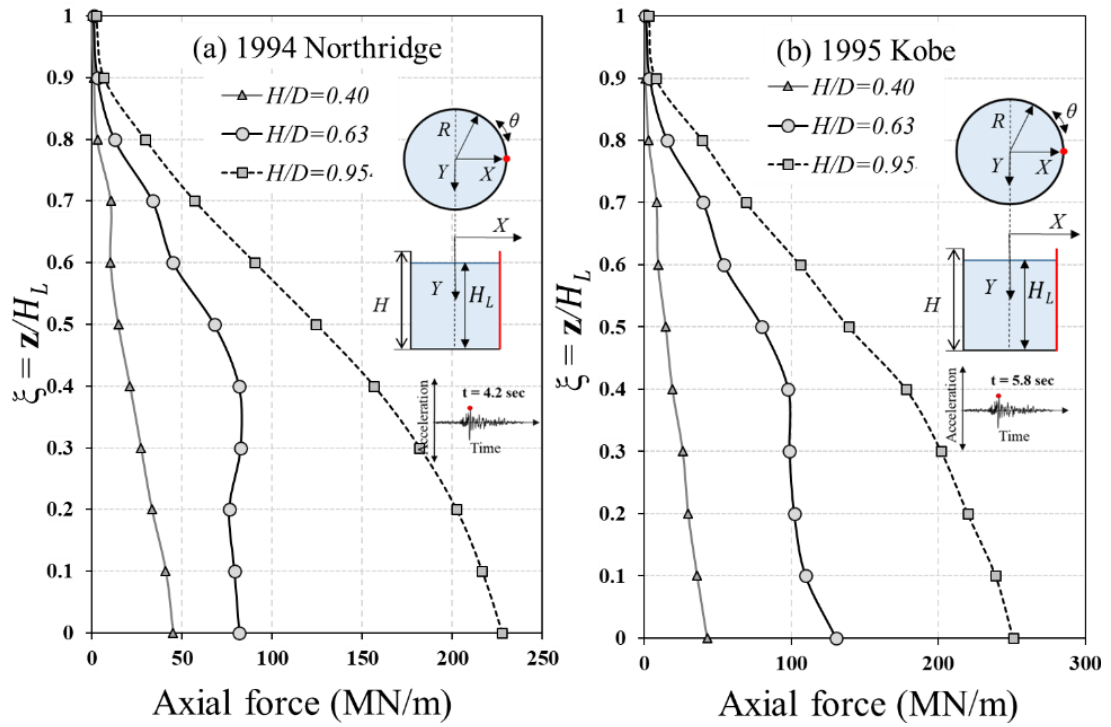
Figure 6.12 Distribution of the axial forces in the tank wall at $\theta = 0°$, (a) 1994 Northridge Earthquake, (b) 1995 Kobe earthquake.
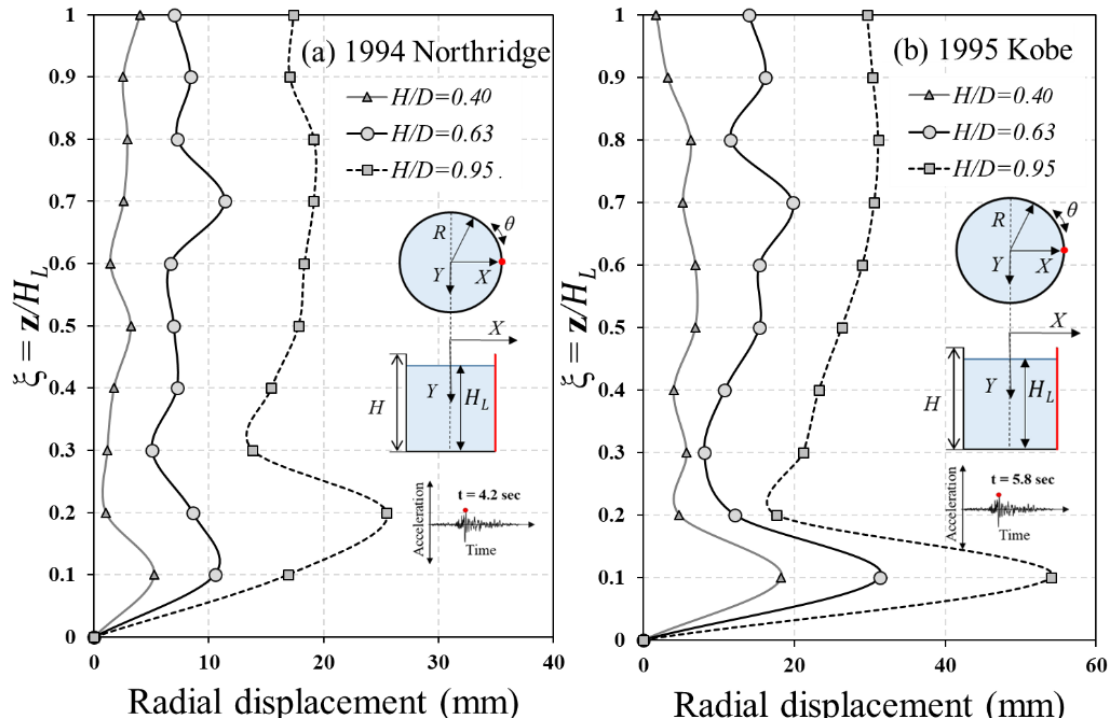
Figure 6.13 Distribution of the radial displacement along the normalized liquid height level of the three aspect ratio tank walls at $\theta = 0°$ for (a) 1994 Northridge Earthquake, (b) 1995 Kobe earthquake.

Interrogating the nonlinear time-history numerical analysis results showed that the developed stresses in board and medium LNG tanks remained below the yield stress limit at all locations under both the 1994 Northridge and the 1995 Kobe earthquakes meaning no plastic buckling. Referring to Figure 6.14b, elastic buckling was observed for medium Tank B ($H/D = 0.63$) with inward buckling at the upper portion of the tank walls, which corresponds to the secondary diamond buckling mode. Increasing the H/D ratio to 0.95 (tall tank) raised the damage and failure risk. Referring to Figure 6.14c, the von Mises stresses on the tall Tank A exceed the yield stress limit and the elastic-plastic outward shell bulging at the lower portion of the tank wall (i.e. elephant's foot buckling) occurred. Figure 6.15 shows the distribution of the von Mises stresses at the tall Tank A wall together with the time variation of von Mises stresses for the selected node A near the tank base level, which resulted in the elephant's foot buckling for tall Tank A.

(a) Tank C (H/D=0.40). (b) Tank B (H/D=0.63). (c) Tank A (H/D=0.95).
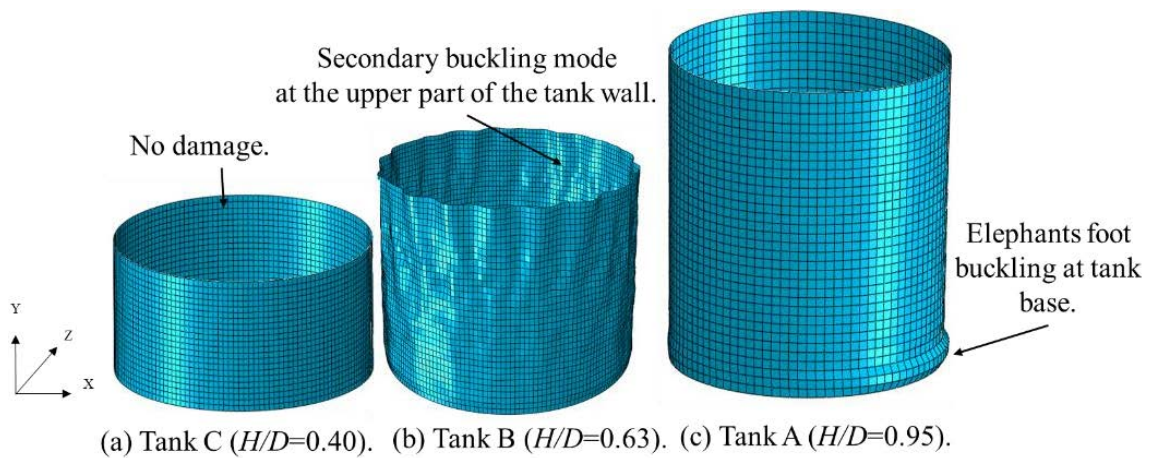
Figure 6.14 Damage extend to the LNG tanks, (a) Broad tank C (no damage), (b) Medium tank B (secondary elastic buckling mode), and (c) Tall tank A (elephant's foot buckling).
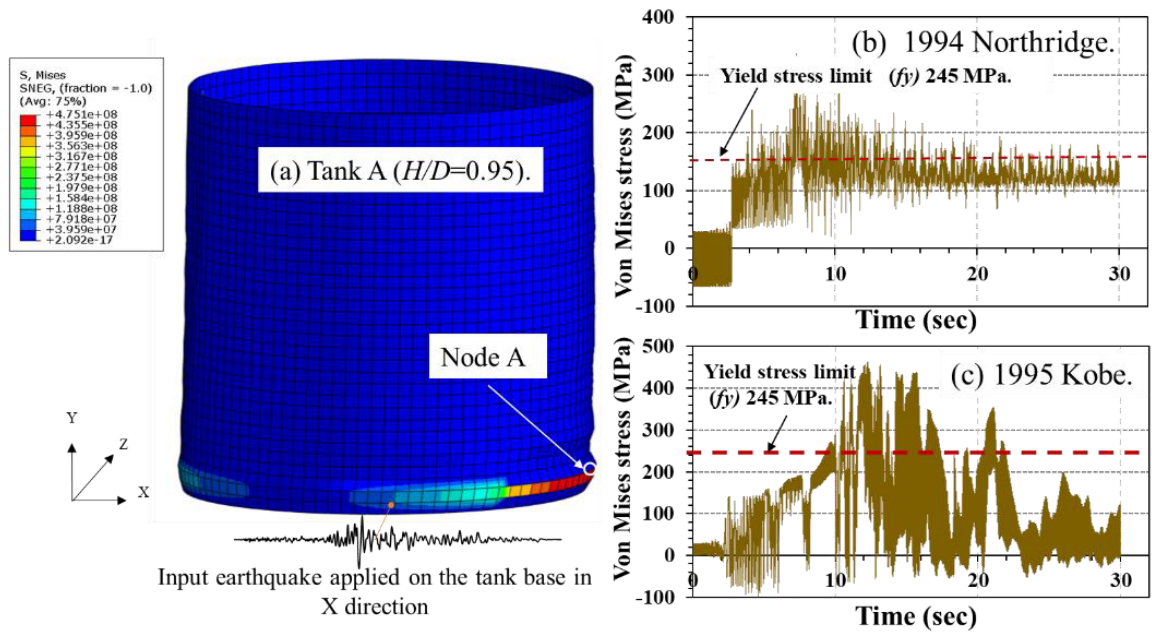
Figure 6.15 Formation of the elephant's foot buckling in tall Tank A (*H/D* = 0.95): (a) distribution of the von Mises stresses exceeding the yield stress limit near the tank base (i.e. Node A), (b) von Mises stresses (Pa) at Node A under 1994 Northridge earthquake and (c) von Mises stresses at Node A under 1995 Kobe earthquake.

6.3 Impact of wall support conditions on seismic response of ground-supported reinforced concrete containment tanks

6.3.1 Introduction

The ground supported concrete storage tanks are widely used for water, refined petroleum products, and chemicals due to their large capacity and economic efficiency. These tanks may be used in high seismicity regions and therefore assessing their seismic safety in those regions is essential.

For some cases such as liquefied natural gas (LNG) tanks, the double-wall containment system is often used. Indeed, the natural gas is condensed to a liquid state by cooling it to a very low temperature (approximately -168°C) at atmospheric pressure (Zhai et al. 2019) , thus LNG needs to be stored in the primary inner steel tank to meet the ductility requirements of the tank, while the secondary outer tank is used for external protection (Lee et al. 2016) . The secondary containment tank is usually made of reinforced or prestressed concrete without any direct contact or interaction with the stored liquid in the normal conditions. Most of the previous studies had focused on the seismic behaviour of the inner steel tank considering the FSI, while the studies on the secondary concrete containment tanks have been less popular (Khansefid et al. 2019). Christovasilis and Whittaker (2008) considered the efficiency of seismic base isolation on the performance of the LNG tanks and compared the results with the conventional tank. They concluded that the acceleration response reduced after using the base isolators, similar to the base shear and global overturning moment at the tank base. Some researchers had assessed the performance of the secondary concrete containment LNG tanks against external forces, such as blast (Lee et al. 2016) and airplane impact (Zhai et al. 2019). This study presents a rigorous 3D nonlinear time history analysis of an empty ground

supported circular reinforced concrete containment tank subjected to seismic action for hinged and fixed wall to base support conditions.

6.3.2 Description of adopted LNG tank

A 30,000 m³ reinforced concrete outer LNG tank is adopted in this study. The adopted tank is composed of a reinforced concrete roof fixed to the wall sitting on a rigid foundation (Figure 6.16). This LNG tank is an example of the modular LNG tanks used in highly seismic regions as reported in the literature (Shu 2007).
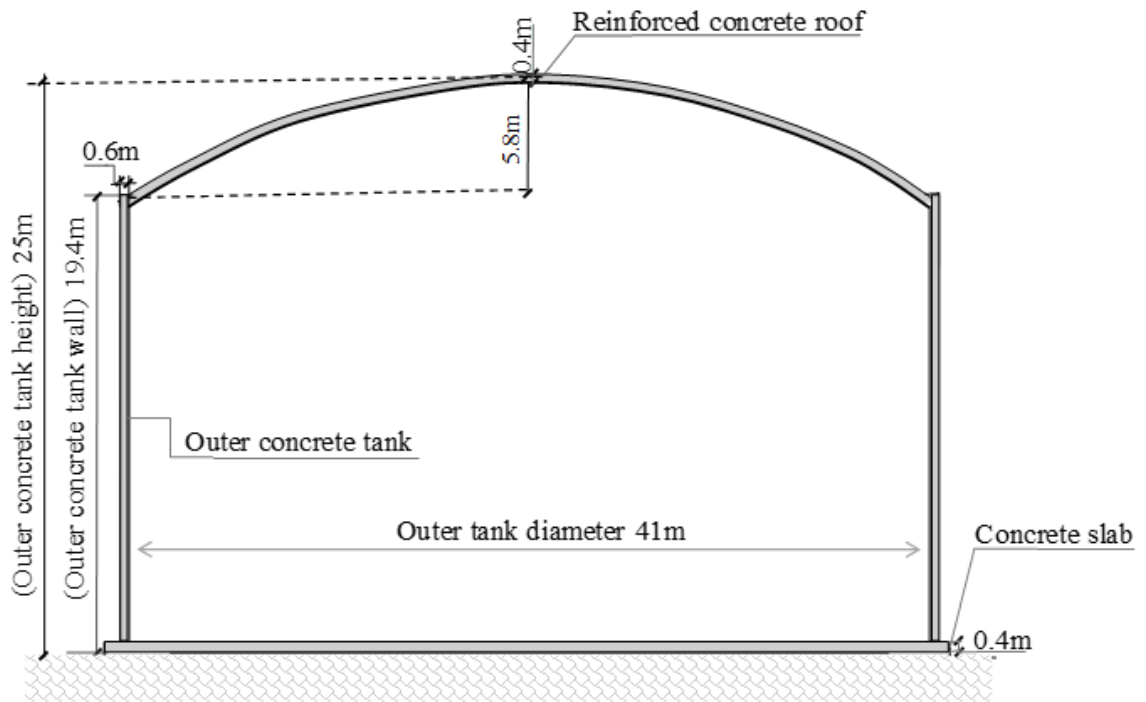
Figure 6.16 Schematic view of the adopted reinforced concrete outer LNG tank.

Since this study only investigates the effects of the wall to foundation slab connection on the seismic behaviour of the LNG concrete containment, only the outer tank with the roof and foundation slab was considered in the numerical analysis. The outer diameter of the concrete tank is 41 m, the height is 25 m and the wall thickness is 0.6 m. The reinforced concrete roof is 5.8 m high and 0.4 m thick. The concrete which is used to build this LNG tank is grade *C40* which had a compressive strength of 40 MPa and a

unit weight of 26.40 kN/m^3. Additionally, the ordinary reinforcing steel with the yield strength of 400 MPa, the ultimate tensile strength of 600 MPa corresponding to the ultimate tensile strain of 0.14, the modulus of elasticity 2×10^5 MPa, and unit weight of 78 kN/m^3, are used. The prestressing tendons are used in the tank wall which had the yield strength of 1581 MPa, the ultimate tensile strength of 1860 MPa corresponding to the ultimate tensile strain of 0.0575, and unit weight of 78kN/m^3. The vertical rebars in the tank wall spaced around the circle every 3˚ and the circumferential steel rebars were spaced every 0.6 m along the tank wall, which are similar to the recommendations in the existing literature (Christovasilis and Whittaker 2008).

6.3.3 Numerical modelling

6.3.3.1 General model description

The finite element software ABAQUS (2018) was used to develop the numerical model for both fixed base and hinged base concrete LNG tanks and perform modal analyses as well as the time history analyses. Figure 6.17 presents the numerical model of the entire tank. The tank wall, roof and base slab were modelled using 4-noded shell element S4R, while the rebars were defined as layers of uniaxial reinforcement in the shell elements as recommended by other researchers (Hafez 2012). The LNG tank model consist of 11648 elements which were utilised for this analysis.

Input earthquake applied
on the tank base
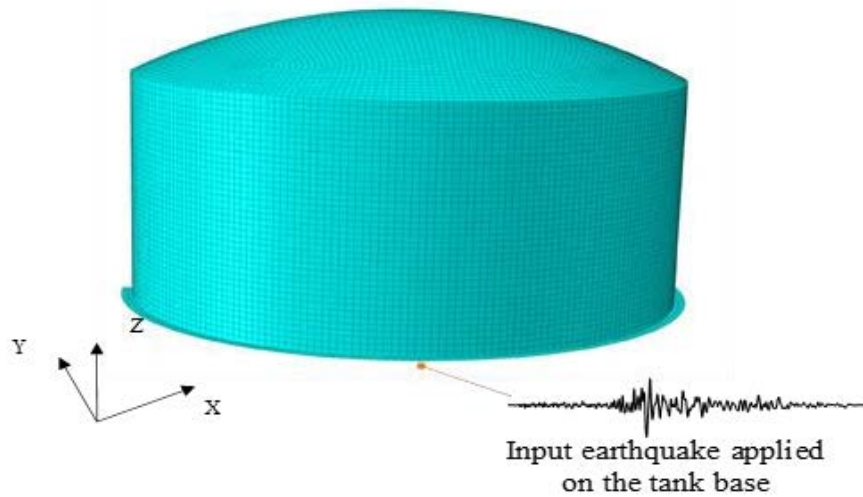
Figure 6.17 Three-dimensional numerical model of the concrete LNG tank

6.3.3.2 *Adopted material model for reinforced concrete*

To represent the elasto-plastic behaviour of the concrete tank under the seismic loads, the concrete damage plasticity (CDP) model was used in this study. This constitutive model, available in ABAQUS, considers two failure mechanisms for the concrete: the tensile cracking and the compressive crushing (Lee et al. 2016). Under the uniaxial tension, the stress-strain relation follows the linear elastic behaviour until the failure stress σ_{to} is reached, beyond which the cracks are generated in the concrete that leads to softening of stress-strain response of the concrete. The degradation of the elastic stiffness is considered by two damage variables, named d_t and d_c, for tension and compression respectively, which are assumed to be functions of the plastic strains. These damage variables represent the stiffness recovery after the cracks are generated in the concrete, thai is very important for the response of the concrete subjected to the cyclic loading such as seismic loads (Saenz 1965). The experimental observations available in the literature showed that when the load changes from tension to compression in concrete, the compressive stiffness recovers as the cracks close under compression (Lee et al. 2016), while the tensile stiffness does not recover after the crushing as micro-crack

230

develop. The stiffness recovery variables can take a value between 1 and 0, representing a full recovery and total loss of the stiffness, respectively. CDP model represents the elasto-plastic behaviour of the plain concrete, while the effects associated with the reinforcements as the bond slip and dowel action were modelled by introducing tension stiffening to include the load transfer process through the cracks by the rebars. As mentioned early, the rebars were modelled using layers of uniaxial reinforcement in the shell elements for both vertical and circumferential directions. The essential constitutive parameters for the concrete *C40* used in this study are summarised in Table 6.2, while the uniaxial compression and tension stress-strain curves of the concrete obtained from existing literature (Saenz 1965; Nayal and Rasheed 2006) are presented in Figure 6.18. For the rebars the the kinematic hardening law was used with the material characteristics that mention previously.
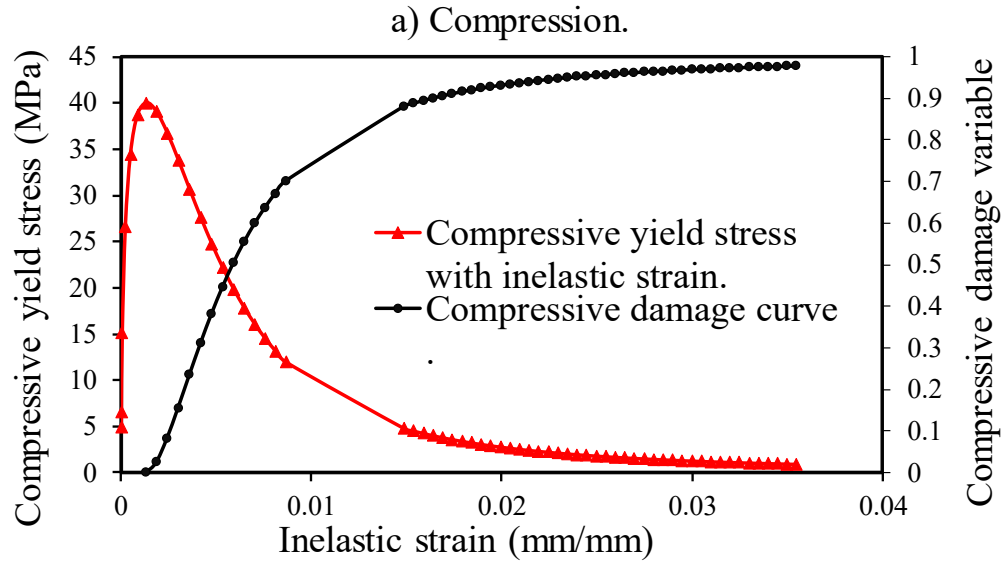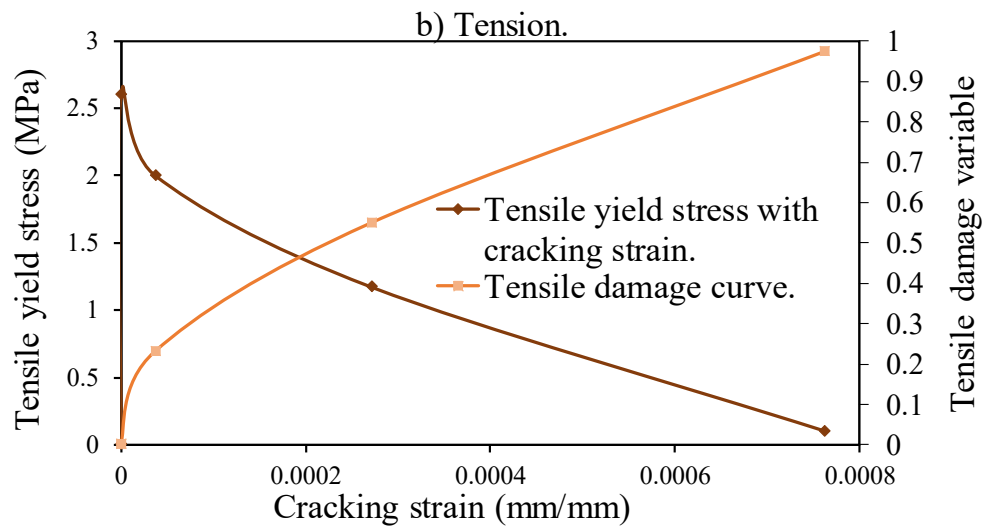
a) Compression.

Figure 6.18 Uniaxial stress-strain curves of concrete and the damage variables with the strain for concrete *C40*: (a) compression; (b) tension.

Table 6.2 Adopted parameters for simulation of concrete in this study

Parameter name	Symbol	Value	Reference
Dilation angle	ψ	36°	(Nayal and
Eccentricity	ϵ	0.1	Rasheed 2006)
Biaxial/uniaxial compressive yield strength ratio	f_{b0}/f_{c0}	1.16	(Lee et al. 2016)
The hydrostatic effective stress ratio	K	0.667	(Hafez 2012)
Compressive stiffness recovery parameter	w_c	1	
Compressive stiffness recovery parameter	w_t	0	

6.3.3.3 *Connection details and adopted earthquakes*

The conducted analyses included two parts, the modal analysis and the time history analysis. According to ACI 350.3-06 (2008), the wall base connection of the ground supported tanks can be classified as a fixed or hinged base support condition. For the fixed base condition (it can come in two forms as shown in Figure 6.19a), no rotation and relative movement are allowed at the connection of the wall to the base, and the vertical reinforcement connects the wall with the foundation and extends across the joints to resist

the bending moment at the tank base. For fixed base arrangement with closure strip instead of the vertical reinforcement, the tank wall is connected via the closure strip to the foundation to overcome the potential concrete shrinkage issues (Hafez 2012). For the hinged base connection (which can also come in two forms as shown in Figure 6.19b), the rotation is allowed and thus no considerable bending moment can be transmitted between the tank wall and the base.
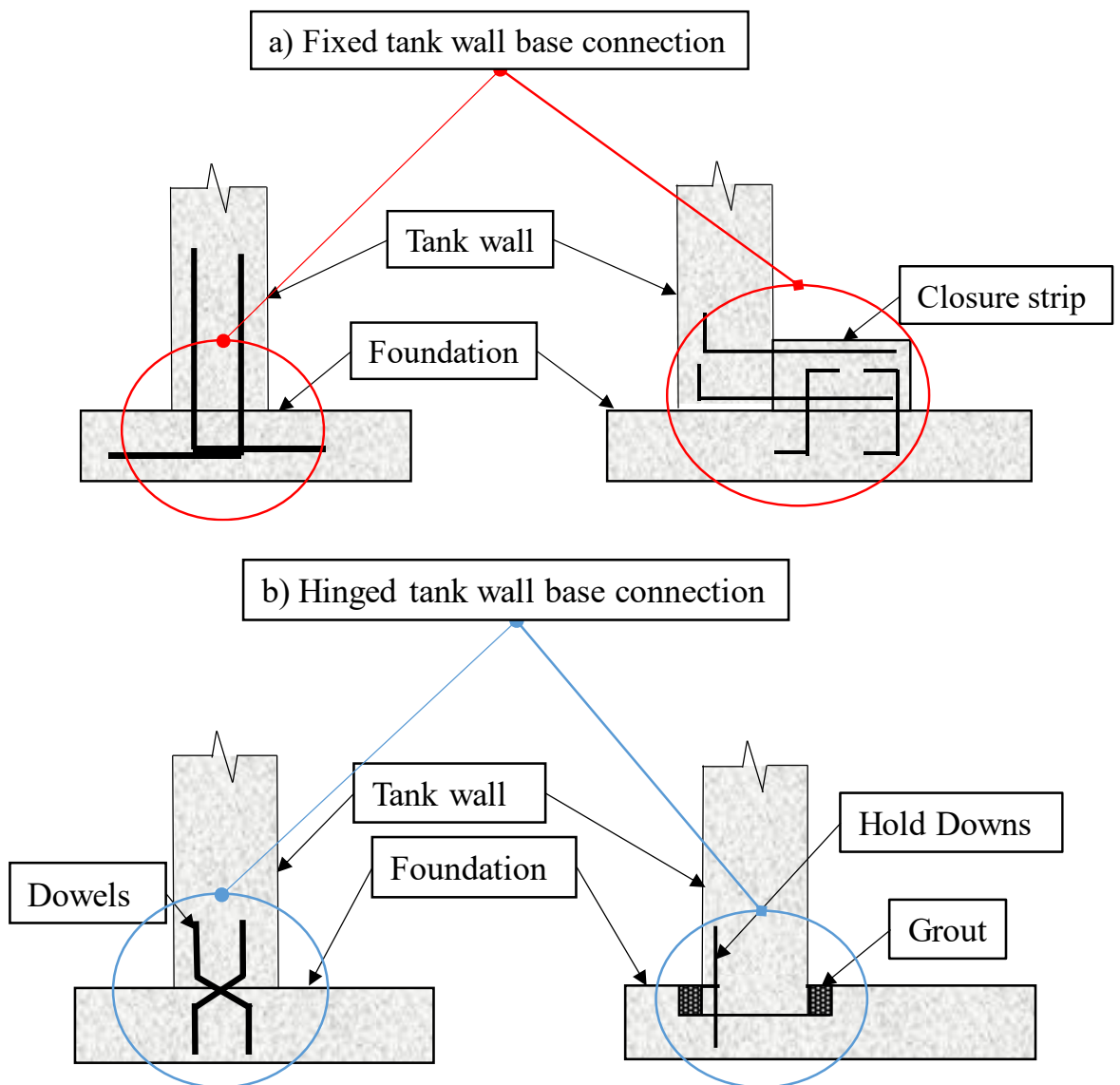
Figure 6.19 Ground supported tank support connections: (a) fixed base condition; (b) hinged base condition based on ACI 350.3-06 (2008).

The modal analyses were conducted to obtain the natural frequencies of the tank

using Block Lanczos algorithm, and the details of mode shapes were captured. After establishing the initial equilibrium under the gravity loading, the earthquake excitations namely the 1995 Kobe earthquake and the 1994 Northridge earthquake as shown in Figure 6.20, were applied to the model in the time history analysis, assuming that the LNG tank was sitting on a hard rock site. No vertical ground motions are considered.
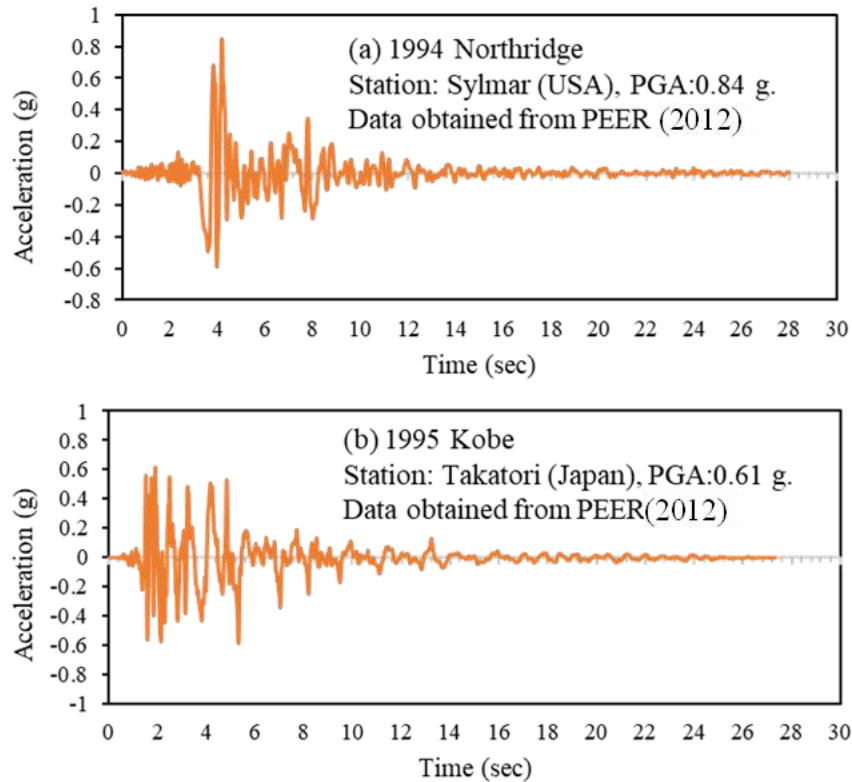
Figure 6.20: Adopted time histories of the ground accelerations for: (a) 1994 Northridge Earthquake and; (b) 1995 Kobe Earthquake.

6.3.4 Results and discussion

6.3.4.1 Modal analysis

A modal analysis was conducted for the empty reinforced concrete tanks with two wall foundation conditions, i.e. the fixed base condition and hinged base condition, using Block Lanczos algorithm. The natural frequencies and periods for the first mode of vibration for the adopted tanks are summarised in Table 6.3. As expected, the natural

period for the hinged base concrete LNG tank is slightly larger than the fixed base due to the reduction of the stiffness and the ability of tank wall to rotate around the foundation slab.

Table 6.3 Fundamental vibration period of the fixed base and hinged base tank conditions.

Tank base condition	Fundamental natural frequency (Hz)*	Corresponding fundamental natural period (s)
Fixed base	10.2 (m=1, n=4)	0.098
Hinged base	8.8 (m=1, n=5)	0.12

As the shell wall of the cylindrical tanks can be vibrated in two directions of the cylindrical coordinates; i.e. the circumferential (definite by circumferential wave number n) and the axial direction (definite by the axial wave number m), the fundamental mode shape for both tanks is extracted and reported in Figure 6.21 The first fundamental mode captures wall deformation in the radial direction of the cylindrical coordinates, while no major deformation occurred on the tank roof in both fixed base (Figure 6.21a) and hinged base (Figure 6.21b) conditions. The circumferential wave numbers were n = 4 for the fixed base condition and n = 5 for the hinged base condition while the axial wave number was m = 1 for both conditions.
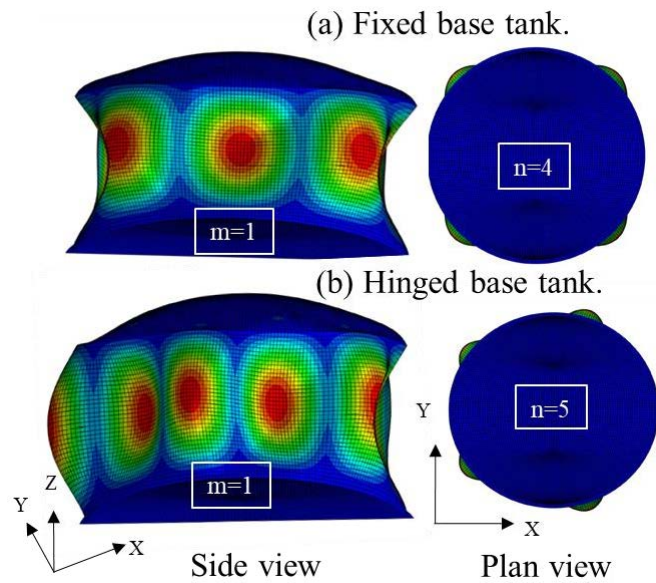
Figure 6.21 The fundamental mode shape: (a) for the fixed base tank; (b) for the hinged base condition tank.

6.3.4.2 *Non-linear dynamic time history analysis*

Non-linear dynamic time history analyses were performed on the concrete LNG tanks with different base conditions. As explained earlier, two large bedrock earthquake time-histories, namely 1994 Northridge, 1995 Kobe earthquakes, were applied. Figure 6.22 shows the response spectrums of these earthquakes. Assuming that the LNG tank was sitting on a hard rock site, these earthquakes were applied to the base of the model in the horizontal direction and the predicted structural responses of the tanks are summarised in Table 6.4.
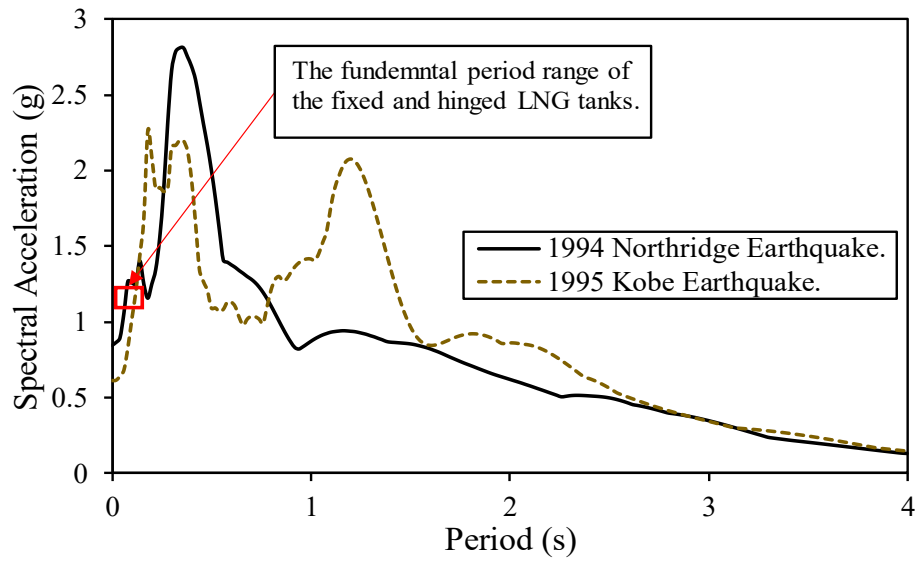
Figure 6.22 Acceleration response spectrum for the selected earthquakes.

Table 6.4 Structural response of the tanks with the fixed and hinged base conditions.

Earthquake	Tank base condition	Base shear force (MN)	Hoop force at the top of the tank wall (MN/m)	Bending moment at the top of the tank wall (kN.m/m)	Radial displacement at the top of the tank wall (mm)
1994 Northridge	Fixed	72.6	0.8	65.9	9.7
	Hinged	83.6	1.17	138	13.3
	Fixed	48.2	1.65	47.9	3.7
	Hinged	59.8	2.45	115.5	4.6

The structural responses are presented in Table 6.4, which are reported at the locations of the maximum response within the tank wall, and it is considered as per circumferential unit width of the wall (i.e. for Hoop force and bending moment). Figures 6.24, 6.25 and 6.26 shows the values of the hoop forces, bending moments, and radial displacements along the wall height (along Section A-A in Figure 6.23) for the fixed and hinged tanks due to 1994 Northridge and 1995 Kobe earthquakes, respectively.

(a) Section A-A side view

Selected nodes along
the wall height

Input earthquake (in X direction)

(b) Section A-A plan view

Element A
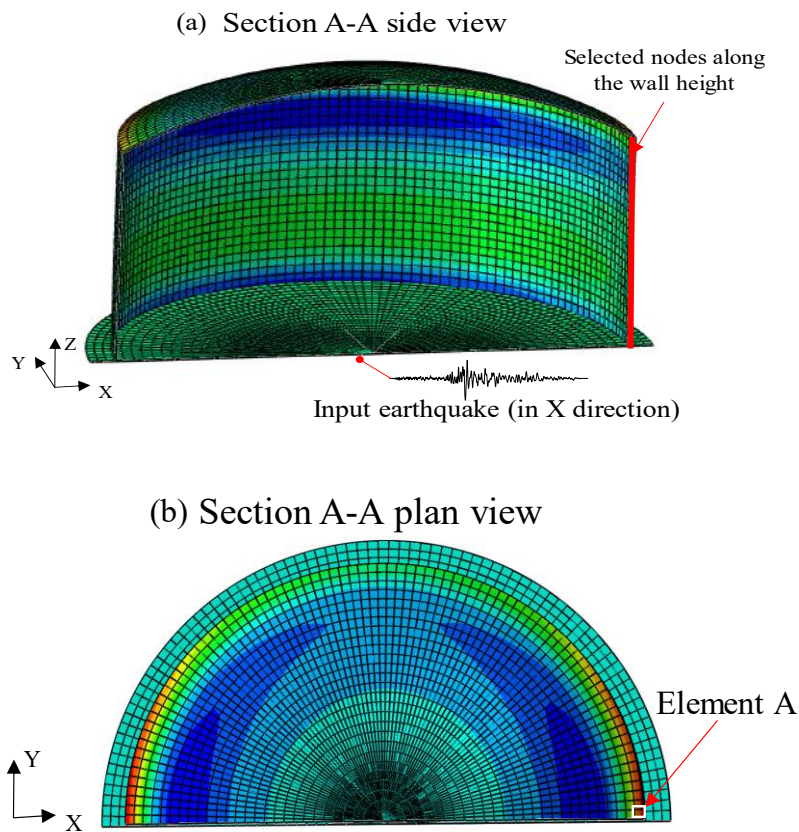
Figure 6.23 Section A-A of the tank, (a) side view, (b) plan view.

Referring to Table 6.4 and Figure 6.22, the base shear force occurred at the base of the hinged base tank is larger than the fixed base tank, as the shear force increased from 72.6 MN to 83.6 MN under 1994 Northridge and from 48.2 MN to 59.8 MN under 1995 Kobe (i.e. 24% more); as the natural period increased for the hinged base tank compared with the fixed base tank in the short period range, which caused the increase in the base shear force for the hinged base tank.

Figure 6.24 shows the hoop forces for the fixed base and hinged base tank along the height of the tank wall due to 1994 Northridge (Figure 6.24a) and 1995 Kobe (Figure 6.24b). In general, the maximum hoop forces occurred at the top of the tank wall, while the hinged base tank experienced higher hoop force at the wall top compared with the fixed base tank. Indeed, mentioning the Table 6.4, the maximum hoop forces increased from fixed base tank to hinged base tank with 46% for 1994 Northridge and 48% for 1995

Kobe earthquakes. This observation is related to the fixed roof effect on the hoop forces; the roof exerts more hoop force for hinged base tank compared with the fixed base tank because of the reduction of the lateral stiffness at the tank base.
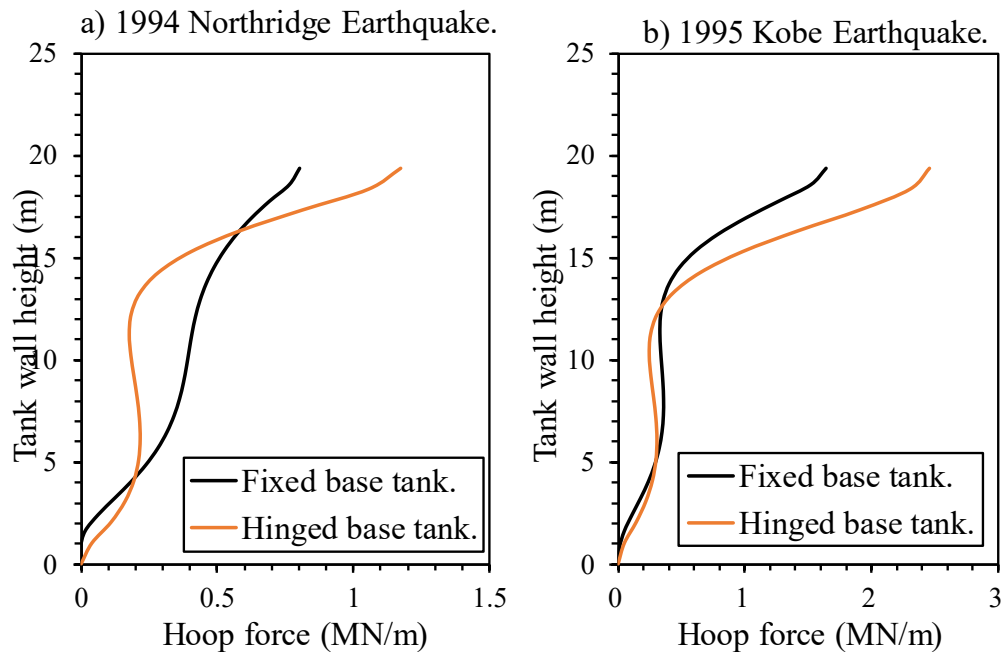
Figure 6.24 Distribution of hoop force along the height of the tanks wall along Section A-A when the maximum hoop force was observed for (a) 1994 Northridge earthquake and (b) 1995 Kobe earthquake.

On the other hand, Figure 6.25 represents the bending moment for the fixed base condition and hinged base condition along the height of the tank wall due to 1994 Northridge (Figure 6.25a) and 1995 Kobe (Figure 6.25b). For hinged base condition, as expected the bending moment is zero at the wall base for both earthquakes, while the corresponding bending moments at the base for the fixed base condition are 68.7 kN.m/m under 1994 Northridge earthquake, and 51.4 kN.m/m under 1995 Kobe earthquake. However, the hinged base tank experiences more bending moment for the upper part of the tank wall compared with the fixed base tank. In general, more contribution of higher structural modes is observed in the hinged base tank compared with the fixed base tank.
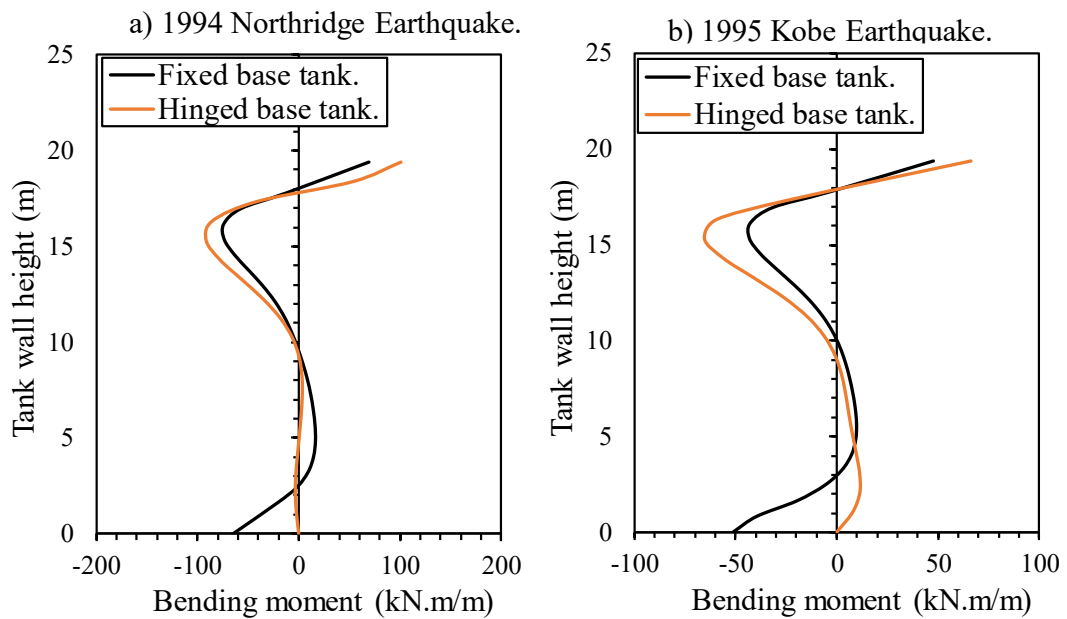
Figure 6.25 Distribution of the bending moments along the height of the tanks wall along Section A-A when the maximum bending moment was observed for: (a) 1994 Northridge and (b) 1995 Kobe.

In addition, Figure 6.26 shows the radial displacements of the fixed and hinged base tank conditions under 1994 Northridge (Figure 6.26a) and 1995 Kobe (Figure 6.26b) earthquakes. As the hinged base tank has the ability to rotate in the radial direction, the radial/lateral displacements on the hinged base tank are more than the fixed base tank subjected to both earthquakes. Referring to Figure 6.26, the maximum lateral displacements which occurred at the wall-roof connection, were 13.3 mm and 4.6 mm for the hinged base tank subjected to the 1994 Northridge and the 1995 Kobe earthquakes, respectively. The corresponding values for the fixed base condition were 9.7 mm and 3.7 mm.
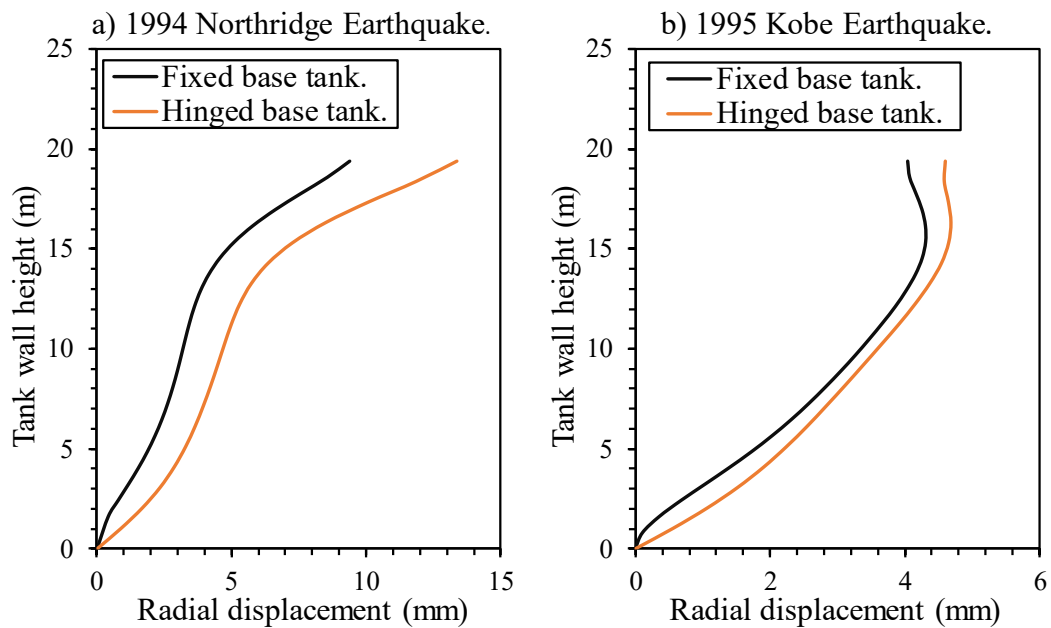
Figure 6.26 Distribution of radial displacements along the height of the tank wall along Section A-A when the radial displacement was observed for: (a) 1994 Northridge and (b) 1995 Kobe.

To evaluate the damage of the LNG concrete tanks under large earthquakes, the strain time history for a selected element (i.e. Element A as shown in Figure 6.23b) which experienced tensile damage is compared. Figure 6.27 shows the strain time history of the Element A (wall-roof joint) for the fixed and hinged base conditions under 1994 Northridge earthquake. It is evident that the strain increased to 0.005% due to the dead load and then started to oscillate around this value during the 1994 Northridge earthquake excitation. Indeed, Element A constantly experienced tension (as the strain was mostly kept above zero), which means the compressive damage was not observed. Then at about t = 5 s, when the peak acceleration (PGA = 0.84 g) occurred, the strain increased considerably to 0.016% well exceeding the cracking strain of 0.0087%. However, the strain time history for the fixed base condition oscillated around the initial strain due to self-weight while the maximum strain was 0.013% at t = 5 s. In general, the Element A in hinged base tank experienced higher strains compared with the fixed base counterpart, under both earthquakes (see Figure 6.27a and Figure 6.27b). The maximum predicted

tensile strain for the hinged base condition under 1995 Kobe was 0.013%, and the corresponding value for the fixed base counterpart was 0.011% (i.e. 20% more). This observation is in line with the structural response reported in Figure 6.26, where more displacements were induced in the hinged base tank wall compared with the fixed based tank, creating more strains and thus damage the wall-roof joint in the hinged base tank.
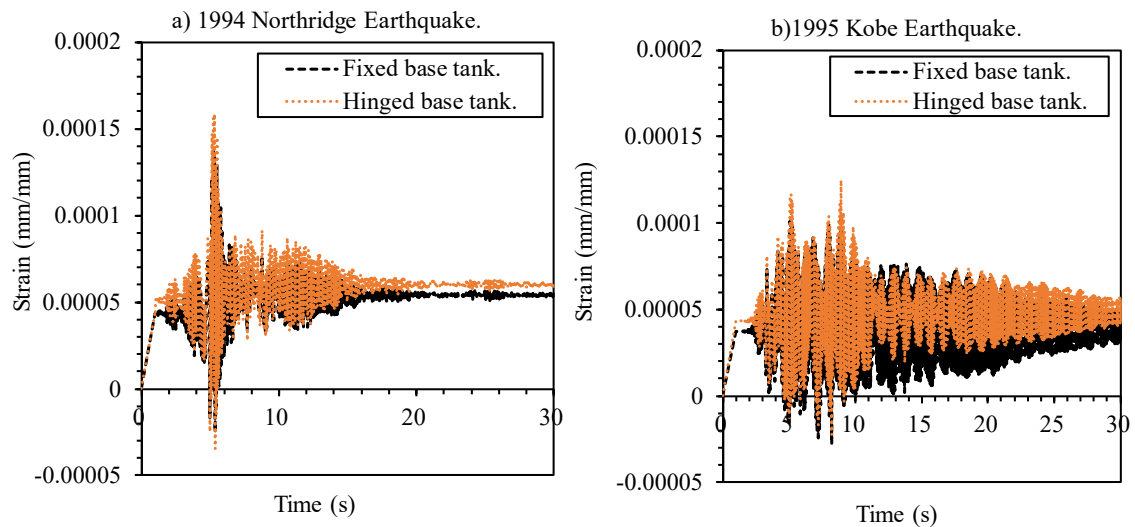
Figure 6.27 Strain time histories for the fixed base and hinged base tanks under at Element A (wall-roof joint); (a) 1994 Northridge, (b) 1995 Kobe.

The tensile damage parameter for the fixed and hinged base condition of the LNG tanks under 1994 Northridge and 1995 Kobe earthquakes is extracted and shown in Figure 6.28. The pattern of the damage with the estimation of the stiffness degradation are illustrated for both hinged and fixed base under 1994 Northridge earthquake in Figure 6.26a, and under 1995 Kobe earthquake in Figure 6.26b. The tensile damage variable due to cracking, as it characterises the stiffness degradation of the concrete, which takes values from zero (undamaged material) to one (total loss of stiffness). Figure 6.26 proves that the tensile stiffness reduction in the hinged base tank reached 64%, while for the fixed base it reached 55% under the 1994 Northridge earthquake. And the stiffness reduction for the hinged and fixed base tanks under 1995 Kobe earthquake were 43% and 36% respectively. Indeed, the cracks were generated in the tank roof only; which has less

section thickness compared with the top of tank wall. These predicted stiffness degradation and damage variations are in line with the strain variations reported in Figure 6.26.
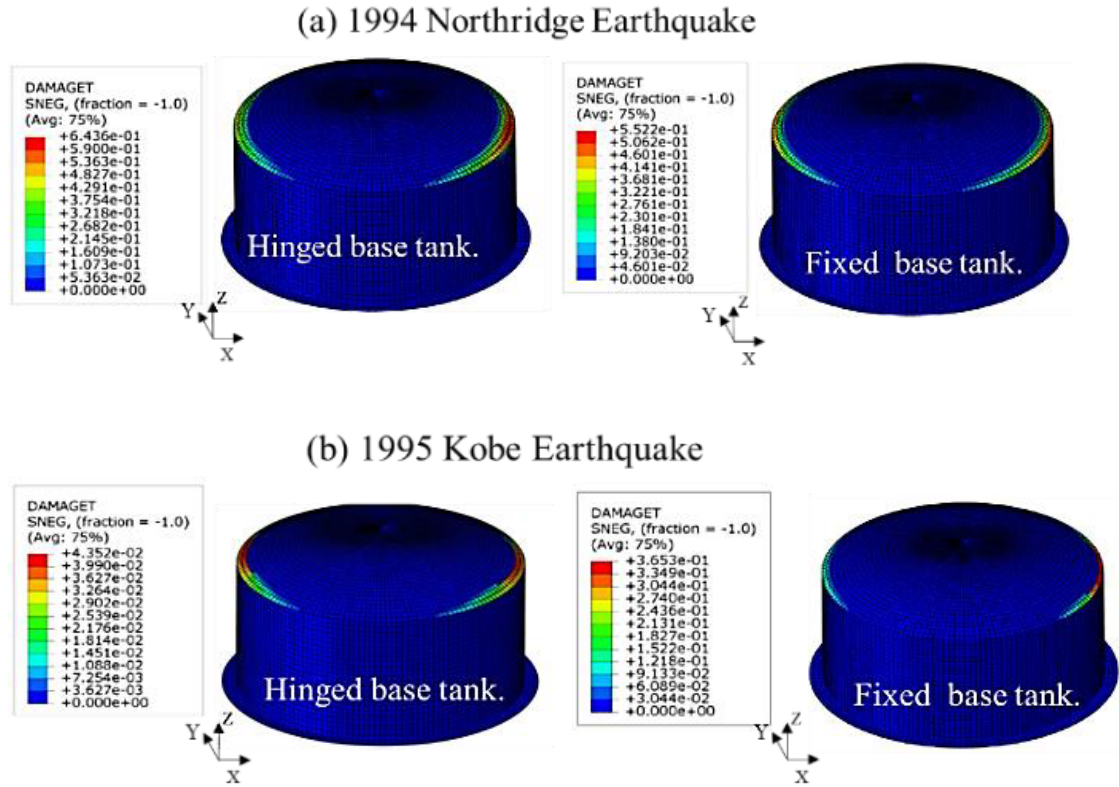
Figure 6.28 Maps of the damage and stiffness degradation of the hinged and fixed base tanks under: (a) 1994 Northridge, (b) 1995 Kobe.

6.4 Summary

This chapter investigated the seismic vulnerability of the inner steel LNG tanks with varying height (H) to diameter (D) aspect ratios. Dynamic FSI was modelled using the added-mass method, and tank walls were modelled using general-purpose finite element software ABAQUS (version 2018), considering the material and geometric nonlinearities. The horizontal acceleration was applied at the tank base using rigid boundary conditions, assuming a fixed base condition often observed when tank sits of strong bedrock. The modal analysis was conducted using the Block Lanczos algorithm. The results highlighted

how the tank aspect ratio can change the deformed shape of the tank during an earthquake associated with the fundamental mode of tanks changing with the aspect ratio. For the tall tank, the fundamental mode shape was a bending mode of a cantilever beam. For the medium tank, the deformed shape captured a bulge formed near the mid-height of the wall. In addition, the nonlinear time-history analysis results predicted elastic secondary buckling for the medium tank at the upper portion of the tank wall. Moreover, the von Mises stresses exceeded the stress yield limit at the tank base level for the tall tank, and elephant's foot buckling (i.e. elastic-plastic buckling) was observed. It should be noted that no damage was observed for the broad tank. The results also demonstrated the importance of selection of the tank aspect ratio to meet the design safety requirements (i.e. avoid buckling). The results highlighted that the selection of optimum aspect ratio, particularly in areas with moderate to high seismicity, can result in a safe and economic seismic design.

In addition, the nonlinear behaviour of ground supported RC containment under seismic loads was examined for two wall support connection types; namely, hinged and fixed. A three-dimensional finite element model including the material nonlinearities was adopted. The CDP model was adopted to capture the possible tensile cracking and compressive crushing under seismic load. The results found that the walls experience higher seismic demand in the hinged tank compared to the fixed base tank, mainly in the mid-height region of the tank wall. Contrarywise, the fixed tank base was experienced higher shear forces and bending moments than the hinged tank base. Under the influences of rapid seismic shaking, both tanks were damaged, yet more seismic forces for the case of hinged tank could potentially create more damage.

CHAPTER 7   CONCLUSIONS AND RECOMMENDATIONS

7.1   General

Growing demand for large-capacity tanks to store LNG, offering transition source of energy to green future is evident. In the current research project, an advanced numerical model to simulate LNG tank system, including Soil-Foundation-Structure Interaction (SFSI) and Fluid-Structure Interaction (FSI) effects was developed for assessing the seismic resilience under different sub-soil conditions. A series of numerical simulations were conducted to investigate the effect of pile foundation arrangements and the presence of liquefiable soil deposit on the seismic resilience of LNG tanks including material and geometric nonlinearities. Modal analyses were performed to evaluate the effect of SFSI and FSI on the dynamic properties of LNG tanks under different sub-soil conditions. The nonlinear time-history analyses were conducted adopting the direct method of analysis to evaluate the inertial and kinematic interaction effects on the LNG tank and the supporting pile foundation system. The developed models were capable of capturing the inelastic behaviour of several components of the LNG tank including the buckling of the inner steel tank, plastic hinge formations in the pile foundation, and the hysteresis damping with stiffness degradation for the clay soils to achieve a realistic response of the LNG tank. More specific conclusions from each section of the thesis reported earlier are presented in the following sections.

7.2 Conclusions related to importance of pile foundation arrangement on seismic response of LNG tanks

This part of research presented the results of seismic analysis of a 63,000 m^3 full containment LNG tank built on different pile foundations considering SFSI and the FSI. In particular, the impacts of the type of pile foundation and the load transfer mechanism (i.e. end-bearing versus frictional pile-raft foundation types) and the pile length were investigated. The results show the SFSI significantly alerted the dynamic characteristics of the LNG tanks for all adopted foundation options and thus consideration of SFSI for LNG tank on pile foundation is essential. In addition, the results show that the deep foundation type could influence the dynamic characteristics and response of LNG tank-foundation-soil system as the spectral acceleration as well as the system period changed slightly, with the tanks on the end-bearing pile foundation experiencing larger spectral accelerations in comparison to the other two frictional pile foundation options. The results of this study show that the end-bearing pile foundation (i.e. stiffer foundation system) directed more seismic energy to the LNG tank compared with the other two pile-raft foundation alternatives (i.e. Overdesigned). Indeed, an increase in the pile length for the pile-raft foundation resulted in more interaction between the soil and foundation and thus transferred more seismic forces to the piles and superstructure. This observation highlights the importance of considering the combined effects of the kinematic and inertial interactions influencing the forces on piles, which cannot be captured accurately in sub-structuring technique, where the superstructure (i.e. LNG tank) and pile foundation are modelled separately.

7.3 Conclusions related to capabilities of kinematic hardening model for capturing the seismic wave propagation in clay soil deposit

This section of study aimed at assessing the suitability of nonlinear kinematic hardening (NKH) model available in common structural software packages such as ABAQUS for simulation of response of saturated clay deposit under seismic loading. Thus, results of the site response analysis for three different soil stiffnesses, namely, Site Classes C, Site Class D, and Site Class E, with shear wave velocity V_s =564 m/s, 270 m/s, and 160 m/s, respectively, were presented. The seismic site response analyses were conducted by adopting four benchmark earthquakes (two near field and two far field earthquakes), and in addition to the original bedrock records, three different hazard levels based on annual probabilities exceed levels (i.e. seismic demand levels) were used for scaling the records to cover a wider range of earthquake characteristics. The numerical predictions adopting the nonlinear kinematic hardening (NKH) model programmed in ABAQUS were compared with well-established stiffness degradation with hysteresis damping (SDHD) soil model available in FALC 3D for validation purposes. A three-dimensional numerical model was developed in both ABAQUS and FLAC3D software packages, where the infinite element and viscous boundaries were implemented, respectively, to model the far-field soil and absorb the seismic energy of the unbounded soils. The calibrations of the NKH soil model were explained in details and the parameters were selected based on the well-established data available in the literature for the different site classes. Then, the site response analysis was conducted adopting fully nonlinear analysis in the time domain, the results of both NKH and SDHD models show that reduction in the soil stiffness (i.e. shear wave velocity) resulted in higher shear strains in the soil and amplified hysteresis damping as a result of more seismic energy dissipation for all adopted earthquakes. Moreover, both numerical models showed horizontal

earthquake amplification as the seismic wave propagated from the bedrock to the ground surface, where more significant amplifications were evident for far field earthquakes. Moreover, it is observed that earthquake with lower dominant frequency (i.e. 1994 Northridge) experienced acceleration amplification over longer duration of earthquake. Indeed, the results of the acceleration response spectrum from both NKH and SDHD soil models showed that the dynamic propertied of the soil deposit and the characteristics of the adopted earthquake records at the bedrock impact the ground surface vibration. In particular, results show that near field earthquakes propagating via stiff soil deposit resulted in earthquake acceleration amplification in low period range (T < 0.3 s), where the natural period of the stiff deposit aligned with dominant periods of the earthquakes and thus mobilising higher seismic energy. Moreover, reducing the soil stiffness resulted in shifting the peak acceleration response spectrum to intermediate and high period ranges. Furthermore, the numerical predictions from both NKH (ABAQUS) and SDHD (FLAC 3D) models highlighted the importance of hazard level on site amplification factors since earthquake scaling by matching relevant target response spectrum could alert the earthquake characteristics and seismic site response results. Comparison of the shear stress – strain response, acceleration time history and earthquake response spectra from different earthquakes and soil deposits showed a good agreement between predictions of NKH soil model programmed in ABAQUS and benchmark exercise adopting SDHD soil model available in FLAC 3D. Thus, results of this study can give further confidence to practicing engineers to adopt nonlinear kinematic hardening (NKH) for soil modelling for seismic analysis and design. It is recommended in future research to further verify suitability of NKH model for complex vibration scenarios such as combined vertical and horizontal earthquake wave propagation.

7.4   Conclusions related to effect of liquefied soil deposit on seismic resilience of LNG tank

This part of study presented the results of seismic analysis of a 160,000 m^3 full containment LNG tank considering SFSI and FSI while assessing the impacts of the depth of soil liquefaction on performance of different components of the system. Four different soil deposit scenarios were investigated, namely, non-liquefied soil deposit (Scenario I), and liquefied soil deposit with their liquefied layer depth increasing from 5.0 m (Scenario II) to 10.0 m (Scenario III) and 15.0 m (Scenario IV). A three-dimensional numerical model of the entire tanks, piles and soil system was developed, and the free vibration and time history analyses were conducted adopting fully nonlinear analysis in the time domain. Indeed, direct method of analysis was adopted in which the LNG tank, foundation and soil were simulated and analysed in one step.

The free vibration analyses were performed for the LNG tank using Block Lanczos algorithm, and the results showed that the presence of the liquefied soil significantly alerted the dynamic characteristics of the LNG tank, impacting the seismic performance of the tank system. The ground response analysis showed the liquefied soil layer reduced the spectral acceleration in short period range and amplified the spectral accelerations in the long period range, while increasing the liquefied soil depth lengthened the natural period of the LNG tank.

The nonlinear time history results showed that the seismic forces developed in the inner and outer tank systems reduced as the depth of liquefaction increased. Indeed, increased soil damping and increased structural flexibility directed less seismic forces to LNG tank, and thus the case with non-liquifiable soil deposit resulted in the maximum forces and stresses in the superstructure. The observed potential failure of the inner steel

tank was the elastic - plastic buckling mode at the mid-height of the inner tank wall, as the von Mises stresses exceed the yield stress for Scenario I. Since, increasing the depth of the liquefied soil, reduced the seismic response of the superstructure, no damage or failure was observed in the inner steel tank for Scenarios II to IV, while localised von Mises stress were observed near the base of the tank. However, when the liquefied soil depth increase, the impulsive forces along the tank wall decreased, while amplification of convective forces particularly for Scenarios III and IV were observed, since the dominant frequency of the seismic wave was reduced which in turn induced increased convective forces.

On the other hand, soil liquefaction and its depth impacted the seismic response of the pile foundation adversely, due to the observed amplified shear forces, bending moments and deflections in the piles. Moreover, presence of liquefied soil layer exacerbated the inability of the piles to match the deformation of the surrounding soil, and thus resulted in more kinematic interaction induced loads (i.e. shear forces and bending moments). Indeed, with the increase in the thickness of the liquefied layer, although the loads due to inertial interaction decreased, the loads developed in the piles due to kinematic interaction increased and extended deeper, and eventually additional localised plastic deformations in the piles were observed at depths well below the pile head.

7.5 Conclusions related to Effect of height to diameter aspect ratios on seismic response of LNG tank.

In this part of thesis, the seismic performance of a broad, medium and tall 9% Ni steel LNG tanks with different aspect ratios (*H/D*) under two strong near-field earthquake ground motions (1994 Northridge and 1995 Kobe earthquakes) were investigated. The modal analysis showed that the deformed shape associated with fundamental mode of tall tank (*H/D* =0.95) is comparable with a bending mode of a cantilever beam, while for medium Tank (*H/D* = 0.63) the deformed shape captured a bulge formed near the mid-height of the wall. The nonlinear time-history analysis results predicted elastic secondary buckling for the medium tank at the upper portion of the tank wall. The von Mises stresses exceeded the stress yield limit at the tank base level for the tall tank and elephant's foot buckling (i.e. elastic-plastic buckling) was observed. No damage observed for the broad tank (*H/D* =0.40). For the investigated cases, increasing the tank aspect ratio (*H/D*) from 0.63 to 0.95 (i.e. medium to tall tank) can offer around 20% more storage capacity; however, it increases the base shear forces by 60% and the overturning moments by 50% meaning thicker tank walls are required to meet the design safety requirements (i.e. avoid buckling). The selection of optimum tank ratio particularly in areas with moderate to high seismicity is critical for a safe and economic seismic design.

7.6 Conclusions related to effects of wall support condition on seismic response of reinforced concrete containment tank.

In this part of thesis, the effects of the type of wall to base slab connection (i.e. hinged or fixed) on the nonlinear seismic response of a reinforced concrete LNG tank was investigated. To capture the inelastic behaviour of the tank, the concrete damage plasticity (CDP) model was adopted, which could capture the permanent damage to the concrete

tank during the seismic excitation. Modal and time history analyses were conducted. The results showed that the hinged base tank experienced slightly higher base shear forces, and higher radial/lateral displacements, which results in significant tensile damage, cracking and stiffness degradation for the hinged tank under 1994 Northridge and 1995 Kobe earthquakes. While, the fixed base tank experienced higher bending moment at the tank base compared with the hinged base tank, nevertheless, no damage was observed at the wall - base connection. It can be concluded that adding structural flexibility at the tank base can potentially lead to higher seismic forces on the tank wall and more damage particularly for the large containment tanks subjected to large earthquakes, which means for hinged base tank the roof needs to strengthen by increasing the reinforcement to prevent any damage. Since, the natural period of the considered tanks is located in the response spectrum short-period of the applied earthquakes, enlargement the period as a result of hinging the wall to base connection would result in more base shear force being transferred to the LNG concrete tank. Indeed, for building structures with high natural frequency (or low natural period), providing more flexibility leads to reduction in the seismic demand.

7.7   Recommendations for future research

The current study was focused on developing the advanced numerical model for LNG tanks, including SFSI and FSI effects, for assessing the seismic resilience of LNG tanks under different sub-soil conditions. Rigorous numerical simulations were conducted to investigate the effect of pile foundation arrangements and the liquefiable soil deposit on the seismic response of LNG tanks. While this study covered various issues concerning seismic resilience of LNG tanks, further numerical and experimental studies are recommended for future studies and can be done in the following parts:

- Enhancing the developed numerical model by incorporating more advanced FSI modelling techniques to capture the effect of LNG sloshing on the fixed RC roof and upper section of the inner steel tank walls is recommended. More rigorous method to capture FSI technique can result in a more accurate and realistic illustration of the convective hydrodynamic components by capturing the sloshing waves at the liquid surface. Combination of CFD and FEM is recommended for further studies.

- Assessing the effects of level of LNG in the tank and how it can impact the seismic forces applied to different components of the system

- Investigating the effects of different earthquake components including both vertical and horizontal components on the global seismic performance of LNG tanks is recommended. Indeed, consideration of the vertical component of the earthquake can impact the FSI and SFSI.

- Developing step by step design guidelines for practicing engineers to analysis and design LNG tank systems on deep foundations capturing inertial and kinematic interaction effects.

- Conducting shaking table tests to validate the effectiveness of the proposed numerical model experimentally considering FSI and SFSI.

REFERENCES

Abdoun, T., and Dobry, R. (2002). "Evaluation of pile foundation response to lateral spreading". Soil Dynamics and Earthquake Engineering, 22(9-12), 1051-1058.

ACI 350.2R, (2009), "Concrete Structures for Containment of Hazardous Materials", An American Concrete Institute Standard. Farmington Hills

Agalianos, A., De Coquereaumont, O. D. C., and Anastasopoulos, I. (2020). "Rigid slab foundation subjected to strike–slip faulting: mechanisms and insights". Géotechnique, 70(4), 354-373.

Aki, K. (1993). "Local site effects on weak and strong ground motion". Tectonophysics, 218(1-3), 93-111.

Alsaleh, H., and Shahrour, I. (2009). "Influence of plasticity on the seismic soil–micropiles–structure interaction". Soil Dynamics and Earthquake Engineering, 29(3), 574-578.

Ambrosini, R. D. (2006). "Material damping vs. radiation damping in soil–structure interaction analysis". Computers and Geotechnics, 33(2), 86-92.

Ambrosini, R. D., and Luccioni, B. M. (2006). "Craters produced by explosions on the soil surface". 33(2), 890-900.

Anand, V., and Kumar, S. S. (2018). "Seismic soil-structure interaction: a state-of-the-art review". Paper presented at the Structures. (16), 317-326

Anastasopoulos, I., Gerolymos, N., Gazetas, G., and Bransby, M. (2008). "Simplified approach for design of raft foundations against fault rupture. Part II: Soil-structure interaction". Earthquake Engineering and Engineering Vibration, 7(2), 165-179.

Anastasopoulos, I., Gerolymos, N., Drosos, V., Kourkoulis, R., Georgarakos, T., and Gazetas, G. (2007). "Nonlinear response of deep immersed tunnel to strong seismic shaking". Journal of Geotechnical and Geoenvironmental Engineering, 133(9), 1067-1090.

Anastasopoulos, I., Gerolymos, N., Gazetas, G., and Bransby, M. (2008). "Simplified approach for design of raft foundations against fault rupture. Part II: Soil-structure interaction". Earthquake Engineering and Engineering Vibration, 7(2), 165-179.

Anastasopoulos, I., Kourkoulis, R., Gazetas, G., and Tsatsis, A. (2013). "Interaction of piled foundation with a rupturing normal fault". Géotechnique, 63(12), 1042-1059.

Animah, I., and Shafiee, M. (2020). "Application of risk analysis in the liquefied natural gas (LNG) sector: An overview". Journal of Loss Prevention in the Process Industries, 63, 103980. doi:https://doi.org/10.1016/j.jlp.2019.103980

Armstrong PJ, Frederick C (1966) A mathematical representation of the multiaxial Bauschinger efect, vol 731. Central Electricity Generating Board and Berkeley Nuclear Laboratories, Berkeley

API 620 (American Petroleum Institute Standards). 2013. Design and Construction of Large, Welded, Low-Pressure Storage Tanks. API 620. Washington, DC.

API 650 (American Petroleum Institute Standards). 2007. Welded steel tanks for oil storage. API 650. Washington, DC: API.

AS/NZS1170.5. (2004). Standards New Zealand. In Structural Design Actions, Part 5: Earthquake Actions New Zealand.: Wellington.

ASTM. 2017. Standard specification for pressure vessel plates, alloy steel, double-normalized and tempered 9% nickel. ASTM A353-17.West Conshohocken, PA: ASTM.

Assimaki, D., and Gazetas, G. (2004). "Soil and topographic amplification on canyon banks and the 1999 Athens earthquake". Journal of earthquake engineering, 8(01), 1-43.

Assimaki, D., Kausel, E., and Gazetas, G. (2005). "Soil-dependent topographic effects: a case study from the 1999 Athens earthquake". Earthquake Spectra, 21(4), 929-966.

Assimaki, D., and Shafieezadeh, A. (2013). "Soil–pile–structure interaction simulations in liquefiable soils via dynamic macroelements: Formulation and validation". Soil

Dynamics and Earthquake Engineering, 47, 92-107.

Association of Fire Protaction NFPA 59A (2019). Standard for the Production, Storage, and Handling of Liquefied Natural Gas (LNG). In: National Fire Protection Association.

Bandyopadhyay, K., Cornell, A., Costantino, C., Kennedy, R., Miller, C., and Veletsos, A. (1995). "Seismic Design and Evaluation Guidelines for the Department of Energy High-Level Waste Storage Tanks and Appurtenances." Engineering Research and Applications Division, Department of Advanced Technology, Brookhaven National Laboratory, Upton, New York.

Banerjee, S., Goh, S., and Lee, F. (2014). "Earthquake-induced bending moment in fixed-head piles in soft clay". Géotechnique, 64(6), 431-446.

Bayraktar, A., Sevim, B., Altunışık, A. C., and Türker, T. (2010). "Effect of the model updating on the earthquake behavior of steel storage tanks". Journal of Constructional Steel Research, 66(3), 462-469.

Belostotskiy, A. M., Akimov, P. A., Afanasyeva, I. N., Usmanov, A. R., Scherbina, S. V., and Vershinin, V. V. (2015). "Numerical simulation of oil tank behavior under seismic excitation. fluid–structure interaction problem solution". Procedia Engineering, 111, 115-120.

Bernier, C., and Padgett, J. E. (2020). "Fragility Assessment of Floating Roof Storage Tanks during Severe Rainfall Events". Journal of Performance of Constructed Facilities, 34(6), 04020101.

Beskos, D. E. (1997). "Boundary element methods in dynamic analysis. Applied Mechanics Review 1987; 40:1–23

Bhattacharya, S., and Madabhushi, S. (2008). "A critical review of methods for pile design in seismically liquefiable soils". Bulletin of earthquake engineering, 6(3), 407-446.

Bohlen, T., and Saenger, E. H. (2006). "Accuracy of heterogeneous staggered-grid finite-difference modeling of Rayleigh waves". Geophysics, 71(4), 109-115.

Bonnet, M. (1999). "Boundary integral equation methods for solids and fluids".

Meccanica, 34(4), 301-302.

Booth, E., and Fenwick, R. (1994). Concrete structures in earthquake regions: design and analysis: Longman Scientific & Technical Harlow, 105-108.

Borcherdt, R. D. (1970). "Effects of local geology on ground motion near San Francisco Bay". Bulletin of the Seismological Society of America, 60(1), 29-61.

Boulanger, R. W., Kamai, R., and Ziotopoulou, K. (2014). "Liquefaction induced strength loss and deformation: simulation and design". Bulletin of earthquake engineering, 12(3), 1107-1128.

Bradley, B. A. (2012). "Empirical correlations between peak ground velocity and spectrum-based intensity measures". Earthquake Spectra, 28(1), 17-35.

Brunelli, A., de Silva, F., Piro, A., Parisi, F., Sica, S., Silvestri, F., and Cattari, S. (2021). "Numerical simulation of the seismic response and soil–structure interaction for a monitored masonry school building damaged by the 2016 Central Italy earthquake". Bulletin of earthquake engineering, 19(2), 1181-1211.

Brunesi, E., Nascimbene, R., Pagani, M., and Beilic, D. (2015). "Seismic performance of storage steel tanks during the May 2012 Emilia, Italy, earthquakes". Journal of Performance of Constructed Facilities, 29(5), 04014137.

Buratti, N., and Tavano, M. (2014). "Dynamic buckling and seismic fragility of anchored steel tanks by the added mass method". Earthquake Engineering & Structural Dynamics, 43(1), 1-21.

Calderón, M., Illing, D., and Veiga, J. (2016). "Facilities for bunkering of liquefied natural gas in ports". Transportation research procedia, 14, 2431-2440.

Cavalieri, F., Correia, A. A., Crowley, H., and Pinho, R. (2020). "Seismic fragility analysis of URM buildings founded on piles: influence of dynamic soil–structure interaction models". Bulletin of Earthquake Engineering, 18(9), 4127-4156.

Chang, S. E. (2010). "Urban disaster recovery: a measurement framework and its application to the 1995 Kobe earthquake". Disasters, 34(2), 303-327.

Chen, J. H., Froment, B., Liu, Q. Y., and Campillo, M. (2010). "Distribution of seismic

wave speed changes associated with the 12 May 2008 Mw 7.9 Wenchuan earthquake". Geophysical Research Letters, 37(18).

Chen, Q.-S., Wegrzyn, J., and Prasad, V. (2004). "Analysis of temperature and pressure changes in liquefied natural gas (LNG) cryogenic tanks". Cryogenics, 44(10), 701-709.

Chong, X., Xiwei, X., Xiyan, W., Fuchu, D., Xin, Y., and Qi, Y. (2013a). "Detailed catalog of landslides triggered by the 2008 Wenchuan earthquake and statistical analyses of their spatial distribution". J. Eng. Geol, 21(1), 25-44.

Chopra, A. K., and Kan, C. (1973). "Effects of stiffness degradation on ductility requirements for multistorey buildings". Earthquake engineering & structural dynamics, 2(1), 35-45.

Christovasilis, I. P., and Whittaker, A. S. (2008). "Seismic analysis of conventional and isolated LNG tanks using mechanical analogs". Earthquake Spectra, 24(3), 599-616.

Chun, B., Jinn, J., and Lee, J. (2002). "Modeling the Bauschinger effect for sheet metals, part I: theory". International Journal of Plasticity, 18(5-6), 571-595.

Chung, M., Kim, J., and Kim, J.-K. (2019). "Feasibility study on the wide and long 9% Ni steel plate for use in the LNG storage inner tank shell". Steel and Composite Structures, 32(5), 571-582.

Cicekli, U., Voyiadjis, G. Z., and Al-Rub, R. K. A. (2007). "A plasticity and anisotropic damage model for plain concrete". International Journal of Plasticity, 23(10-11), 1874-1900.

Colombo, S., El Harrak, M., and Sartori, N. (2016). "The future of natural gas: Markets and geopolitics.". Rabat, Morocco: Policy Center for the New South.

Dangla, P., Semblat, J.-F., Xiao, H., and Delépine, N. (2005). "A simple and efficient regularization method for 3D BEM: application to frequency-domain elastodynamics". Bulletin of the Seismological Society of America, 95(5), 1916-1927.

Das, B. M., and Larbi-Cherif, S. (1983). "Bearing capacity of two closely-spaced shallow

foundations on sand". Soils and Foundations, 23(1), 1-7.

Di Sarno, L., and Karagiannakis, G. (2020). "On the seismic fragility of pipe rack—piping systems considering soil–structure interaction". Bulletin of Earthquake Engineering, 1-35.

Dobry, R., and Gazetas, G. (1988). "Simple method for dynamic stiffness and damping of floating pile groups". Geotechnique, 38(4), 557-574.

Dogangun, A., Karaca, Z., Durmus, A., and Sezen, H. (2009). "Cause of damage and failures in silo structures". Journal of Performance of Constructed Facilities, 23(2), 65-71.

Dong, Y., Burd, H., and Houlsby, G. (2016). "Finite-element analysis of a deep excavation case history". Géotechnique, 66(1), 1-15.

Driver, R. G., Kulak, G. L., Kennedy, D. L., and Elwi, A. E. (1998). "Cyclic test of four-story steel plate shear wall". Journal of Structural Engineering, 124(2), 112-120.

Dulinska, J. M., and Jasinska, D. (2014). "Performance of steel pipeline with concrete coating (modeled with concrete damage plasticity) underseismic wave passage". Paper presented at the Applied Mechanics and Materials. (Vol. 459, pp. 608-613).

Dulinska, J. M., and Szczerba, R. (2013). "Assessment of concrete bridge performance under moderate seismic shock using concrete damage plasticity model". Procedia engineering, 57, 1319-1328.

Dutta, A., and Talukdar, S. (2004). "Damage detection in bridges using accurate modal parameters". Finite Elements in Analysis and Design, 40(3), 287-304.

Dutta, S. C., and Roy, R. (2002). "A critical review on idealization and modeling for interaction among soil–foundation–structure system". Computers and structures, 80(20-21), 1579-1594.

El Naggar, M., and Novak, M. (1996). "Nonlinear analysis for dynamic lateral pile response". Soil Dynamics and Earthquake Engineering, 15(4), 233-244.

Elia, G., and Rouainia, M. (2016). "Investigating the cyclic behaviour of clays using a kinematic hardening soil model". Soil Dynamics and Earthquake Engineering, 88,

399-411.

Esteva, L. (1987). "Earthquake engineering research and practice in Mexico after the 1985 earthquakes". Bulletin of the New Zealand Society for Earthquake Engineering, 20(3), 159-200.

Elwardany, H., Seleemah, A., Jankowski, R., and El-Khoriby, S. (2019). "Influence of soil–structure interaction on seismic pounding between steel frame buildings considering the effect of infill panels". Bulletin of Earthquake Engineering, 17(11), 6165-6202.

Eurocode-8. (2006). Design of structures for earthquake resistance, part 4: Silos, tanks and pipelines. In. Brussels, Belgium.

EN B 14620-2 (2006). Design and manufacture of site built, vertical, cylindrical, flat bottomed steel tanks for the storage of refrigerated, liquefied gases with operating temperatures between 0~ C and-165~ C.In Part2 (Vol. 2).

Faria, R., Oliver, J., and Cervera, M. (1998). "A strain-based plastic viscous-damage model for massive concrete structures". International journal of solids and structures, 35(14), 1533-1558.

Fatahi, B., Van Nguyen, Q., Xu, R., and Sun, W.-j. (2018). "Three-dimensional response of neighboring buildings sitting on pile foundations to seismic pounding". International Journal of Geomechanics, 18(4), 04018007.

Field, E. H., and Jacob, K. H. (1995). "A comparison and test of various site-response estimation techniques, including three that are not reference-site dependent". Bulletin of the Seismological Society of America, 85(4), 1127-1143.

Figini, R., Paolucci, R., and Chatzigogos, C. (2012). "A macro-element model for non-linear soil–shallow foundation–structure interaction under seismic loads: theoretical development and experimental validation on large scale tests". Earthquake engineering & structural dynamics, 41(3), 475-493.

Frankel, A., and Vidale, J. (1992). "A three-dimensional simulation of seismic waves in the Santa Clara Valley, California, from a Loma Prieta aftershock". Bulletin of the Seismological Society of America, 82(5), 2045-2074.

Frémond, M., and Nedjar, B. (1995). "Damage in concrete: the unilateral phenomenon". Nuclear engineering and design, 156(1-2), 323-335.

Furumura, T., and Kennett, B. (1998). "On the nature of regional seismic phases—III. The influence of crustal heterogeneity on the wavefield for subduction earthquakes: the 1985 Michoacan and 1995 Copala, Guerrero, Mexico earthquakes". Geophysical Journal International, 135(3), 1060-1084.

Galal, K., and Naimi, M. (2008). "Effect of soil conditions on the response of reinforced concrete tall structures to near-fault earthquakes". The Structural Design of Tall and Special Buildings, 17(3), 541-562.

Gazetas, G., and Apostolou, M. (2004). "Nonlinear soil–structure interaction: foundation uplifting and soil yielding". Paper presented at the Proceedings Third UJNR Workshop on Soil-Structure Interaction.(1), 29-30.

Gazetas, G., and Ziotopoulou, A. (2010). "Binormalized response spectrum for a rational soil-structure interaction analysis". Paper presented at the Workshop on soil structure interaction (SSI) knowledge and effect on the seismic assessment of NPPS structures and components, Otawa, Canada.

Genikomsou, A. S., and Polak, M. A. (2015). "Finite element analysis of punching shear of concrete slabs using damaged plasticity model in ABAQUS". Engineering Structures, 98, 38-48.

Ghandil, M., and Behnamfar, F. (2015). "The near-field method for dynamic analysis of structures on soft soils including inelastic soil–structure interaction". Soil Dynamics and Earthquake Engineering, 75, 1-17.

Gičev, V., Trifunac, M. D., and Orbović, N. (2016). "Two-dimensional translation, rocking, and waves in a building during soil-structure interaction excited by a plane earthquake SV-wave pulse". Soil Dynamics and Earthquake Engineering, 88, 76-91.

Gičev, V., and Trifunac, M. D. (2019). "Reduction of peak ground velocity by nonlinear soil response–I: Excitation by SH pulse". Soil Dynamics and Earthquake Engineering, 127, 105810.

Gilbert, R. I., and Warner, R. F. (1978). "Tension stiffening in reinforced concrete slabs". Journal of the structural division, 104(12), 1885-1 Graczyk, M., and Moan, T. (2008). "A probabilistic assessment of design sloshing pressure time histories in LNG tanks". Ocean Engineering, 35(8-9), 834-855900.

Gürsan, C., and de Gooyert, V. (2021). "The systemic impact of a transition fuel: Does natural gas help or hinder the energy transition?". Renewable and Sustainable Energy Reviews, 138, 110552.

Hafez, A. (2012). "Seismic response of ground-supported circular concrete tanks". esis, Ryerson University, Toronto, Canada.

Hardin, B. O., and Drnevich, V. P. (1972). "Shear modulus and damping in soils: design equations and curves". Journal of the Soil Mechanics and Foundations Division, 98(7), 667-692.

Haroun, M. A., and Housner, G. W. (1981). "Earthquake Response of Deformable Liquid Storage Tanks". Journal of Applied Mechanics, 48(2), 411-418.

Haroun, M. A. (1983). "Vibration studies and tests of liquid storage tanks". Earthquake engineering & structural dynamics, 11(2), 179-206.

Haroun, M. A., and Housner, G. W. (1981). "Seismic design of liquid storage tanks". Journal of the Technical Councils of ASCE, 107(1), 191-207.

Hartzell, S., Leeds, A., Frankel, A., Williams, R. A., Odum, J., Stephenson, W., and Silva, W. (2002). "Simulation of broadband ground motion including nonlinear soil effects for a magnitude 6.5 earthquake on the Seattle fault, Seattle, Washington". Bulletin of the Seismological Society of America, 92(2), 831-853.

Hasheminezhad, A., and Bahadori, H. (2021). "Three dimensional finite difference simulation of liquefaction phenomenon". International Journal of Geotechnical Engineering, 15(2), 245-251.

Hashiguchi, K., and Ueno, M. (2017). "Elastoplastic constitutive equation of metals under cyclic loading". International Journal of Engineering Science, 111, 86-112.

Hattne, J., Shi, D., Glynn, C., Zee, C.-T., Gallagher-Jones, M., Martynowycz, M. W., Gonen, T. (2018). "Analysis of global and site-specific radiation damage in cryo-

EM". Structure, 26(5), 759-766. e754.

Helwany, S. (2007). Applied soil mechanics with ABAQUS applications: John Wiley and Sons. New York.

Hennessey, C., Castelluccio, G. M., and McDowell, D. L. (2017). "Sensitivity of polycrystal plasticity to slip system kinematic hardening laws for Al 7075-T6". Materials Science and Engineering: A, 687, 241-248.

Hokmabadi, A., Leung, E., So, M., and Yiu, J. (2019). "Impact of Soil-Structure Interaction on the Seismic Design of Large LNG Tanks". In Transformation in geotechnical engineering—Technology, digital and innovation. Hong Kong: HKIE Geotechnical Div.

Hokmabadi, A. S., and Fatahi, B. (2016). "Influence of foundation type on seismic performance of buildings considering soil–structure interaction". International Journal of structural stability and dynamics, 16(08), 1550043.

Hokmabadi, A. S., Fatahi, B., and Samali, B. (2015). "Physical modeling of seismic soil-pile-structure interaction for buildings on soft soils". International Journal of Geomechanics, 15(2), 04014046.

Hokmabadi, A. S., E. H. Y. Leung, J. Yiu, and J. W. Pappin. 2018. "Seismic design of pile foundations: Kinematic interaction in layered soils." In Proc., 16th European Conf. on Earthquake Engineering. Thessaloniki, Greece: European Association of Earthquake Engineering.

Hor, B., Hyun Jee, S., Song, M. J., and Kim, D. Y. (2017). "Ground improvement using rigid inclusion for the foundation of LNG tanks". Paper presented at the Proc. of the 19th Intern. Conf. on Soil Mechanics and Geotechnical Engineering (Sep. 17-22, 2017/COEX, Seoul, Korea) ed. by W. Lee, J.-S. Lee, H.-K. Kim, D.-S. Kim. Seoul.

Housner, G. W. (1957). "Dynamic pressures on accelerated fluid containers". Bulletin of the seismological society of America, 47(1), 15-35.

Hughes, T. J., Reali, A., and Sangalli, G. (2008). "Duality and unified analysis of discrete approximations in structural dynamics and wave propagation: comparison of p-

method finite elements with k-method NURBS". Computer methods in applied mechanics and engineering, 197(49-50), 4104-4124.

IBC. (2012). International building code . In: Dearborn Trade Publishing.

Idriss, I. M., and Boulanger, R. W. (2008). Soil liquefaction during earthquakes: Earthquake Engineering Research Institute, Oakland, CA.

Idriss, I. M., and Boulanger, R. W. (2010). "SPT-based liquefaction triggering procedures." Rep. UCD/CGM-10/02, Center for Geotechnical Modeling, Univ. of California, Davis, CA.

Ihlenburg, F., and Babuška, I. (1995). "Dispersion analysis and error estimation of Galerkin finite element methods for the Helmholtz equation". International Journal for Numerical Methods in Engineering, 38(22), 3745-3774.

Itasca Consulting Group, i. (2005). Fast lagrangian analysis of continua in 3 dimensions user's guide. In: VItasca consulting group, inc Minneapolis, Minnesota 55041, USA

Jacobsen, L. S. (1949). "Impulsive hydrodynamics of fluid inside a cylindrical tank and of fluid surrounding a cylindrical pier". Bulletin of the Seismological Society of America, 39(3), 189-204.

Jacobsen, L. S., and Ayre, R. S. (1951). "Hydrodynamic experiments with rigid cylindrical tanks subjected to transient motions". Bulletin of the Seismological Society of America, 41(4), 313-346.

Jaiswal, O., Rai, D. C., and Jain, S. K. (2007). "Review of seismic codes on liquid-containing tanks". Earthquake Spectra, 23(1), 239-260.

Jiménez, G. A. L., Dias, D., and Jenck, O. (2019). "Effect of the soil–pile–structure interaction in seismic analysis: case of liquefiable soils". Acta Geotechnica, 14(5), 1509-1525.

Jo, H., Kim, J., Lee, S., Lee, K., Oh, S., and Lim, Y. (2018). "Development of Construction Technique of LNG Storage Tank Wall Using Precast Concrete Panels". Paper presented at the IOP Conference Series: Materials Science and Engineering. vol. 431, no. 5, p. 052010. IOP Publishing.

Jones, K. (2021). Numerical investigation of lateral behaviour of a large pile group supporting an LNG tank. Doctoral dissertation.

Kabir, A., Maryak, M., and Bandyopadhyay, R. (1991). Seismic evaluation of a cooling water reservoir facility including fluid-structure and soil-structure interaction effects. (1)214, ASME PVP Conference, San Diego.

Kalantari, Afshin, Mohammad Reza Nikoomanesh, and Mohammad Ali Goudarzi.(2019) "Applicability of Mass-Spring Models for Seismically Isolated Liquid Storage Tanks." *Journal of Earthquake and Tsunami* 13, no. 01 (2019): 1950002.

Kausel, E., Whitman, R. V., Morray, J. P., and Elsabee, F. (1978). "The spring method for embedded foundations". Nuclear Engineering and design, 48(2-3), 377-392.

Kern, A., Schriever, U., and Stumpfe, J. (2007). "Development of 9% nickel steel for LNG applications". steel research international, 78(3), 189-194.

Khaheshi Banab, K., Kolaj, M., Motazedian, D., Sivathayalan, S., Hunter, J. A., Crow, H. L., Pyne, M. (2012). "Seismic site response analysis for Ottawa, Canada: A comprehensive study using measurements and numerical simulations". Bulletin of the Seismological Society of America, 102(5), 1976-1993.

Khansefid, A., Maghsoudi-Barmi, A., and Khaloo, A. (2019). "Seismic protection of LNG tanks with reliability based optimally designed combined rubber isolator and friction damper". Earthquakes and Structures, 16(5), 523-532.

Kianoush, M., and Ghaemmaghami, A. (2011). "The effect of earthquake frequency content on the seismic behavior of concrete rectangular liquid tanks using the finite element method incorporating soil–structure interaction". Engineering Structures, 33(7), 2186-2200.

Kim, J.-M., Chang, S.-H., and Yun, C.-B. (2002). "Fluid-structure-soil interaction analysis of cylindrical liquid storage tanks subjected to horizontal earthquake loading". Structural engineering and mechanics: An international journal, 13(6), 615-638.

Kolbadi, S. M. S., Alvand, R. A., and Mirzaei, A. (2018). "Three dimensional dynamic analysis of water storage tanks considering FSI using FEM". International Journal

of Civil and Environmental Engineering, 12(3), 377-386.

Kontoe, S., Avgerinos, V., and Potts, D. (2014). "Numerical validation of analytical solutions and their use for equivalent-linear seismic analysis of circular tunnels". Soil Dynamics and Earthquake Engineering, 66, 206-219

Koo, S., Han, J., Marimuthu, K. P., and Lee, H. (2019). "Determination of Chaboche combined hardening parameters with dual backstress for ratcheting evaluation of AISI 52100 bearing steel". International Journal of Fatigue, 122, 152-163.

Kramer, S. L. (1996). Geotechnical earthquake engineering: Pearson Education India.

Larkin, T. (2008). Seismic response of liquid storage tanks incorporating soil structure interaction. *Journal of geotechnical and geoenvironmental engineering*, *134*(12), 1804-1814.

Lee, I., Park, J., and Moon, I. (2017). "Conceptual design and exergy analysis of combined cryogenic energy storage and LNG regasification processes: Cold and power integration". Energy, 140, 106-115.

Lee, J., and Fenves, G. L. (1998a). "Plastic-damage model for cyclic loading of concrete structures". Journal of engineering mechanics, 124(8), 892-900.

Lee, J., and Fenves, G. L. (1998b). "A plastic-damage concrete model for earthquake analysis of dams". Earthquake Engineering & Structural Dynamics, 27(9), 937-956.

Lee, S. W., Choi, S. J., and Kim, J.-H. J. (2016). "Analytical study of failure damage to 270,000-kL LNG storage tank under blast loading". Computers and Concrete, 17(2), 201-214.

Lemaitre, J., and Chaboche, J. (1990). "Mechanics of solid mechanics". Cambridge University, Cambridge, United Kingdom, 161-241. \

Leon, G. S., and Kausel, E. A. (1986). "Seismic analysis of fluid storage tanks". Journal of Structural Engineering, 112(1), 1-18.

Lermo, J., and Chávez-García, F. J. (1993). "Site effect evaluation using spectral ratios with only one station". Bulletin of the Seismological Society of America, 83(5),

1574-1594.

Lermo, J., and Chávez-García, F. J. (1994). "Are microtremors useful in site response evaluation?". Bulletin of the Seismological Society of America, 84(5), 1350-1364.

Li, J., You, X., Cui, H., He, Q., and Ju, J. (2015). "Analysis of large concrete storage tank under seismic response". Journal of Mechanical Science and Technology, 29(1), 85-91.

Lin, C., Bennett, C., Han, J., and Parsons, R. L. (2010). "Scour effects on the response of laterally loaded piles considering stress history of sand". Computers and Geotechnics, 37(7-8), 1008-1014.

Lin, C., Bennett, C., Han, J., and Parsons, R. L. (2012). "Integrated analysis of the performance of pile-supported bridges under scoured conditions". Engineering Structures, 36, 27-38.

Lisowski, E., and Czyżycki, W. (2011). "Transport and storage of LNG in container tanks". Journal of KONES, 18, 193-201.

Liu, W. K. (1981). "Finite element procedures for fluid-structure interactions and application to liquid storage tanks". Nuclear Engineering and Design, 65(2), 221-238.

Lombardi, D., and Bhattacharya, S. (2014). "Modal analysis of pile-supported structures during seismic liquefaction". Earthquake Engineering & Structural Dynamics, 43(1), 119-138.

Lu, Y., Marshall, A. M., and Hajirasouliha, I. (2016). "A simplified Nonlinear Sway-Rocking model for evaluation of seismic response of structures on shallow foundations". Soil Dynamics and Earthquake Engineering, 81, 14-26.

Lubliner, J., Oliver, J., Oller, S., and Onate, E. (1989). "A plastic-damage model for concrete". International journal of solids and structures, 25(3), 299-326.

Lun, H., Fillippone, F., Roger, D. C., and Poser, M. (2006). "Design and construction aspects of post-tensioned LNG storage tank in Europe and Australasia". Paper presented at the New Zealand Concrete Industry Conference.

Lysmer, J., and Kuhlemeyer, R. L. (1969). "Finite dynamic model for infinite media". Journal of the Engineering Mechanics Division, 95(4), 859-877.

Ma, X., Cheng, Y. M., Au, S., Cai, Y., and Xu, C. (2009). "Rocking vibration of a rigid strip footing on saturated soil". Computers and Geotechnics, 36(6), 928-933.

Malhotra, P. K. (1997). New method for seismic isolation of liquid-storage tanks. *Earthquake engineering & structural dynamics*, *26*(8), 839-847.

Malhotra, P. K., Wenk, T., and Wieland, M. (2000). "Simple procedure for seismic analysis of liquid-storage tanks". Structural engineering international, 10(3), 197-201.

Masing, G. (1926). "Eigenspannumyen und verfeshungung beim messing". Paper presented at the Proc. Inter. Congress for Applied Mechanics.(1) 332-335.

Mazars, J., Berthaud, Y., and Ramtani, S. (1990). "The unilateral behaviour of damaged concrete". Engineering Fracture Mechanics, 35(4-5), 629-635.

McCullough, N., Hoffman, B., Takasumi, D., Anderson, D., and Dickenson, S. (2009). Seismic Site Response for an LNG Facility—Analyses and Lessons Learned. In TCLEE 2009: Lifeline Earthquake Engineering in a Multihazard Environment (pp. 1-12).

McDowell, D. L. (1992). "A nonlinear kinematic hardening theory for cyclic thermoplasticity and thermoviscoplasticity". International Journal of Plasticity, 8(6), 695-728.

Melgar, D., Crowell, B. W., Bock, Y., and Haase, J. S. (2013). "Rapid modeling of the 2011 Mw 9.0 Tohoku-Oki earthquake with seismogeodesy". Geophysical Research Letters, 40(12), 2963-2968.

Mendoza, M., and Auvinet, G. (1988). "The Mexico earthquake of September 19, 1985—behavior of building foundations in Mexico City". Earthquake Spectra, 4(4), 835-853.

Miglietta, P. C., Grasselli, G., and Bentz, E. C. (2016). "Finite/discrete element model of tension stiffening in GFRP reinforced concrete". Engineering Structures, 111, 494-504.

Miladi, S., and Razzaghi, M. S. (2019). "Failure analysis of an un-anchored steel oil tank damaged during the Silakhor earthquake of 2006 in Iran". Engineering Failure Analysis, 96, 31-43.

Mizuno, D., Suzuki, S., Fujita, S., and Hara, N. (2014). "Corrosion monitoring and materials selection for automotive environments by using Atmospheric Corrosion Monitor (ACM) sensor". Corrosion Science, 83, 217-225.

Moczo, P., Kristek, J., Vavrycuk, V., Archuleta, R. J., and Halada, L. (2002). "3D heterogeneous staggered-grid finite-difference modeling of seismic motion with volume harmonic and arithmetic averaging of elastic moduli and densities". Bulletin of the Seismological Society of America, 92(8), 3042-3066.

Montalva, G. A., Chávez-Garcia, F. J., Tassara, A., and Jara Weisser, D. M. (2016). "Site effects and building damage characterization in Concepción after the Mw 8.8 Maule earthquake". Earthquake Spectra, 32(3), 1469-1488.

Mucciacciaro, M., and Sica, S. (2018). "Nonlinear soil and pile behaviour on kinematic bending response of flexible piles". Soil Dynamics and Earthquake Engineering, 107, 195-213.

Murray, A., Gilbert, R. I., and Castel, A. (2018). "A new approach to modeling tension stiffening in reinforced concrete". ACI Structural Journal, 115(1), 127-137.

Mylonakis, G. (2001). "Elastodynamic model for large-diameter end-bearing shafts". Soils and Foundations, 41(3), 31-44.

Mylonakis, G., and Gazetas, G. (2000). "Seismic soil-structure interaction: beneficial or detrimental?". Journal of earthquake engineering, 4(3), 277-301.

Mylonakis, G., Nikolaou, A., and Gazetas, G. (1997). "Soil–pile–bridge seismic interaction: kinematic and inertial effects. Part I: soft soil". Earthquake engineering & structural dynamics, 26(3), 337-359.

Mylonakis, G., Nikolaou, S., and Gazetas, G. (2006). "Footings under seismic loading: Analysis and design issues with emphasis on bridge foundations". Soil Dynamics and Earthquake Engineering, 26(9), 824-853.

Nagashima, M., Tsuchiya, M., and Asada, M. (2011). "Reducing the economic risk of

LNG tank construction under conditions of fluctuating resource prices". Journal of construction engineering and management, 137(5), 382-391.

Nakamura, S., Wakai, A., Umemura, J., Sugimoto, H., and Takeshi, T. (2014). "Earthquake-induced landslides: distribution, motion and mechanisms". Soils and Foundations, 54(4), 544-559.

Nateghi, F., and Yakhchalian, M. (2011). "Seismic behavior of reinforced concrete silos considering granular material-structure interaction". Procedia engineering, 14, 3050-3058.

Navarro, M., García-Jerez, A., Alcalá, F., Vidal, F., and Enomoto, T. (2014). "Local site effect microzonation of Lorca town (SE Spain)". Bulletin of Earthquake Engineering, 12(5), 1933-1959.

Nayal, R., and Rasheed, H. A. (2006). "Tension stiffening model for concrete beams reinforced with steel and FRP bars". Journal of Materials in Civil Engineering, 18(6), 831-841.

Novak, M. (1991). "Piles under dynamic loads". Proc., 2nd Int. Conf. on Recent Advances in Geotech. Engrg. and Soil Dyn., Univ. of Miss.- Rolla, Rolla, 2433–2456.

NZS1170.5. (2004). Structural design actions part 5: Earthquake actions-new zealand-commentary. . In: NZS 1170.5 Supp1: 2004. Standards New Zealand. .

PEER (Pacific Earthquake Engineering Research Center). 2014. "PEER ground motion database." Accessed February 12, 2018.

Pegler, G., and Das, S. (1996). "The 1987–1992 Gulf of Alaska earthquakes". Tectonophysics, 257(2-4), 111-136.

Peiris, N., Cushing, A., Lubkowski, Z., and Scarr, D. (2006). "Dynamic analysis and design of large-diameter LNG tanks to resist seismic events". Paper presented at the First European Conference on Earthquake Engineering and Seismology, 3-8 September, Geneva, Switzerland.

Rahvar. (2006). "Geotechnical investigations and foundation design report of Kooh-e-Noor commercial building". Final Rep. Iran.

Rasouli, H., and Fatahi, B. (2019). "A novel cushioned piled raft foundation to protect buildings subjected to normal fault rupture". Computers and Geotechnics, 106, 228-248.

Rasouli, H., and Fatahi, B. (2021). "Geosynthetics reinforced interposed layer to protect structures on deep foundations against strike-slip fault rupture". Geotextiles and Geomembranes, 49(3), 722-736.

Rawat, A., Matsagar, V., and Nagpal, A. (2020). "Seismic Analysis of Steel Cylindrical Liquid Storage Tank Using Coupled Acoustic-Structural Finite Element Method For Fluid-Structure Interaction". International Journal of Acoustics & Vibration, 25(1).

Rayamajhi, D., Nguyen, T. V., Ashford, S. A., Boulanger, R. W., Lu, J., Elgamal, A., and Shao, L. (2014). "Numerical study of shear stress distribution for discrete columns in liquefiable soils". Journal of Geotechnical and Geoenvironmental Engineering, 140(3), 04013034.

Razzaghi, M. S., and Eshghi, S. (2015). "Probabilistic seismic safety evaluation of precode cylindrical oil tanks". Journal of Performance of Constructed Facilities, 29(6), 04014170.

Riepl, J., Bard, P.-Y., Hatzfeld, D., Papaioannou, C., and Nechtschein, S. (1998). "Detailed evaluation of site-response estimation methods across and along the sedimentary valley of Volvi (EURO-SEISTEST)". Bulletin of the Seismological Society of America, 88(2), 488-502.

Rodriguez, M. E., and Montes, R. (2000). "Seismic response and damage analysis of buildings supported on flexible soils". Earthquake engineering & structural dynamics, 29(5), 647-665.

Rostami, R., Hytiris, N., Bhattacharya, S., and Giblin, M. (2017). "Seismic analysis of pile in liquefiable soil and plastic hinge". Geotechnical Research, 4(4), 203-213.

Saenz, L. P. (1964). "discussion of" Equation for the Stress-Strain Curve of Concrete" by Desayi and Krishnan". Journal of the American Concrete Institute, 61, 1229-1235.

Şafak, E. (2001). "Local site effects and dynamic soil behavior". Soil Dynamics and

Earthquake Engineering, 21(5), 453-458.

Sakr, M. A., Sleemah, A. A., Khalifa, T. M., and Mansour, W. N. (2019). "Shear strengthening of reinforced concrete beams using prefabricated ultra-high performance fiber reinforced concrete plates: Experimental and numerical investigation". Structural Concrete, 20(3), 1137-1153.

Satake, K., and Abe, K. (1983). "A fault model for the Niigata, Japan, earthquake of June 16, 1964". Journal of Physics of the Earth, 31(3), 217-223.

Sato, Y., Kano, N., Okamai, A., and Kataoka, S. (2020). "Features of LNG tank Civil Engineering". JGC Technical Journal Vol.7 No.2.

Seed, H. B., and Idriss, I. M. (1969). "Influence of soil conditions on ground motions during earthquakes". Journal of the Soil Mechanics and Foundations Division, 95(1), 99-137.

Seed, H. B., Wong, R. T., Idriss, I., and Tokimatsu, K. (1986). "Moduli and damping factors for dynamic analyses of cohesionless soils". Journal of geotechnical engineering, 112(11), 1016-1032.

SeismoMatch. (2016). Seismosoft. Seismomatch.A computer program for adjusting earthquake records to match a specific target response spectrum. . Pavia.

Semblat, J.-F., and Brioist, J. (2009). "Efficiency of higher order finite elements for the analysis of seismic wave propagation". arXiv preprint arXiv:0901.3715.

Semblat, J.-F., Gandomzadeh, A., and Lenti, L. (2010). "A simple numerical absorbing layer method in elastodynamics". Comptes Rendus Mecanique, 338(1), 24-32.

Shing, P. B., and Tanabe, T.-a. (2001). Modeling of inelastic behavior of RC structures under seismic loads: Dearborn, MI: American Society of Civil Engineers.

Shu, L., Gu, H., Shi, G., You, Y., and Zhen, J. (2007). "Design and construction techique of large LNG PC Tank". Industrial Buildings, 11, 32-44.

Solakivi, T., Laari, S., Kiiski, T., Töyli, J., and Ojala, L. (2019). "How shipowners have adapted to sulphur regulations–Evidence from Finnish seaborne trade". Case Studies on Transport Policy, 7(2), 338-345.

Son, I.-M., and Kim, J.-M. (2019). "Evaluation of Soil-Structure Interaction Responses of LNG Storage Tank Subjected to Vertical Seismic Excitation Depending on Foundation Type". Journal of the Computational Structural Engineering Institute of Korea, 32(6), 367-374.

Spritzer, J., and Guzey, S. (2017a). "Nonlinear numerical evaluation of large open-top aboveground steel welded liquid storage tanks excited by seismic loads". Thin-Walled Structures, 119, 662-676.

Spritzer, J., and Guzey, S. (2017b). "Review of API 650 Annex E: Design of large steel welded aboveground storage tanks excited by seismic loads". Thin-Walled Structures, 112, 41-65.

Spyrakos, C., Koutromanos, I., and Maniatakis, C. A. (2009). "Seismic response of base-isolated buildings including soil–structure interaction". Soil Dynamics and Earthquake Engineering, 29(4), 658-668.

Standards Australia. 2007. Structural design actions; Part 4: Earthquake actions in Australia. AS1170.4. Sydney, NSW, Australia: Standards Australia.

Standards Australia. 2017. The storage and handling of liquefied natural gas. AS 3961. Sydney, NSW, Australia: Standards Australia.

Stewart, J. P., Seed, R. B., and Fenves, G. L. (1999). "Seismic soil-structure interaction in buildings. II: Empirical findings". Journal of Geotechnical and Geoenvironmental Engineering, 125(1), 38-48.

Sun, J., and Cui, L. (2015). "Seismic Response for Base Isolation of Storage Tanks with Soil-Structure Interaction". Physical and Numerical Simulation of Geotechnical Engineering(18), 64.

Sun, J. I., Golesorkhi, R., and Seed, H. B. (1988). Dynamic moduli and damping ratios for cohesive soils: Earthquake Engineering Research Center, University of California Berkeley.

Tabatabaiefar, H. R., and Fatahi, B. (2014). "Idealisation of soil–structure system to determine inelastic seismic response of mid-rise building frames". Soil Dynamics and Earthquake Engineering, 66, 339-351.

Tabatabaiefar, H. R., and Massumi, A. (2010). "A simplified method to determine seismic responses of reinforced concrete moment resisting building frames under influence of soil–structure interaction". Soil Dynamics and Earthquake Engineering, 30(11), 1259-1267.

Tahnat, Y. B. A., Dwaikat, M. M., and Samaaneh, M. A. (2018). "Effect of using CFRP wraps on the strength and ductility behaviors of exterior reinforced concrete joint". Composite Structures, 201, 721-739.

Tokimatsu, K., Mizuno, H., and Kakurai, M. (1996). "Building damage associated with geotechnical problems". Soils and foundations, 36, 219-234.

Trifunac, M., and Todorovska, M. (1996). "Nonlinear soil response—1994 Northridge, California, earthquake". Journal of geotechnical engineering, 122(9), 725-735.

Tucker, B., King, J., Hatzfeld, D., and Nersesov, I. (1984). "Observations of hard-rock site effects". Bulletin of the Seismological Society of America, 74(1), 121-136.

Van Nguyen, Q., Fatahi, B., and Hokmabadi, A. S. (2016). "The effects of foundation size on the seismic performance of buildings considering the soil-foundation-structure interaction". Structural Engineering and Mechanics. 58 (6), 1045-1075.

Van Nguyen, Q., Fatahi, B., and Hokmabadi, A. S. (2017). "Influence of size and load-bearing mechanism of piles on seismic performance of buildings considering soil–pile–structure interaction". International Journal of Geomechanics, 17(7), 04017007.

Veletsos, A. (1974). "Seismic effects in flexible liquid storage tanks". Paper presented at the Proceedings of the 5th world conference on earthquake engineering. (Vol. 1, pp. 630-639)

Veletsos, A., and Tang, Y. (1990). "Soil-structure interaction effects for laterally excited liquid storage tanks". Earthquake Engineering & Structural Dynamics, 19(4), 473-496.

Veletsos, A. S., and Meek, J. W. (1974). "Dynamic behaviour of building-foundation systems". Earthquake engineering & structural dynamics, 3(2), 121-138.

Veletsos, A. S., and Tang, Y. (1987). "Rocking response of liquid storage tanks". Journal

of Engineering Mechanics, 113(11), 1774-1792.

Virella, J., Godoy, L., and Suárez, L. (2006). "Dynamic buckling of anchored steel tanks subjected to horizontal earthquake excitation". Journal of Constructional Steel Research, 62(6), 521-531.

Virella, J. C., Godoy, L. A., and Suárez, L. E. (2006). "Fundamental modes of tank-liquid systems under horizontal motions". Engineering Structures, 28(10), 1450-1461.

Wahalathantri, B., Thambiratnam, D., Chan, T., and Fawzia, S. (2011). "A material model for flexural crack simulation in reinforced concrete elements using ABAQUS". Paper presented at the Proceedings of the first international conference on engineering, designing and developing the built environment for sustainable wellbeing. pp. 260-264. Queensland University of Technology, Australia.

Wang, D., Randolph, M., and White, D. (2013). "A dynamic large deformation finite element method based on mesh regeneration". Computers and Geotechnics, 54, 192-201.

Wang, S., and Hao, H. (2002). "Effects of random variations of soil properties on site amplification of seismic ground motions". Soil Dynamics and Earthquake Engineering, 22(7), 551-564.

Wang, S., and Hao, H. (2002). "Effects of random variations of soil properties on site amplification of seismic ground motions". Soil Dynamics and Earthquake Engineering, 22(7), 551-564.

Westergaard, H. M. (1933). "Water pressures on dams during earthquakes". Transactions of the American Society of Civil Engineers, 98(2), 418-433.

Willford, M., Sturt, R., Huang, Y., Almufti, I., and Duan, X. (2010). "Recent advances in nonlinear soil-structure interaction analysis using LS-DYNA". Paper presented at the Proceedings of the NEA-SSI Workshop. (pp. 6-8)

Wolf, J. P., and Song, C. (2002). "Some cornerstones of dynamic soil–structure interaction". Engineering Structures, 24(1), 13-28.

Wolf, J. (1985). "Dynamic soil-structure-interaction Englewood Cliffs". Inc., Prentice-Hall, New Jersey.USA.

Xu, R., and Fatahi, B. (2018). "Influence of geotextile arrangement on seismic performance of mid-rise buildings subjected to MCE shaking". Geotextiles and Geomembranes, 46(4), 511-528.

Xu, R., and Fatahi, B. (2019). "Novel application of geosynthetics to reduce residual drifts of mid-rise buildings after earthquakes". Soil Dynamics and Earthquake Engineering, 116, 331-344.

Yan, C., Zhai, X.-m., and Wang, Y.-h. (2019). "Numerical study on the dynamic response of a massive liquefied natural gas outer tank under impact loading". Journal of Zhejiang University-SCIENCE A, 20(11), 823-837.

Yeganeh, N., and Fatahi, B. (2019). Effects of choice of soil constitutive model on seismic performance of moment-resisting frames experiencing foundation rocking subjected to near-field earthquakes. *Soil Dynamics and Earthquake Engineering*, *121*, 442-459

Yunita, H., and Apriadi, D. (2015). An Overview of Soil Models for Earthquake Response Analysis. *Journal of Engineering & Technological Sciences*, *47*(1).

Zakavi, S., Ajri, M., and Golshan, V. (2014). "The ratcheting behaviour of plain carbon steel pressurized piping elbows subjected to simulated seismic in-plane bending". World Journal of Mechanics. (4) 07-09

Zalachoris, G., and Rathje, E. M. (2015). "Evaluation of one-dimensional site response techniques using borehole arrays". Journal of Geotechnical and Geoenvironmental Engineering, 141(12), 04015053.

Zhai, X., Zhao, X., and Wang, Y. (2019). "Numerical modeling and dynamic response of 160,000-m 3 liquefied natural gas outer tank under aircraft impact". Journal of Performance of Constructed Facilities, 33(4), 04019039.

Zhang, C., Wan, L., Magee, A. R., Han, M., Jin, J., Ang, K. K., and Hellan, (2019). "Experimental and numerical study on the hydrodynamic loads on a single floating hydrocarbon storage tank and its dynamic responses". Ocean Engineering, 183, 437-452.

Zhang, L. X., Tan, X. J., Liu, J. P., and Zhong, J. R. (2012). "Seismic response analysis

of large liquid storage tank considering fluid-structure interaction". Paper presented at the Advanced Materials Research. (Vol. 368, pp. 983-987)

Zhang, R., Jia, J., Wang, H., and Guan, Y. (2018). "Shock response analysis of a large LNG storage tank under blast loads". KSCE Journal of Civil Engineering, 22(9), 3419-3429.

Zhang, R., Weng, D., and Ren, X. (2011). "Seismic analysis of a LNG storage tank isolated by a multiple friction pendulum system". Earthquake Engineering and Engineering Vibration, 10(2), 253-262.

Zhang, Y., and Wan, D. (2019). "MPS-FEM coupled method for fluid–structure interaction in 3d dam-break flows". International Journal of Computational Methods, 16(02), 1846009.

Zhang, Y., Zhang, J., Chen, G., Zheng, L., and Li, Y. (2015). "Effects of vertical seismic force on initiation of the Daguangbao landslide induced by the 2008 Wenchuan earthquake". Soil Dynamics and Earthquake Engineering, 73, 91-102.

Zhao, Y., Li, H.-N., Zhang, S., Mercan, O., and Zhang, C. (2020). "Seismic Analysis of a Large LNG Tank Considering Different Site Conditions". Applied Sciences, 10(22), 8121.

Zhu, X.-K. (2019). "Effect of Plastic Hardening Models on Fatigue Life Simulation of Pipeline Elbows Under Operating Pressure and Cyclic Bending". Journal of Pressure Vessel Technology, 141(6), 061407.

Zhuang, H., Hu, Z., Wang, X., and Chen, G. (2015). "Seismic responses of a large underground structure in liquefied soils by FEM numerical modelling". Bulletin of Earthquake Engineering, 13(12), 3645-3668.

Ziegler, H. (1959). "A modification of Prager's hardening rule". Quarterly of Applied mathematics, 17(1), 55-65.

Zienkiewicz, O., Emson, C., and Bettess, P. (1983). "A novel boundary infinite element". International Journal for Numerical Methods in Engineering, 19(3), 393-404.

Zlatanović, E., Lukić, D. Č., Prolović, V., Bonić, Z., and Davidović, N. (2015). "Comparative study on earthquake-induced soil–tunnel structure interaction

effects under good and poor soil conditions". European Journal of Environmental and Civil Engineering, 19(8), 1000-1014. *3*(1), 1-7.